UNIVERSIDADE FEDERAL DO RIO GRANDE DO SUL

PROGRAMA DE PÓS-GRADUAÇÃO EM FÍSICA

Tese de Doutorado

Perfis de duplo-pico: revelando a presença de discos de acreção na região de linhas largas de galáxias ativas *

Jáderson da Silva Schimoia

Tese realizada sob orientação da Professora Dra. Thaisa Storchi Bergmann e apresentada ao Instituto de Física da UFRGS em preenchimento parcial dos requisitos para a obtenção do título de Doutor em Ciências.

Porto Alegre

Setembro, 2015

*Trabalho financiado pela CAPES.

Resumo

A energia emitida pelos núcleos ativos de galáxias (AGN's) é provida através do escoamento acretivo de matéria em direção ao buraco negro super massivo central (SMBH). Tal escoamento se dá sob a forma de um disco de acreção. As principais evidências observacionais da presença do disco são: (i) sua emissão térmica nos AGN's mais luminosos, que dá origem ao chamado *big blue bump* observado na região espectral do ultravioleta e (ii) a emissão de linhas largas com duplo-pico, entendidas como provenientes da recombinação do Hidrogênio nas regiões mais externas do disco de acreção. Os AGN's menos luminosos, LLAGN's, não apresentam o *big blue bump*, o que sugere que o disco de acreção tem uma natureza diferente; sua distribuição espectral de energia tem sido modelada através de um disco que é espesso na região interna, num regime de acreção de gás "radiativamente ineficiente"(RIAF), que é responsável pela emissão de fótons de mais alta energia (raios-X). Neste trabalho, apresentamos o monitoramento espectral de 2 LLAGN's que apresentam linhas de emissão largas de Hα (FWHM $\sim$10.000 km/s) com duplo-pico: NGC 1097 e NGC 7213. Acredita-se que estas linhas sejam emitidas pelo gás que se encontra na parte mais externa do disco de acreção, que é ionizado pelos raios-X emitidos pelo RIAF central. No caso de NGC 1097, monitoramos o AGN em raios-X e UV – usando o satélite Swift, e também o perfil em duplo-pico – usando o telescópio SOAR entre agosto de 2012 e fevereiro de 2013. Este monitoramento permitiu que estudássemos a amplitude variacional de cada uma das curvas de luz obtidas e também aplicássemos a técnica de correlação cruzada entre as curvas de luz de raio-X e do ótico com o objetivo de elucidar se as variações no perfil em duplo-pico são reverberações das variações do contínuo ionizante de alta energia. Através deste monitoramento conseguimos colocar vínculos do limite superior para a escala de variabilidade mais curta do perfil, $\sim$ 5 dias, assim como através da modelagem dos perfis colocar vínculos na estrutura da região emissora. No caso de NGC 7213 monitoramos o perfil em duplo-pico do AGN entre setembro de 2011 e julho de 2013. Observamos variabilidades do perfil em duas escalas de tempo: (1) a *mais curta*, entre 7 e 28 dias, associada as variações do fluxo total integrado do perfil e outra (2) *mais longa* $\gtrsim$ 3 meses, nas variações da intensidade relativa dos fluxos dos lados azul e vermelho do perfil e associada a escala de tempo dinâmica do disco de acreção. Modelamos a emissão em duplo-pico deste objeto como originária de um disco de acreção Kepleriano e relativístico, cujas características de variabilidade observadas podem ser explicadas através da rotação de um braço espiral no disco cuja emissão é maior do que a do disco subjacente. Por fim, estendemos a modelagem dos perfis de emissão largos de Hα para as galáxias Seyfet 1 do Palomar Sky Survey of Nearby Galaxies que apresentam emissão em duplo-pico: NGC 3516, NGC 4151, NGC 4235, NGC 5273, NGC 5548. Concluímos que os perfis de emissão largos nesses objetos mais luminosos requerem uma modelagem com duas componentes: (1) uma muito larga e de duplo-pico que é originária da emissão do gás no disco de acreção; (2) e outra componente Gaussian de mais baixa velocidade para reproduzir a parte mais central do perfil, associada ao gás localizado além do disco. Identificamos que a componente disco é dominante em relação a emissão e que o ângulo de inclinação do disco é o parâmetro mais importante na modelagem do perfil desses objetos.

A geometria tipo disco tem implicações para a determinação da massa do buraco negro em galáxias ativas através do produto virial $M_\bullet = f \times \frac{R_{BLR}\Delta V^2}{G}$ e identificando a relação entre o fator f e a largura da linha propomos um aprimoramento na obtenção de $M_\bullet$ em galáxias ativas.

Abstract

The energy emitted by active galactic nuclei (AGN) is powered via accretion flows onto the central supermassive black hole (SMBH), usually in the form of an "accretion disk"in which the gas slowly spirals towards the SMBH. The most clear spectral signatures of accretion disks are: (i) their thermal emission in the most luminous AGN, which originates the so called *big blue bump* observed in the ultravaviolet and (ii) the emission of broad double-peaked lines, which are thought to originate via recombination of H and He atoms in the outer parts of the accretion disk. The low luminosity AGN's (LLAGN), usually do not show the *big blue bump*, suggesting that their accretion flows are distinct; indeed, their spectral energy distribution have been modeled by an accretion disk in which the innermost part is geometrically thick, accreting in a radiativelly inefficient regime (RIAF) that emits high energy fotons (X-rays). In this work, we present the spectral monitoring of 2 LLAGN – NGC 1097 and NGC 7213 – that show broad (10,000 $\mathrm{km\,s^{-1}}$) double-peaked Hα emission lines, thought to be emitted by the gas in the outer parts of the accretion disk, which is ionized by the X-rays emitted by the central RIAF. In the case of NGC 1097, we monitored the AGN in X-rays and UV – using the Swift satellite, and also the double-peaked profile – using the SOAR telescope between 2012 August and 2013 February. This monitoring allowed us to study the variability amplitude of each light curve as well as to apply the cross correlation technique to the light curves in X-rays and optical in order to investigate if the variations in the double-peaked profile are a reverberation of the variations in X-rays and UV (ionizing radiation). The monitoring allowed us to put constraints on the minimum variability timescale and on the structure of the line-emiting region. In the case of NGC 7213 we monitired the broad double-peaked profile between 2011 September and 2013 July. We detected variabiliy of the profile in two timescales: (1) the shortest, beween 7 and 28 days, associated with vatiations in the integrated flux of the double-peaked line and another (2) larger, $\gtrsim$ 3 months, associated with variations in the relative intensity of the fluxes of the blue and red sides of the profile and identified with the dynamical timescale of the accretion disk. We modeled the double-peaked emission of this object as due the gas emission in a Keplerian and relativistic accretion disk, whose the variability features can be explained via rotation of a spiral arm in the disk which is brigther than the underlying disk. Finally, we extended the study of the modeling of broad Hα profiles to Seyfet 1 galaxies that display double-peaked profiles in the Palomar Sky Surver of Nearby Galaxies, namely NGC 3516, NGC 4151, NGC 4235, NGC 5273, NGC 5548. We concluded that the broad Hα emission profiles of these galaxies require a two component modeling: (1) a very broad and double-peaked component originating from the gas in the accretion disk and another (2) low-velocity Gaussian component required to reproduce the center of the profile, associated with gas at lower velocities probably beyond the disk. We concluded that the disk component dominates at highest velocities and the inclination is the most important parameter in the determination of the width of the double-peaked profiles. The disk-like geometry has implications for the determination of the mass of the central SMBH in AGN via the virial product $M_\bullet = f \times \frac{R_{BLR}\Delta V^2}{G}$ and by identifying

a relation between the factor f and the width of the broad line we propose an improvement in the estimate of the SMBH masses in Type 1 AGN.

Sumário

Lista de Tabelas

Lista de Figuras

Lista de Abreviaturas

AGN *active galactic nucleus*

CCD *Charge-Coupled Device*

FWHM *full width at half maximum*

GMOS *Gemini Multi-Object Spectrograph*

ICCF *Interpolated Cross Correlation Function*

IRAF *Image Reduction and Analysis Facility*

LINER *low-ionization emission-line region*

NGC *New Galactic Catalog*

QSRS *quasi-stellar radio source (Quasar)*

RM *Reverberation Mapping*

RIAF *radiatively inefficient accretion flow*

SED *spectral energy distribution*

SMBH *supermassive black hole*

SOAR *Southern Astrophysical Research Telescope*

UV *Ultravioleta*

UVOT *Ultraviolet/Optical Telescope*

XRT *X-ray Telescope*

3C *3rd Cambridge Catalog*

Capítulo 1

Introdução

1.1 A atividade nuclear e seu papel na evolução das galáxias

A hipótese de que as regiões centrais das galáxias poderiam abrigar poderosas e compactas fontes de energia começou a ganhar força na década de 1960 a partir das observações espectroscópicas dos Quasares (*Quasi stellar rádio sources*). Os *redshifts* desses objetos os colocavam dentre os mais distantes objetos astronômicos conhecidos na época, e isto implicava que deveriam ser pelo menos 40 vezes mais brilhantes do que as galáxias mais luminosas já conhecidas. A evidência de que realmente os quasares tratavam-se de regiões extremamente luminosas residindo no núcleo das galáxias veio somente na década de 1980. Por exemplo, Boroson & Oke (1982) examinaram a luz difusa ao redor do Quasar 3C 48, e descobriram que tratava-se na verdade da luz estelar de uma galáxia. Entretanto, ainda faltava explicar como essas regiões compactas poderiam gerar as quantidades copiosas de energia que eram observadas.

A descoberta dos Quasares motivou os trabalhos de Zel'dovich (1964), Salpeter (1964) e Lynden-Bell (1969), que, de maneira independente, propuseram que a acreção de matéria a buracos negros supermassivos (SMBH - *super massive black holes*), com massas da ordem de um bilhão de massas solares, poderia ser o mecanismo responsável por gerar as altas quantidades de energia emitidas por estes núcleos compactos. Nos anos que seguiram à proposta, intenso trabalho teórico foi realizado na tentativa de formular um modelo físico detalhado de como ocorreria a acrecão de gás a objetos massivos. Em 1972 Pringle & Rees (1972) e em 1973 Shakura & Sunyaev (1973) apresentaram uma forma plausível para a acreção de matéria em direção a SMBH's. Nesse modelo, à medida que o gás circundante espirala em direção ao SMBH central num disco chamado de "disco de acreção"(*accretion disk*), a energia potencial gravitacional é convertida em radiação com alta eficiência, o que implica a emissão de grandes quantidades de energia.

Longe de serem objetos raros, atualmente acredita-se que os SMBH's habitam os núcleos da maioria das galáxias do Universo. Entretanto, a atividade nuclear é observada apenas quando há um reservatório de gás disponível para 'alimentar' (*feed*) o SMBH. As altas luminosidades não são os únicos processos observados como decorrentes da atividade nuclear. Também podem ser observados outros processos de "retro-alimentação"do SMBH (*feedback*). Estes processos de *feedback* incluem a emissão de radiação, e também ejeções de gás (*outflows*) gerados a partir do disco de acreção. As ejeções podem ser na forma de jatos de partículas relativísticas, originados na borda interna do disco de acreção e que podem alcançar, nos casos mais extremos, distâncias bem maiores do que o limite da galáxia. Há 'outflows' também na forma de ventos originados das partes mais externas do disco de acreção. Simulações cosmológicas recentes têm mostrado que processos de fusão entre galáxias, além de disparar a formação estelar, provocam também influxos de gás em direção a região central das galáxias. Quando tal influxo chega ao núcleo e começa a alimentar (*feed*) o SMBH, dispara a atividade nuclear, produzindo emissão de radiação e os *outflows*. Estes processos de feedback

injetam energia no meio interestelar da galáxia e fornecem um possível mecanismo para regular o crescimento da galáxia: já que essa injeção de energia impede que o gás colapse para formar novas estrelas, cessando a formação estelar, acaba 'regulando' o crescimento do bojo da galáxia (Di Matteo et al., 2005, 2008).

A idéia de que a presença do *feedback* do AGN pode influenciar os processos de formação estelar em larga escala da galáxia tem implicações na evolução das galáxias, e na sua distribuição morfológica no Universo local. É sabido que galáxias do Universo local ($z \leq 1$) exibem uma bimodalidade no diagrama que relaciona a sua cor, U-B, com a sua massa $\log_{10} M_{gal}$. As galáxias mais massivas, em sua maioria gigantes elípticas, são também as mais vermelhas e compõem a chamada sequência vermelha (*red sequence*), enquanto que as galáxias mais azuis, tipicamente galáxias espirais e menos massivas, se concentram na nuvem azul (*blue cloud*) (Baldry et al., 2004). O principal argumento usado para explicar a bimodalidade é que as galáxias migram da nuvem azul em direção a sequência vermelha através de dois mecanismos: (i) o cessamento abrupto da da formação estelar na galáxia e de (ii) *wet mergers*, que são fusões entre galáxias ricas em gás. Uma vez estando na sequência vermelha, as galáxias sofrem *dry mergers*, que são fusões entre galáxias pobres em gás, formando assim as galáxias vermelhas mais massivas encontradas no topo da sequência vermelha (Faber et al., 2007). A região intermediária do diagrama, entre a *blue cloud* e a *red sequence*, é comumente referida como vale verde (*green valey*) e é povoada por uma fração significativa das galáxias com núcleos ativos do Universo local. De fato, Kauffmann et al. (2003) mostraram que galáxias com AGN's apresentam uma mistura de população estelar jovem e velha, e, devido a isto, as suas cores no diagrama cor-massa estão sobre o *green valley*. Isto sugere que se realmente a retro-alimentação do AGN está associada ao cessamento da formação estelar da galáxia, a presença do AGN contribui para a migração das galáxias entre a *blue cloud* e a *red sequence*. Do ponto de vista observacional, ainda são necessários mais vínculos que reforcem a hipótese de que o *feedback* do AGN pode influenciar de fato a formação estelar na galáxia. Nesse sentido, extensivo trabalho tem sido feito com o intuito de quantificar as taxas de influxo (*feeding*) e as taxas de ejeção (*feedback*) de matéria nas regiões centrais ($< 1\,\mathrm{kpc}$) de galáxias ativas, bem como de mapear espacialmente estes mecanismos (e.g., Storchi-Bergmann, 2014, Riffel et al., 2014, Schnorr-Müller et al., 2014b).

1.2 O paradigma da atividade nuclear

Núcleos ativos (AGN's) são regiões espacialmente não resolvidas no centro das galáxias, de raio menor que um parsec, cuja distribuição espectral de energia (*Spectral Energy Distribution* – SED) não pode ser explicada somente como sendo originada a partir da radiação proveniente de estrelas. Os AGN's menos luminosos, como os LINER's (*Low-ionization emission-line region*, Heckman, 1980), possuem

luminosidades bolométicas no intervalo $L_{Bol} \sim 10^{42-43}\,\mathrm{erg\,s^{-1}}$ enquanto que os mais luminosos, chamados Quasares, chegam a $L_{Bol} \sim 10^{46-48}\,\mathrm{erg\,s^{-1}}$. Luminosidades intermediárias entre as dos núcleos LINER's e de Quasares são observadas nas galáxias Seyferts, que têm luminosidades típicas de $L_{Bol} \sim 10^{43-46}\,\mathrm{erg\,s^{-1}}$. Para os Quasares e algumas galáxias Seyferts, a luminosidade do AGN supera a luminosidade da própria galáxia hospedeira.

Para entender a origem da energia emitida por um AGN, primeiramente consideremos somente a energia liberada pelos processos nucleares no interior das estrelas. Esses processos têm uma eficiência de $\eta_{star} \sim 0.007$ (Frank et al., 2002) na conversão de matéria em energia. Considerando que a lumminosidade do Sol é $\mathrm{L_\odot} = 3.9 \times 10^{33}\,\mathrm{erg\,s^{-1}}$, concluímos que precisaríamos ter aproximadamente 10^{13} estrelas confinadas em uma região menor que um parsec cúbico para produzir a luminosidade típica de um AGN ($L_{Bol} \sim 10^{45}\,\mathrm{erg\,s^{-1}}$). Uma vez que esse número excede o número de estrelas existentes em uma galáxia, os processos estelares não podem sozinhos explicar as luminosidades observadas dos AGN's.

Por outro lado, considerando o caso de acreção simetricamente esférica de matéria, em que um corpo de massa m 'cai' em direção a um SMBH de massa $\mathrm{M_\bullet}$, podemos estimar a taxa com que a energia potencial gravitacional (U) é liberada na queda do corpo desde o infinito até uma distância radial, r, do SMBH:

$$L = \frac{dU}{dt} = \frac{d}{dt}\left(\frac{GM_\bullet m}{r}\right) = \frac{GM_\bullet \dot{m}}{r} \tag{1.1}$$

onde G é a constante gravitacional.

Para um corpo que "cai"até as proximidades do SMBH, por exemplo até $r \approx 5\,R_{Sch}$ – onde $R_{Sch} = 2GM_\bullet/c^2$ é o raio de Schwarzchild que delimita o horizonte de eventos e c é a velocidade da luz – estimamos que potência liberada é da ordem de:

$$L = \frac{GM_\bullet \dot{m} c^2}{10GM_\bullet} \approx 0.1\dot{m}c^2 \tag{1.2}$$

Podemos expressar este resultado em termos da taxa de conversão da energia de repouso do corpo de massa m em radiação, com uma eficiência η:

$$L = \frac{dE}{dt} = \frac{d(\eta m c^2)}{dt} = \eta \dot{m} c^2 \tag{1.3}$$

A eficiência resultante do processo de queda gravitacional para um buraco negro resulta numa eficiência $\eta \sim 0.1$, muito superior a eficiência dos processos de fusão nuclear em estrelas ($\eta_{star} \sim 0.007$).

A medida que a matéria é acretada, a transformação de energia potencial gravitacional em radiação faz com que haja uma competição entre a força gravitacional e a força exercida pela

pressão de radiação. Podemos obter uma estimativa simples da massa do SMBH central que é necessária para gerar as luminosidades tipicamente observadas nos AGN's equalizando a força de atração gravitacional exercida pelo SMBH com a força exercida pela pressão de radiação (Peterson, 1997):

$$L \leq \frac{4\pi G c m_p M_\bullet}{\sigma_T} \approx 1.26 \times 10^{38} \left(\frac{M_\bullet}{M_\odot}\right) \,\mathrm{erg\,s^{-1}} \tag{1.4}$$

onde m_p é a massa do próton, σ_T é a sessão de choque de espalhamento de Thompson, $M_\odot$ é a massa do Sol e $M_\bullet$ é a massa do SMBH central[1]. Desta forma, sistemas acretantes cujas massas dos buracos negros centrais estão compreendidas entre milhões e bilhões de massas solares ($M_\bullet = 10^{6-9}\,M_\odot$), podem atingir facilmente os valores de luminosidades $L_{bol} \sim 10^{44-48}\,\mathrm{erg\,s^{-1}}$, que são tipicamente observadas nos núcleos ativos de galáxias mais luminosos. Cabe ainda salientar que a máxima luminosidade que um sistema acretante pode ter, ocorre na condição de igualdade da Equação 1.4; essa luminosidade é chamada de *Luminosidade de Eddington*.

1.2.1 As estruturas dos AGN's

Além do SMBH central e do disco de acreção, outras regiões circundantes compõem o que chamamos de AGN's, como ilustrado na Figura 1.1. As principais estruturas que formam um AGN são descritas abaixo:

1. **O SMBH**: com massa entre 10^6 e 10^9 $\mathrm{M}_\odot$, possui um horizonte de eventos delimitado pelo raio de Schwarschild (R_{Sch}):

$$R_{Sch} = \frac{2GM_\bullet}{c^2} \tag{1.5}$$

   Para SMBH's com massas entre 10^6 e 10^9 $\mathrm{M}_\odot$ o raio de Schwarschild fica entre $10^{-7} \lesssim R_{Sch} \lesssim 10^{-4}$ parsec.

2. **O disco de acreção**: Tem papel fundamental no processo de acreção de matéria ao SMBH central, uma vez que, através dele, a energia potencial gravitacional é convertida em energia térmica, cinética e luminosa. As evidência observacionais, térmicas e cinemáticas, dessa estrutura, serão discutidas em detalhes nas sessões §1.3.1 e §1.3.2.

3. **A região de linhas largas – BLR**: muitos AGN's apresentam espectros ópticos com linhas de emissão permitidas do Hidrogênio e Hélio muito largas, com valores de largura a meia altura ou FWHM (*Full Width Half Maximum*) tipicamente na faixa de $2000\,\mathrm{km\,s^{-1}} \lesssim \mathrm{FWHM}_{broad} \lesssim 5000\,\mathrm{km\,s^{-1}}$. Atribui-se o alargamento dessas linhas ao efeito *Doppler* do gás em rotação ao redor do SMBH central e a sua ionização aos fótons emitidos pelo contínuo térmico emitido

[1] Considera-se que apenas a massa do próton e a sessão de choque de espalhamento de Thompson são relevantes para o equilíbrio entre a força devido a pressão de radiação e a atração gravitacional.

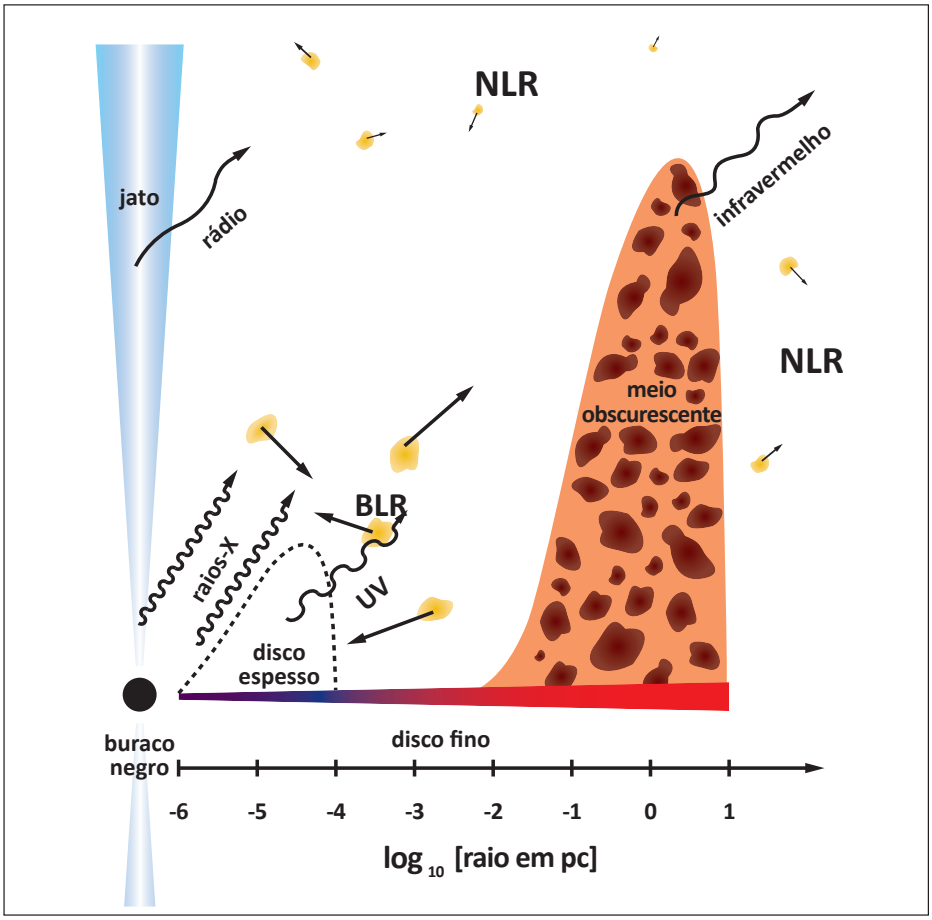

Figura 1.1: Representação esquemática das principais estruturas que compõem os AGN's. Tais estruturas são: o buraco negro supermassivo central (SMBH), o disco de acreção de matéria (fino e/ou espesso), a região de linhas largas (BLR), o meio obscurecente (toróide compostos por aglutinações de poeira), região de linhas estreitas (NLR) e os jatos de partículas relativísticas.

pelo disco de acreção. As dimensões típicas da BLR têm sido estimadas através da técnica de *mapas de reverberação* (Peterson & Wandel, 2000, Peterson et al., 2004, RM – *Reverberation Mapping*). Essa técnica consiste em medir as variações do fluxo do contínuo ionizante e correlacioná-las com as variações do fluxo das linhas largas de emissão (geralmente Hβ). O atraso entre as variações do fluxo das linhas largas de emissão e as variações do fluxo do contínuo são devidos ao tempo de viagem da luz entre o disco de acreção e a região emissora da linha larga; medir este atraso nos permite vincular a distância entre essas duas estruturas. As distâncias típicas medidas para a BLR vão desde algumas horas-luz até algumas semanas-luz.

4. **Meio obscurescedor**: o modelo unificado para os AGN's (Antonucci, 1993) – segundo o qual na maioria das vezes não é possível observar a radiação do disco de acreção nem a BLR – requer a presença de uma estrutura que obscurece a região central, sob a forma de um toróide de gás

molecular e poeira. Este toróide cerca a fonte central, de forma que quando a orientação do AGN em relação àlinha de visada faz com que ele seja visto de perfil, ele intercepta a BLR e não vemos as linhas de emissão largas da BLR. Quando isto acontece estas galáxias são chamadas de Tipo 2 (Seyfert 2, por exemplo). Por outro lado, quando o toróide é visto de cima temos uma visão completa da BLR e enxergamos as linhas de emissão largas, bem como a radiação originada no disco de acreção. Estes AGN's são chamados de Tipo 1 (Seyfet 1, por exemplo). Modelos mais recentes para o toróide sugerem que o mesmo não é uma estrutura contínua de gás e poeira, mas composta de um grande número de nuvens orbitando a região central (Nenkova et al., 2002). As dimensões típicas do raio interno do toróide têm sido obtidas através de mapas de reverberação (Suganuma et al., 2006), em que é medido o atraso entre variações no contínuo óptico (originário da fonte ionizante central) e na banda espectral K (centrada em 2.2 μm). A poeira absorve a radiação ionizante e re-emite no infravermelho com espectro de corpo negro; as regiões mais quentes do toróide tem seu máximo de emissão na banda K. Por exemplo, mapas de reverberação para NGC 4151 (Koshida et al., 2009) mediram um atraso de ≈ 50 dias $= 0.04$ pc entre estas variações, o que corresponderia então ao raio da borda interna do toro, o qual emite como um corpo negro de temperatura ≈ 1000 K (Riffel et al., 2009).

5. **A região de linhas estreitas – NLR**: é localizada a distâncias que variam de dezenas a centenas de parsecs do SMBH central, sendo formada por nuvens de gás a mais baixas velocidades do que as da BLR ($200 \lesssim \mathrm{FWHM}_{narrow} \lesssim 900$ km s^{-1}). A emissão da NRL é portanto estendida, sendo a única estrutura do AGN espacialmente resolvida no óptico para as galáxias ativas mais próximas. As baixas densidades do gás, entre 10^{2-4} cm^{-3}, permitem a presença de linhas de emissão proibidas, que são características da NLR. O gás da NLR apresenta muitas vezes movimento de *outflow*.

6. Jatos de partículas: Além das estruturas já descritas, pode ainda ocorrer a emissão de jatos de partículas relativísticas, colimadas por campos magnéticos, gerados na borda interna do disco de acreção.

1.3 Evidências observacionais do disco de acreção

1.3.1 Assinatura térmica do disco de acreção

No modelo padrão para o disco de acreção, o gás que circunda o SMBH central está em rotação Kepleriana (órbitas circulares), sendo a espessura vertical do disco muito menor do que seu raio; por isto este disco também é chamado de *disco fino* (*thin disk*). Nesse modelo toda a ignorância sobre os processos magneto-hidrodinâmicos é espressa pelo parâmetro α, chamado de parâmetro

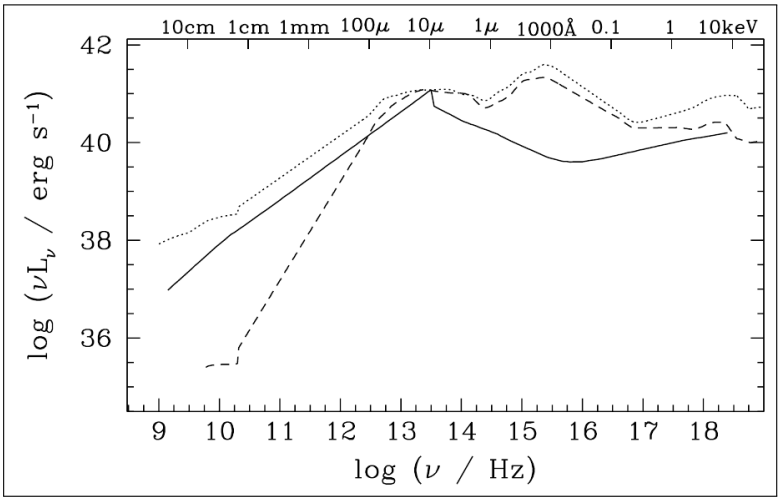

Figura 1.2: A SED média de AGN's de baixa luminosidade (*linha sólida*, adaptada de Ho (1999)). Também mostradas por comparação estão as SED's médias de AGN's *rádio-loud* (*linha pontilhada*) e *rádio-quiet* (Elvis et al., 1994). Todas as SED's estão normalizadas em 10μm. Figura extraída de Ho (2005).

de viscosidade de Shakura & Sunyaev (1973). Esta viscosidade surge devido à rotação diferencial entre órbitas adjacentes do disco, que faz com que hajam torques viscosos, que removem momento angular do gás em rotação fazendo-o espiralar lentamente em direção ao SMBH central. A energia potencial gravitacional liberada quando a matéria se desloca para uma órbita mais interna devido aos processos de dissipação viscosa, se transforma em energia térmica do disco. Este processo faz com que haja um gradiente de temperatura do gás em função da distância ao SMBH central. O gradiente de temperatura de corpo negro de cada anel do disco é descrito pela função (Frank et al., 2002):

$$T(r) \approx 6.3 \times 10^5 (\dot{M}/\dot{M}_E)^{1/4} {M_8}^{-1/4} \left(\frac{r}{R_{Sc}}\right)^{-3/4} \tag{1.6}$$

onde $\dot{M}/\dot{M}_E$ representa a taxa de acreção do SMBH em relação à taxa de acreção de Eddington[2], M_8 é a massa do SMBH em unidades de 10^8 $M_\odot$ e r/R_{Sc} é raio do anel em termos do raio de Schwarschild.

Dessa forma, o gás localizado nas órbitas mais internas é muito mais quente que o gás localizado nas órbitas mais externas do disco. Para um buraco negro de 10^8 $M_\odot$ acretando à taxa de Eddington, a temperatura das regiões mais internas do disco pode ser estimada em $T \approx 6.3 \times 10^5$ K. Para esta temperatura, a emissão de corpo negro tem um pico na freqüência de $\approx 3.6 \times 10^{16}$ Hz, no extremo ultravioleta do espectro, correspondente a uma energia do fóton de ~ 150 eV [3]. Esta

[2] A taxa de acreção de Eddington é a taxa de acreção mínima para que o sistema atinja a Luminosidade de Edington.

[3] Da derivada da função de Planck: $\nu_{máx} = 2.8kT/h$, onde $k = 1.381 \times 10^{-16}$ erg K^{-1} é a constante de Boltzmann e $h = 6.626 \times 10^{-27}$ erg s^{-1} é a constante de Planck.

emissão do contínuo UV do disco de acreção é tipicamente observada na SED de AGN's de galáxias Seyferts e Quasares e é comumente chamada de *big blue bump* (BBB)(Shields et al., 2000, Malkan, 1983). Os trabalhos de Vanden Berk et al. (2001) têm mostrado que quando o BBB está presente na SED dos AGN's, seu espectro UV–óptico é bem reproduzido por uma lei de potência, na forma $f_\nu \propto \nu^{\alpha_\nu}$, com $\alpha_\nu \approx -0.5$. Além disso, estimam que a energia do BBB é suficiente para fornecer todos os fótons ionizantes do AGN. A Figura 1.2 mostra a comparação entre as SED's médias de AGN's luminosos e LLAGN's. Desta figura pode-se perceber que os LLAGN's não apresentam o *big blue bump* em torno de 1000 Å que é claramente visível na SED dos AGN's de Quasares.

1.3.2 Assinatura cinemática do disco de acreção

Até 1989, assinaturas cinemáticas da presença de discos de acreção só eram conhecidas em variáveis cataclísmicas. Estas variáveis são estrelas duplas próximas em que uma das componentes é em geral uma estrela anã branca e captura matéria da companheira. Esta matéria é transferida para a Anã Branca formando um disco de acreção (Robinson, 1976). As assinaturas cinemáticas do disco de acreção são perfis de linhas de emissão do Hidrogênio alargadas, ($\sim$ 1000 km s^{-1}, Syer & Clarke, 1992) com uma estrutura de duplo-pico.

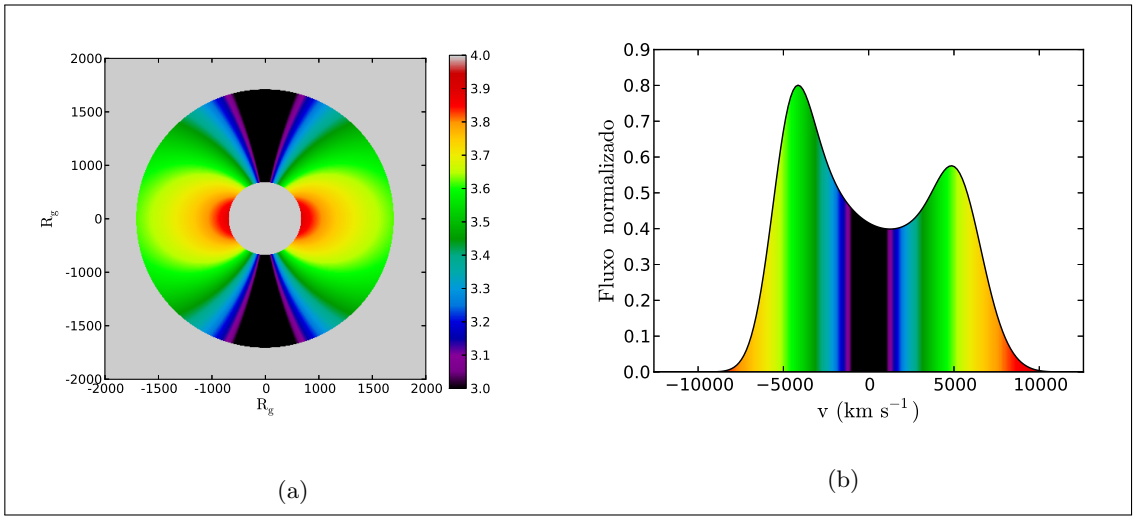

Figura 1.3: (a): mapa de isovelocidades projetadas para um disco em rotação Kepleriana e inclinado de 30° em relação à linha de visada. A barra de corres representa $\log_{10}(v)$ em km s^{-1}, em preto estão marcadas as regiões com menores velocidades, $v \sim 10^3$ km s^{-1}, e em vermelho estão marcadas as regiões com maiores velocidades $v \sim 10^4$ km s^{-1}. (b): perfil de duplo-pico representado no espaço de velocidades. As cores abaixo da curva representam as mesmas velocidades mostradas no painel (a); a região central do perfil, em preto, é originária das regiões de menores velocidades do disco enquanto que as regiões em vermelho são originárias das regiões de maiores velocidades.

Essa interpretação foi utilizada pela primeira vez no contexto de AGN's por Chen et al. (1989). Estes autores modelaram o perfil das linha largas (FWHM da ordem de $\sim 10.000\,\mathrm{km\,s^{-1}}$) de duplo-pico de H$\alpha$ e Hβ do núcleo da galáxia ativa Arp 102B (observada pela primeira vez por Stauffer et al., 1983) através de um modelo de disco de acreção circular, Kepleriano e relativístico. Neste modelo o disco é geometricamente fino, inclinado em relação à linha de visada, e a região emissora de linhas é delimitada por um raio interno não muito menor do que o externo, de forma que a estrutura emisora tem a forma de um anel. O alargamento da linha Hα e sua estrutura em duplo-pico são causados pela rotação do gás no disco. As Figuras 1.3a e 1.3b ilustram como a variação de velocidades no disco de acreção produz o perfil de duplo-pico. O painel esquerdo, 1.3a, ilustra o mapa de isovelocidades projetadas do gás emissor em rotação num disco Kepleriano inclinado em relação à linha de visada. Para um objeto central de massa $M_\bullet \sim 1 \times 10^8\,\mathrm{M_\odot}$ e distâncias entre $0.5 - 1.5{\times}10^3\,r_g$ as velocidades projetadas do gás em rotação ficam entre $10^{3-4}\,\mathrm{km\,s^{-1}}$. O lado de velocidades negativas do perfil, na Figura 1.3b, é chamado de *lado azul* (em *blueshift*) e corresponde à emissão da linha pelo lado do disco que se aproxima do observador; o lado de velocidades positivas, *lado vermelho* (em *redshift*), corresponde à emissão pelo lado do disco que se afasta do observador. As regiões com menores velocidades projetadas contribuem para a região central do perfil enquanto que as regiões com maiores velocidades projetadas contribuem para as *asas* do perfil. Além de explicar os perfis em duplo-pico, quando o disco está pouco inclinado em relação à linha de visada (quase *face on*), a estrutura do campo de velocidades projetadas também pode modelar a emissão de pico único, que são perfis de emissão Gaussianos (Flohic, 2011) tipicamente atribuídos a emissão da BLR.

1.4 Emissores de duplo-pico

O AGN da rádio galáxia Arp 102B pode ser considerado como o protótipo dos núcleos ativos emissores de linhas de duplo-pico. Depois da sua descoberta muitos outros AGN's foram observados apresentando o mesmo perfil: as rádio galáxias 3C 390.3 (Perez et al., 1988), 3C 332 (Halpern, 1990) e Pictor A (Halpern & Eracleous, 1994, Sulentic et al., 1995); e os LINER's
NGC 1097 (Storchi-Bergmann et al., 1993), M 81 (Bower et al., 1996), NGC 4203 (Shields et al., 2000), NGC 4450 (Ho et al., 2000).

Os AGN's emissores de duplo-pico foram estudados pela primeira vez como uma nova *classe* por Eracleous & Halpern (1994), e tem sido reconhecida como *disklike emitters* (na maioria AGN's de rádio galáxias). Muitos deles apresentam as seguintes propriedades em comum:

- FWHM média da linha larga em duplo-pico de $\approx 10000 - 12000\,\mathrm{km\,s^{-1}}$;

- No caso dos núcleos ativos de mais baixa luminosidade, o fluxo do contínuo ao redor da linha larga de Hα tem importante contribuição da população estelar em espectros extraídos com aberturas típicas, que correspondem a dezenas ou centenas de parsecs nas galáxias hospedeiras; tipicamente o a população estelar contribui com cerca 20-100% do fluxo nessa região;

- Grande intensidade relativa das linhas de baixa ionização: [OI]λ6300 e [SII]$\lambda\lambda$6716, 6731, características de um espectro tipo LINER.

Do ponto de vista estatístico, Strateva et al. (2003) estudaram uma amostra de 116 AGN's com duplo-pico com espectros extraídos do Sloan Digital Sky Survey e compararam suas características com as da população total de AGN's até redshift $z = 0.332$, encontrando: (i) os AGN's emissores de duplo-pico tiveram em média a FWHM 6 vezes mais alargada que os AGN's da população total; (ii) tiveram uma probabilidade 60% maior de serem fontes de rádio, sendo 12% classificados como LINERs. Modelando os perfis de duplo-pico da amostra usando os modelos de disco de acreção de Chen et al. (1989) e Eracleous et al. (1995), também encontraram que todos os discos possuem inclinações menores que 50° e que 60% deles exigem algum tipo de assimetria na modelagem. Além disso, estimaram que cerca de 3% da população de AGN's com $z < 0.332$ devem ser do tipo emissor de duplo-pico cuja emissão é proveniente de um disco de acreção. Assim, os emissores de duplo-pico ou *disklike emitters* são uma importante classe numericamente representativa em relação à população total de AGN's no Universo Local, na qual o perfil em duplo-pico da linha Hα é entendido como proveniente das regiões mais externas do disco de acreção.

1.4.1 A variabilidade dos perfis em duplo-pico

As escalas de tempo de variabilidade dos emissores de duplo-pico são de meses a anos, e têm sido monitoradas em alguns casos: 3C390.3 (Dietrich et al., 2012), NGC 1097 (Storchi-Bergmann et al., 2003), Arp 102B (Shapovalova et al., 2013), NGC 3065 (Eracleous & Halpern, 2001). Recentemente Lewis et al. (2010) reportaram os resultados do monitoramento ao longo de quase 10 anos de 20 emissores de duplo-pico, encontrando as seguintes características principais: (i) em todos os objetos o perfil da linha teve variações em escalas de tempo de anos (em alguns casos menos), as quais foram atribuídas a mudanças na emissividade do disco (presença de manchas brilhantes no disco). Eles concluíram que para alguns objetos da amostra essas manchas persistiram ao longo de anos se deslocando ao longo do perfil no espaço de velocidades, enquanto que para outros objetos, manchas apareceram e desapareceram em intervalos de tempo menores do que um ano; (ii) todos os objetos em alguma época apresentaram um perfil em que o pico vermelho estava mais intenso que o pico azul. Isto foi atribuído a assimetrias no disco de acreção pois em um disco axialmente simétrico é esperado que o pico azul seja mais intenso que o pico vermelho devido ao efeito de *Doppler boosting*.

Essas variações do perfil foram modeladas através de discos de acreção axialmente assimétricos – contendo braços espirais, manchas brilhantes, etc. A Figura 1.4 ilustra as variações em longa escala

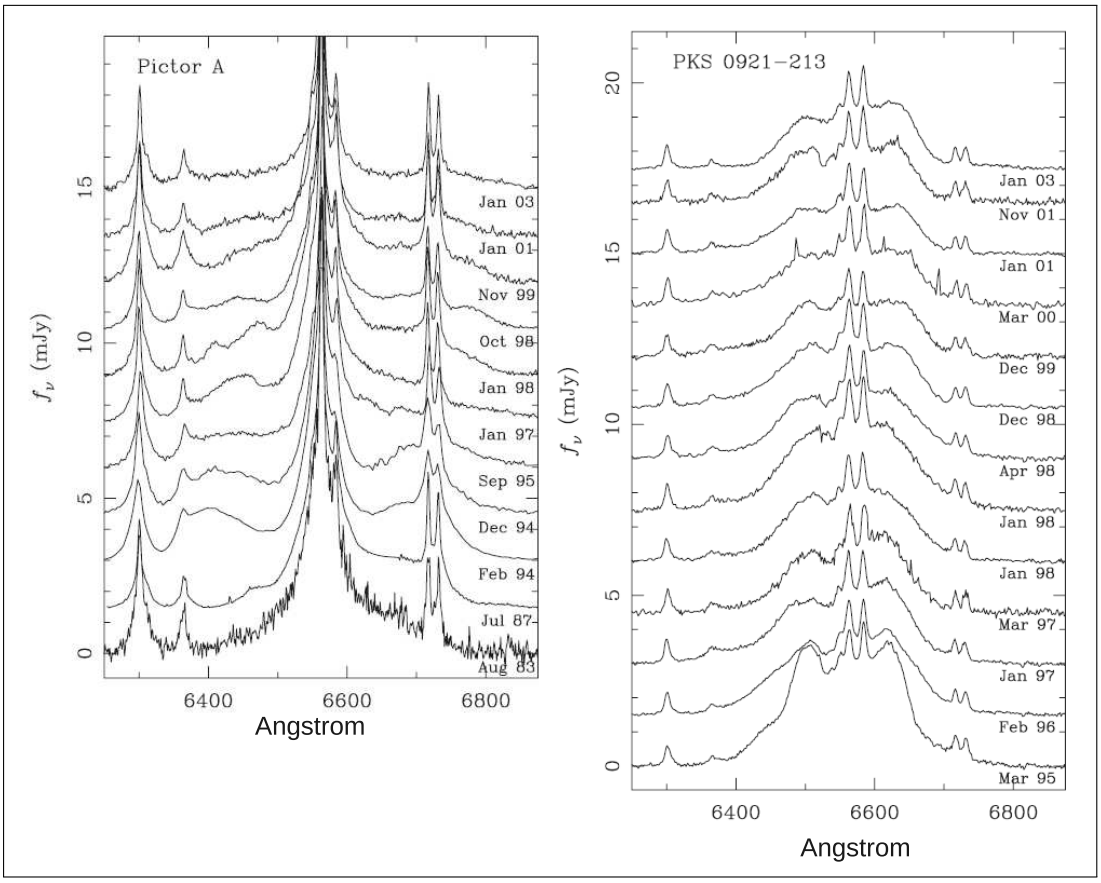

Figura 1.4: Variações da linha larga em duplo-pico de Hα monitoradas em longas escalas tempo. Tanto Pictor A quando PKS 0921–213 apresentaram variações no fluxo integrado da linha larga e assimetrias na forma do perfil. Figura adaptada de Lewis et al. (2010).

de tempo de dois objetos estudados por Lewis et al. (2010). Com base na figura é posível perceber que tando o fluxo da linha larga de duplo-pico quanto a sua forma variaram drasticamente ao longo do período em que o perfil foi monitorado.

1.5 A fonte de ionização do gás no disco

Os AGN's mais luminosos possuem espectros nucleares em que o seu contínuo térmico (*featureless continuum*) é comparável ou até mesmo dominante em relação à população estelar: alguns exemplos são Arp 102B, 3C 390.3 e Pictor A. No caso de 3C 390.3, Dietrich et al. (2012) realizaram um estudo aplicando a técnica de *Reverberation Mapping* correlacionando as variações do fluxo do contínuo do AGN de 3C 390.3 em 5100 Å com as variações no fluxo integrado das linhas largas em duplo-pico da

série de Balmer, Hα e Hβ. Os autores encontraram que as variações do fluxo do perfil em duplo-pico de Hα estão correlacionadas com as variações do fluxo do contínuo com um atraso de $\tau \sim 56$ dias. Assim, a parte emissora de linhas largas teria um comportamento semelhante ao da BLR. Mas ainda há poucos estudos deste tipo. No caso de Arp 102B, Shapovalova et al. (2013) argumenta não ter encontrado correlações evidentes entre as variações do perfil em duplo-pico de Hα e Hβ com o contínuo do AGN.

Nos LLAGN's (*Low Luminosity AGN's*) emissores de duplo-pico, o contínuo térmico do disco de acreção é muito difícil de detectar, pois além de serem objetos pouco luminosos, não apresentam em sua SED o BBB, típico de AGN's mais luminosos (Ho, 2008), o que desfavorece o contínuo óptico/UV como sendo a principal fonte de ionização do gás em rotação no disco de acreção. Poder-se-ia então argumentar que a energia necessária para originar a emissão em Hα tem origem local no disco, por dissipação viscosa. Entretanto, Eracleous & Halpern (2001) e Strateva et al. (2006, 2008) argumentam que existe um déficit no balanço energético entre a luminosidade em Hα da linha larga e a energia disponível devido a dissipação viscosa segundo a prescrição de Shakura & Sunyaev (1973) para o disco de acreção. O problema do balanço energético aparece porque a luminosidade em Hα é muito próxima, ou em alguns casos excede, a energia disponível devido a dissipação viscosa da região emissora da linha no disco, W_{disk}. Os autores acima citados estudaram o déficit energético para 20 emissores em duplo-pico, onde compararam a luminosidade em Hα (L_{H_α}) com W_{disk} e com a luminosidade em raios-X (0.5 – 10 keV) do AGN. Como resultado, encontraram que em 30% dos casos $W_{disk}/L_{H\alpha} < 1.0$, enquanto que a luminosidade em raios-X sempre excede $L_{H\alpha}$. Dessa forma, para produzir linhas de emissão em duplo-pico, o gás no disco precisa ser ionizado por uma fonte externa. Originalmente, Chen et al. (1989) propuseram que o contínuo ionizante seria originado numa estrutura toroidal localizada dentro do raio interno do disco emissor, bem mais espessa do que o disco. O modelo físico para esta estrutura toroidal foi desenvolvido mais recentemente e é conhecido como RIAF (Radiatively Inefficient Accretion Flow, Narayan & McClintock, 2008).

Em um RIAF o aquecimento do gás devido à dissipação viscosa é muito maior que o resfriamento devido à emissão de radiação; dessa forma, a energia térmica é armazenada no gás, que se torna muito quente, e, posteriormente, é acretada pelo SMBH. Os RIAFs são geometricamente espessos e opticamente finos, e sua associação a discos externos geometricamente finos e opticamente espessos tem sido utilizada para explicar a SED de LLAGN's emissores de duplo-pico. A temperatura dos elétrons no toróide de íons é $T_e \sim 10^9$ K e o resfriamento é devido principalmente ao efeito Compton inverso e à radiação sincrotrônica, ambos emitidos principalmente na região espectral dos raios-X. Essa emissão em raios-X dá origem a um contínuo 'duro' não térmico com energia suficiente para ionizar o disco fino, o qual tem temperatura $T \sim 10^4$ K e gera as linhas de Balmer

de duplo-pico. Um esquema do cenário atual proposto para o motor central dos AGN's de baixa luminosidade é apresentado na Figura 1.5.

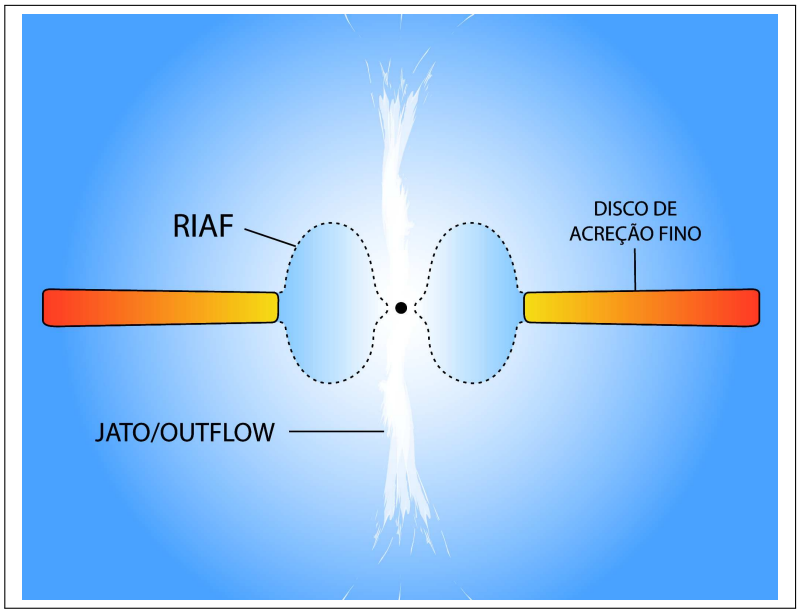

Figura 1.5: Esquema da estrutura de ionização para o disco de acreção em LLAGN's. A parte mais interna é um toróide de íons geometricamente espesso e opticamente fino (RIAF, Narayan & McClintock, 2008) acoplado ao disco externo que é geometricamente fino e ópticamente espesso. A emissão em raios-X do RIAF ioniza as partes mais externas do disco de acreção fino dando origem ao perfil de duplo-pico largo das linhas de emissão.

1.5.1 O caso de NGC 1097

No contexto dos núcleos emissores de perfis com duplo-pico, o núcleo da galáxia NGC 1097 tem notória importância por ser o primeiro LINER descoberto apresentando a linha de emissão larga de Hα com duplo-pico (Storchi-Bergmann et al., 1993). Depois da sua descoberta o perfil foi monitorado ao longo de mais de 20 anos com observações esporádicas, espaçadas por intervalos de tempo de meses a anos. Esse monitoramento permitiu que fossem descobertas variações no fluxo integrado da linha larga com duplo-pico e na intensidade relativa dos picos azul e vermelho (Storchi-Bergmann et al., 1995). Essa assimetria no perfil foi modelada como sendo devida a uma região emissora assimétrica, modelada como um braço espiral superposto ao disco de acreção circular.

Do ponto de vista da distribuição espectral de energia, Nemmen et al. (2006) modelou a SED de NGC 1097 utilizando um motor central para o AGN composto por três componentes principais:

- RIAF: o escoamento acretivo nas vizinhança do SMBH foi modelado como sendo devido a um RIAF. Essa estrutura se estenderia até o raio de transição $r_{tr} = 225\,R_{Sch}$ e seria responsável principalmente pela emissão em alta energia, como os raios-X duros, proveniente do AGN;

- Disco Fino: a partir de $225\,R_{Sch}$ o disco espesso (RIAF) cessaria e daria origem ao disco fino padrão do modelo de Shakura & Sunyaev (1973). O disco fino se estenderia de 225 a $800\,R_{Sch}$, valores dos raios interno e externo do disco fino, respectivamente; estes valores são os mesmos utilizados para a modelagem do perfil em duplo-pico de NGC 1097;

- Jato: a terceira componente do modelo é um jato de partículas relativísticas. A emissão do jato domina principalmente na região espectral de baixas energias (frequências de rádio).

A Figura 1.6 mostra a contribuição relativa de cada uma das componentes utilizadas para modelar a SED do AGN de NGC 1097. Este modelo reproduz de forma consistente a ausência do *big blue bump* e a emissão da linha larga em duplo-pico do AGN. Recentemente, Schimoia et al. (2012) reportaram o monitoramento com freqüência mensal do perfil de duplo-pico de NGC 1097. Neste trabalho, os autores concluíram: (i) que a forma do perfil (em particular as intensidades relativas entre os picos azul e vermelho) variou em escalas de tempo de meses; (ii) o fluxo integrado da linha larga com duplo-pico e a separação entre os picos variaram em escalas de tempo de dias (entre 7 e 20 dias). Este trabalho sugeriu que as variações nos perfis em duplo-pico podem ocorrer em escalas de tempo compatíveis com as escalas de tempo da viagem da luz entre SMBH central e o disco de acreção. De fato, os autores interpretaram as variações rápidas no perfil como sendo uma possível reverberação das variações do fluxo em raios-X (presumidamente emitido pelo RIAF) que ionizaria o gás no disco; esta interpretação foi chamada de *cenário de reverberação*.

1.6 A conexão entre a BLR e o disco de acreção

1.6.1 A região de linhas largas

Uma das características mais predominantes do espectro ultravioleta (UV), óptico, e do infra-vermelho próximo (near infrared - NIR) dos núcleos ativos de galáxias (AGN's) é a presença de linhas de emissão alargadas. Embora saibamos que essas características surgem de escalas espaciais não muito maiores do que o disco de acreção a geometria da BLR e cinemática das nuvens é ainda tema de debate na comunidade astronooômica que estuda AGN's.

Uma característica de particular importância das linhas de emissão alargadas é que elas são, por definição, resolvidas no espaço de velocidades projetadas na linha de visada, e suas grandes larguras, da ordem de 2000 a 5000 $\mathrm{km\,s^{-1}}$, não deixam dúvida que o principal mecanismo causador de tal alargamento é o movimento orbital das nuvens de gás (ou filamentos, ou fluxos de gás) com

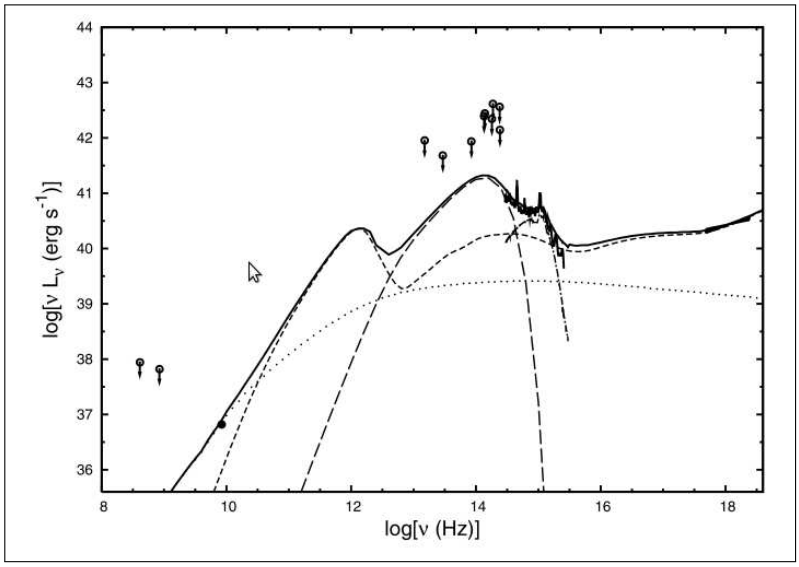

Figura 1.6: Modelos de RIAF (linha tracejada/traços curtos), disco fino (linha tracejada/traços longos), jato (linha pontilhada), e *starburst* obscurecido (linha pontilhada e tracejada) comparados com a SED de NGC 1097. A soma de todas as componentes está mostrada em linha sólida. O disco fino é truncado em $r_{tr} = 225\, R_{Sch}$, dentro do qual há um RIAF. Figura adaptada de Nemmen et al. (2006)

compoem a BLR em torno do SMBH central. Existem evidências observacionais que sugerem que cinemática da BLR pode ser bastante complexa:

1. O gás circundante ao SMBH pode estar fluindo em direção ao centro ajudando a alimentar o SMBH central;

2. Em algumas BLR's há evidência da presença de gás na BLR em rotação num disco, como evidenciado pelo perfil em duplo-pico bem pronunciado em algumas fontes (Eracleous & Halpern, 1994, Strateva et al., 2003, Gezari et al., 2007, Lewis et al., 2010), e por espectropolarimetria (Smith et al., 2004).

3. E também há evidências de que a gravidade do SMBH é dominante para o movimento do gás na BLR, embora em alguns casos a pressão de radiação também possa ter um papel relativamente importante (Marconi et al., 2008, Netzer & Marziani, 2010).

Apesar de existirem vínculos observacionais para velocidades do gás na BLR, ela ainda não pode ser resolvida espacialmente e estabelecer a sua cinemática é algo bastante difícil pois o problema da inversão é degenerado, ou seja, diferentes distribuições de nuvens combinadas com campos de velocidades diferentes, podem fornecer ajustes igualmente satisfatórios.

Dessa forma, o desconhecimento sobre os detalhes da dinâmica do gás na BLR representa uma séria lacuna no nosso entendimento dos AGN's e das calibrações necessárias para o estudo da

co-evolução entre os SMBH e suas galáxias hospedeiras. Mesmo frente a todas estas dificuldades, nas últimas décadas, observações espectroscópicas das linhas largas de Balmer têm se mostrado um excelente recurso para a determinação da massa dos SMBH's e também das condições físicas do gás circundante. Neste sentido, a técnica de Mapas de Reverberação (*Reverberation Mapping* – RM) tem notória importância.

1.6.2 Mapas de Reverberação

A técnica de Mapas de Reverberção tem sido utilizada com o objetivo de entender a estrutura e a cinemática da BLR. Esta técnica consiste em assumir que o contínuo ionizante do AGN (com energia maior que 13,6 eV), a saber, o contínuo azul, UV e raios-X *soft*, é produzido pela emissão de corpo negro das regiões do disco de acreção mais internas e que estão mais próximas do buraco negro, onde as temperaturas podem chegar a ser da ordem de 10^5 K ou maiores. O gás da BLR, é então ionizado por tal contínuo, e dependendo das condições de temperatura e densidade, pode ocorrer a recombinação entre os elétrons e íons do gás ionizado. Uma das principais linhas permitidas de recombinação produzidas na BLR é a linha Hβ da série de Balmer, que é amplamente observada nas campanhas de RM.

Uma vez que a produção linha de emissão larga é uma consequência direta do processo de ionização pelo contínuo do AGN, quando ocorrem variações do fluxo ionizante, tais variações somente serão percebidas pelo gás da BLR depois de um tempo que é igual ao tempo que a radiação leva para viajar entre os arredores do SMBH e a BLR. Dessa forma, a aplicação mais simples desta técnica consiste em monitorar as variações do fluxo do contínuo ionizante, geralmente o fluxo do contínuo em 5100 Å, e o fluxo integrado da linha larga Hβ. As variações do fluxo da linha vão estar correlacionadas com as variações do contínuo ionizante através de um *delay*, que é exatamente a distância entre a fonte ionizante central e a BLR, vincula-se assim, a distância média da BLR com respeito ao SMBH central.

Outras linhas de emissão do UV, como por exemplo as linhas Lyα λ1215, C IV λ1550, e Si IV λ1400, também têm sido estudadas com o objetivo de entender a estrutura e cinemática da BLR. Recentemente, essas linhas de emissão foram todas simultanamente monitoradas na galáxia Seyfert 1 NGC 5548 (De Rosa et al., 2015) e os delays encontrados nas variações dos fluxos dessas linhas com relação ao contínuo ficaram em torno de $\sim$5 – 6 dias. Para a linha Hβ, os valores mínimo e máximo dos atrasos medidos, quando o AGN estava respectivamente em um estado de baixa e alta luminosidade, são $\tau(H_\beta) \sim 4.2^{+0.9}_{-1.3}$ (Bentz et al., 2009) e $\tau(H_\beta) \sim 26.5^{+4.3}_{-2.2}$ (Peterson et al., 2002). Dessa forma, as linhas de emissão do UV, mencionadas anteriormente para essa galáxia, sugerem que há uma estratificação da BLR, ou seja, o gás que emite as linhas de emissão com mais alto potencial de ionização está localizado, em média, mais próximo do SMBH central.

1.6.3 Determinação de $M_\bullet$ e o fator f

Com o objetivo de determinar a massa do buraco negro central, é necessário ter observações de algum traçador do potencial gravitacional do buraco negro (geralmente observações de estrelas ou gás). Neste sentido, Mapas de Reverberação, podem fornecer as observações da BLR fotoionizada cujos movimentos, na ausência de pressão de radiação muito intensa, estão dominados pelo poço de potencial do buraco negro.

Uma vez que a técnica de RM permite determinar a distância média entre a BLR e o SMBH central, combinando esta medida com a largura de linha larga de Hβ, a qual se assume que reflete a dispersão de velocidade do gás quando o movimento deste está dominado pelo potencial gravitacional do buraco negro, pode-se estimar a massa do SMBH através do Teorema do Virial. De Peterson et al. (2004):

$$M_\bullet = f \times \frac{R_{BLR}\Delta V^2}{G} \tag{1.7}$$

onde:

- $M_\bullet$: massa do SMBH central;
- R_{BLR}: é o raio da BLR, obtido do produto entre a velocidade da luz e o tempo de atraso, τ, entre as variações do fluxo do contínuo ionizane e o fluxo da linha larga de Hβ;
- ΔV: é uma medida da dispersão de velocidades orbitais típica das nuvens. Geralmente esta medida é tomada como largura a meia altura do perfil de emissão (*full width at half maximmum* – FWHM) ou a dispersão da linha, ou seja, o segundo momento do perfil da linha. Essa medida é realizada tipicamente no espectro variacional da linha larga (*espectro de rms*) (Grier et al., 2012, Denney et al., 2010);
- f: fator numérico da relação, associado às incertezas na determinação da geometria (incluindo a inclinação) e cinemática (rotação, fluxo de gás para o centro ou para fora) da BLR;
- G: é a constante de gravitação Universal.

1.6.4 Linhas de emissão largas com duplo-pico em galáxias Seyfert 1

A maioria das observações de monitoramento de emissores de duplo-pico foram feitas tipicamente através observações mensais ou ainda mais esparsas. Recentemente observações do núcleo de NGC 1097 por Schimoia et al. (2012) incluiram algumas observações com intervalos semanais e mostraram que existem variações no fluxo total integrado da linha e na separação entre os picos azul e vermelho em escalas de tempo de uma semana.

Esta escala de tempo de variabilidade curta, de aproximadamente uma semana, observada para o perfil em duplo-pico da NGC 1097 é da ordem dos atrasos (*delays*) encontrados entre as variações do fluxo do contínuo ionizante e o fluxo da linha larga emitida pela BLR nos estudos de *Reverberation Mapping*. Isto indica que o disco emissor da linha (exatamente modelado como um anel, mas continuará sendo referido como disco ao longo do texto) na NGC 1097 está a uma distância da fonte ionizante central que é tipica da região de linhas largas de galáxias Seyfert 1 próximas (Peterson et al., 2004) de luminosidade comparáveis.

Como mencionado anteriormente, algumas galáxias Seyfert 1 apresentam, em pelo menos alguma ocasião, evidência de uma componente tipo disco no perfil das linhas da BLR. Duplos-picos ou "ombros" são frequentemente vistos nas linhas de emissão largas da série de Balmer em fontes altamente variáveis e frequentemente monitoradas como a NGC 5548 (Sergeev et al., 2007). Estas varias observações conduzem ao questionamento se os perfis das linhas de emissão largas de Balmer de todas as galáxias Seyfert 1 possuem uma componente proviente das regiões mais externas do disco de acreção. Uma hipótese simples é que os perfis de Balmer em galáxias Seyfert 1 sejam compostos por:

1. Uma componente tipo disco, proveniente da região mais externa do disco de acreção;
2. Uma componente adicional originária de nuvens de gás mais distantes.

Um modelo composto por uma componente disco mais outra componente larga foi proposto para reproduzir os perfis da BLR de galáxias Seyfert 1 e Quasares por Popovic et al. (2004) e colaboradores (Bon et al., 2009, La Mura et al., 2009). Um estudo teórico de Elitzur et al. (2014) também argumenta que a região de linhas largas das galáxias Seyfert 1 possui duas partes: um disco e um sistema de nuvens que são parte do vento emanado pelo disco de acreção. A medida que a razão de Eddington diminui, o gás que possui uma densidade de coluna mais alta e que está presente apenas no disco, domina a emissão e isto leva aos perfis em duplo-pico observados. A componente originada no vento seria mais forte para altas taxas de acreção. Isto explicaria naturalmente a relativa proeminência das componente com duplo-pico (disco) em AGN's de baixa luminosidade e a relativa dificuldade de identificar componentes disco em objetos mais luminosos, e com maiores taxas de acreção: a componente originada no vento seria tão intensa que impediria a observação clara do perfil de duplo-pico subjacente

Se a componente de duplo-pico proveniente do disco estiver sempre presente nas linhas da BLR de AGN's de Tipo 1, haverão implicações diretas no cálculo da massa do SMBH através do produto virial (Equação 1.7), pois o fator f está diretamente associado a geometria da BLR.

1.7 Motivação e Objetivos

Neste trabalho propomos aprofundar a análise da origem das linhas de emissão de duplo-pico através de dois tipos de análise: (1) monitoramento espectroscópico do perfil largo de duplo-pico na linha de emissão Hα dos núcleos ativos tipo LINER/Seyfert 1 de NGC 1097 e NGC 7213 e subsequente ajuste de modelos de disco aos perfis; (2) Ajuste de modelos de disco a observações espectroscópicas de somente uma época dos perfis de galáxias do Palomar Survey of Nearby Galaxies (Ho et al., 1995, 1997b).

1.7.1 Monitoramento espectroscópico

NGC 1097

No caso de NGC 1097 pudemos realizar um monitoramento, não só do perfil largo de duplo-pico de Hα usando o telescópio SOAR, mas também nas bandas UV ($\sim$ 2246 Å) e em raios-X (0.3 – 10 keV) com o telescópio espacial Swift. As observações com o satélite espacial tiveram o objetivo de monitorar o contínuo duro ionizante do AGN, presumidamente proveniente do RIAF central. Com este monitoramento conjunto *Swift* + SOAR, os principais pontos que pretendemos investigar são:

- Estudar se o contínuo duro do AGN apresenta de fato variabilidade em raios-X e UV, e em caso afirmativo, quantificar essas variabilidades;
- Monitorar o perfil da linha larga em duplo-pico em escalas de tempo muito curtas, através de observações semanais, a fim de estimar um limite inferior para a escala de variabilidade do perfil;
- Correlacionar as curvas de luz em raios-X, UV e no fluxo integrado da linha larga em duplo-pico, com o objetivo principal de investigar se o fluxo em raios-X é responsável por ionizar o disco dando origem à emissão em duplo-pico, ou seja, testar o *cenário de reverberação*;
- Reproduzir a evolução do perfil em duplo-pico através de modelos de disco de acreção e comparar os resultados obtidos com aqueles de trabalhos anteriores. Por exemplo, o modelo de disco de acreção com um braço espiral ainda é válido?

NGC 7213

Embora o fato de que os perfis de duplo-pico variam em escalas de tempo da ordem de meses e anos já esteja bem estabelecido, não se sabe se as variações em escalas de tempo curtas, como as vistas em NGC 1097, estão presentes em outros AGN's. Com o telescópio Gemini-Sul propusemos o monitoramento espectroscópico do perfil de duplo-pico de Hα para NGC 7213, com observações

espaçadas por intervalos de tempo de semanas a meses. Os principais pontos que pretendemos investigar são:

- Se o perfil em duplo-pico de NGC 7213 apresenta variações em escala de tempo curta (semanas/meses), e caso esteja presente, quantificar a sua variabilidade;
- Verificar se seu perfil em duplo-pico e suas variações (caso sejam observadas) podem ser reproduzidos usando o modelo de disco de acreção que reproduz a variabilidade do perfil de duplo-pico em Hα de NGC 1097 e obter os parâmetros do disco;
- Comparar as escalas de tempo de variabilidade, ou a ausência delas com as escalas de tempo típicas esperadas para o modelo de disco de acreção de Shakura & Sunyaev (1973). Esta comparação pode elucidar qual são os principais processos físicos (fotoionização, rotação, viscosidade, etc.) responsáveis pela origem e variabilidade dos perfis em duplo-pico.

1.7.2 Ajuste de modelos aos espectros do Palomar

Muitas galáxias Seyfert 1 são vistas apresentando o perfil largo em duplo-pico das linhas de emissão de Balmer diretamente nos espectros; ou quando são monitoradas, no espectro médio ou espectro variacional resídual (espectro de *rms –root mean square*) (Grier et al., 2012, Denney et al., 2010). Isto sugere que existe uma componente disco que está presente, mesmo quando não a vemos diretamente no espectro. Selecionamos uma amostra de 5 galáxias ativas do Palomar Survey of Nearby Galaxies que apresentam emissão larga em duplo-pico para estender a análise do modelo de disco de acreção para galáxias tipo Seyfert 1.

- Estender a modelagem dos perfis de duplo-pico para galáxias Seyfert 1 emissoras de duplo-pico do Palomar Survery of Nearby Galaxies, procurando reproduzir principalmente as regiões correspondentes às mais altas velocidades projetadas do perfil. Através da modelagem, estimar os parâmetros do disco de acreção, como por exemplo a extensão da região emissora e inclinação do disco.
- Identificar se nessas galáxias a emissão do disco de acreção consegue sozinha reproduzir o perfil da linha, ou se componentes adicionais são requeridas para explicar os perfis observados. Caso mais de uma componente seja necessária, estimar qual a importância de cada componente para o perfil de emissão largo.
- Um vez que o Palomar Survey of Nearby Galaxies possui uma amostra representativa das galáxias do Universo local, discutiremos as implicações da modelagem do perfil em duplo-pico e da geometria tipo disco para a região emissora de linhas largas das galáxias do Universo local para a determinação da massa dos seus SMBH centrais através do produto virial.

Este trabalho está assim organizado: no Capítulo 2 apresentamos a descrição dos dados obtidos durante o monitoramento dos núcleos ativos de NGC 1097 e NGC 7213, assim como o processo de redução aplicado aos dados. Nesse mesmo Capítulo descreveremos a amostra de galáxias Tipo 1 que selecionamos do Palomar Spectroscopic Survey of Nearby Galaxies para estender o estudo da modelagem dos perfis em duplo-pico à galáxias Seyfert 1. No Capítulo 3 descrevemos a metodologia aplicada na análise dos dados e também o ajuste dos perfis de duplo-pico através de modelos de disco de acreção. Os resultados para a galáxia NGC 1097 estão apresentados no Capítulo 4 na forma de um artigo recém publicado, enquanto que os resultados para a galáxia NGC 7213 será apresentado no Capítulo 5 na forma de um artigo em fase final de revisão pelos colaboradores. O capítulo 6 apresenta os resultados da análise da amostra de galáxias do Palomar Spectroscopic Survey of Nearby Galaxies na forma de um outro artigo que está em fase final de revisão. No Capítulo 7 são apresentadas as conclusões deste trabalho.

Capítulo 2

Dados

2.1 Observações de NGC 1097 com o satélite *Swift*

Durante o período de 26 de julho de 2012 a 30 de janeiro de 2013 (MJD 56134 - 56327) realizamos um monitoramento do núcleo de NGC 1097 com o satélite *Swift*. Este projeto foi realizado em colaboração com o pesquisador Dirk Grupe da Universidade do Estado da Pensilvânia (EUA) que ficou responsável pela redução dos dados obtidos com o satélite. O monitoramento foi realizado utilizando dois telescópios: o telescópio de raios-X (*X-ray telescope* – XRT, Burrows et al., 2005) e o telescópio UV/óptico (UV/Optical Telescope – UVOT, Roming et al., 2005).

O telescópio XRT operou no modo de contagem de fótons (*Photon-Counting Mode*). Este modo permite obter informações espectrais no intervalo de energias 0.3 – 10 keV em um campo de visão (*Field of View* – FOV) de $23\farcm6\times23\farcm6$ com uma escala espacial de $2.36''$ pixel^{-1}. A *point spread function* (PSF) do telescópio varia de $18''$ em 1.2 keV a $22''$ em 8.1 keV. Os dados foram reduzidos utilizando a tarefa *xrtpipeline* versão 0.12.3, do pacote HEASOFT versão 6.12 (`http://heasarc.nasa.gov/lheasoft/`). As contagens da região nuclear foram extraídas de uma região circular de 20 pixeis $\approx 47''$ de raio centradas em $\alpha = 02h\,46m\,18.6s$ e $\delta = -30^\circ\,16'\,25.6''$. As contagens do céu foram extraídas de uma região sem fontes com um raio de $235''$ utilizando a tarefa *xselect* (versão 2.4b). Os arquivos de resposta foram criados utilizando a tarefa *xrtmkarf*. Os espectros foram re-binados na sua dimensão espectral, para manter pelo menos 20 contagens por bin, utilizando a tarefa *grppha*. Os espectros re-binados foram calibrados em fluxo utilizando os arquivos de resposta e em seguida modelados no intervalo de 0.3 – 10 keV utilizando o pacote XSPEC (*X-ray Spectral Fitting*) utilizando uma única lei de potência e uma absorção Galáctica correspondente a uma densidade de coluna de Hidrogênio de $N_H = 2.03\times10^{20}$ cm^{-2} (Kalberla et al., 2005).

O telescópio UVOT tem um FOV de $17'\times17'$, uma PSF de $2.5''$ e uma escala de placa de $0.502''$ pixel^{-1}. O telescópio operou no modo de imageamento utilizando o filtro *uvm2*, cujo comprimento de onda central é 2246 Å e tem uma largura de banda (FWHM) de ∼510Å. As contagens da região nuclear foram extraídas de uma região circular de raio $3''$ centrada em $\alpha = 02h\,46m\,18.6s$ e $\delta = -30^\circ\,16'\,25.6''$, enquanto as contagens do céu foram extraídas de uma região de $20''$ de raio fora da galáxia. As extrações foram realizadas com a tarefa *uvotsource*. A calibração fotométrica foi realizada utilizandos a metodologia mais recente (Poole et al., 2008). O último passo foi realizar a correção pelo avermelhamento galáctico, de acordo com Roming et al. (2009), que utilizou a lei de avermelhamento de Cardelli et al. (1989).

Durante o monitoramento com o satélite Swift, foram realizadas um total de 45 visitas com observações dos dois telescópios, o XRT e o UVOT. O intervalo de tempo médio entre as observações ficou em torno de $\sim$ 4.2 dias. A Tabela com as datas das observações e as medidas dos fluxos é apresentada no Capítulo 4.

2.2 Observações com o telescópio SOAR

Juntamente com o monitoramento no UV e raios-X, realizado com o satélite *Swift*, monitoramos espectroscopicamente o núcleo de NGC 1097 na região óptica do espectro utilizando o telescópio SOAR, cujo espelho primário possui 4.1 m de diâmetro, e está localizado no *Cerro Pachón* no Chile. Para o monitoramento utilizamos o espectrógrafo GOODMAN e a seguinte configuração instrumental: observações no modo fenda-longa com uma largura de fenda de 1.″03; a rede de 600 l mm^{-1} com uma dispersão de 0.65 Å pixel^{-1} (no modo de dispersão *Mid*); esta rede forneceu uma cobertura espectral de 4500 – 7250 Å e uma resolução espectral de ∼5.5 Å, FWHM medida a partir dos perfis das linhas de emissão da lâmpada de calibração. Nesta configuração cobrimos o espectro desde a linha Hβ até além de Hα. A largura da fenda de 1.″03 foi escolhida para que fosse possível incluir toda a emissão nuclear sem que houvesse perda de fluxo significativa devido ao efeito de *seeing*. Além disso, essa largura é a mesma utilizada em observações anteriores desse objeto, o que permite a comparação dos dados com os de trabalhos anteriores, bem como a sua "normalização"através dos fluxo das linhas proibidas (que não variam nas escalas de tempo das observações). Juntamente com as observações de NGC 1097, a cada noite foi também observada a estrela de calibração *LTT1020* (Baldwin & Stone, 1984) com um tempo de exposição de 480 s.

A cadência das observações foi programada para que fosse realizada uma observação a cada ∼7 dias, frequência esta motivada pelo fato de que em Schimoia et al. (2012) não observamos variações no perfil de duplo-pico em intervalos de tempo menores do que 7 dias. O monitoramento óptico foi feito entre 07 de agosto de 2012 e 26 de janeiro de 2013 totalizando 22 observações. realizadas, na sua maior parte, com o tempo brasileiro no SOAR, e em menor parte com o tempo da Michigan State University, numa colaboração com os pesquisadores Jack Baldwin e Michael Eracleous.

A Tabela 2.1 apresenta todas as observações realizadas com o SOAR. As colunas (1) e (2) listam a data e a data juliana modificada (*Modified Julian Date* – MJD), respectivamente, enquanto que a coluna (3) lista o número e o tempo de cada uma das exposições realizadas. A maioria das observações foi dividida em várias exposições de 1200 s com o objetivo de evitar a saturação das linhas de emissão estreitas de Hα e [NII] λ6584, que são bastante intensas na região nuclear; além disso, combinando as várias exposições podemos corrigir melhor os dados pela contaminação por raios cósmicos.

Tabela 2.1: Observações de NGC 1097 com o telescópio SOAR.

Data (1)	MJD (2)	Tempo de exposição (s) (3)
07 Ago 2012	56147.356	3×1200
09 Ago 2012	56149.368	3×1200
10 Ago 2012	56150.360	3×1200
24 Ago 2012	56164.349	2×1200
31 Ago 2012	56171.388	2×1200
08 Set 2012	56179.370	3×1200
16 Set 2012	56187.222	3×1200
23 Set 2012	56194.256	2×1500
27 Set 2012	56198.175	5×1200
12 Out 2012	56213.316	3×1200
18 Out 2012	56219.316	3×1200
25 Out 2012	56226.048	3×1200
28 Out 2012	56229.229	3×1200
02 Nov 2012	56234.086	3×1200
12 Nov 2012	56244.074	3×1200
23 Nov 2012	56255.068	3×1800
08 Dez 2012	56270.206	3×1800
15 Dez 2012	56277.142	3×1800
23 Dez 2012	56285.097	3×1200
28 Dez 2012	56290.074	3×1200
17 Jan 2013	56310.047	4×1200
26 Jan 2013	56319.067	3×1200

2.3 Observações com o telescópio Gemini das galáxias NGC 1097 e NGC 7213

Também obtivemos dados do projeto *GS-2012A-Q-86* no telescópio Gemini-Sul (cujo espelho primário tem 8.0 m de diâmetro). Em tal projeto recebemos um máximo de ∼42h de tempo de telescópio em banda 4 (*poor weather*), e assim obtivemos dados de espectroscopia de fenda-longa na região do óptico dos AGN's das galáxias NGC 7213 e NGC 1097. A configuração instrumental comum para todas as observações é a seguinte: espectrógrafo GMOS (*Gemini Multi-Object Spectrograph*) no modo fenda-longa com uma largura de fenda de 1.″0, com a rede de dispersão de B600-G5323 que fornece uma cobertura espectral de ∼2760 Å e uma resolução espectral R ≈ 1688 (∼177km s^{-1}). Para cada galáxia solicitamos comprimentos de onda centrais e tempos de exposição diferentes, como descrito a seguir:

1. NGC 1097: para o núcleo de NGC 1097 obtivemos apenas uma única observação, que foi realizada em 03 de setembro de 2012. Realizamos esta observação com o objetivo de comparar o espectro com os obtidos com o telescópio SOAR durante o monitoramento conjunto

SOAR+*Swift*. Como o fluxo na linha larga estava muito baixo, realizamos esta observação com o telescópio Gemini-Sul para investigar se este baixo fluxo poderia ser devido ao fato de que o SOAR não teria a sensitividade necessária para detectar o fluxo. Mas com esta observação obtivemos um espectro e fluxo na linha larga de duplo-pico comparável aos fluxos medidos com o telescópio SOAR (ver Figura 2 no Capítulo 4). Dessa forma, confirmamos que o fluxo do perfil estava realmente mais baixo que o esperado, e que o SOAR tinha a sensitividade necessária para medir o perfil, mesmo com o fluxo baixo. As configurações específicas para esta observação foram: 6 exposições de 600 s com a rede centrada em 6600 Å.

2. NGC 7213: para NGC 7213 utilizamos um tempo de exposição total de 2700 s dividido em exposições individuais de 450 s. O comprimento de onda central foi 5700 Å, escolhido de acordo com o *redshift* da galáxia (z=0.00580) de modo a cobrir o espectro desde Hβ até além de Hα. As observações do núcleo desta galáxia iniciaram em 21 de julho de 2012 e terminaram em 23 de julho de 2013. A Tabela 2.2 lista todas as observações realizadas com este projeto. A primeira observação listada na tabela foi obtida com espectroscopia de campo integral (IFU) por Schnorr-Müller et al. (2014b) e está inclusa neste trabalho como parte da análise do monitoramento.

Os tempos de exposição acima foram estimados para que obtivéssemos uma razão sinal-ruído (S/N –*signal to noise ratio*) de ∼20 no contínuo para regiões a 2.″0 do núcleo. Destas regiões foram extraídos os espectros a partir dos quais sintetizamos a distribuição espectral de energia da população estelar que utilizamos para subtrair sua contribuição ao espectro nuclear (ver detalhes no Capítulo 3). Para a calibração relativa em fluxo, sempre que possível, foi observada a estrela FEIGE 110 (Oke, 1990) com um tempo de exposição de 450 s.

Tabela 2.2: Observações de fenda-longa das regiões nucleares de NGC 7213

NGC 7213			
Data	Tempo de exposição (s)		
27 Set 2011	55831.130	IFU	12×350
21 Jul 2012	56129.155	Longslit	6×450
30 Jul 2012	56138.422	Longslit	6×450
15 Out 2012	56215.111	Longslit	6×450
22 Nov 2012	56253.047	Longslit	6×450
13 Abr 2013	56395.383	Longslit	6×450
11 Mai 2013	56423.386	Longslit	6×450
20 Mai 2013	56432.315	Longslit	6×450
30 Mai 2013	56442.334	Longslit	6×450
14 Jun 2013	56457.399	Longslit	6×450
30 Jun 2013	56473.310	Longslit	6×450
07 Jul 2013	56480.218	Longslit	6×450
23 Jul 2013	56496.278	Longslit	6×450

2.3.1 Redução dos dados de espectroscopia óptica

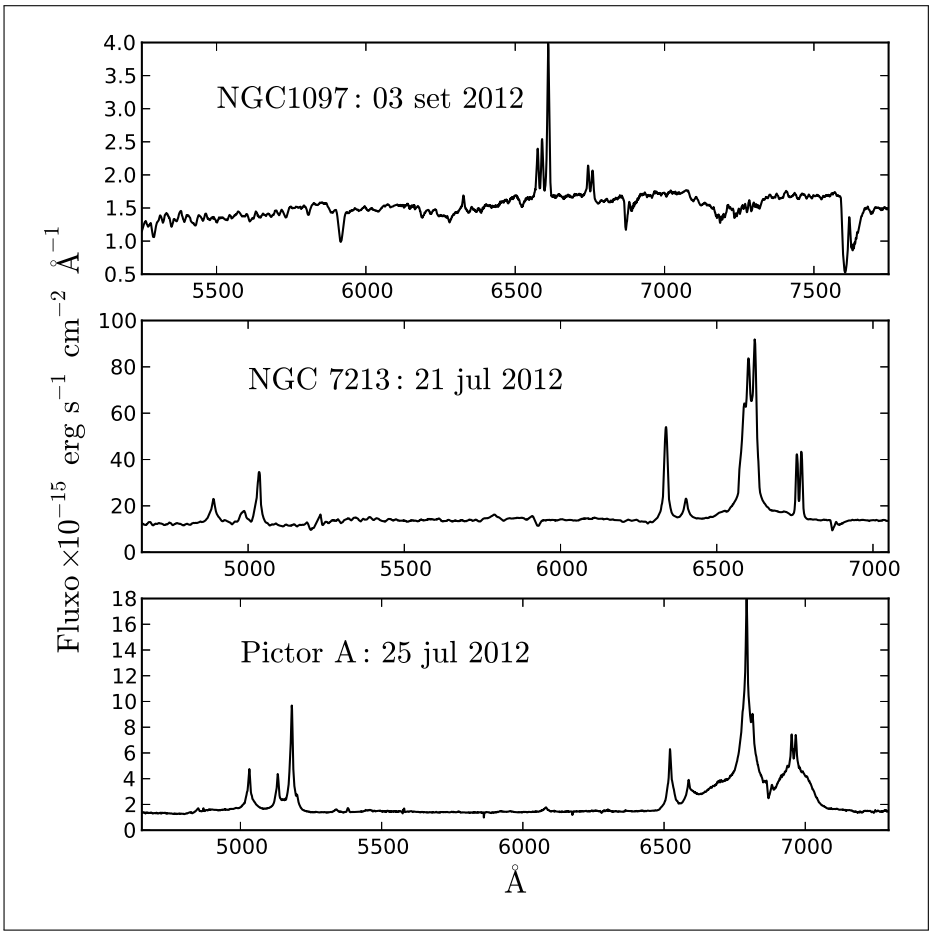

Figura 2.1: Extrações nucleares de $1\farcs0 \times 1\farcs0$ dos espectros de fenda longa de NGC 1097, NGC 7213 e Pictor A obtidas com o telescópio Gemini Sul. Foram obtidos também dados da galáxia Pictor A, mas que serão analisadas somente em um trabalho futuro.

Todos os dados de espectroscopia óptica foram reduzidos utilizando o *software* IRAF (*Image Reduction and Analysis Facility*[1]). Na redução dos dados obtidos com o telescópio SOAR foram utilizadas as tarefas padrões do IRAF, enquanto que na redução dos dados obtidos com o telescópio Gemini-Sul foram utilizadas as tarefas do pacote distribuído pelo próprio observatório. Embora os dados tenham sido obtidos com telescópios diferentes, são todos de espectroscopia de fenda-longa. Assim, descrevo a seguir as principais etapas comuns do processo de redução de todos os dados ópticos.

A redução dos espectros de fenda longa das galáxias consistiu das seguintes etapas: (i) subtração do *bias* (também chamado de nível *zero*); (ii) divisão pela resposta espectral do *flatfiled*

[1]IRAF é distribuído pelo*National Optical Astronomy Observatories* (NOAO).

espectroscópico. Os espectros das lâmpadas de calibração foram processadas pelos passos (i) e (ii) e em seguida utilizadas para (iii) gerar a solução de *calibração em comprimento de onda*; (iv) esta solução foi então aplicada aos espectros das galáxias. Depois dos dados terem sido calibrados em comprimento de onda foi (v) subtraída a contribuição do céu.

A solução da calibração relativa em fluxo foi realizada a partir das observações das estrelas padrões de fluxo. As principais estrelas utilizadas para esta calibração foram LTT1020, e FEIGE 110. Os espectros destas estrelas foram processados através das etapas (i) até (v); (vi) espectros unidimensionais das estrelas foram então extraídos. (vii) Com estes espectros foram geradas as curvas de *sensitividade*. (vii) Após a subtração do céu, os espectros das galáxias foram então calibrados (utilizando as curvas de sensitividade previamente geradas).

As extrações dos espectros nucleares foram realizadas em janelas de $1\farcs0 \times 1\farcs0$ para os dados do Gemini-Sul e $1\farcs0 \times 1\farcs03$ para os dados do SOAR. Essas extrações foram centradas no pico de emissão do contínuo, onde espera-se encontrar o AGN, e traçadas ao longo da direção espectral para evitar perdas devido a curvatura do espectro (devido a refração atmosférica). A Figura 2.1 mostra os espectros nucleares das galáxias NGC 1097 (painel superior), NGC 7213 (painel central) e Pictor A (painel inferior), resultantes de extrações de $1\farcs0 \times 1\farcs0$ dos dados obtidos com o telescópio Gemini-Sul. Além das extrações nucleares foram realizadas extrações extranucleares com o objetivo de obter espectros característicos da população estelar da região central da galáxia que não apresentassem fortes linhas de emissão. Os detalhes das extrações extranucleares estão descritos no Capítulo 3.

2.4 As galáxias do Palomar Sky Survey of Nearby Galaxies

O Palomar Survey of Nearby Galaxies (Filippenko & Sargent, 1985, Ho et al., 1995, 1997b) foi realizado em meados dos anos 90 e teve como principal finalidade mapear as galáxias do Universo local, com dados de espectroscopia óptica de alta qualidadade. O *survey* utilizou dois CCD's e um espectrógrafo montados em um telescópio de 5m. Foram obtidos espectros de fenda longa de alta qualidade, com resolução moderada até uma magnitude limite ($B_T \leq 12.5$ mag) de uma amostra de 486 galáxias do norte ($\delta > 0°$). Os espectros cobrem simultaneamente o rango espectral de 6210 – 6860 Å com uma resolução de $\sim$ 2.5 Å e o rango espectral de 4230 – 5110 Å com uma resolução de $\sim$4 Å. A maioria das observações foi realizada com uma fenda de ($1''$– $2''$), e os relativamente longos tempos de exposição forneceram altas razões *sinal-ruído*. Ele é também um dos mapeamentos mais sensíveis, a largura equivalente (*equivalent width*) do limite de detecção das linhas de emissão é de EW$\approx$0.25 Å. Este mapeamento contém um dos mais completos bancos de dados de espectros ópticos, homogêneos e de alta qualidade, de galáxias próximas. Os criterios de seleção garantiram que a amostra fornecesse uma representação adequada da população local de galáxias

(z≈0), e a proximidade dos objetos (distância média 17 Mpc) resultou em uma resolução espacial relativamente boa (tipicamente $\lesssim$200 pc). Essas propriedades do Palomar Survey o fazem ideal para o estudo da demografia e propriedades físicas de galáxias próximas, e especialmente de AGN's de baixa luminosidade.

2.4.1 As galáxias Tipo 1 emissoras de duplo-pico

A Tabela 1 de Ho et al. (1997b) lista as propriedades de 46 AGN's Tipo 1 da amostra do Palomar: 34 são classificados como mostrando detecção "definitiva" da linha larga de Hα, enquanto que para os 12 restantes, há apenas uma "provável" detecção de uma fraca componente larga de Hα. O ajuste dos perfis de linha desses casos "prováveis" mostra qua a componente larga não é bem vinculada e pode ser devido a complexa cinemática da NLR. Inspecionamos os perfis de Hα dos espectros do Palomar dos 34 núcleos considerados como tendo detecção definitiva da componente larga de Hα e encontramos que 12 galáxias possuem claramente um perfil de duplo-pico ou com uma parte central "achatada". Com o objetivo de demonstrar que os perfis em duplo-pico que aparecem no Palomar podem ser atribuídos à emissão da linha das partes mais externas de um disco de acreção, nós selecionamos para o presente trabalho as galáxias cujos espectros mostravam razão sinal-ruído suficiente para o ajuste do perfil: NGC 3516, NGC 4151, NGC 4235, NGC 5273 e NGC 5548.

Capítulo 3

Metodologias

3.1 Subtração da contribuição da população estelar

A maioria dos espectros nucleares analisados mostram fortes linhas de absorção estelares, evidenciando que a contribuição estelar estelar domina o contínuo óptico (ver Figura 2.1). Para melhor medir o perfil e fluxo das linhas de emissão é necessário subtrair a contribuição da população estelar.

No caso de NGC 1097 e NGC 7213 o método utilizado para fazer esta subtração é o mesmo utilizado por Storchi-Bergmann et al. (2003), e está descrito a seguir. Os espectros nucleares foram extraídos utilizando janelas de $1\farcs03 \times 1\farcs0$ and $1\farcs0 \times 1\farcs0$ para os dados do SOAR e Gemini, respectivamente (ver Figura 3.1a, região *(A)*). As extrações nucleares foram centradas no pico da emissão do contínuo, assumido como correspondente ao núcleo da galáxia. Esta posição coincide também com a localização da fonte não resolvida de onde o perfil em duplo-pico de Hα é proveniente. Após a extração do espectro nuclear, foram extraídos espectros adicionais de janelas centradas a $2\farcs0$ de distância da janela de extração nuclear (Figura 3.1a, regiões *(B)* e *(C)*); as dimensões dessas extrações são as mesmas dimensões utilizadas na extração nuclear. Utilizando esses espectros extranucleares, calculamos um espectro médio (Figure 3.1b, espectro do meio). Este espectro médio exibe as mesmas características de absorção estelar presentes no espectro nuclear, fracas linhas de emissão estreitas e não apresenta a linha de emissão larga em duplo-pico (presente apenas no espectro nuclear). As linhas de emissão estreitas foram removidas utilizando como padrão um espectro sintético obtido com o programa STARLIGHTv04 (Cid Fernandes et al., 2005). Sob a hipótese de que este espectro médio é representativo da população estelar presente no núcleo, ele foi normalizado pelo contínuo do núcleo e então subtraído do espectro nuclear. Este processo resultou como sendo bastante eficiente em isolar a emissão nuclear (Figure 3.1b, espectro de baixo). Ainda é importante notar que, como foi discutido no Capítulo 1, após a subtração da contribuição da população estelar, não se pode ver nenhum contínuo residual do AGN, indicando que o mesmo é muito fraco, se estiver presente.

Após a subtração da contribuição da população estelar, o próximo passo foi a normalização do espectro de emissão nuclear utilizando espectros de referência calibrados em fluxo absoluto. Para NGC 1097 foi utilizado como referência o espectro de 2 de Novembro de 1991 (Storchi-Bergmann et al., 1993), escolhido por ser o mesmo espectro que foi utilizado para calibrações anteriores (Storchi-Bergmann et al., 2003, Schimoia et al., 2012). Para NGC 7213 utilizamos como referência o espectro obtido em 27 de Setembro de 2011, pois além de ser o primeiro espectro a ser utilizado na análise, também é o espectro que apresenta maior razão sinal-ruído (12 exposições de 350s).

No caso de NGC 1097, para realizar este processo de calibração, assumimos que o fluxo das linhas estreitas Hα, [N II] $\lambda\lambda$6548,6584, e [S II] $\lambda\lambda$6717,6731 não variou ao longo do período em que cada objeto foi monitorado. Esta hipótese é comumente utilizada porque a a emissão das linhas estreitas se origina de regiões estendidas, com escalas espaciais muito maiores ($\sim$ 100–1000 pc) do

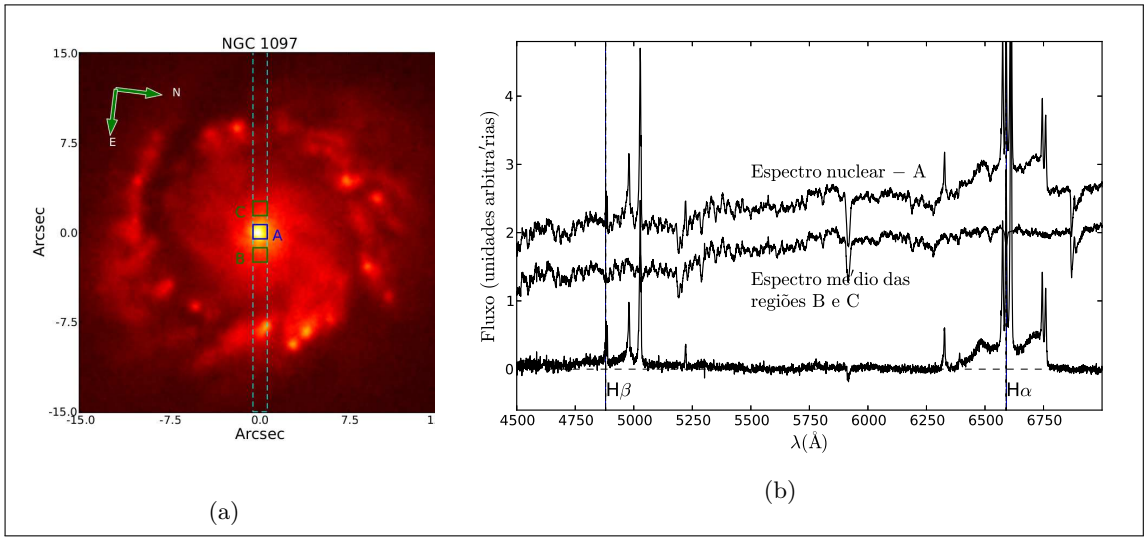

Figura 3.1: (a): imagem de aquisição da região nuclear de NGC 1097 obtida com o telescópio SOAR em 23 de setembro de 2012. As linhas tracejadas em ciano representam a largura da fenda, 1.″03. O quadrado azul *(A)* mostra a janela de extração do espectro nuclear (1.″0 × 1.″03). Os quadrados verdes *(B) e (C)*, centrados a 2.″0 do núcleo mostram as janelas utilizadas para extrair os espectros da população estelar. (b): em cima está o espectro nuclear extraído da janela *(A)*; no meio está o espectro médio de *(B)* e *(C)*, adotado como sendo representativo da população estelar do núcleo; em baixo está a o espectro resultante após a subtração do espectro da população estelar do espectro nuclear, no qual vemos a emissão nuclear isolada.

que as do disco de acreção ($\sim 10^{-3}$ pc). Isto significa que a NLR deve responder às variações do contínuo ionizante em escalas de tempo de pelo menos centenas de anos. Esta escala de tempo é muito maior do que a escala de tempo de resposta da região emissora do perfil em duplo-pico. Já no caso de NGC 7213 as linhas estreitas Hα, [N II] $\lambda\lambda$6548,6584 são mais alargadas do que na NGC 1097, e também no perfil em duplo-pico a asa vermelha se estende até comprimentos de onda maiores do que as linhas [S II] $\lambda\lambda$6717,6731. Dessa forma optamos por intercalibrar os espectros nucleares de NGC 7213 utilizando o fluxo das linhas estreitas [O I]λ6300 Å and [O I]λ6363 Å pois estas linhas estão menos afetadas pela presença do perfil em duplo-pico. Ao longo do restante do texto os espectros de emissão nucleares, corrigidos pela subtração da população estelar e calibrados pelo fluxo das linhas estreitas, serão referenciados apenas como *espectros de emissão nucleares*.

Para as galáxias do Palomar Survey of Nearby Galaxies também realizamos o mesmo processo de subtração estelar pois quase todas as galáxias selecionadas apresentaram um contínuo dominado pela população estelar. A única excessão é a galáxia NGC 5548, cuja emissão do contínuo está dominada pelo AGN e não pela população estelar. A principal diferença no processo de subtração da população estelar nas galáxias do Palomar está no fato de que nesse mapeamento foram observados apenas os núcleos das galáxias, não há espectros extranucleares. Dessa forma, utilizamos

como espectros padrão para a subração os espectros nucleares de galáxias não-ativas, que também foram observadas pelo mesmo survey (Ho et al., 1997a). Para cada espectro nuclear das galáxias da amostra, selecionamos o espectro de uma galáxia não-ativa de (Ho et al., 1997a) que mais se assemelhou à população estelar presente nos espectros nucleares.

3.1.1 Suavização dos espectros

Apesar do cuidadoso processo utilizado para isolar e calibrar o espectro de emissão nuclear, alguns espectros de NGC 1097 obtidos com o SOAR ficaram bastante ruidosos. Isto aconteceu principalmente porque o fluxo do perfil em duplo-pico permaneceu em um estado bem baixo, quando comparado com as observações de trabalhos anteriores (ver a discussão no Capítulo 4).

Nos espectros mais ruidosos é difícil medir as propriedades do perfil, como por exemplo, os comprimentos de onda onde ocorrem os picos azul e vermelho. Além disso, a forma do perfil também ficou comprometida. Com o objetivo de minimizar as dificuldades introduzidas pelo ruído, foi aplicada uma suavização Gaussiana aos espectros de emissão nucleares de NGC 1097. A suavização foi realizada através da convolução do espectro nuclear com uma função Gaussiana normalizada definida por uma única FWHM, correspondente a uma dispersão σ_G. Os valores testados para σ_G variaram de uma a cinco vezes o valor da resolução espectral: $\sigma_G \sim 5.5 - 27.5$ Å. Os valores de $\sigma_G = 5.5, 11e16.5$ Å testados forneceram resultados similares: (i) para os espectros mais ruidosos a suavização Gaussiana aprimorou a forma do perfil de duplo-pico no sentido de fornecer picos azul e vermelho melhor definidos, enquanto que os espectros em que os picos azul e vermelho já estavam bem definidos ficaram praticamente inalterados; (ii) depois da suavização, tornou-se muito mais fácil de medir todas as características do perfil, como descrito a seguir na sessão §3.2.

A suavização Gaussiana foi utilizada principalmente nos espectros de NGC 1097 obtidos com o SOAR. O processo de suavização não foi aplicado aos dados de NGC 7213 obtidos com o telescópio Gemini Sul, pois para esses dados obtivemos melhor sinal para o fluxo da linha larga em duplo-pico.

3.2 Medidas das características do perfil de duplo-pico

NGC 1097

Para estudar as propriedades do perfil de duplo-pico de NGG 1097, definimos um conjunto de parâmetros que são listados a seguir:

- λ_i e λ_f: λ_i é o *comprimento de onda inicial*, definido como o comprimento de onda no qual o fluxo do lado azul do perfil + a sua incerteza associada atingem intensidade zero. Similarmente,

λ_f é o *comprimento de onda final*, onde o fluxo do lado vermelho do perfil atinge intensidade zero. Esses dois parâmetros definem o intervalo espectral da linha larga de duplo-pico de Hα;

- F_B e λ_B: F_B é o *fluxo do pico azul*, definido como o máximo fluxo do lado azul do perfil (região espectral entre λ_i e 6564.61 Å) e λ_B é o comprimento de onda em que F_B ocorre;

- F_R e λ_R: possuem as mesmas definições de F_B e λ_B só que para o lado vermelho do perfil (comprimento de onda entre 6564.61 Å e λ_f). Os valores dos parâmetros λ_R e λ_B são especialmente importantes porque são os comprimentos de onda de onde há maior emissão da linha em cada lado do perfil;

- F_{broad}: fluxo integrado da linha larga de duplo-pico. Para calculá-lo foi necessário eliminar a contribuição do fluxo das linhas estreitas aos espectros de emissão nuclear. As linhas estreitas Hα + [N II] $\lambda\lambda$6548, 6584 foram ajustadas simultaneamente com três Gaussianas, uma para cada linha estreita, e os perfis ajustados foram subtraídos do espectro de emissão nuclear; o mesmo processo foi realizado para [S II] $\lambda\lambda$6717, 6731 com duas Gaussianas. Após eliminar a contribuição das linhas estreitas, o fluxo da linha larga de duplo-pico F_{broad} foi obtido integrando o espectro entre λ_i e λ_f.

A Figura 3.2 ilustra as características dos perfis de duplo-pico descritas acima no espectro de emissão nuclear de NGC 1097 obtido em 23 de setembro de 2012 com o telesccópio SOAR.

NGC 7213

Assim como na NGC 1097, antes de medirmos as propriedades do perfil em duplo-pico, para a NGC 7213 também subtraímos a contribuição das linhas estreitas do perfil. Notamos que as linhas estreitas de NGC 7213 são mais alargadas do que as linhs estreitas de NGC 1097, isso torna mais difícil o ajuste de uma forma funcional que consiga separar eficientemente cada componente estreita. Dessa forma, ao invés de ajustarmos e subtrairmos componentes Gaussianas às linhas estreitas de Hα, [N II] $\lambda\lambda$6548,6584, e [S II] $\lambda\lambda$6717,6731, optamos apenas por interpolar um contínuo linear sob essas linhas. Após a subtração da contribuição das linhas estreitas definimos os seguintes parâmetros para estudar a variabilidade do perfil:

- λ_i e λ_f: exatamente como na NGC 1097 esses parâmetros são respectivamente os comprimentos de onda inicial e final que definem o intervalo espectral da linha larga em duplo-pico;

- F_{Blue}, F_{Red}: devido ao fato dos picos do perfil de NGC 7213 serem menos marcados do que os picos dos perfis em NGC 1097, ao invés de medirmos a posição em comprimento de onda e fluxo dos picos, definimos outras propriedades para estudar a variabilidade dos lados zul e vermelho do perfil. F_{Blue} é o fluxo integrado do lado azul do perfil, isto é, integrado entre

λ_i e 6564.61 Å (comprimento de onda de referência de Hα); F_{Red} é o fluxo integrado do lado vermelho do perfil, entre 6564.61 Å e λ_f;

- F_{Broad}: fluxo integrado do perfil entre λ_i e λ_f, ou seja, a soma de F_{Blue} e F_{Red}.

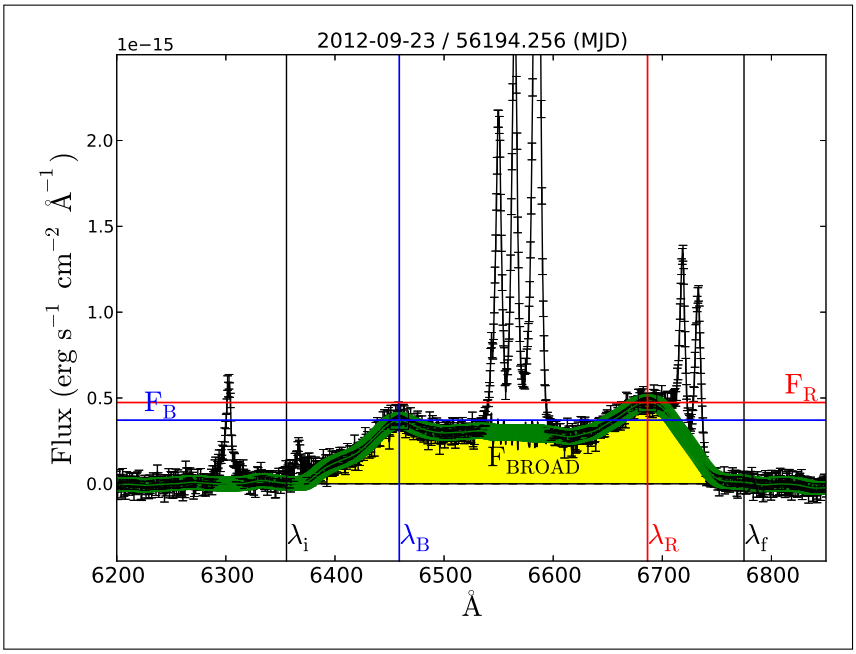

Figura 3.2: Representação visual das propriedades medidas do perfil de duplo-pico de Hα para a observação de 23 de setembro de 2012. As linhas verticais em preto marcam os comprimentos de onda inicial e final λ_i e λ_f, respectivamente. A linha horizontal azul marca o fluxo máximo do lado azul do perfil, F_B, enquanto que a linha azul vertical marca λ_B, comprimento de onda onde F_B ocorre. A linha horizontal vermelha marca o fluxo máximo do lado vermelho, F_R, e a linha vertical vermelha marca λ_R. A região amarela representa o fluxo integrado da linha larga em duplo-pico.

3.3 Estudo de variabilidade

No Capítulo 1 foi discutido que os perfis em duplo-pico podem apresentar variações na sua forma e fluxo integrado (Figura 1.4) ao longo do tempo. O monitoramento da emissão da região nuclear de NGC 1097 em raios-X, UV e do perfil em duplo-pico de Hα forneceu três curvas de luz distintas para estudarmos a variabilidade do AGN desta galáxia. Com o objetivo de quantificar as variações de fluxo em cada curva de luz obtida foi utilizado o método de análise proposto por O'Brien et al. (1998). Neste método, os principais parâmetros de interesse são: N é o número de medidas obtidas ao longo do monitoramento; $\overline{F}$ and σ_F são, respectivamente, o fluxo médio e o desvio padrão do fluxo. O parâmetro F_{var} é a estimativa da amplitude média variacional corrigida pelas incertezas, o

qual é obtido como:

$$F_{var} = \frac{\sqrt{{\sigma_F}^2 - \Delta^2}}{\overline{F}} \tag{3.1}$$

onde Δ é a média dos quadrados dos valores individuais das incertezas, ϵ_i, para i = 1, 2, 3, ..., N observações. Assim:

$$\Delta^2 = \frac{1}{N}\sum_{i=1}^{N} {\epsilon_i}^2 \tag{3.2}$$

As principais vantagens deste método são: (i) F_{var} é uma estimativa global de variabilidade, e permite uma comparação direta entre as amplitudes variacionais de curvas de luz distintas; (ii) no cálculo de F_{var} são descontados os valores das incertezas das medidas, de maneira que F_{var} pode ser interpretado como um parâmetro que mede a *varição global líquida* de uma curva de luz.

3.4 Análise da série temporal

O método de Função de Correlação Cruzada (*Cross Correlation Function – CCF*) tem sido utilizado amplamente nas campanhas de mapas de reverberação para estimar os 'atrasos' entre as variações do contínuo ionizante – chamada de curva de luz geradora (*driven light curve*) – e as variações do fluxo das linhas de emissão – chamadas de curvas de luz de resposta (*response light curve*). Durante o monitoramento de NGC 1097 obtivemos uma curva de luz da emissão do contínuo em raios-X entre 0.3 - 10 keV, e uma curva de luz de emissão do contínuo UV (banda centrada em 2246 Å). Adotamos a hipótese de que essas seriam as curvas de luz geradoras, pois estas duas bandas emitem fótons com energias acima de 13.6 eV, que podem ionizar o gás (Hidrogênio) no disco de acreção. A curva de luz de resposta, por sua vez, é a curva de luz das medidas de F_{broad} obtidas do monitoramento óptico.

O objetivo principal de aplicar o método de CCF é encontrar o atraso – *lag* – no qual existe maior correlação entre a *driven light curve* e a *response light curve*. Para estudar as correlações entre as curvas de luz de NGC 1097 foi utilizado o método de Função de Correlação Cruzada com Interpolação (*Interpolated Cross Correlation Function* – ICCF) descrito em Gaskell & Peterson (1987), White & Peterson (1994), Peterson et al. (2004, 1998), cujo código computacional foi cedido pelo colaborador Bradley M. Peterson para aplicação neste trabalho. Do ponto de vista computacional, os principais passos no cálculo da ICCF, são:

1. Os pontos da curva de luz geradora e os pontos da curva de luz de resposta são interpolados linearmente em pontos correspondentes a múltiplos de um determinado intervalo de tempo Δt de maneira que o número de pontos final em cada curva de luz é N, onde N é obtido dividindo o intervalo de tempo em que desejamos testar a correlação por Δt;

2. Calcula-se $ICCF(\tau)$ nos valores τ, múltiplos de Δt:

$$ICCF(\tau) = \frac{1}{N}\sum_{i=1}^{N}\frac{\left[L(t_i)-\overline{L}\right]\left[C(t_i-\tau)-\overline{C}\right]}{\sigma_C\,\sigma_L} \tag{3.3}$$

onde $t_{i+1} - t_i = \Delta t$ para $1 \leq i \leq N-1$, $\overline{C}$ e σ_C são os valores do fluxo médio e do desvio padrão calculados para a curva de luz do contínuo (*driver light curve*) e $\overline{L}$ e σ_L são as mesmas estimativas para a curva de luz da linha de emissão (*response light curve*). O lado direito da Equação 3.3 é simplesmente o cálculo do coeficiente de correlação linear entre as duas curvas de luz, após deslocar a curva de luz do contínuo por um valor τ.

3. A realização do cálculo de $ICCF(\tau)$ para todos os valores de τ no intervalo desejado gera a distribuição de valores de $ICCF$ como função de τ. O valor de τ correspondente ao máximo de $ICCF$ é chamado de τ_{peak} e é interpretado como o 'atraso' (*lag*) entre as duas curvas de luz, para o qual elas estão maximamente correlacionadas.

Se as curvas de luz estiverem correlacionadas, $\tau_{peak} \times c$, onde c é avelocidade da luz, pode ser diretamente interpretado como a distância entre a fonte ionizante central e a região emissora da linha.

3.5 Modelo de disco de acreção

Para modelar o perfil de duplo-pico usamos a prescrição para o disco de acreção de Chen et al. (1989), Chen & Halpern (1989). Nesta prescrição, o disco é geometricamente e opticamente fino, e a região emissora da linha é delimitada por um raio interno ξ_1 e um raio externo ξ_2. As órbitas do gás emissor são Keplerianas e relativísticas e o disco está inclinado em relação a linha de visada por um ângulo i. O fluxo total da linha de emissão, F, é calculado como a integral sobre a intensidade específica emitida I_ν, sobre todas as frequências e sobre o ângulo sólido compreendido entre o disco emissor e o observador:

$$F = \int\int\int I_\nu d\nu d\Omega \tag{3.4}$$

A intensidade específica emitida é assumida como sendo uma função da emissividade superficial do disco $\epsilon(\xi,\phi)$ – onde ξ e ϕ representam, respectivamente, a distância radial e o ângulo azimutal sobre a superfície do disco – e do parâmetro de alargamento σ. O parâmetro σ faz com que cada elemento de área do disco emita radiação com uma distribuição Gaussiana de frequências em torno da frequência de referência:

$$I_{\nu_e}(\xi,\phi,\nu_e) = \frac{\epsilon(\xi,\phi)}{4\pi}\frac{e^{-(\nu_e-\nu_0)^2/2\sigma^2}}{(2\pi)^{1/2}\sigma}, \tag{3.5}$$

onde ν_e é a frequência emitida e ν_0 é a frequência de referência, correspondente à linha Hα. O perfil espectral da linha, F_χ, é expresso de maneira que o fluxo integrado da linha é $F = \int F_\chi d\chi$. De Chen & Halpern (1989), F_χ é calculado como:

$$F_\chi = F_0 \int_{\xi_1}^{\xi_2} \int_0^{2\pi} \exp\left[-\frac{(1+\chi-D)^2\nu_0^2}{2\sigma^2 D^2}\right] \left[1+\xi^{-1}\left(\frac{1-\sin i\cos\phi}{1+\sin i\cos\phi}\right)\right] D^3\,\epsilon(\xi,\phi)\,\xi\,d\xi d\phi \tag{3.6}$$

onde F_0 é uma constante de normalização entre a observação e o perfil modelado e D é o *fator Doppler*:

$$D = \left(1-\frac{3}{\xi}\right)^{1/2}\left(1+\frac{\sin i\sin\phi}{\xi^{1/2}}\right)^{-1} \tag{3.7}$$

Nesta prescrição, os possíveis parâmetros livres do modelo são:

- O raio interno ξ_1, e o raio externo ξ_2, da região emissora de linhas;
- O ângulo de inclinação i, do disco;
- O parâmetro de alargamento σ;
- Todos os parâmetros associados a emissividade superficial do disco, $\epsilon(\xi,\phi)$.

Para o caso de Arp 102B, Chen et al. (1989) modelaram o perfil de duplo-pico assumindo uma emissividade superficial axialmente simétrica para o disco de acreção:

$$\epsilon(\xi,\phi) = \epsilon(\xi) = \epsilon_0\,\xi^{-q} \tag{3.8}$$

onde q é o índice da lei de emissividade. Seguindo essa prescrição eles conseguiram modelar muito bem o pico azul mais intenso que o pico vermelho devido ao *Doppler boosting* da região emissora do disco que se aproxima do observador.

3.5.1 Emissividades superficiais axialmente assimétricas

Atualmente sabe-se que muitos AGN's que apresentam perfis em duplo-pico variáveis exibem em algumas épocas o lado vermelho do perfil mais intenso que o lado azul. Essas assimetrias podem estar associadas a braços espirais Gilbert et al. (1999) ou a manchas brilhantes (*lumps*) no disco de acreção Lewis et al. (2010). De fato, Strateva et al. (2006) encontraram que assimetrias nos perfis de duplo-pico são bastante comuns, sendo que pelo menos 60% dos objetos estudados exigiram algum tipo de assimetria na emissividade do disco de acreção.

Em Schimoia et al. (2012), a evolução do perfil de duplo-pico de NGC 1097 foi modelada seguindo a prescrição de emissividade superficial do disco que chamamos de *Saturated Spiral Model*, em que $\epsilon(\xi,\phi)$ é separada em duas partes, uma parte com dependência apenas radial e outra parte

com dependência apenas azimutal. A dependência azimutal da emissividade, $\epsilon(\phi)$, tem a forma de um braço espiral, cujo contraste com o disco subjacente é definido pelo parâmetro A:

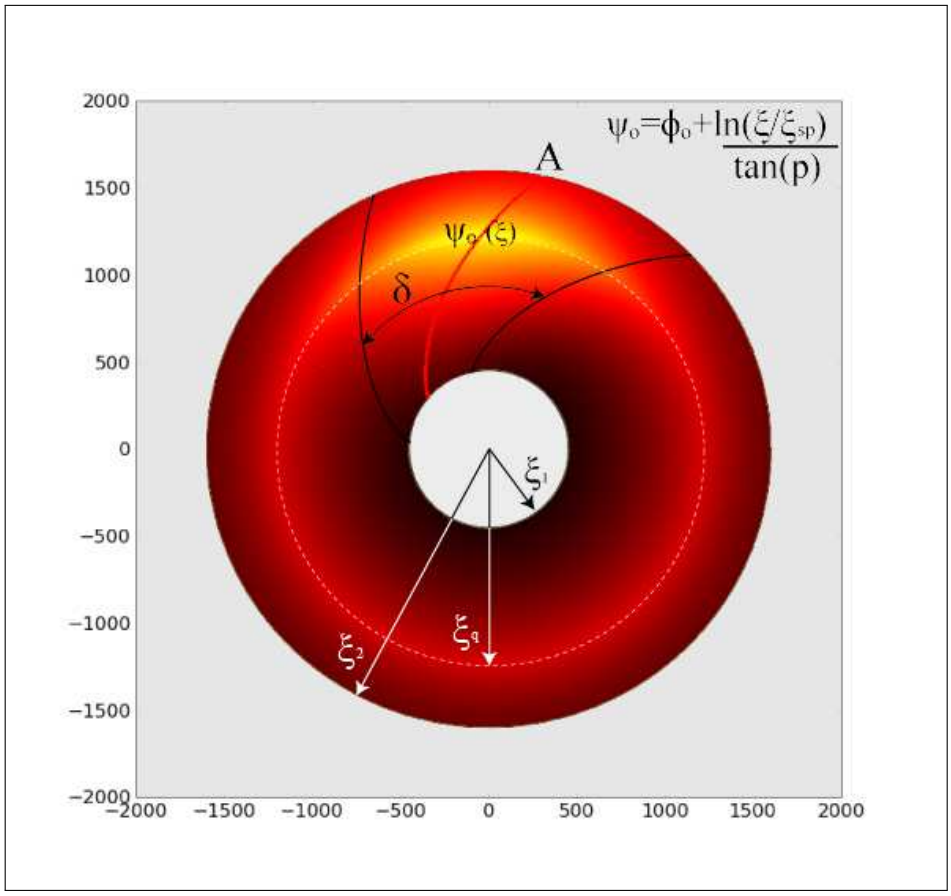

Figura 3.3: Ilustração dos principais parâmetros do modelo de disco de acreção com braço espiral. ξ_1 e ξ_2 são, respectivamente, o raio interno e externo da região emissora da linha. ξ_q é o raio de quebra da emissividade radial. A linha vermelha é a linha de máxima emissividade do disco e o ângulo de posição do braço espiral ψ_0 é definido em função do raio ξ do disco: $\psi_0 = \phi_0 + \ln(\xi/\xi_{sp})/\tan(p)$. A partir do centro do braço espiral definido por ψ_0, a emissividade decai azimutalmente de forma Gaussiana com uma FWMH δ.

$$\epsilon(\phi) = \left\{ \frac{A}{2} \exp\left[-\frac{4\ln 2}{\delta^2}(\phi - \psi_0)^2 \right] + \frac{A}{2} \exp\left[-\frac{4\ln 2}{\delta^2}(2\pi - \phi + \psi_0)^2 \right] \right\}, \tag{3.9}$$

onde a expressão entre colchetes representa o decaimento da emissividade do braço espiral como função da distância azimutal, $\phi - \psi_0$, a partir linha de máxima emissividade. O decaimento azimutal é assumido como tendo uma forma Gaussiana de FWHM δ, chamada de largura azimutal do braço espiral. A relação entre o ângulo azimutal, ϕ_0, e a posição angular, ψ_0, da linha de máxima

emissividade do braço espiral é dada por:

$$\psi_0 = \phi_0 + \frac{\ln(\xi/\xi_{sp})}{\tan p}, \tag{3.10}$$

onde ϕ_0 é a orientação azimutal do padrão espiral, p é o *pitch angle* e ξ_{sp} é o raio mais interno a partir do qual inicia o braço espiral.

A emissividade axialmente simétrica do disco, $\epsilon(\xi)$, é dada por:

$$\epsilon(\xi) = \begin{cases} \epsilon_0 \xi^{-q_1} & , \xi_1 < \xi < \xi_q \\ \epsilon_0 {\xi_q}^{-(q_1-q_2)} \xi^{-q_2} & , \xi_q < \xi < \xi_2 \end{cases} \tag{3.11}$$

onde ξ_q é o raio de máxima emissividade, ou *raio de saturação*, no qual a lei de emissividade muda; q_1 é o índice da lei de emissividade para as regiões internas a ξ_q ($\xi_1 < \xi < \xi_q$); q_2 é o índice da lei de emissividade para as regiões externas a ξ_q ($\xi_q < \xi < \xi_2$); ξ_1 e ξ_2 são o raio interno e externo, respectivamente. A emissividade total para o disco de acreção é então:

$$\epsilon(\xi, \phi) = \epsilon(\xi)\,[1 + \epsilon(\phi)] \tag{3.12}$$

onde $\epsilon(\xi)$ é dado pela Equação 3.11 e $\epsilon(\phi)$ é dado pela Equação 3.9.

A Figura 3.3 ilustra os principais parâmetros do modelo de emissividade superficial com braço espiral e lei de emissividade quebrada (*Saturated Spiral Model*). Neste modelo, em adição aos parâmetros já descritos anteriormente, os possíveis parâmetros livres durante a modelagem dos perfis de duplo-pico são:

- O contraste do braço espiral A;
- O ângulo de orientação azimutal do braço espiral ϕ_0;
- O *pitch* angle p;
- A largura azimutal do braço espiral δ;
- O raio onde inicia o braço espiral ξ_{sp};
- O índice da lei de emissividade, q_1, para raios $\xi_1 < \xi < \xi_q$;
- O raio de quebra da lei de emissividade, ξ_q;
- O índice da lei de emissividade, q_2, para raios $\xi_q < \xi < \xi_2$.

Capítulo 4

Resultados para a galáxia NGC 1097

Os resultados obtidos para a galáxia NGC 1097 estão descritos no artigo a seguir, o qual foi publicado na revista arbitrada *The Astrophysical Journal*.

‘MONITORAMENTO EM CURTA ESCALA DE TEMPO DOS RAIOS-X, UV E DA LINHA DE EMISSÃO EM DUPLO-PICO DO NUCLEO DE NGC 1097’

The Astrophysical Journal, 800:63 (13pp), 2015 February 10 doi:10.1088/0004-637X/800/1/63

SHORT-TIMESCALE MONITORING OF THE X-RAY, UV, AND BROAD DOUBLE-PEAK EMISSION LINE OF THE NUCLEUS OF NGC 1097

Jaderson S. Schimoia[1,2], Thaisa Storchi-Bergmann[1,3], Dirk Grupe[4,10], Michael Eracleous[5,11,12], Bradley M. Peterson[2,6], Jack A. Baldwin[7], Rodrigo S. Nemmen[8,13,14,15], and Cláudia Winge[9]
[1] Instituto de Física, Universidade Federal do Rio Grande do Sul, Campus do Vale, Porto Alegre, RS, Brazil; silva.schimoia@ufrgs.br
[2] Department of Astronomy, The Ohio State University, 140 West 18th Avenue, Columbus, OH 43210, USA
[3] Harvard-Smithsonian Center for Astrophysics, 60 Garden Street, Cambridge, MA 02138, USA
[4] Space Science Center, Morehead State University, 235 Martindale Drive, Morehead, KY 40351, USA
[5] Department of Astronomy and Astrophysics and Institute for Gravitation and the Cosmos, Pennsylvania State University, 525 Davey Lab, University Park, PA 16802, USA
[6] Center for Cosmology and AstroParticle Physics, The Ohio State University, 191 West Woodruff Avenue, Columbus, OH 43210, USA
[7] Department of Physics and Astronomy, Michigan State University, East Lansing, MI 48864, USA
[8] Instituto de Astronomia, Geofísica e Ciências Atmosféricas, Universidade de São Paulo, São Paulo, SP 05508-090, Brazil
[9] Gemini South Observatory, c/o AURA Inc., Casilla 603, La Serena, Chile
Received 2014 July 28; accepted 2014 November 5; published 2015 February 10

ABSTRACT

Recent studies have suggested that the short-timescale ($\lesssim$7 days) variability of the broad ($\sim$10,000 km s^{-1}) double-peaked Hα profile of the LINER nucleus of NGC 1097 could be driven by a variable X-ray emission from a central radiatively inefficient accretion flow. To test this scenario, we have monitored the NGC 1097 nucleus in X-ray and UV continuum with *Swift* and the Hα flux and profile in the optical spectrum using SOAR and Gemini-South from 2012 August to 2013 February. During the monitoring campaign, the Hα flux remained at a very low level—three times lower than the maximum flux observed in previous campaigns and showing only limited ($\sim$20%) variability. The X-ray variations were small, only $\sim$13% throughout the campaign, while the UV did not show significant variations. We concluded that the timescale of the Hα profile variation is close to the sampling interval of the optical observations, which results in only a marginal correlation between the X-ray and Hα fluxes. We have caught the active galaxy nucleus in NGC 1097 in a very low activity state, in which the ionizing source was very weak and capable of ionizing just the innermost part of the gas in the disk. Nonetheless, the data presented here still support the picture in which the gas that emits the broad double-peaked Balmer lines is illuminated/ionized by a source of high-energy photons which is located interior to the inner radius of the line-emitting part of the disk.

Key words: accretion, accretion disks – galaxies: individual (NGC 1097) – galaxies: nuclei – galaxies: Seyfert – line: profiles

1. INTRODUCTION

The energy emitted by active galaxy nuclei (AGNs) is provided by accretion of mass onto a supermassive black hole (SMBH), via an accretion disk, whose emission is observed in the UV continuum of Seyfert galaxies and quasars (e.g., Frank et al. 2002). The optical spectra of some AGN show extremely broad ($\sim$10,000 km s^{-1}) double-peaked emission lines that are thought to originate in the outer extension of the accretion disk. Indeed, models of ionized gas emission rotating in a relativistic Keplerian accretion disk around an SMBH have been generally successful in accounting for the double-peaked profiles (Chen et al. 1989; Chen & Halpern 1989; Storchi-Bergmann et al. 2003; Strateva et al. 2003; Lewis et al. 2010). These models explain self-consistently most observable features of the double-peaked profiles (Eracleous & Halpern 2003). Long timescale monitoring (years to decades) has revealed variability of the double-peaked profiles in several objects, including the radio galaxy 3C390.3 (Shapovalova et al. 2010), the LINER NGC 1097 (Storchi-Bergmann et al. 2003), the radio galaxy Pictor A, and other radio-loud AGNs (Gezari et al. 2007; Lewis et al. 2010).

The variations in double-peaked profiles can provide an effective probe of disk models and lead to understanding of the physical mechanisms that cause profile variability. For this reason, we have monitored the double-peaked Hα profile in the nuclear spectrum of NGC 1097. We were fortunate enough to obtain a few Gemini-South spectra separated by less than a week, which revealed much shorter timescale profile variability than had been seen before in this source. Our observations constrain the variability timescale of the integrated flux of the profile and the velocity separation between the blue and red peaks to approximately seven days (Schimoia et al. 2012). This is the shortest timescale variability ever seen in the double-peaked profile of this object, and coincides with the estimated light travel time between the nucleus and the line-emitting region of the disk.

The short-timescale variations suggest that the line emission is driven by the central source. A number of studies have compared the available energy due to local viscous dissipation in the accretion disk with the observed luminosity of emission lines and concluded that there is indeed the need for an external

[10] Also at Swift Mission Operation Center, 2582 Gateway Drive, State College, PA 16801, USA.
[11] Also at Center for Relativistic Astrophysics, Georgia Institute of Technology, Atlanta, GA 30332, USA.
[12] Also at Department of Astronomy, University of Washington, Seattle, WA 98195, USA.
[13] Also at NASA Goddard Space Flight Center, Greenbelt, MD 20771, USA.
[14] Also at Center for Research and Exploration in Space Science and Technology (CRESST).
[15] Also at Department of Physics, University of Maryland, Baltimore County, 1000 Hilltop Circle, Baltimore, MD 21250, USA.

ionizing source to power the observed luminosity of the double-peaked emission lines. This has been argued by Eracleous & Halpern (1994), Strateva et al. (2006, 2008), and Luo et al. (2013). In the case of NGC 1097, Nemmen et al. (2006) have proposed that the ionizing source is a radiatively inefficient accretion flow (RIAF; Narayan & McClintock 2008) located in the center (or inner rim) of the disk. The seven-day timescale is consistent with an origin of the emission-line variability as a reverberation signal of the varying X-ray emission from the inner RIAF in the line-emitting portion of the disk.

In our previous studies of profile variability in the spectrum of NGC 1097 (Schimoia et al. 2012) we also found an inverse correlation between the flux of the line and the velocity separation between the two peaks of the profile, confirming the previous result reported by Storchi-Bergmann et al. (2003). This inverse correlation also supports the reverberation scenario: when the flux is higher, the RIAF at the center is more luminous and illuminates/ionizes farther out in the accretion disk, where the disk rotational velocities are lower (thus the profile is narrower); conversely, when the flux from the RIAF is lower, the disk emissivity is weighted more heavily toward smaller radii where the velocities are higher, hence the profile is broader. A similar behavior is also observed in 3C 390.3 by Shapovalova et al. (2001, see their Figure 4).

In order to test the hypothesis that the Hα variability is a reverberation response to variations of the X-ray and UV continuum emitted by the inner RIAF, we undertook a campaign to monitor the X-ray and Hα emission in NGC 1097. From 2012 August to 2013 February, we monitored the emission from the nucleus of NGC 1097 in three different wavelengths bands. The high-energy continuum (presumably emitted by the RIAF) was monitored with the *Swift* satellite, using the X-ray telescope (XRT) telescope to obtain X-ray fluxes and the UVOT(M2) to obtain the UV fluxes. The spectral monitoring of the Hα double-peaked profile was performed using the GOODMAN spectrograph at the SOAR telescope. In this contribution, we report on the results of this campaign. In Section 2, we describe the observations and the data reduction and, in Section 3, we present the measurements of the properties of the Hα double-peaked profile and the flux measurements of X-ray/UV bands as well as the main results from our monitoring campaign. In Section 4, we discuss the results and their physical implications to the reverberation scenario and the emitting structure of the double-peaked profile. Our conclusions are summarized in Section 5.

2. OBSERVATIONS AND DATA REDUCTION

2.1. X-Ray and Ultraviolet Observations with Swift

Observations were made with X-ray and ultraviolet (UV) telescopes on *Swift* between 2012 July 26 and 2013 January 30 (MJD[16] 56134 to 56327).

The *Swift* XRT (Burrows et al. 2005) was operated in photon counting mode (Hill et al. 2004). The data were reduced by the task `xrtpipeline` version 0.12.6., which is included in the HEASOFT package 6.12. Source counts were measured inside a circle of radius 47″ and the background was determined from a source-free region of radius of 235″ using the task `xselect` (version 2.4b). Auxiliary response files were created using the XRT task `xrtmkarf`. The spectra were rebinned with 20 counts per bin using the task `grppha` and the response files `swxpc0to12s6_20010101v013.rmf` were applied. The rebinned spectra were modeled over the range 0.3–10 keV in XSPEC v.12.7 with a single power law and correction for Galactic absorption corresponding to a hydrogen column density $N_{\rm H} = 2.03 \times 10^{20}$ cm^{-2} (Kalberla et al. 2005), which is very close to the value of $N_{\rm H} = 2.3 \times 10^{20}$ cm^{-2} determined from a *Chandra* observation by Nemmen et al. (2006).

We analyzed all available data obtained with the *Swift* UV/Optical Telescope (UVOT; Roming et al. 2005) during this period. We restrict our attention to data obtained through the UVM2 (2246 Å) filter as it is the cleanest of the UVOT filters (Breeveld et al. 2010). We employed the UVOT software task `uvotsource` to extract counts within a circular region of 3.″0 radius for the nucleus of NGC 1097 and used 20″ radius to determine the background. The UVOT count rates were aperture corrected and then converted into magnitudes and fluxes based on the most recent UVOT calibration as described by Poole et al. (2008) and Breeveld et al. (2010). The flux measurements were corrected for Galactic reddening ($E_{B-V} = 0.027$ mag) following the corrections given by Roming et al. (2009), based on standard reddening correction curves from Cardelli et al. (1989). X-ray and UV measurements from *Swift* are given in Table 1.

2.2. Optical Observations with SOAR

The Hα region of the optical spectrum was monitored at the SOAR Telescope using the Goodman High-Throughput Spectrograph in long-slit mode. Observations were obtained approximately every 7 days in queue mode from MJD56147 to MJD56319 for a total of 22 epochs (Program SO2012B-020). A few scheduled observations were lost to poor weather so the actual mean interval between observations is ∼7.5 days. A log of observations appears in Table 2.

The observations employed a 600 l mm^{-1} grating, yielding a dispersion of 0.065 nm pixel^{-1} in the "Mid" mode. A GG455 filter was used to block second-order contamination. This setup provides wavelength coverage 450–725 nm and spectral resolution of ∼0.55 nm, measured as the FWHM of the lines in the arc spectrum. The spectrograph slit was set to a projected width of 1.″03 (∼80 pc at the galaxy), because it is usually larger than the average seeing during the observations. The same slit width was used in our previous observations (SB03), which allows us to scale the new spectra to match the narrow emission line fluxes observed in our previous studies. This allows us to "normalize" the spectra to a common flux scale.

2.3. Gemini Data

Motivated by the low Hα flux in the SOAR spectra obtained early in this campaign compared to what had been observed previously (Schimoia et al. 2012), a single long-slit spectrum was obtained with the Gemini-South Multi-Object Spectrograph on MJD56173. This observation was obtained as part of an active "Poor Weather" project on the Gemini-South telescope (Program GS-2012A-Q-86). For this observation, we used a slit width of 1.″0, the B600 grating, and a GG455 filter. The resulting spectrum covers the range from 510 nm to 800 nm with a resolution of ∼0.45 nm. The data were reduced using the standard procedures in the *IRAF*[17] software package.

[16] For brevity, we use only the five least-significant digits of the modified Julian Date (MJD); MJD56134 refers to JD 2456134.

[17] IRAF is distributed by the National Optical Astronomy Observatory, which is operated by the Association of Universities for Research in Astronomy, Inc., under cooperative agreement with the National Science Foundation.

Table 1
X-ray and UV Measurements from *Swift*

UT Date	MJD	F_X	α_X	F(M2)
2012 Jul 26	56134.374	$3.88^{+1.15}_{-0.55}$	0.58 ± 0.32	0.92 ± 0.06
2012 Jul 30	56138.928	$3.47^{+0.60}_{-0.43}$	0.59 ± 0.30	1.05 ± 0.07
2012 Aug 3	56142.342	$4.93^{+0.62}_{-0.58}$	0.83 ± 0.40	1.01 ± 0.07
2012 Aug 7	56146.819	$5.94^{+0.82}_{-0.55}$	0.97 ± 0.39	1.01 ± 0.07
2012 Aug 11	56150.781	$2.70^{+0.50}_{-0.30}$	1.15 ± 0.46	1.01 ± 0.07
2012 Aug 15	56154.631	$5.17^{+0.66}_{-0.74}$	0.65 ± 0.36	1.00 ± 0.06
2012 Aug 19	56158.967	$3.63^{+0.60}_{-0.31}$	0.72 ± 0.33	0.92 ± 0.06
2012 Aug 23	56162.712	$4.20^{+0.77}_{-0.55}$	0.76 ± 0.29	0.88 ± 0.06
2012 Aug 27	56166.786	$3.65^{+0.51}_{-0.29}$	0.91 ± 0.30	1.02 ± 0.07
2012 Aug 31	56170.586	$4.00^{+0.61}_{-0.63}$	0.75 ± 0.29	0.99 ± 0.06
2012 Sep 4	56174.538	$2.69^{+0.28}_{-0.23}$	1.17 ± 0.32	0.98 ± 0.06
2012 Sep 8	56178.213	$2.95^{+0.40}_{-0.32}$	1.03 ± 0.33	0.98 ± 0.06
2012 Sep 12	56182.295	$3.45^{+0.52}_{-0.43}$	0.80 ± 0.34	0.96 ± 0.06
2012 Sep 16	56186.561	$3.80^{+0.76}_{-0.50}$	0.99 ± 0.35	0.98 ± 0.06
2012 Sep 20	56190.781	$4.28^{+1.89}_{-0.56}$	1.12 ± 0.90	1.07 ± 0.09
2012 Sep 24	56194.715	$8.41^{+4.98}_{-2.28}$	0.28 ± 0.67	0.98 ± 0.09
2012 Oct 2	56202.063	$4.23^{+0.61}_{-0.49}$	0.71 ± 0.28	0.91 ± 0.06
2012 Oct 6	56206.406	$3.32^{+0.71}_{-0.39}$	0.73 ± 0.33	0.96 ± 0.06
2012 Oct 10	56210.958	$3.61^{+1.10}_{-0.46}$	0.76 ± 0.40	0.93 ± 0.06
2012 Oct 14	56214.900	$3.24^{+0.34}_{-0.42}$	0.81 ± 0.30	0.94 ± 0.06
2012 Oct 18	56218.039	$3.14^{+0.46}_{-0.52}$	0.69 ± 0.32	0.99 ± 0.06
2012 Oct 22	56222.231	$4.35^{+0.46}_{-0.52}$	0.84 ± 0.27	0.95 ± 0.06
2012 Oct 26	56226.722	$2.89^{+0.50}_{-0.40}$	0.91 ± 0.36	0.96 ± 0.06
2012 Oct 30	56230.864	$2.52^{+0.46}_{-0.29}$	1.26 ± 0.48	0.89 ± 0.06
2012 Nov 3	56234.130	$2.09^{+0.48}_{-0.26}$	1.37 ± 0.46	0.96 ± 0.06
2012 Nov 7	56238.066	$3.39^{+0.57}_{-0.56}$	0.61 ± 0.35	0.97 ± 0.06
2012 Nov 15	56246.648	$2.95^{+0.56}_{-0.44}$	0.87 ± 0.38	0.97 ± 0.06
2012 Nov 19	56250.828	$3.15^{+0.39}_{-0.42}$	0.79 ± 0.33	0.95 ± 0.06
2012 Nov 27	56258.854	$3.12^{+0.72}_{-0.52}$	0.78 ± 0.36	0.94 ± 0.06
2012 Dec 1	56262.323	$2.87^{+0.47}_{-0.40}$	0.96 ± 0.37	0.85 ± 0.05
2012 Dec 5	56266.800	$2.01^{+0.43}_{-0.25}$	0.90 ± 0.36	0.87 ± 0.05
2012 Dec 9	56270.465	$3.05^{+0.51}_{-0.38}$	1.08 ± 0.31	0.95 ± 0.06
2012 Dec 13	56274.674	$4.35^{+0.82}_{-0.60}$	0.77 ± 0.39	0.91 ± 0.06
2012 Dec 17	56278.610	$3.00^{+0.68}_{-0.40}$	0.95 ± 0.40	0.88 ± 0.06
2012 Dec 21	56282.482	$3.35^{+0.59}_{-0.40}$	1.04 ± 0.37	0.88 ± 0.05
2012 Dec 25	56286.829	$5.05^{+1.08}_{-0.75}$	0.67 ± 0.35	0.93 ± 0.06
2012 Dec 29	56290.834	$3.36^{+0.64}_{-0.66}$	0.76 ± 0.32	0.89 ± 0.06
2013 Jan 2	56294.041	$2.78^{+0.62}_{-0.27}$	0.52 ± 0.60	0.88 ± 0.06
2013 Jan 6	56298.645	$2.99^{+0.59}_{-0.49}$	0.62 ± 0.32	0.89 ± 0.06
2013 Jan 10	56302.618	$2.04^{+0.46}_{-0.24}$	1.01 ± 0.43	0.87 ± 0.06
2013 Jan 14	56306.397	$2.49^{+0.60}_{-0.38}$	0.69 ± 0.43	0.90 ± 0.06
2013 Jan 18	56310.286	$2.90^{+0.46}_{-0.40}$	1.06 ± 0.30	0.97 ± 0.06
2013 Jan 22	56314.755	$3.66^{+0.52}_{-0.35}$	1.00 ± 0.28	0.95 ± 0.06
2013 Jan 26	56318.159	$2.62^{+0.37}_{-0.27}$	1.05 ± 0.33	0.93 ± 0.06
2013 Jan 30	56322.089	$3.82^{+0.55}_{-0.32}$	0.74 ± 0.29	0.85 ± 0.05

Notes. Column 1 gives the date of observations while Column 2 gives the Modified Julian Date (JD−2400000.5). Column 3 gives the 0.3–10 keV flux in units of 10^{-12} erg s^{-1} cm^{-2} and the X-ray power-law slope appears in Column 4. Column 5 gives the UV M2 (∼2246 Å) flux in units of 10^{-15} erg s^{-1} cm^{-2}.

The resulting GMOS spectrum demonstrated that despite the low Hα flux, the double-peaked profiles obtained at SOAR were sufficiently reliable for detailed analysis.

Table 2
Observation Log

Telescope	UT Date	MJD	Exposure Time (s)	P.A. (°)
SOAR	2012 Aug 7	56147.356	3 × 1200	260
SOAR	2012 Aug 9	56149.368	3 × 1200	262
SOAR	2012 Aug 10	56150.360	3 × 1200	262
SOAR	2012 Aug 24	56164.349	2 × 1200	264
SOAR	2012 Aug 31	56171.388	2 × 1200	90
Gemini South	2012 Sep 03	56173.305	6 × 600	280
SOAR	2012 Sep 8	56179.370	3 × 1200	89
SOAR	2012 Sep 16	56187.222	3 × 1200	260
SOAR	2012 Sep 23	56194.256	2 × 1500	90
SOAR	2012 Sep 27	56198.175	5 × 1200	257
SOAR	2012 Oct 12	56213.316	3 × 1200	94
SOAR	2012 Oct 18	56219.316	3 × 1200	96
SOAR	2012 Oct 25	56226.048	3 × 1200	251
SOAR	2012 Oct 28	56229.229	3 × 1200	90
SOAR	2012 Nov 2	56234.086	3 × 1200	360
SOAR	2012 Nov 12	56244.074	3 × 1200	259
SOAR	2012 Nov 23	56255.068	3 × 1800	261
SOAR	2012 Dec 8	56270.206	3 × 1800	98
SOAR	2012 Dec 15	56277.142	3 × 1800	95
SOAR	2012 Dec 23	56285.097	3 × 1200	360
SOAR	2012 Dec 28	56290.074	3 × 1200	91
SOAR	2013 Jan 17	56310.047	4 × 1200	93
SOAR	2013 Jan 26	56319.067	3 × 1200	97

Notes. The telescope used is given in Column 1 and the date of observation appears in Column 2 while Column 3 gives the Modified Julian Date (JD−2400000.5). Columns 4 and 5 give the exposure time and slit position angle, respectively.

3. DATA ANALYSIS

3.1. The Hα Profile

3.1.1. Nuclear Extractions and the Stellar Population Contribution

We extracted the nuclear spectra using windows of 1.″03 × 1.″0 and 1.″0 × 1.″0 for SOAR and Gemini data, respectively (Figure 1). The nuclear extraction windows were centered at the peak of the continuum emission, which coincides with the location of the unresolved source of the broad Hα line. Since the nuclear spectrum shows strong absorption lines from the underlying stellar population (Figure 1), we subtracted the stellar population contribution in order to isolate the Hα profile. For each epoch, we extracted and then averaged two additional spectra with extraction windows centered 2.″0 away from the nuclear window (Figure 1). The average extranuclear spectra display the same absorption features as the nuclear spectra, and are only weakly "contaminated" by narrow emission lines which were excised by using a synthetic spectrum obtained by running the `starlight-v04` code of Cid Fernandes et al. (2005) as a template. We assume that this spectrum is representative of the nuclear stellar population and scale and subtract it from the nuclear spectrum, thus isolating the emission-line spectrum, as shown in Figure 1. As in our previous studies, the nuclear spectrum shows no detectable non-stellar continuum emission, only line emission.

We then normalized in flux the nuclear emission spectra using as reference a previous flux-calibrated spectrum from 1991 November 2 (Storchi-Bergmann et al. 1993), as we have in previous studies (Storchi-Bergmann et al. 2003; Schimoia et al. 2012). We assume that the fluxes in [N II] λλ6548, 6584, [S II] λλ6717, 6731, and the narrow component of Hα

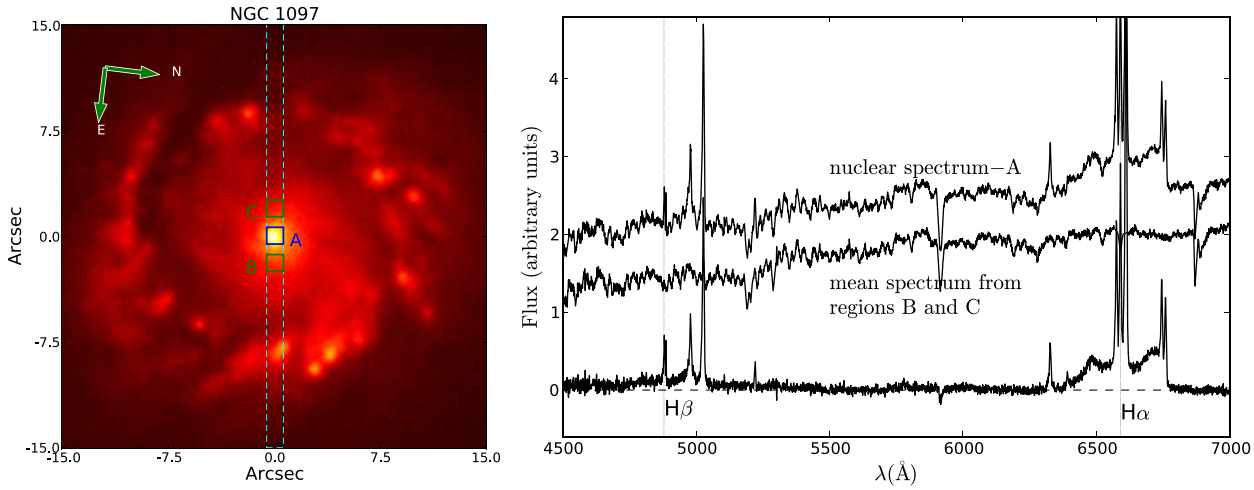

Figure 1. Left: acquisition image of the nuclear region of NGC 1097 from the SOAR observation of MJD56194. The cyan dashed line represents the slit (width of 1.″03). The blue square (A) shows the extraction window (1.″03 × 1.″0) of the nuclear spectrum. The green squares (B and C), centered at 2.″0 from the nucleus show the windows used to extract stellar population spectra. Right: (a) top: nuclear spectrum extracted from window A; (b) middle: mean spectrum of B and C, adopted as representative of the nuclear stellar population; (c) bottom: difference between (a) and (b) (after scaling), which isolates the nuclear emission.

have not varied since our 1991 observation because of the long light travel time across the region as well as the long recombination time at low densities (although these assumptions may not hold for higher-ionization narrow lines, see Peterson et al. 2013). Hereafter we refer to the flux-calibrated starlight-corrected nuclear emission spectra simply as the "nuclear emission spectra."

As we noted earlier, the broad Hα flux is lower than it had been in our earlier observations, and consequently some of the spectra are noisy. This leads to some ambiguity in measuring profile parameters (as described in the next section) such as the wavelengths of the red and blue peaks. We therefore smoothed the spectra with a Gaussian function. We experimented with Gaussian smoothing functions between one and five times the spectral resolution (i.e., FWHM between 5.5 and 27.5 Å), finally settling on FWHM = 11 Å. This resulted in much better defined profile parameters for noisier spectra without altering the measurements for the less noisy spectra.

3.1.2. Salient Features of the Hα Profile Variations

The smoothed nuclear emission spectra are shown in Figure 2. The most conspicuous characteristics of the evolution of the profile during the monitoring campaign are:

1. The double-peaked profile remained asymmetric, although the relative intensity of the blue and red peaks changed during the campaign. At the beginning of the observations, MJD56147, the maximum flux of the blue peak, F_B, was slightly stronger than the maximum flux of the red peak, F_R. The profile changed gradually until the red peak was much stronger than the blue peak by MJD56194. After that, the blue peak became increasingly prominent, becoming stronger than the red peak by MJD56277. This is similar to the results of our previous studies that showed that the relative intensity of the blue and red peaks changes on a timescale of months (Storchi-Bergmann et al. 2003; Schimoia et al. 2012).
2. Besides the changes in the relative intensity of the peaks, the integrated flux of the broad Hα line, $F_{\rm broad}$, also varied significantly. The first remarkable rise in $F_{\rm broad}$ occurred in the interval MJD56187–56194, when it changed from 62.5 (±6.9) × 10^{-15} erg s^{-1} cm^{-2} to 107.9 (±4.4) × 10^{-15} erg s^{-1} cm^{-2}, an increase of ∼70% in just six days. A second, even larger, flux increase of ∼90% occurred in the interval MJD56285–56290, when the Hα flux increased from 43.8 (±8.2) × 10^{-15} erg s^{-1} cm^{-2} to 83.4 (±5.3) × 10^{-15} erg s^{-1} cm^{-2} in only five days.
3. After MJD56277, the red peak became less well-defined, with a shape more like a "plateau." Similar behavior is seen on the blue side of the profile in the observation of MJD56310. By the final observation of the campaign on MJD56319, the double-peaked nature of the profile is barely discernible.

3.1.3. Model-independent Parameterization of the Douple-peaked Profile

Prior to making measurements to parameterize the broad Hα profile, we must first remove the very strong narrow emission lines that are still present in the spectrum. We attempted to remove these features by simultaneously fitting three Gaussians to the Hα narrow component and the [N II] λλ6548, 6584 lines and two more Gaussians to the [S II] λλ6717, 6731 doublet. After removing the narrow components, we made the following measurements: λ_i is the initial wavelength, defined as the wavelength at which the flux of the blue side reaches zero intensity within the uncertainties. Similarly, λ_f is the final wavelength where the flux of the red side of the profile reaches zero intensity. Together these two parameters define the wavelength range of the double-peaked profile. F_B is the maximum intensity of the blue peak (or blue side) of the profile and λ_B is the wavelength where this maximum occurs, while F_R is the maximum intensity of the red peak (or red side) of the profile and λ_R the wavelength where it occurs. We obtained the integrated flux in the broad component of Hα $F_{\rm broad}$ by integrating the flux underneath the profile from λ_i to λ_f. Figure 3 illustrates all these properties, including the results of fitting and subtracting the contribution of the narrow lines. The resulting measurements are listed in Table 3. For most spectra,

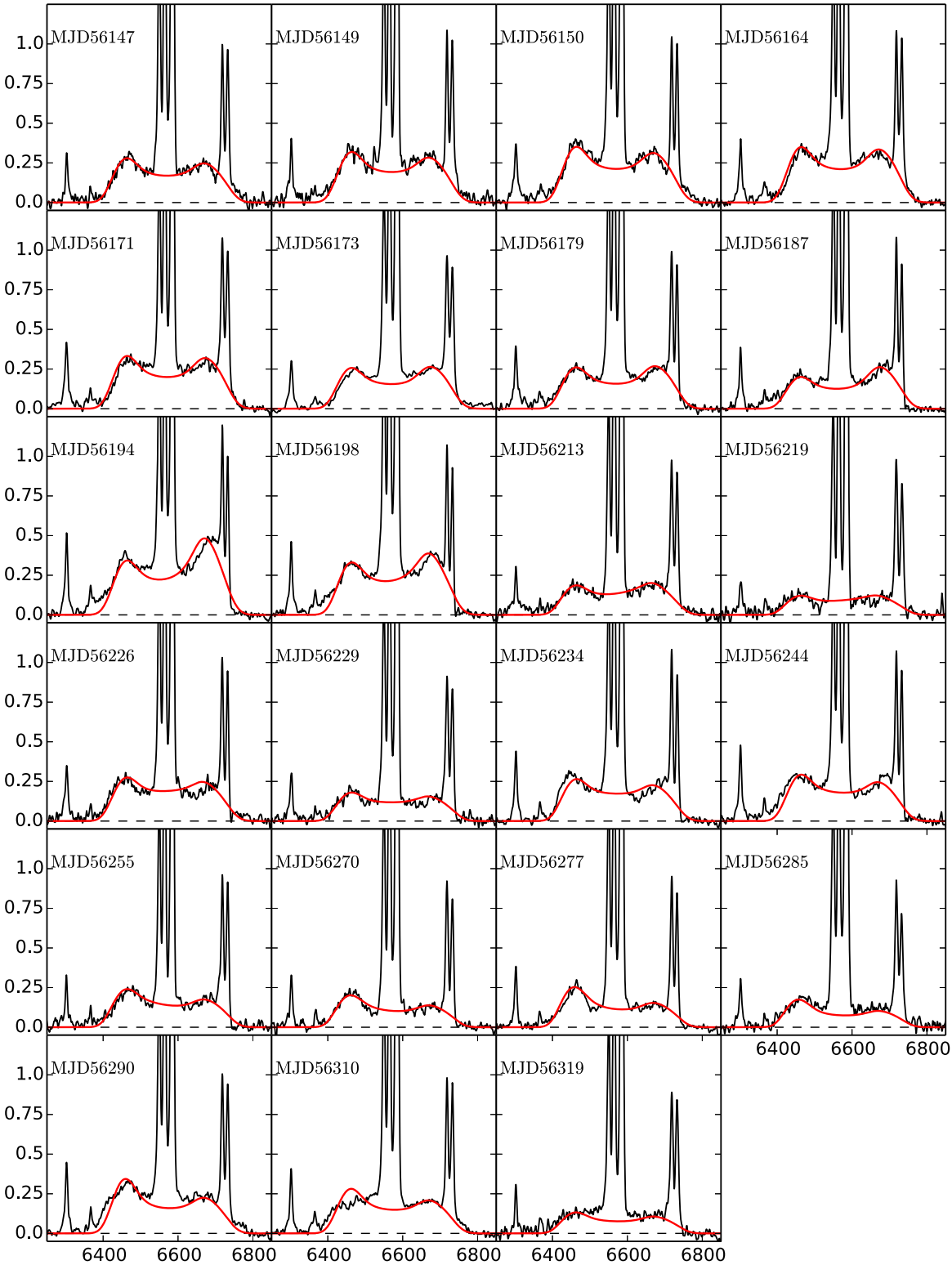

Figure 2. Resulting spectra of each epoch after the subtraction of the stellar population contribution and calibration through the fluxes of the narrow emission lines (which do not vary on such short timescales). For each frame the vertical axis is flux in units of 10^{-15} erg s^{-1} cm^{-2} Å^{-1} while the horizontal axis is wavelength in units of Å. The red solid line is the best fit of the accretion disk model to the data (see Section 4.1 for details).

Table 3
Measurements of the Characteristics of the Double-peaked Profile

UT Date	MJD	$F_{\rm broad}$	$\lambda_{\rm i}$	$\lambda_{\rm f}$	$\lambda_{\rm B}$	$\lambda_{\rm R}$	F_B	F_R
2012 Aug 7	56147.356	71.9 ± 8.9	6381	6784	6469.6 ± 1.1	6665.3 ± 1.8	0.264 ± 0.088	0.231 ± 0.087
2012 Aug 9	56149.368	87.6 ± 10.5	6371	6793	6467.0 ± 4.1	6666.6 ± 5.3	0.304 ± 0.100	0.279 ± 0.099
2012 Aug 10	56150.360	93.3 ± 8.0	6361	6793	6469.9 ± 2.7	6661.2 ± 4.3	0.350 ± 0.074	0.295 ± 0.073
2012 Aug 24	56164.349	90.3 ± 5.7	6367	6781	6473.5 ± 3.4	6660.0 ± 5.5	0.309 ± 0.054	0.295 ± 0.054
2012 Aug 31	56171.388	85.4 ± 5.4	6364	6789	6476.8 ± 2.3	6672.4 ± 1.3	0.291 ± 0.050	0.275 ± 0.050
2012 Sep 3	56173.305	70.9 ± 7.8	6365	6772	6466.8 ± 1.2	6685.3 ± 7.7	0.220 ± 0.078	0.236 ± 0.074
2012 Sep 8	56179.370	70.4 ± 7.1	6365	6772	6463.9 ± 1.2	6684.3 ± 3.1	0.238 ± 0.070	0.247 ± 0.070
2012 Sep 16	56187.222	62.5 ± 6.9	6370	6755	6464.8 ± 2.2	6683.2 ± 1.9	0.197 ± 0.070	0.248 ± 0.071
2012 Sep 23	56194.256	107.9 ± 4.4	6356	6775	6467.4 ± 2.1	6679.3 ± 2.0	0.337 ± 0.042	0.438 ± 0.042
2012 Sep 27	56198.175	92.4 ± 7.1	6365	6776	6465.1 ± 4.6	6669.3 ± 3.7	0.301 ± 0.068	0.354 ± 0.068
2012 Oct 12	56213.316	51.2 ± 9.5	6375	6783	6460.5 ± 2.1	6685.4 ± 2.5	0.169 ± 0.092	0.182 ± 0.093
2012 Oct 18	56219.316	30.6 ± 9.0	6386	6763	6457.8 ± 1.8	6683.7 ± 2.4	0.118 ± 0.045	0.101 ± 0.095
2012 Oct 25	56226.048	66.8 ± 8.3	6374	6800	6465.2 ± 2.3	6682.9 ± 2.4	0.246 ± 0.078	0.206 ± 0.078
2012 Oct 28	56229.229	42.5 ± 8.4	6375	6786	6453.4 ± 2.5	6687.3 ± 4.6	0.171 ± 0.081	0.134 ± 0.081
2012 Nov 2	56234.086	66.5 ± 4.5	6372	6780	6458.3 ± 3.6	6685.2 ± 2.7	0.269 ± 0.044	0.222 ± 0.044
2012 Nov 12	56244.074	75.5 ± 6.4	6363	6785	6475.2 ± 1.6	6678.2 ± 3.9	0.270 ± 0.060	0.256 ± 0.061
2012 Nov 23	56255.068	53.6 ± 8.1	6377	6751	6463.9 ± 3.5	6677.2 ± 5.1	0.219 ± 0.086	0.169 ± 0.086
2012 Dec 8	56270.206	42.7 ± 6.7	6375	6763	6464.0 ± 0.5	6669.0 ± 2.1	0.198 ± 0.071	0.124 ± 0.071
2012 Dec 15	56277.142	47.2 ± 4.8	6369	6762	6471.1 ± 2.8	6670.2 ± 2.0	0.226 ± 0.049	0.133 ± 0.049
2012 Dec 23	56285.097	43.8 ± 8.2	6381	6787	6468.9 ± 2.9	6672.0 ± 2.8	0.179 ± 0.090	0.123 ± 0.046
2012 Dec 28	56290.074	83.4 ± 5.3	6363	6794	6467.6 ± 1.8	...	0.307 ± 0.135	...
2013 Jan 17	56310.047	67.4 ± 5.7	6367	6788	...	6672.2 ± 5.1	...	0.202 ± 0.047
2013 Jan 26	56319.067	40.5 ± 8.0	6376	6753	6496.32 ± 5.2	6686.7 ± 8.5	0.140 ± 0.047	0.125 ± 0.106

Notes. Column 1 gives the date of observations while Column 2 gives the Modified Julian Date (JD−2400000.5). In Column 3, the integrated flux of the double-peaked profile in units of 10^{-15} erg s^{-1} cm^{-2} is shown. In Column 4, the initial wavelength of the double-peaked profile is given and in Column 5 the corresponding final wavelength is given; both are given in Å. In Columns 6 and 7, respectively, the wavelengths in Å where the maximum intensity of the blue and the red peaks occur are given. In Columns 8 and 9 the values of the maximum intensity of the blue and red peaks, respectively, in units of 10^{-15} erg s^{-1} cm^{-2} Å^{-1} are given.

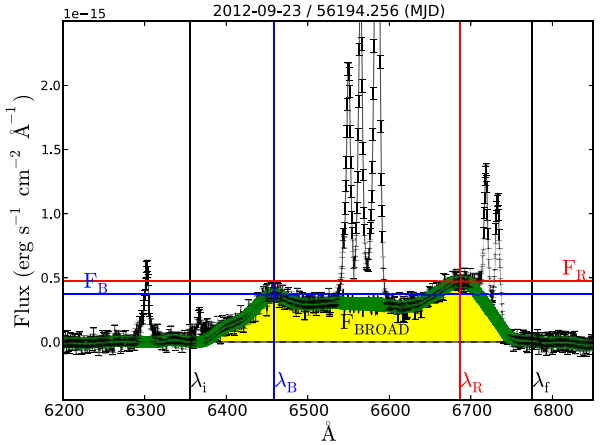

Figure 3. Visual representation of the measured properties of the Hα double-peaked profile for the observation of MJD56194. The vertical black lines mark λ_i and λ_f (respectively the lower and upper wavelength limits of the double-peaked profile). The horizontal blue line marks the maximum flux value for the blue peak, F_B, while the vertical blue line marks λ_B, the wavelength where F_B occurs. The maximum flux of the red peak F_R is marked by the horizontal red line, while λ_R is marked by the vertical red line. The green strip represents the Gaussian smoothing of the spectrum. The yellow region represents $F_{\rm broad}$, after subtracting the contribution of the narrow emission lines.

it was possible to make reliable measurements of the properties describe above. However, the irregular profiles in the final observations (from MJD56285 on) preclude characterization of the blue and red peaks.

3.2. Time-series Analysis

In this section, we characterize the variability of the X-ray and UV continuum and the integrated flux $F_{\rm broad}$ of the broad Hα profile. Figure 4 shows the corresponding light curves obtained over the complete monitoring campaign.

The mean cadence of the observations during the monitoring campaign was based on the results from Schimoia et al. (2012). In this previous work, we did not observe any significant Hα variations within a time interval of seven days. We therefore planned the monitoring campaign to obtain an optical spectrum with SOAR once every 8 days. As the X-rays usually show shorter variability timescale than the optical in AGNs, we requested a *Swift* observation once every four days whenever possible.

For the high-energy continuum emission, 45 *Swift* observations were obtained in each of two bands, the XRT (0.3–10 keV) and UVOT/M2 band ($\lambda_0 \approx 2246$ Å, FWHM ≈ 510 Å), with a mean time interval of ∼4.2 days and minimum and maximum time intervals of ∼3 and 8 days, respectively. The Hα light curve comprises 23 observations with a mean time interval between them of ∼7.5 days, with minimum and maximum time intervals between two consecutive observations of ∼1 and 20 days, respectively.

We characterize the variability of each light curve using the same parameters as O'Brien et al. (1998). The results are given in Table 4, where N is the number of epochs, $\overline{F}$ and σ_F are, respectively the mean flux and standard deviation, and Δ is the mean measurement uncertainty. The parameter $F_{\rm var}$ is an estimate of the amplitude of the variability

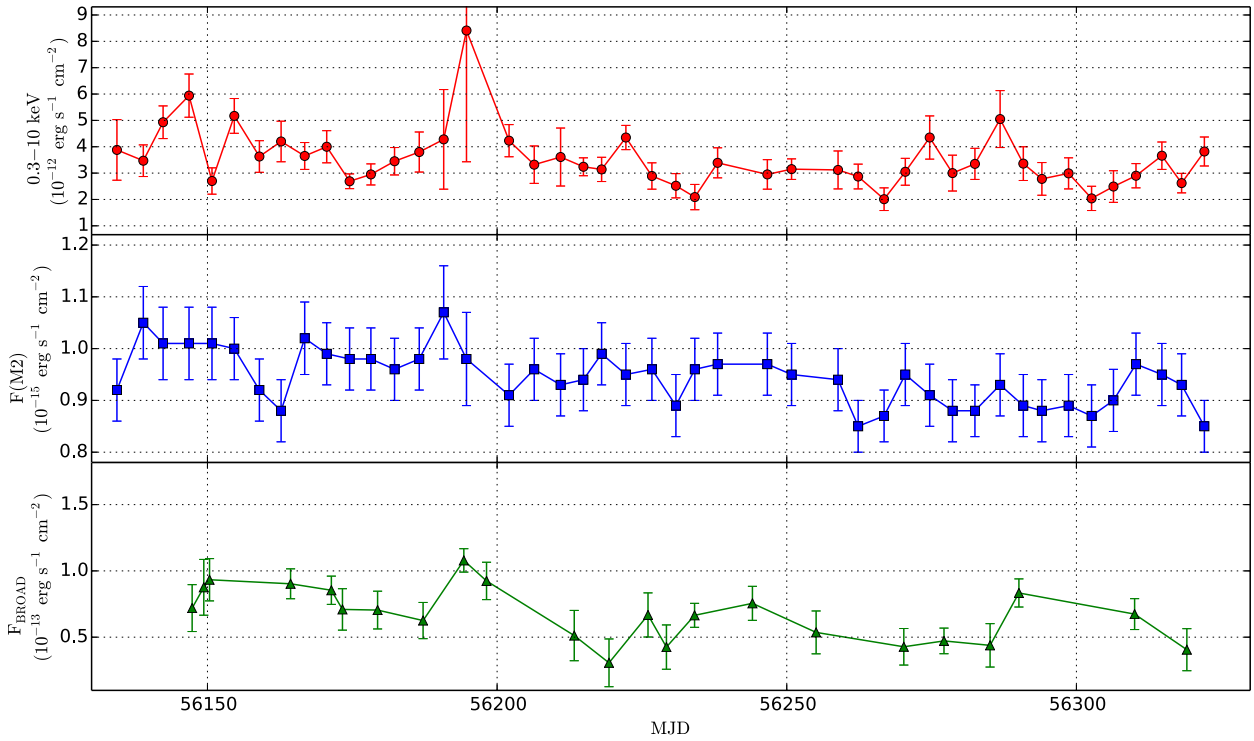

Figure 4. Light curves. Top: integrated flux of the *Swift*/XRT X-ray band, 0.3–10 keV. Middle: UV integrated flux, from the M2 band (∼2246 Å) of *Swift*/UVOT. Bottom: integrated Hα broad-line flux. The largest average variation was observed for the Hα profile, of 20%, followed by the X-rays, which varied by 13%, while the UV did not show significant variation.

Table 4
Variability Parameters

Feature	N	$\overline{F}$	σ_F	Δ	$F_{\rm var}$ (%)	$R_{\rm max}$
XRT[a]	45	3.54	1.1	1.0	13.18	4.18
F(M2)[b]	45	9.44	0.52	0.62	INDEF	1.26
$F_{\rm broad}$[b]	23	6.72	2.01	1.43	20.44	3.52

Notes.
[a] $\overline{F}$, σ_F, and Δ are in units of 10^{-12} erg s^{-1} cm^{-2}.
[b] $\overline{F}$, σ_F, and Δ are in units of 10^{-14} erg s^{-1} cm^{-2}.

relative to the mean flux, corrected by the uncertainties in the measurements, i.e.,

$$F_{\rm var} = \frac{\sqrt{{\sigma_F}^2 - \Delta^2}}{\overline{F}}. \quad (1)$$

The parameter $R_{\rm max}$ is the ratio between the maximum and minimum fluxes in the light curve.

3.2.1. X-Ray

The X-ray variations (Figure 4) were of very low amplitude, with $F_{\rm var} \approx 13\%$. There were two periods of large changes, a large decrease followed by a large increase in flux around MJD56150 and another increase followed by a rapid decrease around MJD56194. These variations imply that the X-ray emitting structure must be smaller than four light days. We note that there is an ultra-luminous X-ray source (ULX) located approximately 27″ away from the nucleus, as pointed out by Nemmen et al. (2006). As the *Swift* measurements employ an aperture of 47″ radius, this source is included in our measured X-ray flux. We have used the information provided by Nemmen et al. (2006) to estimate an upper limit of ∼8% to the flux contributed by this ULX to our measurements. If we correct our measurements by this constant contribution, we expect that $F_{\rm var} \approx 15\%$.

3.2.2. UV

The $F_{\rm var}$ parameter for the M2 *Swift* band is undefined because the variations in the UV flux are smaller than the uncertainties of these measurements.

Nemmen et al. (2006) have used an *Hubble Space Telescope* STIS UV/optical spectrum of the nucleus of NGC 1097 as part of the nuclear spectral energy distribution (SED). With data from radio wavelengths to X-rays, they then modeled the nuclear SED as originating in a RIAF plus the contribution from a radio jet, including also the continuum of the part of the disk which emits also the double-peaked line. Besides these components, it is also necessary to include the contribution of a nuclear starburst (Storchi-Bergmann et al. 2005) to reproduce the UV spectral range. The derived contributions of each of these structures to the luminosity at 2246 Å are $L_{\rm RIAF} = 1.26 \times 10^{40}$ erg s^{-1} from the RIAF, $L_{\rm jet} = 2.57 \times 10^{39}$ erg s^{-1} from the radio jet, $L_{\rm disk} = 5.25 \times 10^{34}$ erg s^{-1} from the thin disk, and $L_{\rm star} = 2.04 \times 10^{40}$ erg s^{-1} from the compact nuclear starburst. We thus conclude that, in the observed UV band, the nuclear starburst, which has a projected distance to the nucleus smaller than 9 pc (Storchi-Bergmann et al. 2005), dominates the luminosity. As the light from the starburst does not vary on the timescales we are considering, it can be concluded that any eventual variation

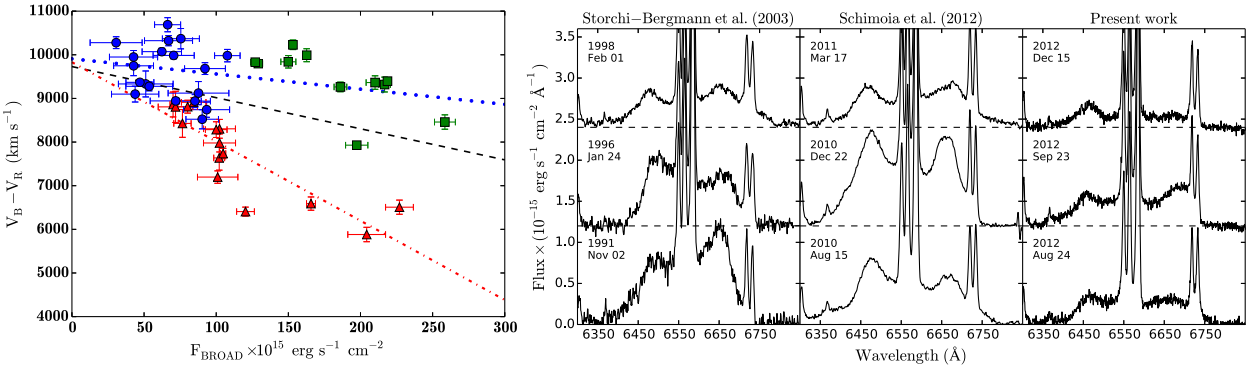

Figure 5. Left: comparison of the relation between the integrated Hα flux, $F_{\rm broad}$, and velocity separation between the blue and red peaks, $\Delta V = V_B - V_R$, for three different monitoring campaigns. The data from the present work are shown as blue circles; the data from Storchi-Bergmann et al. (2003) are shown as red triangles, and the data from Schimoia et al. (2012) are shown as green squares. The comparison shows that during this campaign $F_{\rm broad}$ remained at the lowest fluxes ever seen while $V_B - V_R$ was at a very large separation. This trend is in agreement with that of the previous observations. The blue dotted line represents the linear regression for the data from Schimoia et al. (2012) + that of this work ($r \sim -0.343$); while the dot–dashed line is the linear regression for the data from Storchi-Bergmann et al. (2003) alone ($r \sim -0.823$). The black dashed line is the linear regression for all the data together ($r \sim -0.354$). Right: three representative profiles of each of the three time periods covered by our previous and present work.

of the AGN in this band is probably heavily diluted by the starburst continuum and cannot be detected.

3.2.3. The Hα Emission Line

As we can see in Figure 2, the Hα profile and flux have varied on the shortest timescales probed by the observations. The broad-component flux $F_{\rm broad}$ varied overall by approximately ∼20% ($F_{\rm var} = 20.44\%$) with respect to the mean. The two most remarkable increases in $F_{\rm broad}$ occurred in the interval MJD56187–56194 and MJD56285–56290, when the line flux increased by ∼70% in 7 days and by ∼90% in 5 days, respectively, as seen in Figures 2 and 4. We conclude that a substantial portion of the broad-line luminosity comes from a region that has a size less than 5 light days.

4. DISCUSSION

The double-peaked Hα profile of NGC 1097 has been monitored by our group for more than 20 yr (Storchi-Bergmann et al. 1993, 1995, 1997, 2003). Recently we reported the discovery of short-timescale variability (Schimoia et al. 2012) of ∼7 days, consistent with the shortest timescale variations detected here of $\lesssim$5 days. Another previous finding was an inverse correlation between $F_{\rm broad}$ and the velocity separation between the blue and red peaks, $\Delta V = V_B - V_R$. This inverse correlation supports the reverberation scenario: when the ionizing flux is low, the innermost parts of the accretion disk are relatively more important and the profile becomes weaker and broader, when the ionizing flux is high the inner disk becomes more highly ionized, therefore the bulk of the Balmer line emission moves to larger radii (Dumont & Collin-Souffrin 1990) and the profile becomes both stronger and narrower.

Figure 5 shows, in the left panel, a comparison of the measurements of $F_{\rm broad}$ and ΔV of the present and previous works. The right panel shows three typical profiles for each of the three epochs we have collected the data.

The left panel of Figure 5 shows that in the current campaign, the broad Hα flux $F_{\rm broad}$ reached historically low levels and remained low throughout the campaign, with variations comparable to or just barely larger than the uncertainties in the measurements. The separation ΔV between the blue and red peaks was also at the largest values we have ever observed in this source, what is still consistent with the reverberation scenario.

We now investigate the significance of the inverse correlation between the integrated flux of the Hα double-peaked line and the velocity separation of the blue and red peaks. Figure 5 (left) shows that there is a distinct behavior between the data from Storchi-Bergmann et al. (2003) (red triangles)—taken between 1991 and 2002, and that from our more recent studies, corresponding to the period between 2010–2013, including both the data from Schimoia et al. (2012) and that of the present work (blue circles and green squares).

Between these two data sets there is a temporal gap of approximately 7–8 yr. The right panels of Figure 5 show that in the first data set (1991–2002) the profile showed large variations, both in flux and peak separation, with a strong inverse correlation between the two. In the more recent observations that begun in 2010, the profiles became broader. In order to investigate the significance of the inverse correlation, we have grouped the data as follows: (1) only the data from Storchi-Bergmann et al. (2003); (2) only the most recent data of Schimoia et al. (2012) + that of the present work; and (3) all the data together. The resulting linear regressions are shown as dashed lines in Figure 5.

We have calculated the correlation coefficient and respective significance for the three different groups of data above:

1. For the data from Storchi-Bergmann et al. (2003) alone we found a linear correlation coefficient $r = -0.823^{+0.034}_{-0.038}$, which implies significance levels from 99.95% to 99.99%;
2. For the data from Schimoia et al. (2012) plus that of this work we found a correlation coefficient $r = -0.343^{+0.049}_{-0.050}$, which gives significance levels from 89.25% to 97.17%;
3. For all data together we found a correlation coefficient of $r = -0.354^{+0.029}_{-0.029}$, and the respective significance levels are 97.05% and 99.06%.

Thus we conclude that for any set of data there is an inverse correlation with a significance level $\gtrsim$90%, while for the complete data set the correlation is ∼97%. The data are thus consistent with a low-flux state corresponding to the widest separation between the two peaks, which leads us to the conclusion that the overall data are consistent with the reverberation scenario.

4.1. An Accretion Disk Model

In order to test further the scenario we have proposed for the accretion disk (Schimoia et al. 2012), we modeled the Hα profiles using the accretion disk model described by Gilbert et al. (1999), Storchi-Bergmann et al. (2003), and Schimoia et al. (2012). In this formulation, the broad double-beaked emission line originates in a relativistic Keplerian disk of gas surrounding the SMBH. The line-emitting portion of the disk is circular and located between an inner radius ξ_1 and an outer radius ξ_2 (where ξ is the disk radius in units of the gravitational radius $r_g = GM_{\rm BH}/c^2$, c is the speed of light, G is the gravitational constant, and $M_{\rm BH}$ is the mass of the black hole). The disk has an inclination i relative to the line of sight (i.e., zero degrees is face-on). Superimposed on the axisymmetric emissivity of the circular disk, there is a perturbation in the form of a spiral arm. We adopted the "saturated spiral model" (Schimoia et al. 2012) for the total emissivity of the accretion disk, as it best reproduces the data. This emissivity law is given by

$$\epsilon(\xi,\phi) = \epsilon(\xi)\left\{1 + \frac{A}{2}\exp\left[-\frac{4\ln 2}{\delta^2}(\phi-\psi_0)^2\right] + \frac{A}{2}\exp\left[-\frac{4\ln 2}{\delta^2}(2\pi-\phi+\psi_0)^2\right]\right\}, \quad (2)$$

where

$$\epsilon(\xi) = \begin{cases} \epsilon_0\xi^{-q_1}, & \xi_1 < \xi < \xi_q \\ \epsilon_0{\xi_q}^{-(q_1-q_2)}\xi^{-q_2}, & \xi_q < \xi < \xi_2 \end{cases} \quad (3)$$

is the axisymmetric emissivity of the disk. The parameter ξ_q is the radius of maximum emissivity, or saturation radius, at which the emissivity law changes; q_1 is the index of the emissivity law for $\xi_1 < \xi < \xi_q$; q_2 is the index for $\xi_q < \xi < \xi_2$. A is the brightness contrast between the spiral arm and the underlying disk, and the expression between square brackets represents the decay of the emissivity of the arm as a function of the azimuthal distance $\phi - \psi_0$ from the ridge line to both sides of the arm, assumed to be a Gaussian function with FWHM $= \delta$ (azimuthal width).

The relation between the azimuthal angle ϕ_0 and the angular position ψ_0 of the ridge of emissivity on the spiral arm is given by

$$\psi_0 = \phi_0 + \frac{\ln(\xi/\xi_{sp})}{\tan p}, \quad (4)$$

where ϕ_0 is the azimuthal angle of the spiral pattern, p is the pitch angle, and ξ_{sp} is the innermost radius of the spiral arm.

The specific intensity from each location in the disk, in the frame of the emitting particle is calculated as

$$I(\xi,\phi,\nu_e) = \frac{\epsilon(\xi,\phi)}{4\pi}\frac{e^{-(\nu_e-\nu_0)^2/2\sigma^2}}{(2\pi)^{1/2}\sigma}, \quad (5)$$

where ν_e is the emission frequency and ν_0 is the rest frequency corresponding to Hα λ6564.6 and σ is the local "broadening parameter" (Chen & Halpern 1989).

We fixed the following model parameters: $q_1 = -2.0$, $q_2 = 3.0$, $\xi_{sp} = \xi_1$, $p = 50^\circ$, $\delta = 70^\circ$ and $i = 34^\circ$, which are the same values adopted in previous works (Storchi-Bergmann et al. 2003; Schimoia et al. 2012). Thus, the only parameters we allowed to vary are A, ξ_q and ϕ_0. In practice, ξ_q regulates the width of the profile: when ξ_q is closer to ξ_1 the profile is broader, when ξ_q is closer to ξ_2 the profile becomes narrower; ϕ_0 is the orientation of the spiral pattern and by allowing this parameter to increase monotonically, we can reproduce the variation of the relative intensity of the blue and red peaks as due to the rotation of the spiral arm.

Table 5
Parameters of the Accretion Disk Model

UT Date	MJD	ξ_q	$\phi_0 - 760^\circ$ ($^\circ$)	A
2012 Aug 7	56147.356	550	15	0.2
2012 Aug 9	56149.368	570	20	0.2
2012 Aug 10	56150.360	580	20	0.2
2012 Aug 24	56164.349	580	30	0.5
2012 Aug 31	56171.388	570	35	0.5
2012 Sep 3	56173.305	550	35	0.8
2012 Sep 8	56179.370	550	40	0.8
2012 Sep 16	56187.222	540	45	2.0
2012 Sep 23	56194.256	580	50	2.5
2012 Sep 27	56198.175	570	50	1.5
2012 Oct 12	56213.316	525	60	1.5
2012 Oct 18	56219.316	500	65	1.5
2012 Oct 25	56226.048	545	70	0.3
2012 Oct 28	56229.229	515	75	0.5
2012 Nov 2	56234.086	545	75	0.2
2012 Nov 12	56244.074	560	80	0.2
2012 Nov 23	56255.068	530	90	0.0
2012 Dec 8	56270.206	515	100	0.0
2012 Dec 15	56277.142	520	105	0.0
2012 Dec 23	56285.097	515	110	0.0
2012 Dec 28	56290.074	570	115	0.0
2013 Jan 17	56310.047	545	130	0.0
2013 Jan 26	56319.067	510	135	0.0

Notes. The date of observations are given in Column 1 while Column 2 gives the Modified Julian Date (JD−2400000.5). The resulting parameters of the modeling are given in the following columns: Column 3 gives the radius of maximum emissivity of the accretion disk, Column 4 gives the azimuthal orientation of the spiral arm, and Column 5 gives the contrast between the spiral arm and the underlying disk.

For direct comparison with the scenario proposed by Schimoia et al. (2012), we adopt their derived angular velocity of the spiral arm, of $\dot{\phi}_0 \approx 0.^\circ 680\ {\rm day}^{-1}$, which corresponds to a rotation period of ∼18 months. Using this prescription, we estimate the value of ϕ_0 for the first optical observation (MJD56147) as 775°, which means that the spiral arm should have completed one rotation since the last observation of Schimoia et al. (2012) for which $\phi_0 = 400^\circ$. The best-fitting models are compared with the observed line profiles in Figure 2, and the corresponding parameter values are listed in Table 5. The disk emissivity for each epoch is illustrated in Figure 6.

As can be seen in Figure 2, the model can indeed reproduce the observed variations of the double-peaked profile. We have tested many values for ξ_q in the range between the inner and outer radius, $\xi_1 = 450$ and $\xi_2 = 1600$. However, we achieved the best fits by keeping ξ_q close to the inner radius, in the range $\xi_q \sim 500$–600. This is consistent with the fact that during the monitoring campaign we observed the broadest profiles ever seen for this object.

In order to improve the fitting we also had to apply an overall blueshift of about $-250\,{\rm km\,s^{-1}}$ to all model profiles. Such a velocity shift has been noted in our previous studies (Storchi-Bergmann et al. 2003; Schimoia et al. 2012), in which they were attributed to possible winds from the accretion disk. Another

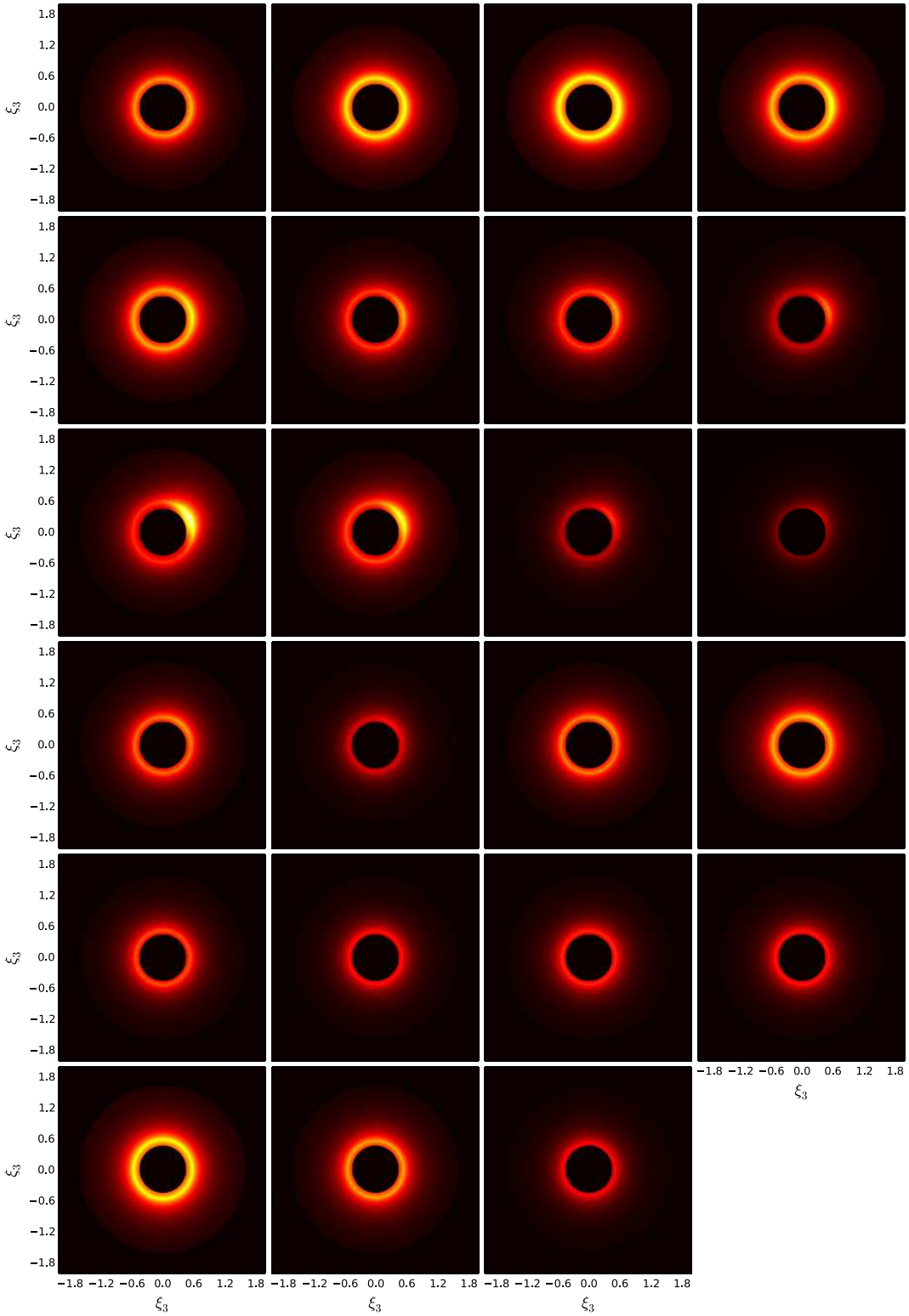

Figure 6. Image showing the disk emissivity utilized to model the double-peaked profile for each epoch of observation of Figure 2. White represents the brightest regions, and the observer is to the bottom. The disk parameters for these epochs are listed in Table 5. On each frame the axis is expressed in terms of $\xi_3 = 10^{-3}\xi$.

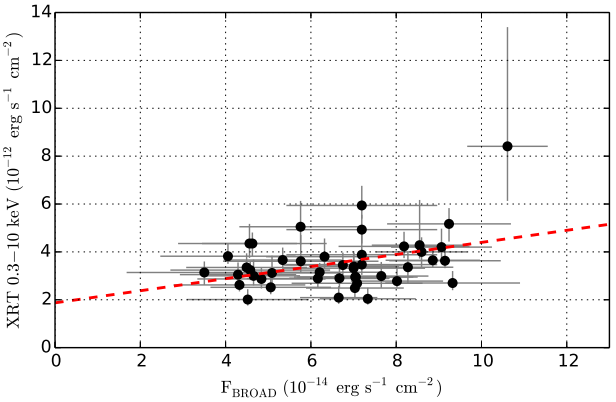

Figure 7. Correlation between X-ray and optical data, where black points represent the fluxes of the X-ray band and the broad profile for the same MJD (after interpolation of the optical light curve to match the epochs of *Swift* observations). The red dashed line is the best linear correlation between the data. The median value of the correlation coefficient is $r = 0.253^{+0.105}_{-0.133}$ which corresponds to a level of significance of 56.8%–98.4%.

possible explanation for the velocity shifts is the presence of the spiral pattern, since the spiral arm also slightly modifies the velocity field and makes it depart from a pure Keplerian velocity field. We note that some epochs require blueshifts somewhat higher or lower than $-250\,\mathrm{km\,s^{-1}}$; however, the corresponding improvements in the fit are smaller than the uncertainties. Thus, we adopt the mean blueshift value of $-250\,\mathrm{km\,s^{-1}}$.

Modeling the present data revealed that the parameter ξ_q—the "break" radius, corresponding to the region with strongest emission in the disk—must be kept close to the inner radius in order to reproduce the observed double-peaked profiles. This result is consistent with the scenario in which the central ionizing source is faint and able to power just the innermost region of the accretion disk. The mean value of ξ_q over all the observations is $\overline{\xi_q} = 545 \pm 25$. Assuming the black hole mass is $M_{\rm BH} = 1.2 \times 10^8\,M_\odot$ (Lewis & Eracleous 2006), at this radius the dynamical timescale of the accretion disk is $\tau_{\rm dyn} \approx 3$ months and the rotation period ($2\pi\,\tau_{\rm dyn}$) is ∼18 months, which is consistent with the estimated rotation period for the spiral arm. A property of the double-peaked profile that varies on this timescale is the relative intensity of the blue and red peaks: for instance, from MJD56194 to MJD56277 (see Figure 2) the profile changed from a dominant red peak to a dominant blue peak in ∼3 months. We note that the light travel timescale, at $\xi_q = 545$ is just 4 days, which is consistent with the upper limit of ∼5 days for the timescale for the Hα flux variations.

4.2. Correlation Between X-Rays and Hα

In order to look for a direct reverberation signal between the X-rays (presumably emitted by the RIAF) and the response of the line-emitting portion of the disk, we applied the interpolated cross-correlation function method (Gaskell & Peterson 1987; White & Peterson 1994; Peterson et al. 1998, 2004) between the X-ray and Hα light curves. Unfortunately, we are unable to constrain the lag between the X-ray and Hα light curves. We are similarly unable to constrain any possible lag between the X-rays and the UV continuum. The main reason that the time-series analysis fails to yield results is primarily the absence of strong flux variations in every band in this campaign. It also seems apparent that, at least in this low-luminosity state, the time sampling was not frequent enough. This conclusion is supported by the fact that we could detect significant variations in the X-rays and Hα light curves on time intervals as short as our mean sampling time interval.

In order to take into account the effect of the uncertainties of the flux measurements in the correlation, we proceeded as follows. Before calculating the correlation coefficient, we scattered each flux measurement using a Gaussian probability distribution in which the mean value of the Gaussian corresponded to the value of the flux measurement and the root mean square of the Gaussian corresponded to the mean squared value of the lower and upper uncertainties. We repeated this process 10^5 times and calculated the median value for the distribution of values of the correlation coefficient as $\bar{r} = 0.253^{+0.105}_{-0.133}$. We show the correlation between the X-ray and optical data in Figure 7. The upper and lower limits correspond to ±34.1% of the distribution around the median. The lower and upper limits for the correlation coefficient imply a significance level of 56.8%–98.4%

In order to take into account the effect of the uncertainties of the fluxes measurements in the correlation, we proceeded as follows: before calculating the correlation coefficient, we scattered each flux measurement using a Gaussian probability distribution in which the mean value of the Gaussian corresponded to the value of the flux measurement and the root mean square of the Gaussian corresponded to mean squared value of the lower and upper uncertainties. We repeated this process 10^5 times and calculated the median value for the distribution of values of the correlation coefficient as $\bar{r} = 0.253^{+0.105}_{-0.133}$. The upper and lower limits correspond to ±34.1% of the distribution around the median. The lower and upper limits for the correlation coefficient imply a significance level of 56.8%–98.4%.

We can thus conclude that there is a marginal correlation between the X-ray and Hα flux variations; the variations are not completely random. Nevertheless the correlation is not tight enough to confirm that the two fluxes vary together. The weakness of the correlation is almost certainly attributable to the low amplitude of the variations during the monitoring campaign. The lack of variability in the UV precluded any similar analysis in that band.

4.3. Comparison with other Objects and Accretion Disk Models

Monitoring of "double-peaked" emitters have been used as a probe for testing accretion disk models and to understand what are the physical mechanisms responsible for the observed changes in the double-peaked profiles. In this subsection we make a comparison between the observed properties of the NGC 1097 double-peaked profile and two other also very well studied double-peaked emitters: Arp 102B and 3C390.3.

In the case of 3C 390.3, many works have reported spectroscopic long-term monitoring (years do decades) (Shapovalova et al. 2001; Sergeev et al. 2002; Shapovalova et al. 2010) or short-term monitoring (a few months) (Dietrich et al. 2012) of the AGN optical continuum around 5100 Å and the variations of the broad Balmer double-peaked emission lines, Hα and Hβ. Common to these works is the conclusion that the broad double-peaked Balmer lines flux variations do follow the optical continuum variations with time delays of $\tau(\mathrm{H}\alpha) \gtrsim 56$ days and $\tau(\mathrm{H}\beta) \gtrsim 44$ days. Also, Dietrich et al. (1998) found that the flux variations of the Balmer lines of Arp 102B seems to be correlated with the X-ray flux variations with a time delay of ∼20 days. However, for the case Arp 102B the variations of the flux of the Balmer broad double-peaked emission lines do not appear to be strongly correlated with the variations of the AGN optical continuum (Shapovalova et al. 2013). In spite

of the weak correlation, the authors estimate a time delay of $\tau(\mathrm{H}\beta) \sim 20$ days.

In the case of NGC 1097, we were never able to detect the AGN optical continuum (Storchi-Bergmann et al. 1993, 2003; Schimoia et al. 2012), and this was the motivation for us to look for the continuum in X-rays and UV. Unfortunately, the variations were small during our campaign, but in Section 4.2 we have nevertheless shown that the profile variations are weakly correlated with the X-ray continuum variations, indicating that the X-rays could indeed be the driver of the double-peaked profile.

In the case of Arp 102B the variations of the relative intensity of the blue and red peaks were first modeled by Newman et al. (1997) in the context of a relativistic accretion disk in which the non axisymmetric emissivity part of the disk has the shape of a *hot spot* that rotates in the disk around the central SMBH in the dynamical timescale. In the case of 3C390.3 the *hot spot* model have been used to explain the observed flux "outbursts" of the blue peak of the profile (Jovanović et al. 2010). Lewis et al. (2010) have reported a long-term monitoring of a few radio galaxies in which the double-peaked profiles display small flux *bumps* that move in the velocity space and are attributed to hot spots in the accretion disk. Nevertheless, in almost all cases the hot spots are short lived: they have been observed to appear and are more likely to last from several months to a few years. In contrast, the alternating relative intensity of the blue and red peaks of NGC 1097 have lasted for more than 20 yr, suggesting that the features producing the variation of the relative intensity of the blue and red peaks are longer lived than the hot spots observed in other double-peaked emitters. The variations in the relative intensity of the blue and red peaks in NGC 1097 have been clearly observed both when the flux of the broad line is in a high state (higher line flux and narrower profile) as well as when the flux is in a low state (low line flux and broader profile). On the other hand, we note that the emissivity of the *saturated spiral model* adopted in our modeling is not that different from that of a *hot spot*, in the sense that the spiral arm + broken power-law emissivity component can effectively concentrate the non-axisymmetric emissivity in a structure very similar to a hot spot (see Figure 6, MJD56194). Nevertheless, we favor the scenario of the *saturated spiral model* for NGC 1097 due the fact that the fast timescale variations of the profile, namely in the velocity separation of the peaks and integrated flux of the broad profile, occur in timescales of a few days to a few weeks. At these short timescales, these variation can only be attributed to changes in the illumination/ionization of the disk, which have been modeled by changing the break radius, ξ_q, while the rotation of the non axissymetric pattern allow us to simultaneously model the variations of the relative intensity of the blue and red peaks.

Finally, we point out that at some epochs there is a flux excess in the high velocities of the blue wing of the double-peaked profile (see Figure 2, for instance MJD56194 and 56290), that was also observed in previous works (Storchi-Bergmann et al. 2003; Schimoia et al. 2012). The origin of this excess is not completely understood. In Storchi-Bergmann et al. (2003) it was proposed that it could be due to the presence of a wind emanating from the disk, what is not taken into account in the model.

5. CONCLUSIONS

We monitored the AGN in NGC 1097 for ∼6 months, from 2012 August to 2013 February, in three spectral bands: in the X-ray (0.3–10 keV), using the *Swift*/XRT, in the UV, using the *Swift*/UVOT telescope, and in the double-peaked Hα profile, with data from the SOAR and Gemini-South telescopes. Our main conclusions are:

1. The X-ray fluxes varied on the shortest timescale probed by the observations, 4 days, indicating that the emitting structure has a size smaller than 4 light days; the maximum variation observed between two consecutive dates was 97%, but the average variation over the whole period was only 13%.
2. The Hα flux also varied on the shortest timescale probed by the observations, ∼5 days. The maximum variation observed was 90%, but the average variation over the whole period was 20%.
3. To within the uncertainties, the UV flux did not vary. This can be due to the contribution of the compact nuclear starburst previously found within the inner 9 pc, that dominates the UV continuum emission, and is probably diluting the contribution of a variable source.
4. Although we have not found a clear reverberation signal in our most recent data, when we consider this data together with the previous ones from epochs 1991–2001 and 2010–2012, they are consistent with the reverberation scenario, as we can still observe, in the overall data, an inverse correlation between the Hα flux and the separation between the red and blue peaks of the Hα profile, as noted in previous studies.
5. We were able to reproduce the variations of the double-peaked profile using the same accretion disk model of Schimoia et al. (2012); in particular, we kept the same inner and outer radii, as well as the 18 month rotation period for a spiral arm in the disk, that, combined with variations in the contrast of the spiral arm, successfully reproduces the variation of the relative intensity of the blue and red peaks.
6. The small range of variation of the width of the double-peaked profiles was reproduced by keeping the ξ_q values (radius of maximum emissivity) close to the inner radius. This radius corresponds to a rotation period of 18 months and a light travel time of ∼4 days, in agreement with the shortest variation timescales observed.
7. We find only a marginal correlation between the X-ray and Hα flux variations, although the analysis reveals the need for more frequent monitoring of this source, particularly when it is in such a low-luminosity state.

The presence of some correlation between the X-ray flux and the broad Hα profile, even though we could get only an upper limit on the shortest variation timescale, leads us to the conclusion that the variations of the broad Hα line profile do follow the variations of the X-ray flux. But we also note that the Hα flux remained at the lowest levels we have ever observed, and the blue and red peaks of the double-peaked profile remaining at the widest separation. This indicates that we have caught the AGN in NGC 1097 in a very low activity state, in which the ionizing source was very weak and capable of ionizing just the innermost part of the gas in the disk. Nonetheless, the data presented here still support the picture in which the gas that emits the double-peaked Balmer lines is illuminated/ionized by a source of high-energy photons which is located interior to the inner radius of the line-emitting part of the disk.

J.S.S. acknowledges CNPq, the National Council for Scientific and Technological Development—Brazil, for support and

The Ohio State University for their hospitality. At Penn State, D.G. and M.E. acknowledge support from the NASA Swift program through contract NAS5-00136. Additionally, M.E. acknowledges the warm hospitality of the Center for Relativistic Astrophysics at Georgia Tech and the Department of Astronomy at the University of Washington. B.M.P. is grateful for support by the NSF through grant AST-1008882 to The Ohio State University.

This research has made use of the XRT Data Analysis Software (XRTDAS) developed under the responsibility of the ASI Science Data Center (ASDC), Italy. This research has made use of data obtained through the High Energy Astrophysics Science Archive Research Center Online Service, provided by the NASA/Goddard Space Flight Center. This research is based on observations obtained at the Southern Astrophysical Research (SOAR) telescope, which is a joint project of the Ministério da Ciência, Tecnologia, e Inovação (MCTI) da República Federativa do Brasil, the U.S. National Optical Astronomy Observatory (NOAO), the University of North Carolina at Chapel Hill (UNC), and Michigan State University (MSU). This research is also based on observations obtained at the Gemini Observatory, which is operated by the Association of Universities for Research in Astronomy, Inc., under a cooperative agreement with the NSF on behalf of the Gemini partnership: the National Science Foundation (United States), the National Research Council (Canada), CONICYT (Chile), the Australian Research Council (Australia), Ministério da Ciência, Tecnologia e Inovação (Brazil) and Ministerio de Ciencia, Tecnología e Innovación Productiva (Argentina).

REFERENCES

Breeveld, A. A., Curran, P. A., Hoversten, E. A., et al. 2010, MNRAS, 406, 1687
Burrows, D. N., Hill, J. E., Nousek, J. A., et al. 2005, SSRv, 120, 165
Cardelli, J. A., Clayton, G. C., & Mathis, J. S. 1989, ApJ, 345, 245
Cid, Fernandes, R., Mateus, A., Sodré, L., Stasińska, G., & Gomes, J. M. 2005, MNRAS, 358, 363
Chen, K., & Halpern, J. P. 1989, ApJ, 344, 115
Chen, K., Halpern, J. P., & Filippenko, A. V. 1989, ApJ, 339, 742
Dietrich, M., Peterson, B. M., Albrecht, P., et al. 1998, ApJS, 115, 185
Dietrich, M., Peterson, B. M., Grier, C. J., et al. 2012, ApJ, 757, 53
Dumont, A. M., & Collin-Souffrin, S. 1990, A&A, 229, 313
Eracleous, M., & Halpern, J. P. 1994, ApJS, 90, 1
Eracleous, M., & Halpern, J. P. 2003, ApJ, 599, 886
Frank, J., King, A., & Raine, D. J. 2002, in Accretion Power in Astrophysics (3rd ed.; Cambridge: Cambridge Univ. Press), 398
Gaskell, C. M., & Peterson, B. M. 1987, ApJS, 65, 1
Gezari, S., Halpern, J. P., & Eracleous, M. 2007, ApJS, 169, 167
Gilbert, A. M., Eracleous, M., Filippenko, A. V., & Halpern, J. P. 1999, in ASP Conf. Ser. 175, Structure and Kinematics of Quasar Broad Line Regions, ed. C. M. Gaskell, W. N. Brandt, M. Dietrich, D. Dultzin-Hacyan, & M. Eracleous (San Francisco, CA: ASP), 189
Hill, J. E., Burrows, D. N., Nousek, J. A., et al. 2004, Proc. SPIE, 5165, 217
Jovanović, P., Popović, L. Č., Stalevski, M., & Shapovalova, A. I. 2010, ApJ, 718, 168
Kalberla, P. M. W., Burton, W. B., Hartmann, D., et al. 2005, A&A, 440, 775
Lewis, K. T., & Eracleous, M. 2006, ApJ, 642, 711
Lewis, K. T., Eracleous, M., & Storchi-Bergmann, T. 2010, ApJS, 187, 416
Luo, B., Brandt, W. N., Eracleous, M., et al. 2013, MNRAS, 429, 1479
Narayan, R., & McClintock, J. E. 2008, NewAR, 51, 733
Nemmen, R. S., Storchi-Bergmann, T., Yuan, F., et al. 2006, ApJ, 643, 652
Newman, J. A., Eracleous, M., Filippenko, A. V., & Halpern, J. P. 1997, ApJ, 485, 570
O'Brien, P. T., Dietrich, M., Leighly, K. M., et al. 1998, ApJ, 509, 163
Peterson, B. M., Denney, K. D., De, Rosa, G., et al. 2013, ApJ, 779, 109
Peterson, B. M., Ferrarese, K., Gilbert, K. M., et al. 2004, ApJ, 613, 682
Peterson, B. M., Wandes, I., Horne, K., et al. 1998, PASP, 110, 660
Poole, T. S., Breeveld, A. A., Page, M. J., et al. 2008, MNRAS, 383, 627
Roming, P. W. A., Kennedy, T. E., Mason, K. O., et al. 2005, SSRv, 120, 95
Roming, P. W. A., Koch, T. S., Oates, S. R., et al. 2009, ApJ, 690, 163
Schimoia, J. S., Storchi-Bergmann, T., Nemmen, R. S., Winge, C., & Eracleous, M. 2012, ApJ, 748, 145
Sergeev, S. G., Pronik, V. I., Peterson, B. M., Sergeeva, E. A., & Zheng, W. 2002, ApJ, 576, 660
Shapovalova, A. I., Burenkov, A. N., Carrasco, L., et al. 2001, A&A, 376, 775
Shapovalova, A. I., Popović, L. Č., Burenkov, A. N., et al. 2010, A&A, 517, A42
Shapovalova, A. I., Popović, L. Č., Burenkov, A. N., et al. 2013, A&A, 559, A10
Storchi-Bergmann, T., Baldwin, J. A., & Wilson, A. S. 1993, ApJL, 410, L11
Storchi-Bergmann, T., Eracleous, M., Livio, M., et al. 1995, ApJ, 443, 617
Storchi-Bergmann, T., Eracleous, M., Ruiz, M. T., et al. 1997, ApJ, 489, 87
Storchi-Bergmann, T., Nemmen da, Silva, R., Eracleous, M., et al. 2003, ApJ, 598, 956
Storchi-Bergmann, T., Nemmen, R. S., Spinelli, P. F., et al. 2005, ApJL, 624, L13
Strateva, I. V., Brandt, W. N., Eracleous, M., & Garmire, G. 2008, ApJ, 687, 869
Strateva, I. V., Brandt, W. N., Eracleous, M., Schneider, D. P., & Chartas, G. 2006, ApJ, 651, 749
Strateva, I. V., Strauss, M. A., Hao, L., et al. 2003, AJ, 126, 1720
White, R. J., & Peterson, B. M. 1994, PASP, 106, 879

Capítulo 5

Resultados para a galáxia NGC 7213

Os resultados obtidos para a galáxia NGC 7213 estão descritos no artigo a seguir, o qual está na fase de avaliação pelos colaboradores e será submetido a uma revista científica arbitrada.

‘EVOLUÇÃO DO DISCO DE ACREÇÃO AO REDOR DO BURACO NEGRO SUPERMASSIVO DA GALÁXIA NGC 7213’

The Astrophysical Journal, Version of February 2015
Preprint typeset using LaTeX style emulateapj v. 5/2/11

EVOLUTION OF THE ACCRETION DISK AROUND THE SUPERMASSIVE BLACK HOLE OF NGC 7213

Jaderson S. Schimoia, Thaisa Storchi-Bergmann
Instituto de Física, Universidade Federal do Rio Grande do Sul, Campus do Vale, Porto Alegre, RS, Brazil
and
Cláudia Winge
Gemini South Observatory, c/o AURA Inc., Casilla 603, La Serena, Chile
The Astrophysical Journal, Version of February 2015

ABSTRACT

We present the results of an optical spectroscopic campaign to monitor the double-peaked Hα profile emitted by the active nucleus of NGC 7213 using the the Gemini South Telescope between 2011 September 27 and 2013 July 23. We present an analysis of the profile in 12 epochs and report a main variability timescale of $\gtrsim 3$ months corresponding to variations in the relative intensity of the blue and red sides of the profile, which can be identified with the dynamical timescale. The shortest variability timescale, corresponding to a significant variation in the integrated flux of the profile was found to be between 7 and 28 days, consistent with the light travel time between the ionizing source and the disk.This is the first time that the double-peaked profile of this nucleus is reported as variable. We modeled the profiles as due to emission by a Keplerian and relativistic disk of gas surrounding the supermassive black hole, between 300 and 3000 gravitional radii and inclined by 47 degrees with respect to the plane of the sky. Superposed to the disk emissivity there is an asymmetric feature in the shape of a spiral whose period of rotation is ≈21 months and reproduces the variations in the relative intensity of the blue and red sides of the profile. This spiral was found to present a decreasing contrast relative to the underlying disk between the first and last observations of the campaign.

Subject headings: accretion, accretion disks — galaxies: individual (NGC 1097) — galaxies: nuclei — galaxies: Seyfert — line: profiles

1. INTRODUCTION

NGC 7213 is a nearby (z=0.005839) spiral galaxy. The active nucleus was first classified as Seyfert 1 by Phillips (1979) based on its very broad Hα emission line (13,000 $\mathrm{km\,s^{-1}}$ for the full width at zero intensity) and later was also recognized as low-ionization nuclear emission-line region (LINER) by Filippenko & Halpern (1984) based on a study of a variety of optical emission lines which were observed to have full width at half maxima in the range of 200 – 2000 $\mathrm{km\,s^{-1}}$. Its nucleus harbors a supermassive black hole (SMBH) with a mass estimated by Woo et al. (2002) as $\sim 10^8\,\mathrm{M_\odot}$. Its AGN has a bolometric luminosity of $L_{\rm bol} = 7{\times}10^{43}\mathrm{erg\,s^{-1}}$ (Emmanoulopoulos et al. 2012).

The nucleus of NGC 7213 has been well studied with X-ray spectroscopy. XMM-Newton/BeppoSAX observations revealed that the spectrum of the AGN shows no significant Compton reflection component (Bianchi et al. 2003) – what is very peculiar among bright Seyfert 1 AGN's. This observation also revealed the presence of a significant Fe K complex comprising three narrow emission lines: neutral iron at around 6.40 KeV, Fe XXV at around 6.66 keV and Fe XXVI at around 6.94 keV. Additionally, Bianchi et al. (2008) reported the data analysis of a long Chandra HETG observation of NGC 7213 finding that the neutral iron Kα line is resolved with a full width at half-maximum (FWHM) value of $2400^{+1100}_{-600}\,\mathrm{km\,s^{-1}}$ fully consistent with the Hα linewidth ($2640^{+1100}_{-600}\,\mathrm{km\,s^{-1}}$) measured with the European Southern Observatory New Technology Telescope (ESO NTT). They therefore inferred that the neutral Fe K line seen in this object originates in the Compton-thin BLR explaining the lack of evidence for Compton reflection and the absence of any relativistic components in the lines. More recently, Lobban et al. (2010) reproduced the highly ionized iron K lines, Fe XXV (6.66 keV) and (Fe XXVI 6.94 keV), with a photoionization model where gas has a column density of $N_H > 10^{23}\,\mathrm{cm^{-3}}$ and is likely to be located between 10^3 – 10^4 gravitational radii $(\mathrm{R}_G)_g$. The authors suggest that the inner accretion flow is radiatively inefficient (RIAF, Narayan & McClintock 2008), what would explain the photoionization and the absence of the optically thick disk component.

While the active nucleus of NGC 7213 is very well studied in X-rays, there are no observations so far monitoring the variability of the broad Balmer emission lines. The broad Hα emission line of NGC 7213 has been reported in previous works (Phillips 1979; Filippenko & Halpern 1984; Storchi-Bergmann et al. 1996). A recent study by Schnorr-Müller et al. (2014) (see Figure 1) showed the broad component of Hα to present a broad and clearly double-peaked profile. Extremely broad ($10{,}000\,\mathrm{km\,s^{-1}}$) double-peaked emission lines are thought to originate in the outer parts of ana accretion disk. Indeed, models of ionized gas emission rotating in a relativistic Keplerian accretion disk around a SMBH have been successful in accounting for the double-peaked profiles (Chen et al. 1989; Chen & Halpern 1989; Storchi-Bergmann et al. 2003; Strateva et al. 2003; Lewis et al. 2010). These models explain self-consistently most observable features of the double-peaked profiles (Eracleous & Halpern 2003)

Electronic address: silva.schimoia@ufrgs.br

and can help to put constraints on the physical structure of the disk, for instance, the inner and outer limits for the emitting region as well as in its inclination angle.

Also, many AGN's show variability of their double-peaked profiles. This is the case reported by Lewis et al. (2010) for 20 double-peaked emitters. The authors reported a long-term monitoring of these double-peaked emitters with observations taken with time intervals ranging from several months to years, and found that all monitored double-peaked profiles display variability on long (∼years) timescales. Recently, Schimoia et al. (2012, 2015), monitored the double-peaked profile of NGC 1097 on shorter timescales and found that the profile can vary on timescales as short as a week or even shorter. This suggests that there are different timescales of variability that may occur in the double-peaked emitters.

In the present paper we present, for the first time, the modeling of the double-peaked profile of NGC 7213 as due to a Keplerian and relativistic accretion disk surounding the SMBH, and discuss the implications of existence of this region of very broad line emission to the structure of the AGN. We also present the result of spectral monitoring of the profile over a time span of almost two years, from Sep 27 2011 to Jul 23 2013, with time intervals between observations as large as several months and as short as a few days towards the end of the campaign.

This paper is organized as follows: in §2 we describe the observations and the data reduction; in §3 we present the observational results and the adopted accretion disk model; in §4 we discuss the timescales of accretion disk variability, the interpretation and implications of the modeling to the structure of the AGN and explore a determination of the mass of the SMBH through the model. The conclusions of this work are presented in §5.

2. OBSERVATIONS AND DATA REDUCTION

We obtained a total of 13 optical spectra of the nucleus of the galaxy NGC 7213 from 2011 September 27 to 2013 July 23. The observation of 2011 September 27 was obtained with the Integral Field Unit of the Gemini Multi Object Spectrograph (GMOS-IFU) at the Gemini South telescope (Schnorr-Müller et al. 2014, Gemini project GS-2011B-Q-23). The wavelength range of this observation was 5600-7000 Å in order to cover Hα+[N II] $\lambda\lambda$6548,6583 Å and [S II] $\lambda\lambda$6716,6731 Å observed with the grating R400-G5325, which resulted in a resolution of R $\approx$ 2000 ($\sim$150km s^{-1}). The remaining 12 observations were taken between 2012 July 21 and 2013 July 23 with the spectrograph GMOS of the Gemini South telescope in the longslit mode. The width of the slit was 1.″0 and the grating was the B600-G5323 with the central wavelength of 5700 Å chosen to cover the Hα+[N II] $\lambda\lambda$6548,6583 Å and Hβ λ4862 Å and give a spectral resolution of R$\approx$ 1688 ($\sim$178km s^{-1}). Most visits were taken with 6 exposures of 450s each, giving a total of 2700s on source. Table 1 lists the dates of the observations, the instruments, number and time of exposures on each visit. The data were reduced using the standard procedures and packages for IFU and longslit modes in *IRAF*[1].

TABLE 1
Observations of NGC 7213

UT Date	MJD	Mode	Exposures
Sep 27 2011	55831.130	IFU	12×350
Jul 21 2012	56129.155	Longslit	6×450
Jul 30 2012	56138.422	Longslit	6×450
Oct 15 2012	56215.111	Longslit	6×450
Nov 22 2012	56253.047	Longslit	6×450
Apr 13 2013	56395.383	Longslit	6×450
May 11 2013	56423.386	Longslit	6×450
May 20 2013	56432.315	Longslit	6×450
May 30 2013	56442.334	Longslit	6×450
Jun 14 2013	56457.399	Longslit	6×450
Jun 30 2013	56473.310	Longslit	6×450
Jul 07 2013	56480.218	Longslit	6×450
Jul 23 2013	56496.278	Longslit	6×450

Note. — Column (1) gives the date of observations while column (2) gives the Modified Julian Date (JD−2400000.5). Column (3) is the mode of observation and the column (4) gives the number of visits and the exposure time of each visit.

2.1. *Subtraction of the underlying stellar population contribution*

We extracted nuclear spectra from our data using a window of 1.″0×1.″0 centered on the peak of the continuum emission. Within this aperture the continuum was dominated by the underlying stellar population instead of the continuum of the AGN. In order to isolate the nuclear AGN emission we performed the subtraction of the contribution of the stellar population. The process is illustrated in Figure 1, and is described as follows:

- First we extracted the nuclear spectrum using a window of 1.″0×1.″0 centered on the peak of the continuum;
- Two additional extranuclear spectra, also from windows of 1.″0×1.″0, were extracted 2.″0 away from the center of the nuclear extraction;
- The two extranuclear spectra were averaged and then scaled to match the flux of the continuum of the nuclear spectrum. The average extranuclear spectrum displays the same absorption features as the nuclear spectrum, and is only weakly "contaminated" by narrow emission lines which were excised by using a synthetic spectrum obtained running the `starlight-v04` code of Cid Fernandes et al. (2005).
- The scaled and corrected stellar population template was then subtracted from the nuclear spectrum in order to isolate the nuclear AGN emission. As in our previous studies of NGC 1097 Storchi-Bergmann et al. (2003); Schimoia et al. (2015), the nuclear spectrum shows no detectable non-stellar continuum emission, only line emission.

[1] IRAF is distributed by the National Optical Astronomy Observatories, which are operated by the Association of Universities for Research in Astronomy, Inc., under cooperative agreement with the National Science Foundation.

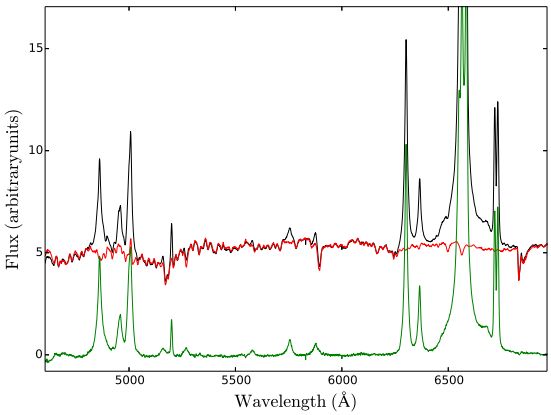

FIG. 1.— Example of the process of stellar population subtraction for the data obtained in 2012 July 27. *Top*: the black solid line is the nuclear extraction of 1.″0×1.″0; the red solid line is the stellar population template obtained by averaging the two extranuclear spectra of the estellar population extracted 2.″0 far from the nuclear extraction, the stellar population is already scaled to match the continuum of the nuclear extraction.*Bottom*: the green solid line is the resulting *nuclear emission spectrum*, after subtracting the stellar population template from the nuclear spectrum.

After the subtraction of the stellar population template we adopted the spectrum of 2011 July 27 (MJD 55831), which has the best signal-to-noise ratio (12×350 s of exposure on the source), as the reference spectrum . We then calibrated the other spectra by the flux of the narrow lines [O I]λ6300 Å and [O I]λ6363 Å. The oxigen narrow emission lines are thought to be originated in a larger region than that where the broad double-peaked Balmer lines are originated, thus the oxigen lines should not display significant variations in their flux during the monitoring campaign. Additionlly, the [O I]λ6300 Å and [O I]λ6363 Å emission lines are superimposed only over the blue wing of the broad Hα emission line, which makes these lines the best option to intercalibrate the spectra using the flux of the narrow lines. After the intercalibration by the oxigen emission lines we measured the flux of the narrow [S II] 6716,6731 Å lines and estimated that the flux calibration between the spectra is good to 7 – 8 %. This uncertainty was added in quadrature to the other uncertainties in our measurements.

3. RESULTS

The resulting nuclear emission spectra, after subtraction of the underlying stellar population and calibration by the narrow emission lines, are shown in Figure 2. In this figure it can be seen that in the first observation of 2011 September 27 (MJD 55831) the two peaks are very proeminent in the Hα profile, with the blue peak higher than the red peak. During the second observation of 2012 July 21 (MJD 56129), taken almost ten months after the first, the double-peaked shape of the broad profile is more subtle, however the asymmetry is present and the red side of the broad profile is more proeminent than the blue side. It can also be noticed that the overall flux of the double-peaked profile decreased from 2011 September 27 to 2012 July 21, thus suggesting that the time interval of ten months between these two observations is enough to allow observable changes in the shape and flux of broad Hα double-peaked profile.

After this long time interval between the first two observations we monitored the profile more frequently in order to look for shorter variability timescales. We found such variations. For instance, from 2012 Jul 30 (MJD 56138) to 2012 October 15 (MJD 56215), the profile changed showing mainly a decrease in flux in the red wing. In the subsequent spectra the profile continued to change, but with the overall flux always lower than that of the first observation. While in the first observation one can clearly see a blue and a red peak in the profile, in most of the other observations the shape of the profile can be better described as showing a double shoulder instead of double-peaks.

3.1. *Measurements of the flux of the broad double-peaked emission line*

In order to quantify the observed variability of the double-peaked profile we proceeded as follows:

- First we removed the contribution of the narrow emission lines interpolating a linear continuum between ∼6513 Å and ∼6648 Å and subtracting the emission lines Hα+[N II] $\lambda\lambda$6548,6583 Å above this continuum. We performed the same process between ∼6703 Å and ∼6751 Å to remove the [S II] $\lambda\lambda$6716,6731 Å emission lines. The removed emission lines are ilustrated as the gray regions in Figure 3.

- After the subtraction of the narrow emission lines we defined two parameters: F_{Blue} which is the integrated flux of the blue side of the broad double-peaked profile, between 6395Å and 6563Å and F_{Red} which is the integrated flux between 6563Å and 6820Å and corresponds to the integrated flux of the red side of the double-peaked profile. F_{Blue} is illustrated as the blue region in Figure 3 while F_{Red} is the red region in the same figure. We note that our definition results that the wavelength range covered by the red window is wider than that of the blue window. This effect is at least partially due to gravitational redshift, since the high velocity wings of the profile come from gas that is closer to the SMBH.

- F_{Broad} is the sum of F_{Blue} and F_{Red} and is the overall integrated flux of the broad double-peaked profile, while F_{Red}/F_{blue} is the ratio between the integrated flux of the red and blue sides of the double-peaked profile.

The parameters defined above are very similar to the parameters used to quantify the variabilty of the double-peaked profile of NGC 1097 (Schimoia et al. 2015). The main difference is that the double-peaked profile of NGC 7213, in some epochs, does not display clear blue and red peaks, but shoulders, instead. Thus, instead of measuring the flux density and position of the blue and red peaks we rather measured the integrated flux of each side of the broad profile, which is much more robust for this case. The values of F_{Blue}, F_{Red}, F_{Broad} and F_{Red}/F_{blue} are listed in Table 2, while the temporal evolution of these parameters is shown in Figure 4.

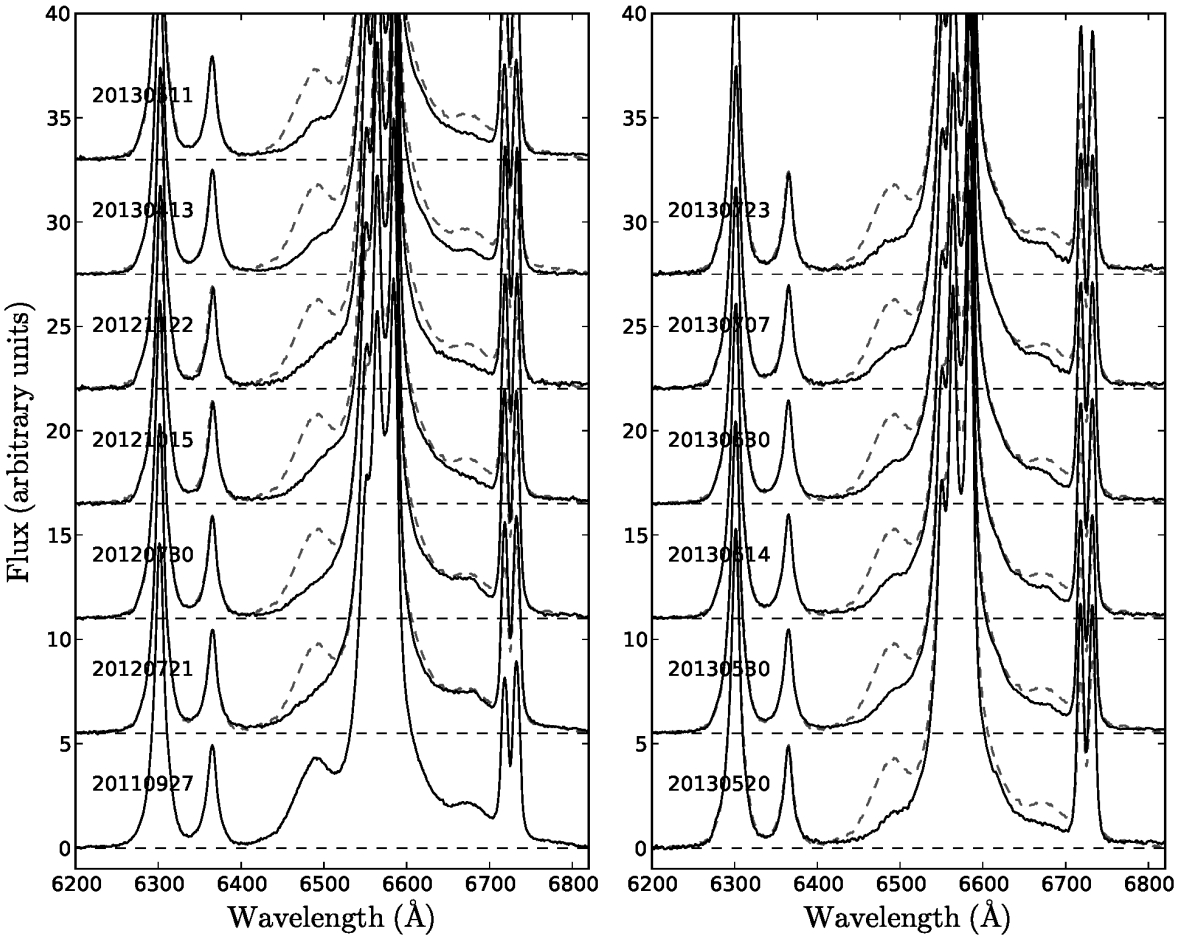

FIG. 2.— Resulting spectra for the observing campaign. The nuclear emission spectra are shown from 2011 July 27 (MJD 55831) to 2013 Jul 23 (MJD 56496). The reference spectrum of 2011 July 27 (MJD 55831) is displayed, as the black dashed line, together with each other spectrum for comparison.

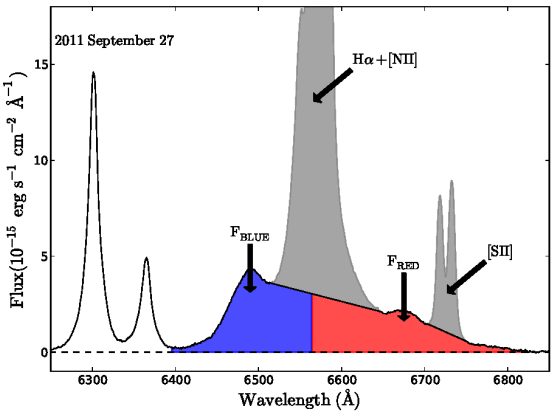

FIG. 3.— Illustration of the properties of the broad Hα double-peaked profile of NGC 7213. The gray regions are emission lines that were removed before measuring the flux of the double-peaked profile. The blue region, between 6395Å and 6563Å shows the integrated area to obtain the flux of the blue side of the profile, F_{Blue}. The red one, between 6563Å and 6820Å shows the integrated flux of the red side of the profile, F_{Red}.

3.2. *Variability Timescales*

From our previous studies of the broad double-peaked Hα profile of NGC 1097 we concluded that there are two main variability timescales in the double-peaked profiles: a long one, related to the dynamical timescale (see §4); and a shorter one that can be identified with the light travel time between the ionizing source and the disk. In NGC 7213, we tentatively identify these timescales as follows:

- *Long variability timescale*: significant changes in the integrated flux of the double-peaked profile can occur on timescales of a few months. For instance, from 2012 July 21 (MJD 56129) to 2012 November 22 (MJD 56253) F_{Broad} varied from 645.7 to 458.2 $\times 10^{-15}$erg s^{-1} cm^{-2}, a variation of ∼30% in approximately 4 months. During the same period, the relative intensity of the red and blue sides of the profile, F_{Red}/F_{blue}, also changed significantly, from 1.4 to 1.9. We note that during the period between 2013 April 13 (MJD 56395) and 2013 July 23 (MJD 56496) a time interval of ∼ 100 days F_{Red}/F_{blue} barely varied, staying around the

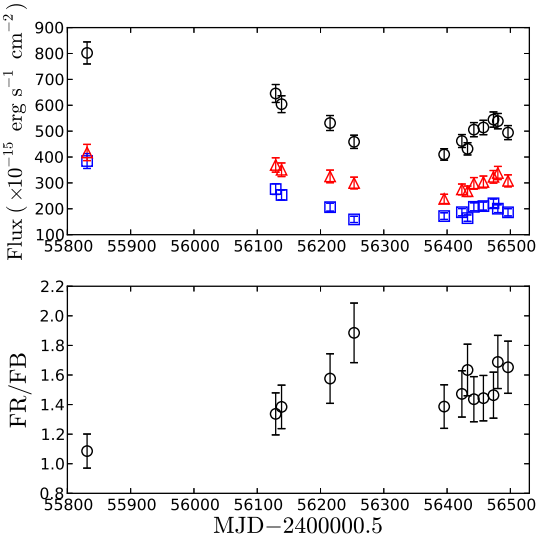

FIG. 4.— *Top pannel*: The black circles represent the integrated flux of the broad double-peaked profile, F_{Broad}. The blue squares represent the integrated flux of the blue side of the broad profile (F_{Blue}), while the red triangles represent the integrated flux of the red side of the profile (F_{Red}). All measurements were performe after the subtraction of the narrow emission lines as illustrated in Figure 3. *Bottom pannel*: the black circles represent the temporal evolution of the relative intensity of the integrated flux of the red and blue sides (F_{Red}/F_{blue}).

value 1.5. Thus, we conclude that the timescale in which F_{Red}/F_{blue} variations can be observed is $\gtrsim$ 3 months.

- *Short variability timescale*: from 2013 April 13 to 2013 Jul 23 we obtained more frequen observations, separated by time intervals as short as a week to a month. The shortest time interval between consecutive observations is 7 days, from 2013 June 30 (MJD 56473.310) to 2013 July 07 (MJD 56480.218). On this timescale F_{Broad} did not display changes larger than the uncertainties in the measurements. During the period from 2013 April 13 (MJD 56395) to 2013 May 11 (MJD 56423) F_{Broad} changed from 409.8 ± 22.1 to $461.6\pm25 \times 10^{-15}$erg s^{-1} cm^{-2} in a time interval of 28 days. We can thus only put limits on the shortest timescale: it is longer than a week but shorter than 28 days.

3.3. *The MEAN, RMS and MIN spectrum*

As discussed in §3.1 significant changes in F_{Broad} and in the shape of the double-peaked profile are only seen on timescales $\gtrsim$ 30 days. So in order to model the changes in the shape of the double-peaked profile, we selected spectra that are separeted by time intervals of the order of 30 days, namely: 2011 September 27, 2012 July 21, 2012 October 15, 2012 November 22, 2013 April 13, 2013 May 20, 2013 June 14, 2013 July 07. These observations are listed in Table 3 and include all the different shapes we observed for the broad profile during the campaign.

We calculated the *mean*, *rms* and *min* spectra considering only the 8 modeled observations. The mean spectrum was calculated by taking the average of the fluxes of the observations in each wavelength:

$$F_{\rm MEAN}(\lambda) = \frac{1}{8}\sum_{i=1}^{8} F_i(\lambda) \qquad (1)$$

where $F_{\rm MEAN}(\lambda)$ representes the flux of the mean spectrum in each wavelength and $F_i(\lambda)$ is the flux in each wavelength for the ith observation. The mean spectrum is shown as the black line in the top panel of Figure 5. From this figure we can see that the mean spectrum also displays double-shoulders, typical of a disk geometry, with the maximum flux density of the blue side of the profile slightly higher than that of the red side.

As can be seen from Figure 2 the broad double-peaked profile clearly varies with time. Variations in the illumination of the disk could result on variations on the overall profile, however the *root mean square* (rms) spectrum can reveal if there are specific regions in the velocity space of profile in which the flux varies more. We calculated the *rms* spectrum, as follows:

$$F_{\rm RMS}(\lambda) = \sqrt{\frac{1}{8}\sum_{i=1}^{8} \left(F_{\rm MEAN}(\lambda) - F_i(\lambda)\right)^2} \qquad (2)$$

where $F_{\rm RMS}(\lambda)$ is the rms flux of the rms spectrum in each wavelength. The rms spectrum is shown in black line in the middle pannel of Figure 5. We note that the most vaiable part of the rms spectrum also displays a double-peaked profile, with the blue peak centered around 6487Å and the red peak around 6684Å, with some contribution of an additional central component. The *rms* spectrum is consistent with a scenario that the most variable part of the profile originates in a disk, with some contribution from material at lower velocites and thus probably further out from the SMBH. The minimun spectrum is constructed by selecting, at each wavelength, the minimum flux density from among all the spectra. This minimum spectrum represents a base profile which is common to all profiles, and is shown at the bottom of Figure 5. The interpretation of the minimum spectrum needs to be taken with caution. In the scenario in which the emission arises from a circular accretion disk with an emissivity enhancement (such as a hot spot or spiral arm), the minimum spectrum would be that of the underlying circular accretion disk. From Figure 5, the minimum spectrum also displays two shoulders, what can be interpreted as due to the fact that the underlying structure is a disk. Together the mean, rms and minimum spectra confirm that the main structure producing the broad, double-peaked profile is indeed a disk.

3.4. *The Accretion Disk Model*

We modeled the Hα profiles using the accretion disk model described by Gilbert et al. (1999), Storchi-Bergmann et al. (2003), and Schimoia et al. (2012, 2015). In this formulation, the broad double-beaked emission line originates in a relativistic Keplerian disk of gas surounding the SMBH. The line-emitting portion of the disk is circular and located between an inner radius ξ_1

TABLE 2
NGC 7213 DOUBLE-PEAKED PROFILE FLUX MEASUREMENTS

UT Date	MJD	F_{Blue}	F_{Red}	F_{Broad}	F_{Red}/F_{blue}
Sep 27 2011	55831.130	384.3±28.8	417.2±31.3	801.5±42.6	1.1±0.1
Jul 21 2012	56129.155	276.4±20.8	369.3±27.7	645.7±34.7	1.3±0.1
Jul 30 2012	56138.422	253.4±19.0	350.6±26.3	604.0±32.5	1.4±0.2
Oct 15 2012	56215.111	206.3±15.5	325.2±24.4	531.5±29.0	1.6±0.2
Nov 22 2012	56253.047	158.6±12.0	299.6±22.5	458.2±25.5	1.9±0.2
Apr 13 2013	56395.383	171.5±12.9	238.3±17.9	409.8±22.1	1.4±0.2
May 11 2013	56423.386	186.9±14.1	274.7±20.6	461.6±25.0	1.5±0.2
May 20 2013	56432.315	164.1±12.4	267.9±20.2	432.0±23.7	1.6±0.2
May 30 2013	56442.334	207.6±15.6	298.1±22.4	505.7±27.3	1.4±0.2
Jun 14 2013	56457.399	210.2±15.8	303.8±22.8	514.0±27.8	1.5±0.2
Jun 30 2013	56473.310	221.1±16.6	323.5±24.3	544.6±29.4	1.5±0.2
Jul 07 2013	56480.218	200.4±15.1	338.1±25.4	538.5±29.6	1.7±0.2
Jul 23 2013	56496.278	186.5±14.1	308.0±23.2	494.5±27.1	1.7±0.2

NOTE. — Column (1) gives the date of observations while column (2) gives the Modified Julian Date (JD−2400000.5). Column (3) integrated flux of the blue side of the profile in units of $10^{-15}\,\mathrm{erg\,s^{-1}\,cm^{-2}}$ and the column (4) gives the integrated flux of the red side of the profile in the same units of (3). Column (5) gives total flux of the broad profile. Column (6) gives the ratio between (4) and (3).

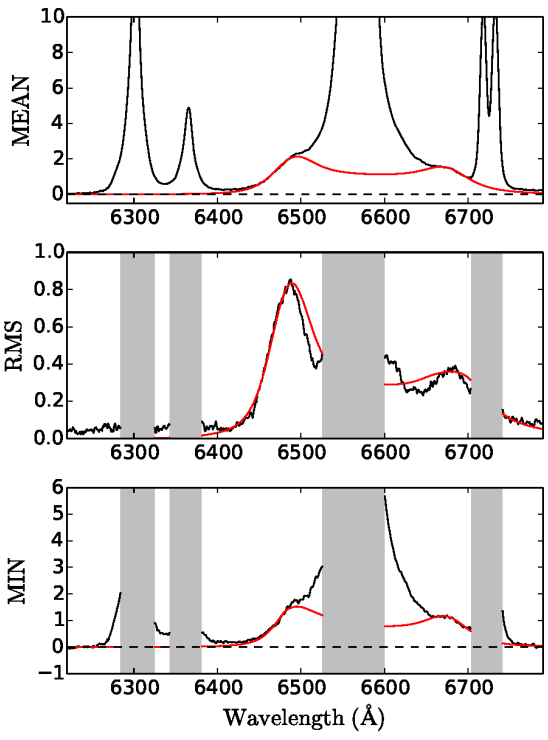

FIG. 5.— *Top*: Comparison between the mean, rms and mim spectra calculated with the obsevations and model of the double-peaked profile. We show, as black lines, in the top, middle and bottom the mean, rms and minimum spectra calculated from the observations. The red lines are the, mean, rms and min spectrum calculated using the models of the profiles (see §4 for details).

and an outer radius ξ_2 (where ξ is the disk radius in units of the gravitational radius $r_g = GM_\bullet/c^2$, c is the speed of light, G is the gravitational constant, and $M_{\rm BH}$ is the mass of the black hole). The disk has an inclination i with respect to the plane of the sky.

In order to take into account the observed asymmetries on the double-peaked profile we adopted the "saturated spiral model" (Schimoia et al. 2012) for the total emissivity of the accretion disk. In this formulation, there is a perturbation on the emissivity in the form of a spiral arm, which is superposed to the underlying emissvity of the circular accretion disk.

This emissivity law is given by

$$\epsilon(\xi,\phi) = \epsilon(\xi)\left\{1 + \frac{A}{2}\exp\left[-\frac{4\ln 2}{\delta^2}(\phi-\psi_0)^2\right] + \frac{A}{2}\exp\left[-\frac{4\ln 2}{\delta^2}(2\pi-\phi+\psi_0)^2\right]\right\}, \quad (3)$$

where

$$\epsilon(\xi) = \begin{cases} \epsilon_0\xi^{-q_1} & , \xi_1 < \xi < \xi_q \\ \epsilon_0{\xi_q}^{-(q_1-q_2)}\xi^{-q_2} & , \xi_q < \xi < \xi_2 \end{cases} \quad (4)$$

is the axisymmetric emissivity of the disk. The parameter ξ_q is the radius of maximum emissivity, or saturation radius, at which the emissivity law changes; q_1 is the index of the emissivity law for $\xi_1 < \xi < \xi_q$; q_2 is the index for $\xi_q < \xi < \xi_2$. A is the brightness contrast between the spiral arm and the underlying disk, and the expression between square brackets represents the decay of the emissivity of the arm as a function of the azimuthal distance $\phi-\psi_0$ from the ridge line to both sides of the arm, assumed to be a Gaussian function with FWHM $= \delta$ (azimuthal width).

The relation between the azimuthal angle ϕ_0 and the angular position ψ_0 of the ridge of emissivity on the spiral arm is given by

$$\psi_0 = \phi_0 + \frac{\ln(\xi/\xi_{sp})}{\tan p}, \quad (5)$$

where ϕ_0 is the azimuthal angle of the spiral pattern, p is the pitch angle, and ξ_{sp} is the innermost radius of the spiral arm.

The specific intensity from each location in the disk, in the frame of the emitting particle is calculated as

$$I(\xi,\phi,\nu_e) = \frac{\epsilon(\xi,\phi)}{4\pi}\frac{e^{-(\nu_e-\nu_0)^2/2\sigma^2}}{(2\pi)^{1/2}\sigma}, \quad (6)$$

where ν_e is the emission frequency and ν_0 is the rest frequency corresponding to Hα λ6564.6 and σ is the local "broadening parameter" (Chen & Halpern 1989).

We kept the emissivity index for radius larger than the break radius as $q_2 = 3$, as proposed by by Dumont & Collin-Souffrin (1990): after the saturation radius the emissivity of the disk is expected to be proportional to ξ^{-3}. We tested many values for the emissivity index for the region between the inner and the saturation radius, $\xi_1 < \xi < \xi_q$, and concluded that $q_1 = -0.2$ gave the best fits; this small value for q_1 is required because, as can be seen in Figure 2 the broad double-peaked profile displays very extended wings. The presence of extended wings means that the inner parts, with higher projected velocities, are important for the emissivity of the disk and the value $q_1 = -0.2$ implies that the emissivity increases slowly until the break radius, what makes the inner parts of the accretion disk important with respect to the outer parts. We also tested differente values for the inner and outer radius, ξ_1 and ξ_2, and the inclination angle, i, and found that the set of values that best reproduced all the data together are $\xi_1 = 300$, $\xi_2 = 3000$ and $i = 47°$, so in the analysis below, we kept these values for the parameters.

In order to reproduce the double-peaked profile variations, namely, in the relative intensity of the blue and red sides of the double-peaked and the broadening/narrowing of the profile, we allowed only 3 parameters to vary: the azimutal orientation of the spiral arm ϕ_0, the contrast between the underlying disk and the spiral arm, A, and the radius where the maximum emissivity occurs, ξ_q. The parameters that define the shape of the spiral arm were kept fixed as $p = 13°$, $\delta = 75°$ and $\xi_{sp} = \xi_1$. Among these parameters, the pitch angle is the less uncertain because it regulates the curling of the spiral arm, and in the case of NGC 7213, a small pitch angle ($p = 13°$) is required to curl the spiral arm close to the inner radius and give relative more importance to the inner regions of the disk, and consequently, better reproduce the wings of the profile. Figure 6 shows the best fits of the model to the data while the corresponding parameters are listed in Table 3. The surface emissivity maps corresponding to the modeling are shown in Figure 7.

We also calculated the *mean*, *rms* and *min* spectra of the theoretical modeled double-peaked profiles. They are shown superposed on the observed profiles in red lines in the pannels of Figure 5. We can see from this figure that the adopted accretion disk model reproduces not only the individual profiles (see Figure 6) but also the overall features of the observed mean, rms and minimum spectra. However we note that there is feature in the rms spectrum that is not well reproduced by the model:the central part, that varies more than predicted by the modeling. We argue that this excess of variability is caused by an additional low velocity component, probably originating in the clouds of the BLR orbiting the SMBH beyond the disk. We estimate that the contribution of this component to the overall variability is only ≈15%. More detailed models, including additional low velocity gas components, may be able to reproduce this central BEL variability, although this fine modeling is beyond the scope of this work.

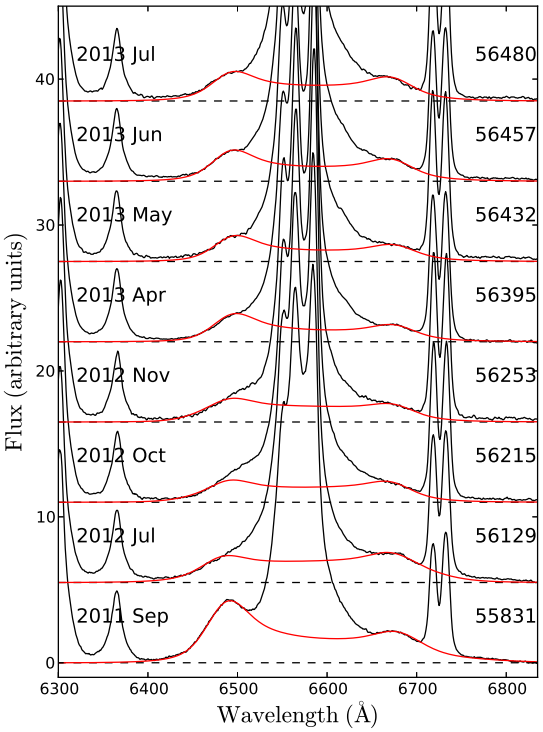

FIG. 6.— The black solid line is the observed spectra during the campaign, after subtraction of the stellar continuum and calibration by the flux of the narrow lines. In each frame the red solid line represents the best modeled broad double-peaked profile using the *Saturated Spiral model* for the accretion disk. The spectra are shifted in flux for better visualization. The parameters of the fits are listed on Table 3.

TABLE 3
NGC 7213 PARAMETERS OF THE BEST FITS

UT Date	MJD	ξ_q	A	$\phi_0(°)$
Sep 27 2011	55831.130	1800	4.0	+280
Jul 21 2012	56129.155	2000	3.0	+205
Oct 15 2012	56215.111	2500	2.0	+45
Nov 22 2012	56253.047	2500	3.0	+25
Apr 13 2013	56395.383	2500	2.0	-30
May 20 2013	56432.386	2500	1.8	-50
Jun 14 2013	56457.399	3000	1.0	-60
Jul 07 2013	56480.218	3000	0.2	-80

NOTE. — Column (1) gives the date of observations while column (2) gives the Modified Julian Date (JD−2400000.5). Column (3) gives the break or saturation radius ξ_q (4) gives contrast of the spial arm, A (3). Column (5) gives orientation of the spiral patern, ϕ_0.

4. DISCUSSION

Differently from what is observed by Schimoia et al. (2015) for the *low state* of the double-peaked profile of NGC 1097, when NGC 7213 is in a low state it is hard to detect the asymmetry in the broad profile, e. g., when the $F_{Broad}$is relatively low, the contrast between the spiral arm and the underlying disk is smaller. This trend is present during all the campaign. At the beginning the contrast parameter was A=4.0 but in the last observa-

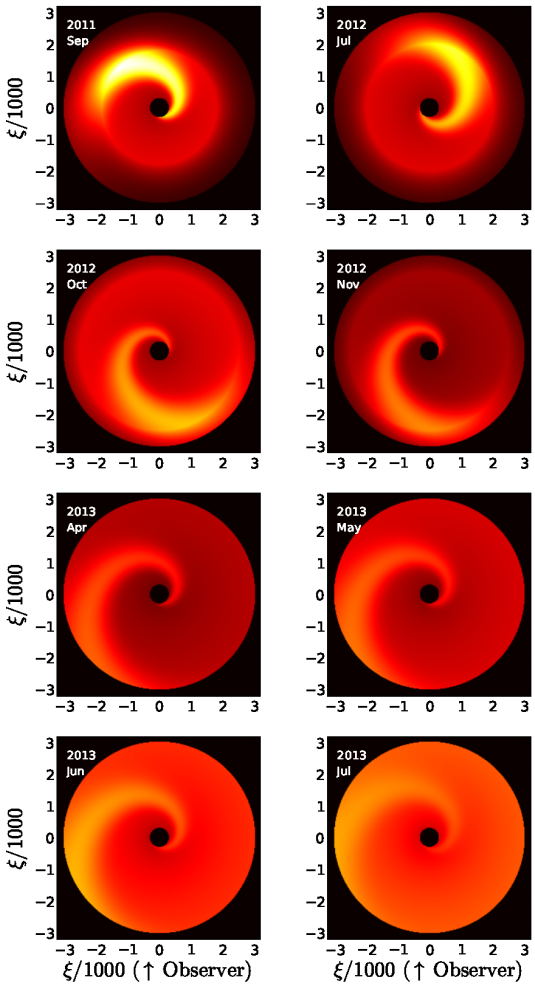

FIG. 7.— In each frame is shown the emissivity map of the accretion disk of NGC 7213 corresponding to the modeled double-peaked profiles of Figure 6. The white represents the the regions of the disk with the highest surface emissivity while the red represents the regions withe the lowest surface emissivity. The non-axisymmetric part of the emissivity has the shape of a spiral arm rotating on the accretion disk. The observer is located on the bottom and the spiral arm is rotating anticlockwise. The epoch of observation is shown on the top left corner of each frame.

tions it was very small: A=0.2. From the first to the last observation the asymmetry, modeled by the position angle of the spiral arm, diminished gradually. This fading can be observed in the emissivity maps of Figure 7. During the last observations, from 2013 April 13 (MJD 5639) until the end of the campaign, even if we were able to detect small variation in the overall flux F_{Broad}, the ratio F_{Red}/F_{blue} is almost the same and around 1.5. This result is in agreement with the decrease in the contrast between the arm and the underlying disk.

4.1. *Implications for the mass of the SMBH*

The only epoch we were able to identify clear peaks in the profile was in 2011 September 27. For this observation, the maximum flux densities for the blue and red peaks were observed at the wavelengths 6488.3 and 6675.4 Å, respectively. This corresponds to a velocity separation between the blue and red peaks of $\Delta_V \approx 8550$ km s^{-1}. Considering half of this velocity as a typical velocity for the gas in the disk, as it aproximately corresponds to the radius of maximum emission, and correcting for the inclination of the disk, we obtain an estimate for the circular velocity $V_C = \frac{8850}{2} \times \frac{1}{\sin(47°)} \sim 6050\,\mathrm{km\,s^{-1}}$.

As discussed on §3, the shortest timescale in F_{Broad} is expected to be between 7 28 days. If we adopt 17 days, the mean time interval, as a measurement for a typical distance between the central SMBH and the disk, we can estimate the mass of the SMBH as $M_\bullet = 1.21 \times 10^8 M_\odot$. Considering the lower and upper limits of 7 and 28 days, respectively we can estimate a range for the mass of the SMBH of $5{\times}10^7 < M_\bullet < 2 \times 10^8\,\mathrm{M}_\odot$.

We can also estimated the mass of the central SMBH via the $M_\bullet - \sigma_\star$ relation of Tremaine et al. (2002):

$$\log\left(\frac{M_\bullet}{M_\odot}\right) = \alpha + \beta \log\left(\frac{\sigma_\star}{\sigma_0}\right) \quad (7)$$

where $\alpha = 8.13 \pm 0.06$; $\beta = 4.02 \pm 0.32$; and $\sigma_0 = 200\,\mathrm{km\,s^{-1}}$. The scatter in the $M_\bullet - \sigma_\star$ relation is not included in the error, but the error bars on the coefficients are.

When we performed the stellar population synthesis with `starlight-v04` we used the simple stelar population templates of Bruzual & Charlot (2003) and allowed the fit of the stellar kinematics. The value we obtained for the velocity dispersion was $vd = 219\,\mathrm{km\,s^{-1}}$. In order to obtain the real velocity dispersion we need to correct this value by the intrumental resolution, σ_{inst}, and the resolution of the template spectra, σ_{base}:

$$\sigma_\star^2 = vd^2 - \sigma_{ins}^2 + \sigma_{base}^2 \quad (8)$$

The B600 grating in the longslit observation has an instrumental resolution of $\sigma_{inst} = 177\,\mathrm{km\,s^{-1}}$, while the Bruzual & Charlot (2003) base of simple stelar population spectra has a resolution of R $\approx$ 2000, $\sigma_{base} \sim 150\mathrm{km\,s^{-1}}$, in the wavelength range 3200 Å to 9500Å. Thus, we estimate the stellar velocity dispersion as $\sigma_\star = 188\,\mathrm{km\,s^{-1}}$, which via Equation 7 gives $M_\bullet = 1.27 \times 10^8\,M_\odot$.

This value for the stellar velocity dispersion is very close to value $\sigma_\star = 185\mathrm{km\,s^{-1}}$ estimated by Woo et al. (2002). The authors also used the $M_\bullet - \sigma_\star$ relation (Tremaine et al. 2002) to estimate the mass of the SMBH, $M_\bullet = 9.77 \times 10^7 \mathrm{M}_\odot$. Considering that there is an intrinsic scatteting of ~ 0.3 dex (a factor ~ 2) in the $M_\bullet - \sigma_\star$ relation, we conclude that our determination of the mass is in very good agreement with the previous one.

4.2. *Varability timescales*

The two shortest variability timescales of the standard accretion disks (Shakura & Sunyaev 1973) are the *light travel timescale*, τ_l, and the *dynamical timescale*, τ_{dyn}:

$$\tau_l = 6 M_8 \xi_3 \quad (9)$$

$$\tau_{dyn} = 6 M_8 {\xi_3}^{3/2} \quad (10)$$

where M_8 is the mass of the SMBH in units of $10^8\mathrm{M}_\odot$ and $\xi_3 = \xi \times 10^{-3}$. The mass of the central SMBH of NGC 7213 is $M_\bullet = 9.77 \times 10^7 M_\odot$ (Woo et al. 2002).

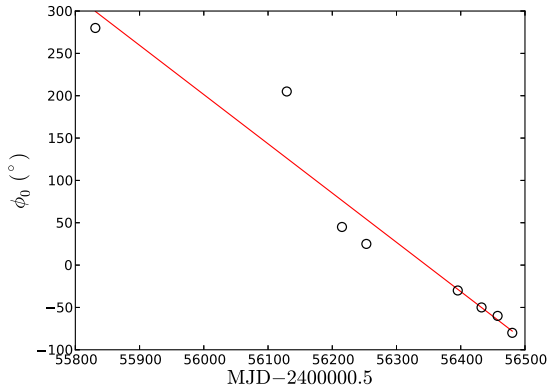

FIG. 8.— The black open circles represent the parameter ϕ_0 for each modeled epoch. The red solid line is the best linear fit to the data, which das angular coefficient of $\alpha \approx -0.58°\,\mathrm{day}^{-1}$. The rotation period corresponds to $P \approx 620$ days or 21 months.

Considering the modeled inner and outer radius of the accretion disk, $0.3 < \xi_3 < 3$, we obtaing a range for the variability timescales of:

- τ_l: 2 – 18 days
- τ_{dyn}: 1 – 31 months

The evolution of the modeled parameter ϕ_0 with time is shown in Figure 8. The linear fit to the data gives an angular velocity of $\alpha \approx -0.58°\,\mathrm{day}^{-1}$, which implies a rotation period of ~ 620 days or 21 months. Considering this period of rotation as a dynamical timescales of the accretion disk, this rotation period occurs around $660\,r_g$, which suggests that at this radius the asymmetric feature of the accretion disk has completed almost one full rotation on the disk.

From Figure 4 it can be seen that the most significant variations in the relative intensity of fluxes of the red and blue sides of the profile,$\mathrm{F_{Red}/F_{blue}}$, occur in the timescale of a few months, for instance $\mathrm{F_{Red}/F_{blue}}$ varied from 1.09 (2011 September 27) to 1.33 (2012 July 21) in almost 10 months and also varied from 1.33 (2012 July 21) to 1.67 (2012 November 22) in approximately 4 months.

This variability timescale is compatible with the modeled rotation of the spiral arm on the accretion disk, which occurs on timescales of the order of the dynamical timescale. Although our relatively sparse monitoring did not allow us to put strong constraints on the shortest variability timescale, the limits we have obtained, between 7 and 28 days are also consistent with the light travel time timescale if we adopt it close to the upper limit of 18 days.

5. CONCLUSIONS

We presented 12 new optical spectroscopic observations of the broad double-peaked Hα profile of the AGN in NGC 7213. Together with the previous observation of Schnorr-Müller et al. (2014) the time span of the monitorig campaign comprised almost two years, with observations sparsed by time intervals from a week to a few months. The main results of this paper are:

- The relative intensity of the integrated flux of the blue and red sides of the profile displayed significant variations on a timescale $\gtrsim 3$ months, consistent with th expected *dynamical timescale* of the accretion disk; it is the first time that variability is reported in the broad double-peaked profile of this AGN;
- We could only obtain lower an upper limits to the variability timescale of the integrated flux of the double-peaked line, that is between 7 days and 28 days, consistent with the *light travel timescale* between the ionizing source and the emitting part of the disk;
- We successfullly modeled the broad double-peaked profile as due to gas emission from a Keplerian and relativistic accretion disk with inner and outer radii of the emitting region of $\xi_1 = 300$ and $\xi_2 = 3000$, repectively, and inclination angle of $i = 47°$. This disk harbors a spiral arm with varying contrast relative to the underlying disk;
- The variations in the relative intensity of the blue and red sides of the profile were modeled as due the rotation of the spiral arm, which we concluded to has a rotation period of ~ 21 months. This arm completed almost on full rotation on the accretion disk during the monitoring campaign;
- Over the two years spanned by the observations, the spiral arm has faded;
- When comparing the the mean, *rms* and min spectrum calculated with the observations and the model, most features of the profiles are very well reproduced. The only discrepancy is the central part of the *rms* spectrum that varies more than predicted. We argue that this may be caused by a region of gas whose emission is also variable and originates in regions farther away from the ionizing source;
- Using the fit of the stellar absorption features with the Starlight code we obtained a velocity dispersion of the bulge of $\sigma_\star = 188\mathrm{km\,s^{-1}}$, what implies a mass for the SMBH of $M_\bullet = 1.27 \times 10^8\,\mathrm{M_\odot}$ via the $M_\bullet - \sigma_\star$ relation, in agreement with previous determinations by other authors;
- We also estimated the mass of the SMBH adopting as a representative velocity of the gas in the disk half the diference in velocity between the red and blue peaks and as the corresponding distance the limits we obtained for the light travel time between the SMBH and the disk, obtaining $5 \times 10^7 < M_\bullet < 2 \times 10^8\,\mathrm{M_\odot}$.

In summary, our proposed scenario is the following: the broad double-peaked emission arises from a Keplerian and relativistic accretion disk, from a region with inner and outer limits for the emitting region of 300 and 3000 gravitional radii, whose inclination angle is 47 degrees and is orbiting a SMBH with a mass of $1.27{\times}10^8\,\mathrm{M_\odot}$. The relative intensity of the flux of blue and red sides of the double-peaked profile changes due the rotation of an spiral arm with a rotation period of 21 months. The

contrast between the emission in the arm and in the underlying disk was high in the beginning but decreased gradually, leading to ever smaller asymmetries between the heights of the blue and red sides of the double peaked profile.

REFERENCES

Bianchi S., Matt G., Balestra I., Perola G. C., 2003, *The origin of the iron lines in NGC 7213*, A&A, 407, L21

Bianchi S., La Franca F., Matt G., Guainazzi M., Jimenez Bailón E., Longinotti A. L., Nicastro F., Pentericci L., 2008, MNRAS, 389, L52

Bruzual G., Charlot S., 2003, MNRAS, 344, 1000

Chen K., Halpern J. P., & Filippenko A. V., 1989, ApJ, 339, 742

Chen K., & Halpern J. P., 1989, ApJ, 344, 115

Cid Fernandes R., Mateus A., Sodré L., Stasińska G., & Gomes J. M., 2005, MNRAS, 358, 363

Dumont A. M., Collin-Souffrin S., 1990, A&A, 229, 313

Emmanoulopoulos D., Papadakis I. E., McHardy I. M., Arévalo P., Calvelo D. E., Uttley P., 2012, MNRAS, 424, 1327

Eracleous M., & Halpern J. P., 2003, ApJ, 599, 886

Filippenko A. V., Halpern J. P., 1984, *NGC 7213 - A key to the nature of liners?*, ApJ, 285, 458

Gilbert A. M., Eracleous M., Filippenko A. V., & Halpern J. P., 1999, ASPC, 175, 189

Lewis K. T., Eracleous M., & Storchi-Bergmann T., 2010, ApJS, 187, 416

Lobban A. P., Reeves J. N., Porquet D., Braito V., Markowitz A., Miller L., Turner T. J., 2010, MNRAS, 408, 551

Narayan R., & McClintock J. E., 2008, NewAR, 51, 733

Schimoia J. S., Storchi-Bergmann T., Nemmen R. S., Winge C., & Eracleous M., 2012, ApJ, 748, 145

Phillips M. M., 1979, ApJ, 227, L121

Schimoia J. S., Storchi-Bergmann T., Grupe D., Eracleous M., Peterson B. M., Baldwin J. A., Nemmen R. S., Winge C., 2015, ApJ, 800, 63

Schnorr-Müller A., Storchi-Bergmann T., Nagar N. M., Ferrari F., 2014, MNRAS, 438, 3322

Shakura N. I., & Sunyaev R. A., 1973, IAUS, 55, 155

Storchi-Bergmann T., Nemmen da Silva R., & Eracleous M., et al., 2003, ApJ, 598, 956

Strateva I. V., Strauss M. A., Hao L., et al., 2003, AJ, 126, 1720

Storchi-Bergmann T., Rodriguez-Ardila A., Schmitt H. R., Wilson A. S., Baldwin J. A., 1996, *Circumnuclear Star Formation in Active Galaxies*, ApJ, 472, 83

Tremaine S., Gebhardt K., Bender R., et al., 2002, *The Slope of the Black Hole Mass versus Velocity Dispersion Correlation*, ApJ, 574, 740

Woo J.-H., Urry C. M., 2002, ApJ, 579, 530

Capítulo 6

Núcleos ativos tipo Seyfert 1 com perfil de duplo-pico

Os resultados obtidos para o estudo das galáxias Seyfert 1 emissoras de duplo-pico estão descritos no artigo a seguir, o qual está na fase de avaliação pelos colaboradores e será submetido a uma revista científica arbitrada.

‘PERFIS DE DUPLO-PICO: ASSINATURAS ONIPRESENTES DE DISCOS NA REGIÃO DE LINHAS LARGAS DE NÚCLEOS ATIVOS ED GALÁXIAS’

Draft version November 17, 2015
Preprint typeset using LaTeX style emulateapj v. 5/2/11

DOUBLE-PEAKED PROFILES: UBIQUITOUS SIGNATURES OF DISKS IN THE BROAD EMISSION LINES OF ACTIVE GALACTIC NUCLEI

T. Storchi-Bergmann [1,2], J.S. Schimoia[1,3], M. Elvis[2], B.M. Peterson[3], K.D. Denney[3] , M. Eracleous[4]
[1]Instituto de Física, Universidade Federal do Rio Grande do Sul, Campus do Vale, Porto Alegre, RS, Brazil
[2]Harvard-Smithsonian Center for Astrophysics, 60, Garden Street, Cambridge, MA 02138, USA
[3]Department of Astronomy, 140 West 18th Avenue, and the Center for Cosmology and AstroParticle Physics, 191 West Woodruff Avenue, The Ohio State University, Columbus, OH 43210, USA and
[4] Department of Astronomy & Astrophysics, The Pennsylvania State University, University Park, PA 16802, USA
Draft version November 17, 2015

ABSTRACT

Broad ($\sim$10,000 km s^{-1}), double-peaked emission-line profiles of Balmer lines emitted by active galactic nuclei (AGN) are thought to originate in the outer parts of an accretion disk surrounding a nuclear supermassive black hole (SMBH), at $\sim$1000 gravitational radii and are most frequently observed in the nuclear spectra of low-luminosity AGN (LLAGN) and radio-galaxies. In the present paper we argue that broad double-peaked profiles are present also in the spectra of other Type 1 AGN, such as Seyfert 1 galaxies, suggesting that the inner part of the broad-line region (BLR) is a disk. In order to demonstrate this we have used the Palomar spectral survey of nearby galaxies to obtain a census of Type 1 AGN presenting double-peaked profiles, showing that the frequency of occurrence of these profiles is consistent with the presentce of a disk in the inner part of the BLR of most AGN. We have fitted a disk model to the Hα profiles of the available spectra to obtain the typical parameters of the disk as well as its inclination i showing it to be in the range $20^\circ \leq i \leq 35$, with a median value of $i = 27^\circ$. The recognition that the most variable part of the BLR has a disk geometry suggests that the factor f in the expression to obtain the SMBH mass in Type 1 AGN $M_{\rm BH} = f\left(R_{\rm BLR}\Delta V^2/G\right)$ is $f = 1/\sin^2 i$. Our median $i = 27^\circ$ implies $f = 4.5$, very close to the most recent value of $f = 4.3 \pm 1.05$, obtained from independent studies, supporting our findings. As the inclination does vary among sources, we have used our fits and modelling to derive a relation bewteen f and the FWHM of the broad profile that may help to reduce the uncertainties in the SMBH mass determinations of AGN.
Subject headings: accretion, accretion disks — galaxies: active — galaxies: Seyfert — line: profiles – galaxies: nuclei

1. INTRODUCTION

Double-peaked emission lines in the spectra of active galactic nuclei (AGN), usually observed in the permited H and He lines, are believed to originate in the outer parts of a disk, typically at about 1000 gravitational radii $R_g = GM_{\rm BH}/c^2$) from the supermassive black hole (SMBH) of mass $M_{\rm BH}$, that is often taken to be the outer regions of the accretion disk that extends down to a few R_g. A disk origin for double-peaked emission lines was first proposed by Chen et al. (1989); Chen & Halpern (1989) for the archetypical "double-peaker" Arp 102B. Subsequent work by Eracleous & Halpern (1994, 2003) found a number of other sources, confirming that a disk (or ring) model does reproduce the double-peaked profiles. A similar conclusion was reached by Strateva et al. (2003) for a sample of 116 AGN with double-peaked Balmer lines profiles selected from the Sloan Digital Sky Survey.

There have been other suggestions for the origin of double-peaked emission-line profiles. Gaskell (1983) and Peterson et al. (1987) suggested that they might be the signature of binary black holes. (Wanders et al. 1995) and (Goad & Wanders 1996) showed that double-peaked profiles could be produced by an anisotropic continuum source; or, for that matter, a highly anisotropic distribution of emission-line gas. The preponderance of evidence, however, still points to a moderately or highly inclined disk-like structure (Eracleous & Halpern 2003).

Some double-peaked profiles have been monitored over timescales of years, at typical intervals of months. Examples are the cases of 3C 390.3 (Veilleux & Zheng 1991; Sergeev et al. 2002; Jovanovic et al. 2010; Shapovalova et al. 2010; Popovic et al. 2011; Sergeev et al. 2011), which has also been monitored on reverberation timescales (Dietrich et al. 1998, 2012), NGC 1097 (Storchi-Bergmann et al. 2003), Arp 102B (Sergeev et al. 2000; Shapovalova et al. 2013), as well as 14 other double-peaked emitters (Gezari et al. 2007; Lewis et al. 2010). These observations have revealed that the double-peaked Balmer lines in these sources display variability timescales ranging from months to years. The changes in the profiles are typically varying asymmetries in the blue and/or red peaks of the profiles and are observed on *dynamical timescales*, associated with the rotation of the gas or patterns in the gas surrounding the SMBH. In the particular case of NGC 1097, during the 30 years it has been spectroscopically monitored (Storchi-Bergmann et al. 2003; Schimoia et al. 2012), the relative intensity of the blue and red peaks has alternated between a stronger blue peak and a stronger red peak on timescales of months, and have been attributed to a spiral arm rotating in the disk, with a rotation period of about $\sim$18 months.

Electronic address: thaisa@ufrgs.br

Most of the monitoring campaigns of *double-peakers* reported to date were carried out using a very sparse cadence, typically one observation per month or even sparser. But recent observations of the nucleus of NGC 1097 by Schimoia et al. (2012) included a few observations at weekly intervals and showed that there are variations in the total flux of the line and in the separation between the blue and red peaks on a timescale of a week. In order to search for possible shorter timescale variations, and to try to identify the driving source of the line variations, we subsequently monitored the double-peaked Hα profile in the nuclear spectrum of NGC 1097 with the SOAR telescope and the *Swift* satelite (Schimoia et al. 2014). These observations confirmed that the integrated flux of the line and the velocity separation betwween the blue and red peaks vary on a timescale as short as 5 days. This timescale is compatible with the light-crossing time between the center of the disk and a typical radius of 1000 R_g, where the emission line originates, according to our models.

The variability timescale of $\sim$ 5 days, observed in NGC 1097 is of the order of the delays found between the variations of the continuum and broad emission lines in reverberation mapping studies of nearby Seyfert 1 galaxies of comparable luminosity. This indicates that the line-emitting disk in NGC 1097 is at a distance from the ionizing source that is typical of the broad-line region (BLR) of nearby Seyfert 1 galaxies (Peterson et al. 2004).

It is also interesting that many Seyfert 1 galaxies show, at least on some occasions, evidence for an underlying disk-like component. Double peaks or shoulders are frequently seen in the Balmer-line profiles of highly variable and closely monitored sources like NGC 5548 (Sergeev et al. 2007). These various observations lead one to consider the possibility that the Balmer-line profiles in all Seyfert 1 galaxies have a disk-like component that could be identified with the outer parts of an accretion disk. A simple hypothesis might be that Balmer-line profiles in Seyfert 1 galaxies are a composite of: (1) a disk-like component, as seen clearly in the spectra of double-peaked emitters, and (2) another separate component originating in more distant clouds.

A model of a disk component plus another narrower broad component to reproduce the broad Balmer line profiles of Seyfert 1 nuclei and quasars has been previously proposed by Popović et al. (2004) and collaborators (Bon et al. 2009; La Mura et al. 2009). A theoretical study by Elitzur (2014) also argues that the broad-line region of Seyfert 1 galaxies has two parts: a disk and a system of clouds that are part of an outflowing disk wind. As the Eddington ratio drops, the high column density gas, which resides only in the disk, dominates the emission and leads to double-peaked line profiles. A disk-wind component would be expected to be stronger at higher Eddington rates, so this might naturally account for the relative prominence of the disk-like component in lower luminosity AGNs (LLAGNs) and the relative difficulty of identifying the disk component in more luminous, higher Eddington rate objects.

In this contribution we study the spectra of all Seyfert 1 galaxies of the Palomar spectroscopic survey (Filippenko & Sargent 1985; Ho, Filippenko & Sargent 1995) – selected for being an homogeneus and representative sample of galaxy nuclear spectra in the near Universe – to show that we can identify disk-like structures in the Balmer-line profiles of many of them. An underlying disk-like component can account for much of the structure and asymmetries seen in Seyfert 1 line profiles, and, combined with another narrower component, attributable to other emitting clouds, can reproduce most of the broad-line profiles. As the Palomar sample is an approximately complete, distance-limited sample, we use our results to obtain statistics of the presence of the disk component, and discuss the implications for the calculation of the mass of the SMBHs in Type 1 AGN.

This paper is organized as follows. In Sec. 2, we describe the disk model that we have used to reproduce the double-peaked profiles of the low-luminosity AGN (LLAGN) in NGC 1097 and other sources. In Sec. 3 we illustrate its use to reproduce the double-peaked Balmer line profiles of LLAGN and Seyfert 1 galaxies of the Palomar survey. In Sec. 4, we show how the profile shape changes as a function of inclination relative to the plane of the sky and the presence of more distant emitting clouds. We use these results and the frequency of occurrence of the double-peaked profiles in the Palomar sample to draw inferences about the presence of disk emission in type 1 AGN. In Sec. 5 we discuss the implications of our findings for the determination of SMBH masses in Type 1 AGN, and in Sec. 6, we present our conclusions.

2. THE DISK MODEL

We use the model described by Schimoia et al. (2012), Gilbert et al. (1999), and Storchi-Bergmann et al. (2003), assuming that the broad double-peaked emission line originates in the outer parts of a relativistic Keplerian disk of gas surrounding the SMBH. The line-emitting portion of the disk is circular and located between an inner radius of ξ_1 and and an outer radius of ξ_2, where ξ is the disk radius in units of the gravitational radius R_g. The plane of the disk has an inclination i relative to the plane of the sky (i.e., zero degrees corresponds to a disk observed face-on). Superimposed on the axisymmetric emissivity of the circular disk, there is a perturbation in the form of a spiral arm. The corresponding emissivity law is given by

$$\epsilon(\xi,\phi) = \epsilon(\xi)\left\{1 + \frac{A}{2}\exp\left[-\frac{4\ln 2}{\delta^2}(\phi-\psi_0)^2\right] + \frac{A}{2}\exp\left[-\frac{4\ln 2}{\delta^2}(2\pi-\phi+\psi_0)^2\right]\right\}, \quad (1)$$

where

$$\epsilon(\xi) = \begin{cases} \epsilon_0\xi^{-q_1} & , \xi_1 < \xi < \xi_q \\ \epsilon_0{\xi_q}^{-(q_1-q_2)}\xi^{-q_2} & , \xi_q < \xi < \xi_2 \end{cases} \quad (2)$$

is the axisymmetric emissivity of the disk. The parameter ξ_q is the radius of maximum emissivity, or saturation radius, at which the emissivity reaches a maximum and changes behavior: q_1 is the index of the emissivity law for $\xi_1 < \xi < \xi_q$ and q_2 is the index for $\xi_q < \xi < \xi_2$. A is the brightness contrast between the spiral arm and the underlying disk, and the expression between square brackets represents the decay of the emissivity of the arm as a function of the azimuthal distance $\phi - \psi_0$ from the ridge line to both sides of the arm, assumed to be a Gaussian function with FWHM = δ (azimuthal width).

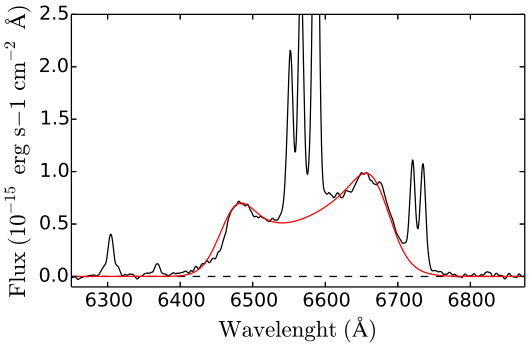

Figure 1. Fit of the accretion disk model to an Hα profile of the LLAGN in NGC 1097 (Schimoia et al. 2012). The solid black line is the observed nuclear emission spectrum and the red solid line is the accretion disk model.

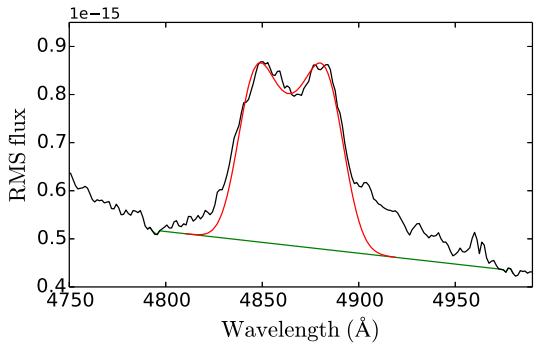

Figure 2. The Hβ *RMS* spectrum of NGC 3227 from Denney et al. (2010): the red solid line is the fitted accretion disk model profile, while the green solid line is the adopted continuum.

The relation between the azimuthal angle ϕ_0 and the angular position ψ_0 of the ridge of emissivity of the spiral arm is given by

$$\psi_0 = \phi_0 + \frac{\ln(\xi/\xi_{sp})}{\tan p}, \quad (3)$$

where ϕ_0 is the azimuthal angle of the spiral pattern, p is the pitch angle, and ξ_{sp} is the innermost radius of the spiral arm.

The specific intensity from each location in the disk, in the frame of the emitting particle is calculated as

$$I(\xi, \phi, \nu_e) = \frac{\epsilon(\xi, \phi)}{4\pi} \frac{e^{-(\nu_e - \nu_0)^2/2\sigma^2}}{(2\pi)^{1/2}\sigma}, \quad (4)$$

where ν_e is the emission frequency and ν_0 is the rest frequency corresponding to Hα λ6564.6 and σ is the local "broadening parameter" (Chen & Halpern 1989).

The fit of this model to the Hα double-peaked profile of NGC 1097 observed on 2010 March 4 is shown in Fig. 1. The model parameters are listed in Table 2. This model has been used also to reproduce varying double-peaked profiles of 5 broad-line radio galaxies by Gilbert et al. (1999) and of 14 other AGNs in Gezari et al. (2007) and Lewis et al. (2010).

3. DOUBLE-PEAKED BALMER-LINE PROFILES IN NEARBY SEYFERT 1 GALAXIES

Although previous studies – as those mentioned above – have focused on fitting the broadest and cleanest double-peaked profiles, many nearby Seyfert 1 nuclei also show broad Balmer lines with double-peaked characteristics. This can be observed, for example, in the nuclear spectra of Seyfert 1 galaxies which have been the subject of spectroscopic monitoring campaigns, such as NGC 4151 (Maoz et al. 1991; Kaspi et al. 1996; Bentz et al. 2006), NGC 5548 (Netzer et al. 1990; Peterson et al. 2002; Bentz et al. 2007, 2009, 2010; Denney et al. 2010), NGC 3227 (Winge et al. 1995; Denney et al. 2010) and NGC 3516 (Denney et al. 2010). Denney et al. (2010) present the results of reverberation mapping of other 4 Seyfert 1 nuclei besides NGC 5548 and NGC 3516. With the exception of one source, either the Hβ profiles are double-peaked or the root-mean-square deviation *RMS* spectra are double-peaked. This indicates that, even if the profile is not clearly double-peaked (e.g. due to the presence of other components), the most variable part of the profile is double-peaked, supporting that the innermost part of the BLR (that varies most, as it is closer to the ionizing source) is a disk.

We show in Fig. 2 the result of our attempt to fit the *RMS* Hβ profile of NGC 3227 using our disk model and data from Denney et al. (2010): although the profiles are not always double-peaked, the *RMS* spectrum is. The parameters of the fit are $\xi_1 = 2000$, $\xi_2 = 5000$, $\xi_q = 3125$, $i = 16°$, $\phi_0 = 20°$, $q_1 = -2.0$, $q_2 = 3.0$, $A = 0.6$, $p = -20°$, $\delta = 40°$, $\sigma = 480\,\mathrm{km\,s^{-1}}$, $\xi_{sp} = \xi_1$. Fig. 2 shows that the model does fit the double-peaked component although there is, in addition, an even broader component, revealed by the extended red wing that could not be fitted by our model. This component probably originates at gas at higher velocities closer to the SMBH and/or in inflow or outflow, for example. This interpretation is in line with the velocity delay map of Denney et al. (2012): they conclude that there is evidence for an overall Keplarian disk-like structure, but potential evidence for an outflow (or inflow) at large velocities, particularly on the red side of the line, that appears to be at larger radii than the disk-like structure found in the main line core velocities. Five other cases of more distant and luminous Type 1 AGN showing similar *RMS* profiles have been reported by Grier et al. (2012a,b),

4. TYPE 1 AGN IN THE PALOMAR SPECTROSCOPIC SURVEY OF NEARBY GALAXIES

The Palomar spectroscopic survey (Filippenko & Sargent 1985; Ho, Filippenko & Sargent 1995; Ho et al. 1997d) – consisting of spectra of 486 northern galaxies – can be considered an homogeneous and representative sample of galaxy nuclear spectra in the near Universe, with a detection limit for emission lines at an equivalent width EW $\gtrsim 0.25$ Å. Of the total sample of 486 galaxies, the nuclear spectra of 211 have been classified as AGN, with 46 among them classified as of Type 1. One of the advantages of the Palomar survey relative to the larger and more recent Sloan Digital Sky Survey SDSS (Abazajian et al. 2003; Pâris et al. 2004) is the smaller extraction aperture ($\sim 1''$ compared to $\sim 3''$ in SDSS), which allows the detection of nuclear activity at fainter levels of contrast relative to host-galaxy starlight.

Table 1 of Ho et al. (1997d) lists the properties of the 46 Type 1 nuclei of the Palomar sample: 34 are classed as

showing "definite" detection of a broad Hα line, while for the remaining 12, there is only a "probable" detection of a faint broad Hα component. The fit of the line profiles in these "probable" cases shows that the broad component is not well constrained and may be due instead to complex kinematics of the narrow-line region (hereafter NLR). We have inspected the Hα profiles in the Palomar spectra of the 34 nuclei considered to present definite detection of a broad Hα line, and searched in the literature for previous studies with analysis of these profiles. We list in the top part of Table 1 the 12 galaxies that show clearly double-peaked or flat-toped Hα profiles, giving in the last column of the table the reference in which the profile is shown to be double-peaked. Some of these profiles were found not in the Palomar spectra but in nuclear spectra obtained with the STIS spectrograph aboard the *Hubble Space Telescope (HST)*: NGC 4203 (Shields et al. 2000), NGC 4450 (Ho et al. 2000) and NGC 4579 (Barth et al. 2001). The higher angular resolution of the *HST* spectroscopy allows the detection of even fainter lines than those detected in the Palomar survey as the contribution of the stellar population decreases even further in the narrower STIS slits ($0\farcs1 - 0\farcs2$).

In order to further support our argument that broad double-peaked profiles are frequently found in Type 1 AGN, we list in the bottom part of Table 1 six additional Seyfert 1 galaxies with broad double-peaked Balmer-line profiles that are not in the Palomar survey (most of them being southern objects), but are Type 1 AGN at distances similar to to those of the Palomar galaxies. The double-peaked profiles of these galaxies were discovered serendiptously.

Table 1
Nearby Type 1 AGN with Double-Peaked Balmer Profiles

Galaxy	Activity	D (Mpc)	Morphology	F_{dp}/F	Ref.
Palomar					
NGC 3031	LLAGN	0.66	SA(s)ab	0.57	A
NGC 3227	Sy 2	20.3	SAB(s)a pec	0.71	B
NGC 3516	Sy 1.5	37.2	(R)SB0^0?(s)	0.91	B
NGC 4051	Sy 1	12.7	SAB(rs)bc	0.74	E
NGC 4151	Sy 1.5	17.0	(R')SAB(rs)ab?	0.63	C
NGC 4203	LLAGN	18.6	SAB0$^-$?	0.34*	D
NGC 4235	Sy 1.2	37.7	SA(s)edge-on	0.84	E
NGC 4395	Sy 1.8	8.0	SA(s)m	0.63	E
NGC 4450	LLAGN	31.1	SA(s)ab	0.20*	F
NGC 4579	Sy 2	25.3	SAB(rs)b	0.21*	G
NGC 5273	Sy 1.9	17.8	SA0^0(s)	0.84	E
NGC 5548	Sy 1.5	73.4	(R')SA0/a(s)	0.96	E
Southern					
NGC 1097	LLAGN	15.1	SB(s)b	...	H
NGC 3065	LLAGN	28.3	SA0^0(r)	...	I
IC 4329A	Sy 1.2	69.6	SA0$^+$? edge-on	...	J
NGC 2617	Sy 1.8	62.3	Sc	...	K
NGC 3783	Sy1.5	44.3	(R')SB(r)ab	...	L
NGC 7213	LLAGN	21.1	SA(s)a?	...	M

Note. — Column (1): Galaxy identification; (2): distance (NED, 3K CMD); (3): galaxy morphology; (4): fractional contribution of broad Hα to the total Hα+[N II] emission; * means that the double-peaked profile was identified only with *HST* STIS spectra; (5): reference for the double-peaked profile: (A)Bower et al. (1996), (B) Denney et al. (2010), (C) Bentz et al. (2006), (D) Shields et al. (2000), (E) Ho et al. (1997d), (F) Ho et al. (2000), (G) Barth et al. (2001), (H) Storchi-Bergmann et al. (1993), (I) Eracleous et al. (2001), (J) Winge et al. (1996), (K) Shappee et al. (2014), (L) Stirpe et al. (1994) (M) Filippenko & Halpern (1984).

4.1. *Fit of the double-peaked profiles of Type 1 AGN in the Palomar sample*

In order to further demonstrate that the profiles that appear double-peaked in the Palomar spectra can be attributed to the outer parts of an accretion disk, we now use our model to fit the broad Hα profile in these spectra (Ho et al. 1997d) for the galaxies of Table 1 that showed high enough signal-to-noise ratio in the broad profiles to constrain the fit: NGC 3516, NGC 4151, NGC 4235, NGC 5273 and NGC 5548.

4.2. *Subtraction of the stellar component*

Most of the spectra of the above galaxies show strong absorption features due the contribution of an underlying stellar population, with the exception of NGC 5548, whose continuum seems to be dominated by the AGN. In order to isolate the gas emission in the other cases, we corrected their nuclear spectra by subtracting a stellar population template, using for this the Palomar spectra of the non-active galaxies (Ho et al. 1997c) that do not show any emission lines. For each active galaxy, we searched for a stellar population template that reproduced its nuclear spectrum well (in the regions where there is no emission lines) and then subtracted a scaled and Gaussian convolved version of the chosen template. We used a continuum wavelength window from 6200Å to 6250Å to determine the scale factor between the nuclear spectrum and the stellar template. This method is very similar to that of Ho et al. (1997c) and the result is illustrated in Figure 3 for NGC 4235. The spectra of the other four galaxies after the subtraction of the stellar component are shown in Figure 4.

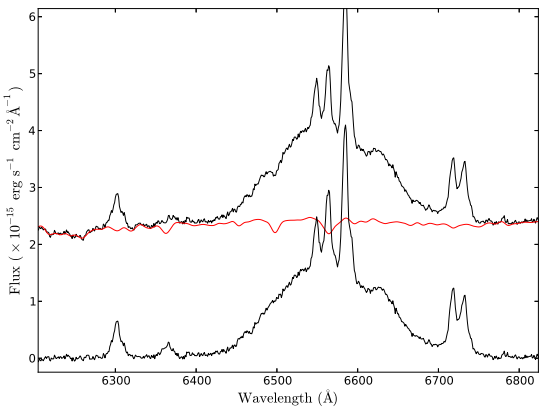

Figure 3. Subtraction of the stellar population template NGC 4235. Top: Palomar spectrum in black; stellar population template (NGC 4371, from Ho et al. (1997c)) in red. Bottom: residual nuclear emission spectrum.

4.3. *Two-component fit*

A close inspection of the Hα broad emission lines (BEL) of the above galaxies and a tentative fit with the disk model reveals that, besides a double-peaked component, at least another component is present, that is singly-peaked and is narrower than the double-peaked component. We thus assume that the BEL has two com-

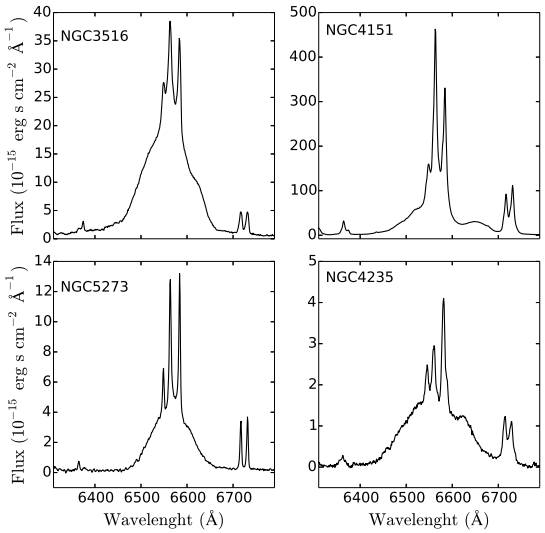

Figure 4. Nuclear emission spectra of NGC 3516, NGC 4115, NGC 4235 and NGC 5273 after the subtraction of the contribution of the stellar population.

ponents: a disk component – or high velocity component, plus a lower velocity component (contributing mostly to the core of the line), originating in more distant clouds. This assumption is similar to that of Popović et al. (2004) and Bon et al. (2009) even when modeling singly-peaked BELs. We have parameterized these two components as follows:

- Accretion disk: We have used the *Saturated Spiral Model*, that has provided the best fits in our previous studies of the Hα double-peaked profile of NGC 1097 and other sources (Schimoia et al. 2012), with the paramenters described in §2;
- Gaussian component: as a first approximation we assume that the more distant clouds produce an emission-line profile described by a Gaussian:

$$F_G(\lambda) = \frac{A_G}{\sqrt{2\pi {\sigma_G}^2}} \exp\left[-\frac{(\lambda - \lambda_0 + \Delta\lambda)^2}{2{\sigma_G}^2}\right] \quad (5)$$

where λ_0 is the rest wavelength of Hα, $\Delta\lambda$ is the displacement of the Gaussian component relatively to the Hα narrow component, σ_G is the standard deviation and A_G is the amplitude of the Gaussian component. Thus, the flux of the BEL, in the observer's rest frame, $F_{BEL}(\lambda)$ is given by

$$F_{BEL}(\lambda) = F_D(\lambda) + F_G(\lambda) \quad (6)$$

where $F_D(\lambda)$ is the specific flux of the disk component.

The best fits of the BELs were obtained in two steps:

1. We first fitted the central Gaussian component allowing all three parameters to vary: $\Delta\lambda$, σ_G and A_G. In order to prevent the Gaussian component from fitting the wings of the profile that should come from the disk component, we applied a constraint on the maximum displacement of the center of the Gaussian relative to the narrow component: -44 Å$< \Delta\lambda < 44$ Å that correspond to relative velocities between -2000 and 2000 km s^{-1};
2. After subtraction of the Gaussian component, we fited the resulting double-peaked profile with the accretion disk *Saturated Spiral Model* (Schimoia et al. 2012) where we fixed the parameter of the emissivity law $q_2 = 3$, for $\xi_q < \xi < \xi_2$, corresponding to the outer parts of the accretion disk; this is motivated by the fact that for an accretion disk ionized/illuminated by an external source above the disk (as usually adopted as the source of ionization for the gas in the disk) the radial dependence of the surface emissivity is $\epsilon(\xi) \propto \xi^{-3}$ (Dumont & Collin-Souffrin 1990). Another parameter that we kept fixed was the inner radius where the spiral arm begins, we fixed this value at $\xi_{sp} = \xi_1$. All the other parameters of the disk were allowed to vary.

Following Popović et al. (2004), we have calculated the relative flux contribution between the Gaussian and disk components as:

$$Q = \frac{\int_{-\infty}^{+\infty} F_G(\lambda) d\lambda}{\int_{-\infty}^{+\infty} F_D(\lambda) d\lambda} \quad (7)$$

4.4. *Results of the two-component fits*

The best fits of the above two components to the BELs are shown in Figure 5, while the corresponding parameters are listed in Table 2. Uncertainties in the parameters of the accretion disk were obtained by perturbing each parameter separately around the best fit value. In the last column of Table 2 we list the average value of the disk parameters.

The main results of the two-component fits are:

- Gaussian component: the Gaussians have full-width at half maximum in the range $1000 \leq FWHM \leq 3000$ km s^{-1}, and displacements in the centroid velocities of the Gaussian component (relative to the narrow-line components) in the range -1920 km s^{-1} $< \Delta v < +180$ km s^{-1}, corresponding mostly to blueshifts, that could be interpreted as due to outflows of the more distant clouds (if we assume that we see more easily the clouds that are closer to us than the ionizing source) or to inflows (if for some reason we are seeing preferrably the clouds that are farther from us than the ionizing source). We note that in the particular case of NGC 3516, X-ray spectra are compatible with the presence of a warm absorber with blueshifts in the range -2000 to -1000 km s^{-1}, thus compatible with the velocity of the Gaussian component, that could be associated with this absorber and in this case would be in outflow.
- Disk component: The inner radius of the disk ranges between 300 and 800 R_g, the outer radius between 1600 and 3500 R_g, and the saturation radius between 1100 and 2600 R_g. Average values

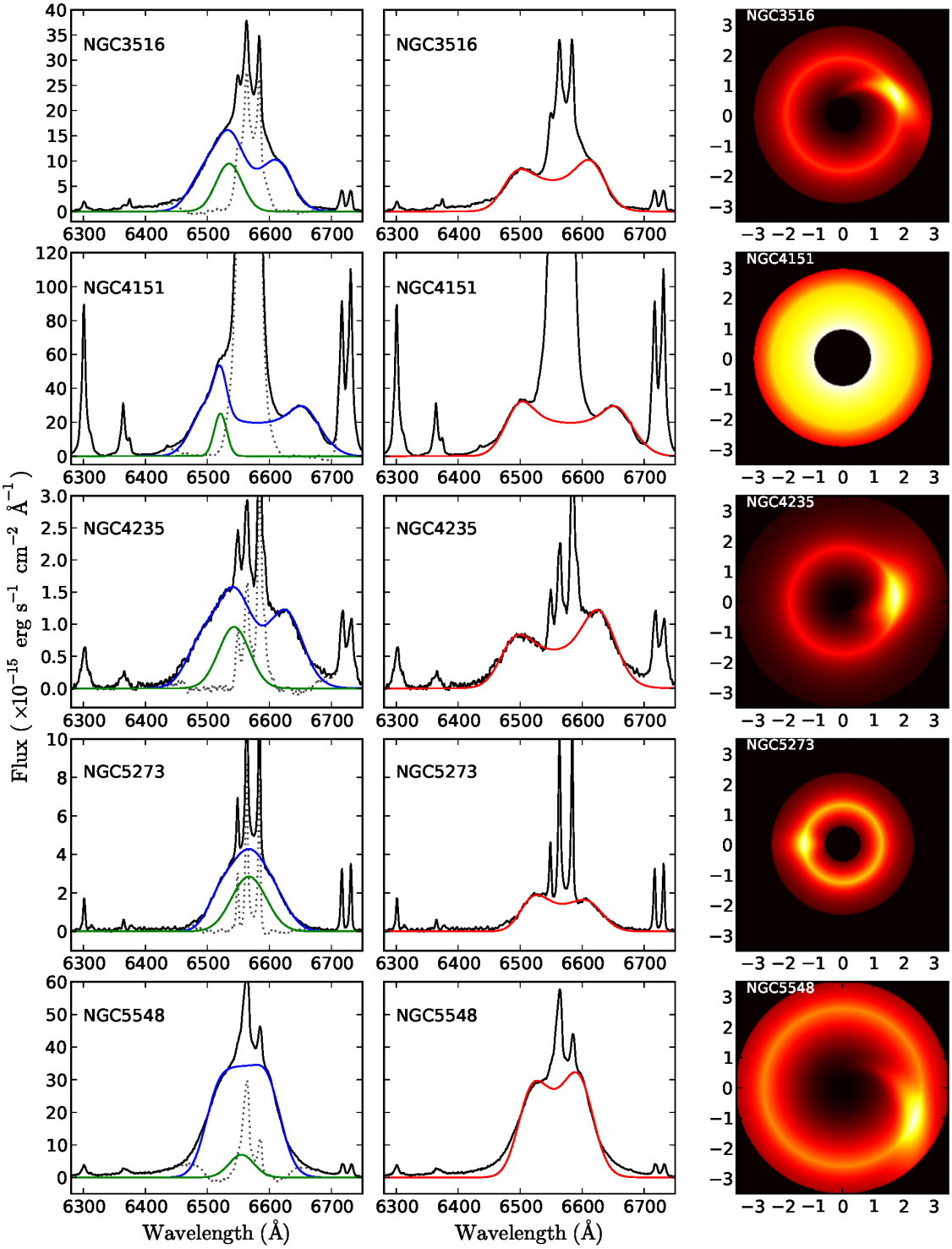

Figure 5. Two component fits of the Hα BELs of NGC 3516, NGC 4151, NGC 4235, NGC 5273 and NGC 5548 - *Left column*: in black, the Palomar spectrum corrected for the stellar population contribution; in green, the Gaussian component; in blue, the combined fit of the accretion disk and Gaussian components; the dotted line shows the residuals between the observed spectra and model (disk + Gaussian). *Central column*: in black, the Palomar spectrum after subtraction of the Gaussian component; in red, the best accretion disk model. *Right column*: emissivity map of the disk component (yellow-white corresponding to the maximum emissivity); the axes are in units of 1000ξ

are listed in the last column of Table 2, showing *rms* variations of ∼30%. The inclination angle of the accretion disk (relative to the plane of the sky) is in the range $17° < i < 35°$, meaning that we are seeing the disk more "face-on" than "edge-on", in agreement with what is expected for Type 1 AGN in the simple Unified Model. The emissivity law of the disk is the same, for all galaxies, showing an increase up to the saturation radius and then a decrease beyond it. NGC 4151 shows a flatter increase in emissivity up to the saturation radius than the other galaxies.

- The parameter Q, that measures the contribution of the Gaussian component relative to the disk component is $Q < 0.5$ for four of the 5 cases we have fitted the two components, showing that the disk component is more luminous than the Gaussian component, e.g., the BEL emission is disk dominated. The exception is NGC 5273 (Q=0.86), for which the fluxes of the Gaussian and disk components are comparable.

The presence of double-peaked components in nearby Type 1 AGNs is also supported by reverberation mapping studies of the Hβ broad line profile. Denney et al. (2010), besides confirmim this for NGC 5548 and NGC 3516, show that the same applies for four other Seyfert 1 nuclei (not in the Palomar survey): either the Hβ profiles or the *RMS* spectra are double-peaked (with the exception of one source). The same is found for other 5 more distant and luminous Type 1 AGN (Grier et al. 2012a,b). Peterson et al. (2004) show that the *RMS* spectrum of NGC 4151 is also double-peaked, while Doroshenko et al. (2012) show the same also for Mrk6.

5. THE STATISTICS OF DOUBLE-PEAKED PROFILE EMITTERS AMONG TYPE 1 NUCLEI

Type 1 AGN in the Palomar Survey comprise between 34 (with "unambiguous" broad lines) and 46 (including broad lines that could be due to multiple components in the narrow lines) of the 211 AGN, thus ∼20% (Ho et al. 1997d; Ho 2008). We will use this percentage to put approximate constraints on the half-openning angle θ_m of the obscuring torus in the simple approximation of the Unified Model scenario in which the geometry of the escaping radiation is that of a cone (Antonucci 1992). We now know that the "torus" is most likely a distribution of dusty clouds, and that its properties vary with the AGN luminosity (e.g., Elitzur 2012; Ichikawa et al. 2015), but the simple Unified Model can give us some insight on relative probabilities. In the simple model, the 20% fraction of Type 1 AGN implies that the "free" solid angle of the AGN is $2\pi[1-\cos(\theta_m)] \approx 20\%$ of 2π, with 80% of 2π being the solid angle covered by the obscuring torus. Thus, in order to see directly the AGN — the accretion disk and BLR — our line-of-sight has to make an angle of at most $\theta_m \approx 37°$ relative to the AGN symmetry axis.

In order to illustrate how the double-peaked profiles would appear as a function of the orientation of our line of sight relative to the AGN, we show in Fig. 6 a series of double-peaked profile models for inclinations ranging from 0 to 35°. The parameters of the model are the average ones we have obtained from the fitted models to the Palomar spectra applied to the Hα profile, which is the most prominent line in the optical spectra of AGN (as it is ∼3 times as strong as Hβ). In this figure, we have superposed the narrow components of Hα and [N II] $\lambda\lambda$6548, 6584 on the broad double-peaked profile. These lines were simulated by Lorentzians with FWHM = 300 km s^{-1}.

Figure 6 shows that, in order for Hα to appear double-peaked, our line-of-sight has to make an angle of at least ∼ 20° relative to the ionization axis of AGN. This means that the disk inclination should be between ∼ 20° and ∼ 37° for the profile to be observed as double-peaked. The inclination angles derived from our fits are between 17° and 35°, thus in good agreement with the predicted range. Previous fits of similar accretion disk models to double-peaked profiles, such as those observed in radio galaxies (Chen & Halpern 1989; Eracleous & Halpern 1994; Lewis et al. 2010), and nearby LLAGN (Ho et al. 2000; Storchi-Bergmann et al. 2003), also show a similar range of inclination values, as is the case also of the dynamical models of Pancoast et al. (2014b). Considering the inclination values listed in Table 2 for the six targets we have fitted with our disk model, we obtain a mean value for the inclination of the disk of $i = 27° \pm 7°$.

Assuming again the conical geometry of the simple model, the solid angle for inclinations between 20° and 35° is 12% of 2π. When we compare this number with the 20% fraction above for type 1 AGN, we conclude that ∼ 60% of type 1 AGN should have double-peaked Balmer-line profiles. According to these predictions, if the total sample of Type 1 nuclei in the Palomar sample is 34 galaxies, we should expect to find ∼ 20 galaxies with double-peaked profiles. We find 12, thus ∼ 35% instead of the predicted 60%. On the other hand, the number we have found may be a lower limit, as, in some cases the double-peaked nature of the line profiles could be observed only in very high-quality *HST* STIS spectra in which the contrast between the emission lines and the host-galaxy starlight is much higher than in the Palomar spectra. As not all the Type 1 AGN of the Palomar sample have been observed with *HST* STIS, this fraction of 35% double-peakers may be a lower limit.

Another consideration to be made is that, in the Palomar spectra, a critical property of the broad line to allow its clear detection is its flux compared with the narrow lines. Inspection of the fits in Figs. 4–14 of Ho et al. (1997d) shows that clear broad Hα components can only be detected when the fraction of the flux in the broad line is larger than 50% of the total flux in the broad plus narrow Hα+[N II] lines. This fraction, obtained from Ho et al. (1997d), is listed in the 4^{th} column of Table 1. The total number of these sources in Ho et al. (1997d) is 14, with 9 (64%) of them having double-peaked profiles, now consistent with the ∼60% prediction above. Another possibility is that the ratio of the outer to inner radius of the disk is >> 10, what would make the line profiles singly-peaked (see Fig. 9 of **?**).

6. DISCUSSION

As mentioned in the Introduction, the fact that broad-line profiles of Seyfert 1 and radio galaxies seem to contain a flattened component has been noted in previous studies, including also those by Wills & Browne (1986); Chen & Halpern (1989); Jackson & Browne (1991);

Table 2
Parameters of the two-component modelling

Component	NGC 1097	NGC 3516	NGC 4151	NGC 4235	NGC 5273	NGC 5548	Aver.
Disk							
ξ_1	450	500	800	300	500	350	483±159
ξ_2	1600	2500	2500	3000	2000	3500	2516±620
ξ_q	1200	1600	2000	1500	1100	2600	1773±636
i	34	25	35	30	17	19	27±7
ϕ_0	140	80	300	120	270	45	159±94
q_1	-2	-2	0.4	-2	-2	-2	-2
q_2	3	3	3	3	3	3	3
A	3.0	2.5	0.0	3.2	1.0	1.5	2.28±1.37
p	50	-20	...	35	90	-20	27±42
$\delta(^\circ)$	70	30	...	50	30	30	42±16
σ	900	900	750	900	850	900	867±55
shift (Å/km s^{-1})	...	-15/-686	+10/457	-10/-457	-4/-183	-10/-457	***
Gaussian							
$\Delta\lambda$ (Å/km s^{-1})	...	-28/-1280	-42/-1920	-20/-914	+4/+180	-8/-365	...
σ_G (Å/km s^{-1})	...	21/960	10/460	25/1243	28/1280	20/914	...
A_G	...	500	630	60	200	350	...
$FWHM$	10555	6253	7908	7715	5102	5754	...
Q	...	0.35	0.11	0.35	0.86	0.09	...

Note. — Units of ξ_1, ξ_2 and ξ_q are gravitational radii.

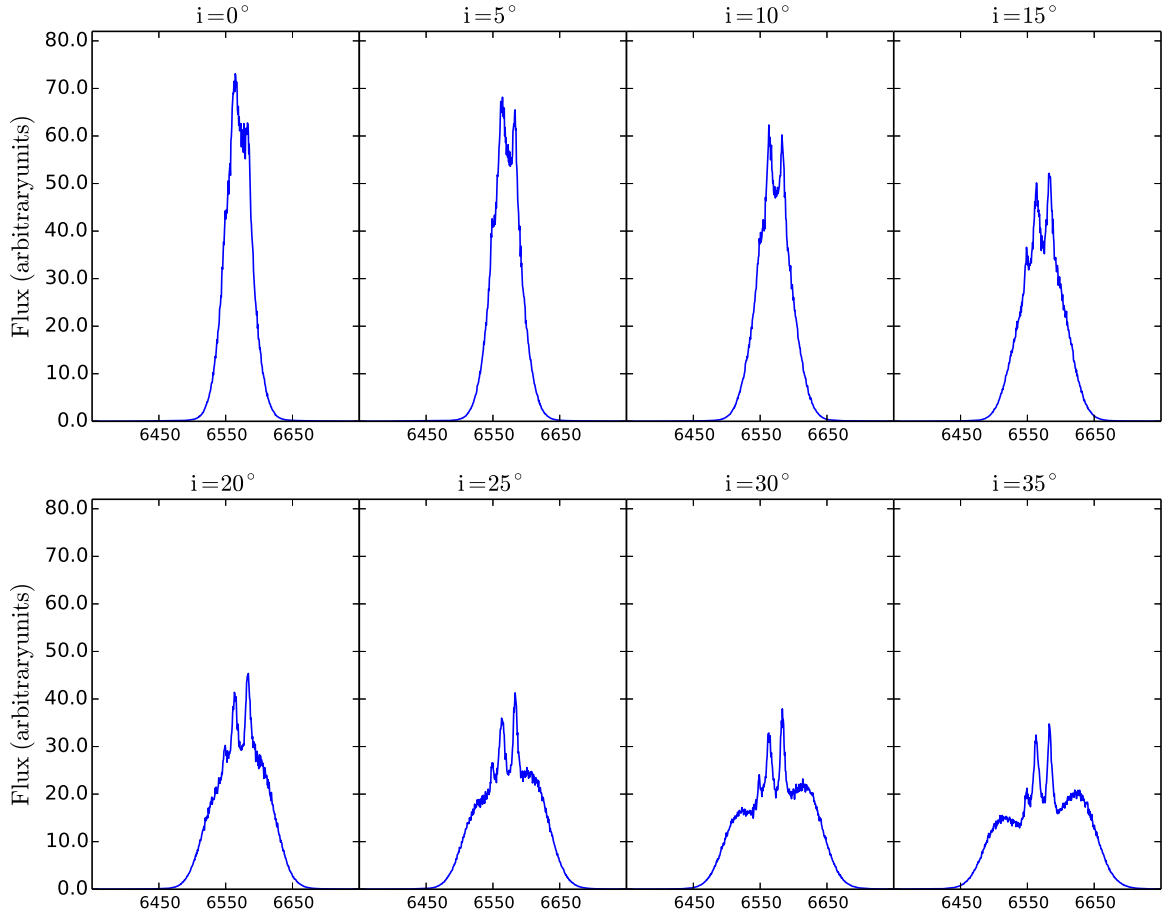

Figure 6. Disk model for the Hα profile as a function of inclination of the disk relative to the plane of the sky. Typical narrow Hα+[NII] emission-line profiles have been superimposed to the broad double-peaked profiles.

Brotherton (1996); Marziani et al. (1996) and Wanders & Peterson (1996). More recently, Pancoast et al. (2014a,b) have performed detailed dynamical modelling of the BLR of five Seyfert 1 nuclei. The main conclusion of Pancoast et al. (2014b) is that the BLR geometry is a thick disk viewed close to face-on, in agreement with our findings. They argue also for the presence of inflows that could be due to the movement of BLR clouds in elliptical orbits around the SMBH Elitzur (2014).

On the basis of this and previous studies we suggest that the disk is present in most BLRs, and at the higher Eddington rates of Seyfert 1 galaxies, we observe additional line-emitting components corresponding to more distant clouds at lower velocities. Some of these clouds may be inflowing (Grier et al. 2013a), just orbiting the SMBH in elliptical orbits as proposed by Pancoast et al. (2014b), or may be part of an outflowing disk wind (Elitzur 2014).

6.1. *Implications for the derivation of Black Hole Masses*

The technique of reverberation mapping has provided valuable tools for the estimation of the mass of SMBHs in AGN up to very large distances in the Universe, solely on the basis of the observed continuum luminosity and width of the broad emission lines. The optical luminosity allows the estimate of the BLR radius (Wandel, Peterson, & Malkan 1999; Kaspi et al. 2005; Bentz et al. 2013), while the width of the broad profile provides the velocity dispersion of the BLR clouds ΔV. Assuming that the motion of the BLR gas is dominated by gravity and that radiation pressure can be neglected, the mass of the central black hole is given by (Peterson et al. 2004):

$$M_{\rm BH} = f\frac{R_{\rm BLR}\Delta V^2}{G} \qquad (8)$$

where $R_{\rm BLR}$ is the radius of the BLR, G is the gravitational constant and f is a numerical factor that depends on the structure, kinematics and orientation of the BLR. The most recent empirical determination of the average scale factor is $\langle f\rangle = 4.31 \pm 1.05$ (Grier et al. 2013b), based on the assumption that the relationship between black hole mass and bulge velocity dispersion is the same for quiescent and active galaxies. The value of f is of fundamental importance in using Equation 8 for the determination of the masses of SMBH's across the Universe, and incorporates the uncertainties due to the geometry and inclination of the BLR.

The recognition that the disk component may be ubiquitous in Type 1 AGN has important implications for the value of f. If we consider that the geometry of the region that varies on the shortest timescale probed by the profile variation is a flat disk, $f = 1/\sin^2 i$, where i is the inclination of the disk relative to the plane of the sky, as the observed width of the lines ΔV is simply the rotational speed projected into the line-of-sight. In particular, for $\langle f\rangle = 4.3$, $\langle i\rangle = 29°$, which is practically the same as the median value that we obtain from the data in Table 2, of $i = 27° \pm 7°$.

Similar disk inclinations have also been reported from the fit of disk models to double-peaked profiles in previous studies (Chen & Halpern 1989; Eracleous & Halpern 1994, 2003).

The fact that the majority of disks are observed with inclinations between 20° and 35° is supported also by predictions of the simple model: if we consider that the maximum opening angle of the torus is $\theta_m \approx 35°$, then the fraction of Type 1 AGN observed with inclinations between 20° and 35% should be ∼80%, while only ∼20% should be observed with inclinations smaller than 20°. This seems to be the case for NGC 5273 for which we obtain $i = 17°$, and for NGC 3227, for which we fit the RMS profile and obtain an inclination of $i = 16°$. These low inclinations imply a larger f ∼12. Using this value of f in equation 8 would result in a mass for the SMBH 3 times larger than that obtained using the average f value.

6.2. *A relation between f and the FWHM of the broad lines*

According to our model, the adoption of a unique value for f is a good approximation for 80% of Type 1 AGN (even though there should be some variation between targets), but for the 20% cases of more pole-on AGNs the use of the constant f implies an underestimation of the SMBH mass.

Our model implies $f = 1/\sin^2 i$ for the disk component. The facts that: (1) the parameters of the disk, and in particular, their inner, outer and saturation radii do not vary much among different Type 1 AGN (∼30%, see Table 2); and (2) that the width (FWHM) of the line strongly depends on the inclination of the disk (see Fig. 6) implies that there should be a relation between the FWHM of the broad profiles and f.

We have used our model to obtain this relation between f and FWHM of the profiles as follows. We have fixed the disk parameter values at the average values listed in the last column of Table 2, except for the inclination i. We have called this model "average model". We have then varied the inclination i between 10° and 50°, to build a sequence of models as a function of i. For each model we measured the value of the FWHM and plotted f as a function of $FWHM$ in Fig.7 as black circles. We have then fitted the relation bewteeen these two quantities with the function:

$$f = \frac{1.76\times10^9}{(FWHM - 224)^{2.22}} \qquad (9)$$

This relation is shown as a red line in Fig. 7. We have also included in Fig. 7 the values obtained from the fit of the profiles of the 5 galaxies in Table 2, shown as blue squares. They follow the relation very well. In the right panel we have included also the result for the fit of the narrower RMS profile of NGC 3227, that suggests that the relation may flatten for lower values of FWHM. The grey band comprises the range of the model values corresponding to the root-mean-square variations of the parameter values listed in the last column of Table 2.

6.3. *Further implications for the Structure of AGN*

It has been argued that the broad double-peaked Balmer lines in LLAGN and radio galaxies originate in the outer parts of an accretion disk that is ionized by an ion torus (Chen & Halpern 1989) or other radiatively inefficient structure – e.g., RIAF or ADAF (Narayan 2005). The RIAF structure develops when the mass accretion

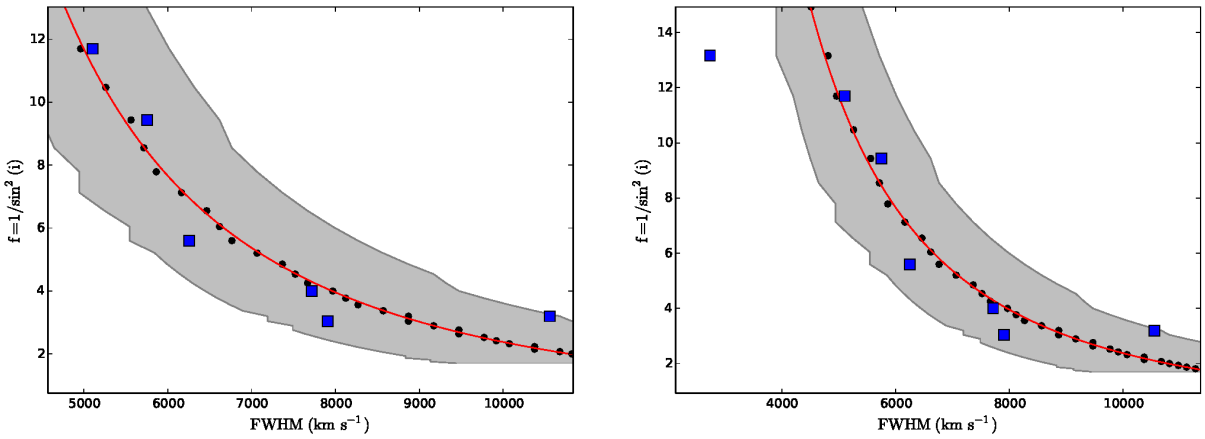

Figure 7. Left: Relation between $f = 1/\sin^2 i$ and the FWHM of the broad line according to our average model (see last column of Table 2, represented by black dots for inclinations in the range $10° \leq i \leq 50°$, and for the broad profiles of the Type 1 AGN of Table 2, represented by blue squares. The grey band shows the range of the model values corresponding to the root-mean-square variations of the parameter values listed in the last column of Table 2. The red line is a fit of the relation implied by the models. Right: same as in the top panel now including the result from the fit of the narrower *RMS* profile of NGC 3227.

rate to the SMBH drops below some minimum fraction of the Eddington rate, of order $\sim 1\%$, which is the case of LLAGN.

LLAGN and Seyfert 1 nuclei have been compared to the two states observed in X-ray binaries (Remillard & McClintock 2006; Narayan & McClintock 2008): the low-luminosity hard state and the more luminous soft state (or thermal state), respectively. The thermal state is the one dominated by the geometrically thin, optically thick disk, analogous to more lumious AGNs (Seyfert galaxies and quasars) where the UV/optical emission is dominated by the "big blue bump" (BBB) from the accretion disk. The low-luminosity hard state is characterized by a harder X-ray spectrum and much lower thermal emission from the thin disk, and this is consistent with the spectral energy distribution (SED) of LLAGN, which lacks the BBB component.

The fact that the double-peaked profiles are observed both in LLAGN and in Seyfert 1 galaxies suggest that the inner structure of the low-luminosity and high-luminosity AGN are not very different. The disk component, that is closer to the ionizing source, is always present. In LLAGN, the disk emission is the only component seen, while in more luminous Type 1 sources, such as Seyfert 1 nuclei and quasars, additional broad-line component that, since the velocity dispersion is smaller, probably originates in more distant clouds than the gas that produces the disk component.

The observation of the more distant clouds leading to the aditional broad component can be understood as due to the higher luminosity of the source, that reaches farther from the nucleus and also to the fact that, at higher accretion rates there should be more gas clouds in the vicinity of the nucleus, either inflowing or originated from an accretion disk wind that gets enhanced with increased accretion rates.

7. CONCLUSIONS

We have used previously published results as well as fits of broad Hα profiles in the spectra of nearby active Type 1 nuclei from the Palomar Survey of Nearby Galaxies to argue that disk-like emission-line profiles double-peaked profiles originating in the outer parts of an accretion disk, at ~ 1000 Schwarzdchild radia are ubiquitous in the BLR of these objects.

We have shown that while "pure" disk profiles are seen mostly in LLAGN nuclei, in Seyfert 1 galaxies the profiles usually present an additional narrower component (FWHM ~ 1000 $3000\,\mathrm{km\,s^{-1}}$) well fitted with a Gaussian function. We attribute this component to more distant BLR gas moving at lower velocities. Our results support previous studies that argue that, while for LLAGN the accretion rate is low and most accreting gas is confined to the disk, for the higher accretion rates that occur in Seyfert galaxies, one can also observe lower velocity ionized gas that is orbiting the SMBH, is in inflow towards the disk or being ejected in a wind from the disk.

The disk component being closer to the ionizing source should be the most variable part of the profile, and indeed many reverberation mapping studies show that the *RMS* spectrum reveals a double-peaked profile.

While previous studies have already argued that the BLR is dominated by a flattened component, our study via the fit of such component to the BLR profiles have allowed us to obtain the parameters of the disk, such as the inner and outer radii and the maximum emission radius. We have found that these parameters do not vary by more than 30% among the different sources, what leads to the conclusion that the main parameter that regulates the width of the double-peaked profile is the inclination of the disk relative to the plane of the sky.

If we can now assume that the geometry of the main component of the BLR is a flat disk with similar properties, the factor f in the formula used to calculate the SMBH mass $M_{\rm BH} = f\left(R_{\rm BLR}\Delta V^2/G\right)$ should be $f = 1/\sin^2 i$. The median inclination of the sources fitted with the disk model in our study, $i = 27°$, corresponds to $f = 4.5$, very close to the most recent value of $\langle f \rangle = 4.3 \pm 1.05$ (Grier et al. 2013b), obtained in a completely independent way.

Having concluded that the main paramenter regulat-

ing the width of the BLR profiles is the inclination of the disk, our study has further allowed us to propose a relation (equation 9) between the value of f and the FWHM of the broad profiles that could lead to an improvement in the determination of SMBH masses.

REFERENCES

Abazajian, K. et al. 2003, AJ, 126, 2081
Antonucci, R. 1992, ARAA, 31, 473
Barth, A. et al. 2001, ApJ, 546, 205
Bentz M. C., Denney K. D., Cackett E. M., et al., 2006, ApJ, 651, 775
Bentz M. C., Denney K. D., Cackett E. M., et al., 2007, ApJ, 662, 205
Bentz M. C., Denney K. D., Grier, C.J., et al., 2013, ApJ, 767, 149
Bentz M. C., Walsh J. L., Barth A. J., et al., 2009, ApJ, 705, 199
Bentz M. C., Walsh J. L., Barth A. J., et al., 2010, ApJ, 716, 993
Bon E., Popović L. C.., avrilović N., Mura G. L., Mediavilla E., 2009, MNRAS, 400, 924
Bower, G. A., Wilson, A. S. Heckman, T. M.& Richstone, D. O. 1996, AJ, 111, 1901
Brotherton M. S., 1996, ApJS, 102, 1
Chen K., Halpern J. P., Filippenko A. V., 1989, ApJ, 339, 742
Chen K., & Halpern J. P., 1989, ApJ, 344, 115
Denney K. D., Peterson B. M., Pogge R. W., et al., 2010, ApJ, 721, 715
Denney K. D., Assef R. J., Horne K., Peterson B. M., Vestergaard M., 2012, ASPC, 460, 103
Dietrich M., Peterson B. M., Albrecht, P., et al., 1998, ApJS, 115, 185
Dietrich M., Peterson B. M., Grier C. J., et al., 2012, ApJ, 757, 53
Doroshenko V. T., Sergeev S. G., Klimanov S. A., Pronik V. I., Efimov Y. S., 2012, MNRAS, 426, 416
Dumont A. M., & Collin-Souffrin S., 1990, A&A, 229, 313
Elitzur, M. 2012, ApJ, 744:L33
Elitzur, M. et al. 2014, MNRAS, 438, 3340
Eracleous M. & Halpern J. P., 1994 ApJS, 90, 1
Eracleous M., Halpern J. P., 2001, ApJ, 554, 240
Eracleous M., Halpern J. P., 2003, ApJ, 599, 886
Filippenko A. V., Halpern J. P., 1984, ApJ, 285, 458
Filippenko A. V., & Sargent, W.L.W. 1985, ApJS 57, 503
Gaskell, C.M. 1983, ub *Quasars and Gravitational Lenses*, Proc. 24th Liège Int. Ap. Coll. (Liège: Institut d'Astrophysique, Université Liège), p. 473
Gezari S., Halpern J. P., Eracleous M., 2007, ApJS, 169, 167
Gilbert, A. M., Eracleous, M., Filippenko, A. V., & Halpern, J. P. 1999, in ASP Conf. Ser. 175, eds. C. M. Gaskell, W. N. Brandt, M. Dietrich, D. Dultzin-Hacyan & M. Eracleous (San Francisco: ASP), 189
Goad, M., & Wanders, I. 1996, ApJ, 469, 113
Grier C. J., Peterson B. M., Pogge R. W., et al., 2012, ApJ, 755, 60
Grier C. J., Peterson B. M., Pogge R. W., et al., 2012, ApJ, 744, L4
Grier C. J., Peterson B. M.,Horne, K. et al., 2013, ApJ, 764, 47
Grier, C.J., Martini, P., Watson, L.C., Peterson, B.M., Bentz, M.C., Dasyra, K.M., Dietrich, M., Ferrarese, L., Pogge, R.W. & Zu, Y. 2013, ApJ, 773, 90
Halpern J. P., Eracleous M., 1994, ApJ, 433, L17
Ho, L.C., Filippenko, A.V. & Sargent, W.L.W. 1995, ApJS, 98, 477
Ho L. C., Filippenko A. V., and Sargent W. L. W., 1997, ApJS, 112, 315
Ho, L. C., Filippenko, A. V., Sargent, W. L. W. , and Peng, C. Y. 1997, ApJS, 112, 391
Ho, L. C., Rudnick, G., Rix, H. W., Shields, J. C., McIntosh, D. H., Filippenko, A. V.;,Sargent, W. L. W., Eracleous, M. 2000, ApJ, 541, 120
Ho, L. C. 2008, ARA&A, 46, 475
Ichikawa, K., et al. 2015, arXiv:1501.06584
Jackson N., Browne I. W. A., 1991, MNRAS, 250, 422
Kaspi, S. et al. 1996, ApJ, 470, 336
Kaspi, S., Maoz, D., Netzer, H., Peterson, B. M., Vestergaard, M., Jannuzi, B. T. 2005 ApJ, 629, 61
Kuehn C. A., Baldwin J. A., Peterson B. M., Korista K. T., 2008, ApJ, 673, 69
Jovanovic, P., Popovic, L.C., Stalevski, M., & Shapovalova, A.I. 2010 ApJ, 718, 168
La Mura, et al. 2009, ApJ, 693, 1437
Lewis K. T., Eracleous M., & Storchi-Bergmann T., 2010, ApJS, 187, 416
Maoz D., Netzer H., Mazeh T., et al., 1991, ApJ, 367, 493
Marziani P., Sulentic J. W., Dultzin-Hacyan D., Calvani M., Moles M., 1996, ApJS, 104, 37
Narayan, R. 2005, Ap&SS, 300, 177
Narayan, R. & McClintock, J. E, 2008 NewAR, 51, 733
Netzer H., Maoz D., Laor A., et al., 1990, ApJ, 353, 108
Pancoast A., Brewer B. J., Treu T., et al., 2014, MNRAS, 445, 3055
Pancoast A., Brewer B. J., Treu T., et al., 2014, MNRAS, 445, 3073
Pâris, I. et al. 2014, A&A, 563, A54
Peterson, B.M., Korista, K.T., & Cota, S.A. 1987, ApJ, 312, L1
Peterson B. M., Barth A. J., Berlind P., et al., 1999, ApJ, 510, 659
Peterson B. M., Berlind P., Bertram R., et al., 2002, ApJ, 581, 197
Peterson B. M., Ferrarese, K., Gilbert, K.M.., et al., 2004, ApJ, 613, 682
Popović L. Č., Mediavilla E., Bon E., Ilić D., 2004,
Popovic, L.C., Shapovalova, A.I., Illić, D., et al., 2011, A&A, 528, 130
Remillard, R. A. & McClintock, J. E. 2006, ARA&A, 44, 49
Schimoia J. S., Storchi-Bergmann T., Nemmen R. S., Winge C., Eracleous M., 2012, ApJ, 748, 145
Schimoia J. S., Storchi-Bergmann T., Grupe, D., Eracleous, M., Peterson, B.M., Baldwin, J.A., Nemmen R. S. & Winge C., 2014, ApJ, in press.
Sergeev S. G., Pronik V. I., Sergeeva E. A., 2000, A&A, 356, 41
Sergeev, S.G., Pronik, V.I., Peterson, B.M., Sergeeva, E.A., & Zheng, W. 2002, ApJ, 576, 660
Sergeev, S.G., Doroshenko, V.T., Dzyuba, S.A., Peterson, B.M., Pogge, R.W., & Pronik, V.I. 2007, ApJ, 668, 708
Sergeev, S.G., Klimanov, S.A., Doroshenko, V.T., et al. 2011, MNRAS, 410, 1877
Shappee, B. J. et al. 2014, ApJ, 788, 48
Shapovalova A. I., Popović L. Č., Burenkov A. N., et al., 2010, A&A, 517, A42
Shapovalova A. I., Popović L. Č., Burenkov A. N., et al., 2013, A&A, 559, A10
Shields, J. C. et al. 2000, ApJ, 534, L27
Stirpe, G. et al. 1994, ApJ, 425, 609
Storchi-Bergmann T., Nemmen da Silva R., & Eracleous M., et al., 2003, ApJ, 598, 956
Storchi-Bergmann T., Baldwin J. A., & Wilson A. S., 1993, ApJ, 410, L11
Strateva, I. et al. 2003,, AJ, 126, 1720
Veilleux S., Zheng W., 1991, ApJ, 377, 89
Wandel, A., Peterson B. M., & Malkan, M.A. 1999, ApJ, 526, 579 ApJ, 466, 174
Wanders, I., et al. 1995, ApJ, 453, L87
Wanders, I. & Peterson B. M. 1996, ApJ, 466, 174
Wills B. J., Browne I. W. A., 1986, ApJ, 302, 56
Winge C., Peterson B. M., Pastoriza M. G., Storchi-Bergmann T., 1996, ApJ, 469, 648
Winge C., Peterson B. M., Horne, K., Pogge, R. W., Pastoriza M. G., Storchi-Bergmann T., 1995, ApJ, 445, 680

Capítulo 7

Conclusões

7.1 Conclusões sobre os monitoramentos e estudo de variabilidade

Neste trabalho pudemos monitorar com espectroscopia óptica a emisssão larga em duplo-pico de Hα dos AGN's de duas galáxias Seyfert 1/LINER: NGC 1097 e NGC 7213.

No caso de NGC 1097 o perfil foi monitorado com os telescópios SOAR (4m) e Gemini-Sul (8m) entre Agosto de 2012 e Janeiro de 2013. Obtivemos 22 observações com o telescópio SOAR e uma única observação com o telescópio Gemini-Sul. O intervalo mínimo entre duas observações consecutivas foi $\sim$ 1 dia, o máximo $\sim$20 dias e o médio $\sim$7.5 dias.

No caso de NGC 7213, o perfil foi monitorado com o Telescópio Gemini Sul. Juntamente com uma observação anterior de Schnorr-Müller et al. (2014a) foram obtidos 13 espectros ao longo de quase dois anos, entre setembro de 2011 e julho de 2013, com observações espaçadas irregularmente por intervalos de tempo variando de uma semana a vários meses.

7.1.1 Monitoramento espectroscópico óptico de NGC 1097 e NGC 7213

- Conseguimos reproduzir os perfis em duplo-pico, para ambas as galáxias, como sendo originários da emissão do gás em um disco de acreção Kepleriano e relativístico orbitando seus SMBH's centrais, cuja lei de emissividade superficial possui um braço espiral e um raio de máxima emissividade (*Saturated Spiral Model,* Schimoia et al., 2012). Os raios interno (ξ_1) e externo (ξ_2) e o ângulo de inclinação (i) dos discos modelados são: NGC 1097 – $\xi_1 = 450$, $\xi_2 = 1600$ e $i = 34°$; NGC 7213 – $\xi_1 = 300$, $\xi_2 = 3000$ e $i = 47°$, sendo que para a NGC 7213 apresentamos pela primeira vez um modelo para a emissão em duplo-pico.

- Em ambas as galáxias, a menor escala de tempo de variabilidade do perfil de duplo pico em Hα corresponde a variações do seu fluxo integrado. Para a NGC 1097 este fluxo variou na escala de tempo mais curta amostrada pelas observações ópticas, $\sim$ 5, dias. A máxima variação observada foi de 90%, mas a média das variações durante todo o período foi de 20%. No caso de NGC 7213 pudemos obter apenas limites inferior e superior para a escala de tempo de variabilidade do fluxo integrado da linha, de 7 e 28 dias, respectivamente, sendo a primeira vez que se identifica o perfil em duplo-pico deste AGN como variável.

  Para ambas as galáxias os limites encontrados para esta escala de variabilidade mais curta são consistentes com as escalas de tempo de viagem da luz entre a fonte ionizante central e a parte emissora da linha no disco – o que sugere que essas variações sejam devidas a variações do fluxo ionizante da fonte central.

- Identificamos em ambos os perfis uma outra escala de tempo de variabillidade, mais longa, associada a variações na intensidade relativa dos lados azul e vermelho no perfil. No caso de NGC 1097 essa escala é da ordem de ≈ 5 meses , obtid através das medidas da intensidade relativa dos picos azul e vermelho, F_B/F_R (Schimoia et al., 2012), bem marcados nesta galáxia; em NGC 7213 medimos a intensidade relativa dos fluxos integrados dos lados azul e vermelho do perfil, F_{Red}/F_{blue}, pois nesta galáxias os picos são difíceis de serem medidos, e estimamos que a escala de tempo de variabilidade é de ≈ 3 meses. Para as duas galáxias essas escalas de tempo de variabilidade são compatíveis com as escalas de tempo dinâmicas de seus respectivos discos de acreção. Modelamos em ambos os casos as variações nas intensidades relativas dos lados azul e vermelho dos perfis como devido a rotação de um braço espiral com contraste variável em relação ao disco subjacente. Para a NGC 1097 o braço espiral mostrou-se importante durante todo o monitoramento – as assimetrias do perfil estavam presentes mesmo quando o fluxo integrado do perfil era baixo. Para a NGC 7213 as variações nas assimetrias do perfil diminuíram ao longo do monitoramento, o que foi modelado com a diminuição do contraste do braço espiral em relação ao disco de acreção. O período de rotação do braço espiral é muito semelhante nos dois objetos: ~ 18 meses para NGC 1097 e 21 meses para NGC 7213.

Conclusões específicas: NGC 1097

- O pequeno intervalo de variações na largura do perfil em duplo-pico foi reproduzido mantendo os valores ξ_q (raio de máxima emissividade) próximo ao raio interno. Este raio corresponde a um período de rotação de 18 meses e um tempo de vigem da luz de $\sim$4 dias, o que está em concordância com a escala de tempo de variabilidade mais curta observada.

- No caso de NGC 1097 embora não se tenha encontrado uma sinal claro de reverberação nos dados mais recentes, quando consideramos estes dados juntamente com os de trabalhos anteriores, de épocas entre 1991 – 2001 e 2010 – 2012, eles são consistentes com o cenário de reverberação, uma vez que ainda consegue-se observar, no conjunto total dos dados, uma correlação inversa entre o fluxo de Hα e a separação entre os picos azul e vermelho do perfil de Hα, como notado em estudos anteriores, pois este resultado implica em que quanto mais intensa a radiação mais estreito é o perfil, já que a radiação ioniza regiões mais distantes do disco (onde a velocidade orbital é menor).

Conclusões específicas: NGC 7213

- Quando comparamos os espectros médio, de *rms* e mínimo calculados com as observações e os modelos, a maioria das características são bem reproduzidas. A única discrepância é a região central do espectro de *rms* que indica uma variação maior do que predita pelo modelo.

Argumentamos que isso pode ser causado por uma região de gás cuja emissão também é variável e se origina em regiões mais afastadas da fonte ionizante;

- Usando o ajuste das absorções estelares com o código `Starlight-v04` nós obtivemos a dispersão de velocidades do bojo, $\sigma_\star = 188\,\mathrm{km\,s^{-1}}$, o que implica uma massa para o SMBH de $M_\bullet = 1.27 \times 10^8 \mathrm{M}_\odot$ através da relação $M_\bullet - \sigma_\star$, que está de acordo com determinações anteriores;

- Também estimamos a massa do SMBH adotando como uma velocidade representativa do gás no disco a metade da velocidade de separação entre os picos azul e vermelho e a distância correspondente como sendo os limites que obtivemos para a escala de tempo de viagem da luz entre o SMBH e o disco, obtendo $5 \times 10^7 < M_\bullet < 2 \times 10^8\,\mathrm{M}_\odot$.

Em resumo, o cenário que propomos para explicar as variabilidades do perfil em duplo-pico observadas nos AGN's de NGC 1097 e NGC 7213 é o seguinte: ambas as emissões são provenientes do gás em discos de acreção Keplerianos e relativisticos inclinados em relação ao plano do céu. Em NGC 1097 a região emissora está entre 450 e 1600 raios gravitacionais e o disco está inclinado em 34 graus em relação ao plano do céu, enquanto que em NGC 7213 a região emissora está entre 300 e 3000 raios gravitacionais e o disco está inclinado por 47 graus. Em ambos os casos, a variabilidade relativa das características dos lados azul e vermelho dos perfis são explicadas como sendo devidas à rotação de um braço espiral com contraste variável em relação ao disco subjacente.

Em termos de escalas de variabilidade e distância ao SMBH, ambos os objetos mostraram escalas de variabilidade e distância muito semelhantes aquelas observadas em BLR de galáxias Seyfert 1, o que revela que as dimensões da parte emissora de linhas do disco de acreção e da BLR são semelhante, o que sugere que sejam a mesma estrutura.

7.1.2 Monitoramento em raios-X e UV de NGC 1097

Além dos dados de espectroscopia óptica obtidos com os telescópios SOAR e Gemini-Sul entre Agosto de 2012 e Fevereiro de 2013, o AGN de NGC 1097 foi monitorado simultaneamente com o satélite *swift* em duas bandas espectrais de mais alta energia: em raios-X (0.3 – 10 keV), utilizando o telescópio espacial *Swift*/XRT, no UV (banda centrada em 2246 Å) usando o telescópio *Swift*/UVOT. Os principais resultados da análise conjuta dos dados óptico, raios-X e UV para NGC1097 estão listados a seguir:

- O fluxo em raios-X apresentou variações na escala de tempo mais curta amostrada pelas observações, 4 dias, o que indica que a estrutura emissora possui um tamanho menor do que 4 dias-luz; a máxima variação no fluxo observada entre duas observações consecutivas foi de 97%, mas a média das variaçõess ao longo de todo o período foi de 13%;

- Considerando as incertezas das medidas, o fluxo UV não apresentou variações significativas. Isto pode ser devido ao *starburst* compacto presente no núcleo, encontrado dentro dos 9 pc centrais, que domina a emissão do contínuo UV, e provavelmente dilui a contribuição da fonte variável.

- Encontramos apenas uma correlação marginal entre os fluxos em raios-X e de Hα, embora a nossa análise sugira a necessidade de um monitoramento mais frequente deste AGN, principalmente quando está em um estado de baixa luminosidade. Mas como as escalas de variabilidade são semelhantes, não podemos descartar a possibilidade de que as variações no perfil de Haα sejam devidas à variabilidade em raios-X, tendo em vista também o fato de que durante todo o monitoramento o fluxo na linha permaneceu muito baixo, dificultando a deteção de sinais de reverberação.

7.2 Galáxias Seyfert 1 emissoras de duplo-pico

Utilizamos resultados publicados na literatura assim como ajustes da linha larga de Hα de espectros nucleares de galáxias ativas próximas de Tipo 1 do Palomar Survey of Nearby Galaxies para argumentar que na maioria destas galáxias a BLR apresenta uma componente de duplo pico originária das partes externas de discos de acreção a cerca de 1000 raios gravitacionais do SMBH.

Mostramos que enquanto perfis de disco "puros" são vistos principalmente em nucleos ativos tipo LINER, nas galáxias Seyfert 1 os perfis geralmente apresentam uma componente adicional mais estreita (FWHM $\sim$ 1000 – 3000 $\mathrm{km\,s^{-1}}$) que é bem ajustada por uma função Gaussiana. Nós atribuímos esta componente a gás mais distante na BLR se movendo a mais baixa velocidade. Nossos resultados corroboram resultados de estudos anteriores que argumentam que, enquanto para os LINER's a taxa de acreção de gás ao SMBH é baixa e a maior parte do gás acretado está confinado ao disco, para taxas de acreção mais altas, que ocorrem em galáxias tipo Seyfert, pode-se também observar gás ionizado a mais baixa velocidade provenientes de regiões mais distantes do SMBH, em nuvens de gás que podem estar orbitando o SMBH, caindo em direção ao disco ou mesmo sendo ejetadas num vento emanado do disco.

A componente disco – que está mais próxima da fonte ionizante central – deve ser a parte mais variável do perfil, e de fato muitos estudos de reverberação entre contínuo e linhas da BLR mostram que o espectro de *rms* tem um perfil de duplo-pico. Enquanto estudos anteriores já argumentaram que a BLR tem uma forma achatada, nosso estudo – através do ajuste de tal componente aos perfis da BLR – permitiu obter os parâmetros do disco, tais como o raio interno, o raio externo e o raio de máxima emissvidade. Encontramos que estes parâmetros não variam por mais de 30% entre as

diferentes fontes, o que leva a conclusão que o principal parâmetro que regula a largura do perfil em duplo-pico é a inclinação do disco com relação ao plano do céu.

Se agora nós assumimos que a geometria da componente principal da BLR é um disco de gás com propriedades similares, o fator f na equação utilizada para calcular a massa do SMBH em galáxias ativas, $M_\bullet = f \times \frac{R_{BLR}\Delta V^2}{G}$ deve ser $f = \frac{1}{sin^2(i)}$. A inclinação média dos objetos ajustados neste estudo é $i = 27°$, o que resulta em $f = 4.5$, muito próximo do valor mais atual de $< f >= 4.3 \pm 1.05$ (Grier et al., 2013), obtido de uma maneira completamente independente.

Tendo concluído que o principal parâmetro que regula a largura dos perfis de emissão da BLR é o ângulo de inclinação do disco, nosso estudo nos permitiu propor uma relação entre o fator f e a FWHM dos perfis largos. Assim, ao invés de adotar um único f, pode-se derivar seu valor para cada galáxia, o que deve diminuir a incerteza na determinação da massa do SMBH em galáxias ativas e consequentemente diminuir o espalhamento na relação $M_\bullet - \sigma_\star$.

Apêndice A: publicações em outras colaborações

SPACE TELESCOPE AND OPTICAL REVERBERATION MAPPING PROJECT. I. ULTRAVIOLET OBSERVATIONS OF THE SEYFERT 1 GALAXY NGC 5548 WITH THE COSMIC ORIGINS SPECTROGRAPH ON HUBBLE SPACE TELESCOPE

The Astrophysical Journal, 806:128 (15pp), 2015 June 10 doi:10.1088/0004-637X/806/1/128

SPACE TELESCOPE AND OPTICAL REVERBERATION MAPPING PROJECT. I. ULTRAVIOLET OBSERVATIONS OF THE SEYFERT 1 GALAXY NGC 5548 WITH THE COSMIC ORIGINS SPECTROGRAPH ON *HUBBLE SPACE TELESCOPE*

G. De Rosa[1,2,3], B. M. Peterson[1,2], J. Ely[3], G. A. Kriss[3,4], D. M. Crenshaw[5], Keith Horne[6], K. T. Korista[7], H. Netzer[8], R. W. Pogge[1,2], P. Arévalo[9], A. J. Barth[10], M. C. Bentz[5], W. N. Brandt[11], A. A. Breeveld[12], B. J. Brewer[13], E. Dalla Bontà[14,15], A. De Lorenzo-Cáceres[6], K. D. Denney[1,2,40], M. Dietrich[16,17], R. Edelson[18], P. A. Evans[19], M. M. Fausnaugh[1], N. Gehrels[20], J. M. Gelbord[21,22], M. R. Goad[19], C. J. Grier[1,11], D. Grupe[23], P. B. Hall[24], J. Kaastra[25,26,27], B. C. Kelly[28], J. A. Kennea[11], C. S. Kochanek[1,2], P. Lira[29], S. Mathur[1,2], I. M. McHardy[30], J. A. Nousek[11], A. Pancoast[28], I. Papadakis[31,32], L. Pei[10], J. S. Schimoia[1,33], M. Siegel[11], D. Starkey[6], T. Treu[28,34,41], P. Uttley[35], S. Vaughan[20], M. Vestergaard[36,37], C. Villforth[6], H. Yan[38], S. Young[18], and Y. Zu[1,39]
[1] Department of Astronomy, The Ohio State University, 140 W 18th Avenue, Columbus, OH 43210, USA
[2] Center for Cosmology and AstroParticle Physics, The Ohio State University, 191 West Woodruff Avenue, Columbus, OH 43210, USA
[3] Space Telescope Science Institute, 3700 San Martin Drive, Baltimore, MD 21218, USA
[4] Department of Physics and Astronomy, The Johns Hopkins University, Baltimore, MD 21218, USA
[5] Department of Physics and Astronomy, Georgia State University, 25 Park Place, Suite 605, Atlanta, GA 30303, USA
[6] SUPA Physics and Astronomy, University of St. Andrews, Fife, KY16 9SS Scotland, UK
[7] Department of Physics, Western Michigan University, 1120 Everett Tower, Kalamazoo, MI 49008-5252, USA
[8] School of Physics and Astronomy, Raymond and Beverly Sackler Faculty of Exact Sciences, Tel Aviv University, Tel Aviv 69978, Israel
[9] Instituto de Física y Astronomía, Facultad de Ciencias, Universidad de Valparaíso, Gran Bretana N 1111, Playa Ancha, Valparaíso, Chile
[10] Department of Physics and Astronomy, 4129 Frederick Reines Hall, University of California, Irvine, CA 92697, USA
[11] Department of Astronomy and Astrophysics, Eberly College of Science, Penn State University, 525 Davey Laboratory, University Park, PA 16802, USA
[12] Mullard Space Science Laboratory, University College London, Holmbury St. Mary, Dorking, Surrey RH5 6NT, UK
[13] Department of Statistics, The University of Auckland, Private Bag 92019, Auckland 1142, New Zealand
[14] Dipartimento di Fisica e Astronomia "G. Galilei," Università di Padova, Vicolo dell'Osservatorio 3, I-35122 Padova, Italy
[15] INAF-Osservatorio Astronomico di Padova, Vicolo dell'Osservatorio 5 I-35122, Padova, Italy
[16] Department of Physics and Astronomy, Ohio University, Athens, OH 45701, USA
[17] Department of Earth, Environment, and Physics, Worcester State University, 486 Chandler Street, Worcester, MA 01602, USA
[18] Department of Astronomy, University of Maryland, College Park, MD 20742-2421, USA
[19] University of Leicester, Department of Physics and Astronomy, Leicester, LE1 7RH, UK
[20] Astrophysics Science Division, NASA Goddard Space Flight Center, Greenbelt, MD 20771, USA
[21] Spectral Sciences Inc., 4 Fourth Avenue, Burlington, MA 01803, USA
[22] Eureka Scientific Inc., 2452 Delmer St. Suite 100, Oakland, CA 94602, USA
[23] Space Science Center, Morehead State University, 235 Martindale Drive, Morehead, KY 40351, USA
[24] Department of Physics and Astronomy, York University, Toronto, ON M3J 1P3, Canada
[25] SRON Netherlands Institute for Space Research, Sorbonnelaan 2, 3584 CA Utrecht, The Netherlands
[26] Department of Physics and Astronomy, Univeristeit Utrecht, P.O. Box 80000, 3508 Utrecht, The Netherlands
[27] Leiden Observatory, Leiden University, P.O. Box 9513, 2300 RA Leiden, The Netherlands
[28] Department of Physics, University of California, Santa Barbara, CA 93106, USA
[29] Departamento de Astronomia, Universidad de Chile, Camino del Observatorio 1515, Santiago, Chile
[30] University of Southampton, Highfield, Southampton, SO17 1BJ, UK
[31] Department of Physics and Institute of Theoretical and Computational Physics, University of Crete, GR-71003 Heraklion, Greece
[32] IESL, Foundation for Research and Technology, GR-71110 Heraklion, Greece
[33] Instituto de Física, Universidade Federal do Rio do Sul, Campus do Vale, Porto Alegre, Brazil
[34] Department of Physics and Astronomy, University of California, Los Angeles, CA 90095-1547, USA
[35] Astronomical Institute "Anton Pannekoek,"University of Amsterdam, Postbus 94249, NL-1090 GE Amsterdam, The Netherlands
[36] Dark Cosmology Centre, Niels Bohr Institute, University of Copenhagen, Juliane Maries Vej 30, DK-2100 Copenhagen, Denmark
[37] Steward Observatory, University of Arizona, 933 North Cherry Avenue, Tucson, AZ 85721, USA
[38] Department of Physics and Astronomy, University of Missouri, Columbia, MO 65211, USA
[39] Department of Physics, Carnegie Mellon University, 5000 Forbes Avenue, Pittsburgh, PA 15213, USA
Received 2015 January 23; accepted 2015 April 24; published 2015 June 12

ABSTRACT

We describe the first results from a six-month long reverberation-mapping experiment in the ultraviolet based on 171 observations of the Seyfert 1 galaxy NGC 5548 with the Cosmic Origins Spectrograph on the *Hubble Space Telescope*. Significant correlated variability is found in the continuum and broad emission lines, with amplitudes ranging from ∼30% to a factor of two in the emission lines and a factor of three in the continuum. The variations of all the strong emission lines lag behind those of the continuum, with He II λ1640 lagging behind the continuum by ∼2.5 days and Lyα λ1215, C IV λ1550, and Si IV λ1400 lagging by ∼5–6 days. The relationship between the continuum and emission lines is complex. In particular, during the second half of the campaign, all emission-line lags increased by a factor of 1.3–2 and differences appear in the detailed structure of the continuum and emission-line light curves. Velocity-resolved cross-correlation analysis shows coherent structure in lag versus line of sight velocity for the emission lines; the high-velocity wings of C IV respond to continuum variations more rapidly than the line core, probably indicating higher velocity broad-line region clouds at smaller distances from the central

[40] NSF Postdoctoral Research Fellow.
[41] Packard Fellow.

engine. The velocity-dependent response of Lyα, however, is more complex and will require further analysis.

Key words: galaxies: active – galaxies: individual (NGC 5548) – galaxies: nuclei – galaxies: Seyfert

Supporting material: machine-readable table

1. INTRODUCTION

1.1. The Broad-line Region (BLR)

One of the most prominent characteristics of the ultraviolet (UV), optical, and near-infrared (NIR) spectra of active galactic nuclei (AGNs) is the presence of broad emission lines. While we know that these features arise on scales not much larger than the accretion disk, their physical nature remains one of the major unsolved mysteries in AGN astrophysics. A particularly important feature of the broad emission lines is that they are, by definition, resolved in line of sight (LOS) velocity, and their large widths leave little doubt that the primary broadening mechanism is differential Doppler shifts due to the motion of individual gas clouds, filaments, or more-or-less continuous flows around the central black hole.

However, it is not possible to establish the BLR kinematics simply by inverting the line profiles because this inverse problem is degenerate, with a wide variety of simple velocity models providing satisfactory fits (e.g., Capriotti et al. 1980). The existing evidence on the BLR kinematics is ambiguous: some of this gas may flow inward, helping to feed the central black hole. Extended, flattened, rotating disk-like structures seem to be important in at least some BLRs, as shown statistically for radio-loud AGNs (Wills & Browne 1986; Vestergaard et al. 2000; Jarvis & McLure 2006), by the pronounced double-peaked profiles observed in some sources (e.g., Eracleous & Halpern 1994, 2003; Strateva et al. 2003; Gezari et al. 2007; Lewis et al. 2010), and from spectropolarimetry (Smith et al. 2004; Young et al. 2007). There is evidence of the importance of the black hole gravity in dominating the motion of the BLR gas (Peterson et al. 2004), although radiation pressure may also play a role (Marconi et al. 2008; Netzer & Marziani 2010).

On the other hand, developments over the last two decades re-open the interesting possibility that much of the emitting BLR gas is due to outflowing winds (e.g., Bottorff et al. 1997; Murray & Chiang 1997; Proga et al. 2000; Everett 2003; Elvis 2004; Young et al. 2007), perhaps connected to the outflows detected in absorption features (e.g., Hamann & Sabra 2004; Krongold et al. 2005, 2007; Kriss et al. 2011; Kaastra et al. 2014; Scott et al. 2014), whose kinematics and energetics are also poorly understood. The unknown dynamics of the BLR gas represents a serious gap in our understanding of AGNs and in the calibrations needed for the study of black hole/host-galaxy co-evolution up to very high redshifts.

There have been many attempts to model the physics of the BLR. In general, photoionization equilibrium models can reproduce the line intensities, but self-consistent models that provide simultaneous solutions to the line intensities, profiles, and variability are lacking. The locally optimally emitting cloud model (Baldwin et al. 1995; Korista & Goad 2000) and the stratified cloud model (Kaspi & Netzer 1999) explain most observed line intensities and some of the observed time lags between the continuum and emission lines. However, they lack the important kinematic ingredients required to explain the observed line profiles.

1.2. Reverberation Mapping (RM)

In order to understand the structure and kinematics of the BLR, we must break the degeneracy that comes from the study of the line profiles alone. We can do this by using RM to determine how gas at various LOS velocities responds to continuum variations as a function of light travel-time delay (Blandford & McKee 1982; Peterson 1993, 2014).

Over the last quarter century, the RM technique has become a standard tool for investigating the BLR. In its simplest form, RM is used to determine the mean time delay between continuum and emission-line variations, typically by cross-correlation of the respective light curves. It is assumed that this represents the mean light-travel time across the BLR. By combining this with the emission-line width, which is assumed to reflect the velocity dispersion of gas whose motions are dominated by the mass of the central black hole, the black hole mass can be estimated. RM in this form has been used to measure the black hole masses in over 50 AGNs (for a recent compilation, see Bentz & Katz 2015) to a typical accuracy of $\sim$0.3 dex. Important findings that have arisen from these RM studies include the following:

1. In a given AGN, emission lines that are characteristic of higher-ionization gas respond more rapidly to continuum flux variations than those characteristic of lower-ionization gas, indicating ionization stratification within the BLR (Clavel et al. 1991; Reichert et al. 1994).
2. There is an inverse correlation between the time delay, or lag τ, for a particular emission line and the Doppler width ΔV of that emission line. The relationship for a given AGN is consistent with the virial prediction $\Delta V \propto \tau^{-1/2}$ (Peterson & Wandel 1999, 2000; Kollatschny 2003; Peterson et al. 2004; Bentz et al. 2010a). Without this relationship, RM masses would be highly dubious.
3. There is an empirical relationship between the AGN luminosity L and the radius of the BLR R (hereafter the R–L relationship) that is well-established only for the Hβ emission line (Kaspi et al. 2000, 2005; Bentz et al. 2006, 2009, 2013). Limited data on C IV λ1549 indicates a similar relationship applies to that line as well (Peterson et al. 2005; Vestergaard & Peterson 2006; Kaspi et al. 2007; Park et al. 2013). The existence of R–L relationships for both low-ionization and high-ionization lines has been independently confirmed by gravitational microlensing observations (Guerras et al. 2013).

The R–L relationship is of particular interest as it allows estimation of the central black hole mass based on a single spectrum from which the line width is measured and the BLR radius is inferred from the AGN luminosity. This neatly bypasses the need for a direct RM measurement of the emission-line time lag. RM is necessarily resource intensive: even to determine the mean time delay for an emission line typically requires some 30–50 well-spaced high-quality spectrophotometric observations or a good measure of luck for fewer observations. The R–L relationship is very important as the RM-based mass determinations anchor empirical scaling

relationships (e.g., McLure & Jarvis 2002; Vestergaard 2002; Shields et al. 2003; Grupe & Mathur 2004; Vestergaard 2004; Greene & Ho 2005; Mathur & Grupe 2005; Kollmeier et al. 2006; Vestergaard & Peterson 2006; Salviander et al. 2007; Treu et al. 2007; McGill et al. 2008; Park et al. 2013, 2015; Netzer & Trakhtenbrot 2014) that are used to estimate the masses of quasar black holes in large numbers (e.g., Vestergaard et al. 2008; Vestergaard & Osmer 2009; Shen et al. 2011; De Rosa et al. 2014). Virtually all quasar mass estimates and their astrophysical uses are tied to RM.

Measurement of the mean lag and line width for a given emission line provides important, though limited, information about the BLR and the central mass of the AGN. We are only now beginning to realize the full power of RM through velocity-resolved investigations of the BLR response. The first generation of successful RM programs provided sufficient understanding of AGN variability and BLR response times to design programs that could effectively extract velocity–dependent information that would lead to an understanding of the structure and kinematics of the BLR through recovery of "velocity–delay" maps from RM data (Horne et al. 2004). The relationship between the continuum variations $\Delta C(t)$ and velocity-resolved emission-line variations $\Delta L(V, t)$ is usually described as

$$\Delta L(V, t) = \int_0^\infty \Psi(V, \tau)\Delta C(t - \tau)d\tau, \quad (1)$$

where $\Psi(V, \tau)$ is the "response function," or velocity–delay map (Horne et al. 2004). As can be seen by inspection, $\Psi(V, \tau)$ is simply the observed emission-line response to a delta-function continuum outburst. The velocity–delay map is simply the BLR geometry and kinematics projected into the two observable quantities of LOS velocity and time delay relative to the continuum. This linearized echo model is justified by the fact that the continuum and emission-line variations are generally quite small (10%–20%) on reverberation time scales (see also Cackett & Horne 2006). The technical goal of a reverberation program such as the one described here is to recover the velocity–delay map $\Psi(V, \tau)$ from the data and thus infer the geometry and kinematics of the BLR.

Time-resolved velocity–delay maps have now been obtained for a handful of AGNs (e.g., Bentz et al. 2010b; Brewer et al. 2011; Pancoast et al. 2012; Grier et al. 2013; Pancoast et al. 2014), but only for optical lines (the Balmer lines, He I λ5876, and He II λ4686). In general, these suggest flattened geometries at small to modest inclinations and some combination of virialized motion and infall. An outflow signature has been observed in only one case, NGC 3227 (Denney et al. 2009).

The lack of velocity–delay maps for UV lines, on the other hand, leaves us with a very incomplete understanding of the BLR. It is, in fact, the high-ionization level UV resonance lines (e.g., C IV λ1549, Si IV λ1400, Lyα λ1215) that might be expected to dominate any outflowing component of the BLR. The optical lines, in contrast, generally seem to arise in disk-like structures with infall components (e.g., Pancoast et al. 2014).

RM studies in the UV have been limited. Several observing campaigns were undertaken with the *International Ultraviolet Explorer (IUE)* or *Hubble Space Telescope (HST)* or both on (i) NGC 5548 (Clavel et al. 1991; Korista et al. 1995), (ii) NGC 3783 (Reichert et al. 1994), (iii) Fairall 9 (Clavel et al. 1989; Rodríguez-Pascual et al. 1997), (iv) 3C 390.3 (O'Brien et al. 1998), (v) NGC 7469 (Wanders et al. 1997), (vi) NGC 4151 (Clavel et al. 1990; Crenshaw et al. 1996; Ulrich & Horne 1996), (vii) Akn 564 (Collier et al. 2001), and (viii) NGC 4395 (Peterson et al. 2005). With the exception of Akn 564, which showed essentially no emission-line variability over a comparatively short campaign, all of these programs yielded emission-line lags, but only limited information about the detailed response of the UV emission lines (e.g., Horne et al. 1991; Krolik et al. 1991; Wanders et al. 1995; Done & Krolik 1996). The existing velocity-delay map for NGC 4151 shows some incipient structure in C IV λ1549 and He II λ1640 and a general shape that seems to be consistent with a virialized BLR (Ulrich & Horne 1996).

1.3. The AGN STORM Project

Given the importance of the UV emission lines in the photoionization equilibrium of the BLR gas and the probable differences between the geometry and kinematics of the high and low-ionization gas in the BLR, we have undertaken a large RM program in the UV using the Cosmic Origins Spectrograph (COS; Green et al. 2012) on *HST* (*HST* Program GO-13330), the AGN Space Telescope and Optical RM (AGN STORM) Project, in the first half of 2014. The program was designed with certain specific goals in mind:

1. Determine the structure and kinematics of the high-ionization BLR through observations of the variations in the C IV λ1549, Lyα λ1215, N V λ1240, Si IV λ1400, and He II λ1640 emission lines.[42]
2. Carry out simultaneous ground-based observations of (a) the high-ionization optical line He II λ4686 for direct comparison with He II λ1640 and (b) the Balmer lines, particularly Hβ λ4861, to determine the structure and kinematics of the low-ionization BLR. Although the optical spectrum is extremely well-studied (Peterson et al. 2002; Bentz et al. 2007, 2010a; Denney et al. 2010, and references therein), simultaneous observations are necessary, as the dynamical timescale for the BLR in NGC 5548 is only a few years.
3. Compare in detail the continuum variations in the UV (at ~1350 Å) with those at other wavelengths (see Edelson et al. 2015, hereafter Paper II) and infer the structure of the continuum-emitting region.

The motivation for the UV/optical continuum comparison is multifold:

1. Delays between continuum variations at longer versus shorter wavelengths have been detected or hinted at in a number of sources (e.g., Wanders et al. 1997; Collier et al. 1998, 2001; Peterson et al. 1998; Sergeev et al. 2005; Cackett et al. 2007; McHardy et al. 2014; Shappee et al. 2014). Such delays can provide insight into the structure, geometry, and physics of the continuum-emitting region.

[42] We note that three of these lines are actually doublets: N V $\lambda\lambda$1239, 1243, Si IV λ1394, 1403, and C IV $\lambda\lambda$1548, 1551. Moreover, the He II feature is blended with O III] $\lambda\lambda$1661, 1665 and Si IV is blended with the quintuplet O IV] $\lambda\lambda$1397.2, 1399.8, 1401.2, 1404.8, 1407.4, where the second, third, and fifth transitions dominate.

2. Velocity–delay maps recovered using the UV continuum as the driving light curve (Equation (1)) are expected to be of higher fidelity than those obtained from the optical continuum because the observable UV is closer in wavelength to the ionizing continuum ($\lambda < 912$ Å) that powers the emission lines. The optical continuum is not only a slightly time-delayed version of the UV continuum, but it seems smoothed somewhat as well (Peterson et al. 2014; Shappee et al. 2014), which might make it difficult to recover detailed structure in the velocity–delay maps.

Our *HST* program afforded a valuable opportunity for exploring AGN behavior at high time resolution for an extended period at wavelengths beyond those covered by our *HST* COS spectra. The *HST* program is the anchor of a much broader AGN STORM project to address broader issues through observations across the electromagnetic spectrum. This paper serves as the first in a series.

Of special interest is the possibility of using short-timescale lags between variations in different continuum bands to map the temperature structure of the accretion disk. The *Swift* satellite (Gehrels et al. 2004) is especially suitable for such a study because of its broad wavelength coverage (hard X-ray through *V*-band) and ability to execute high-cadence observations over an extended period of time. In Paper II, we present the results of a four-month program of high-cadence (approximately twice per day) multiwavelength observations with *Swift*. Additional papers in this series will describe high-cadence ground-based photometry from the near-UV through the NIR. We will also present results from a program of ground-based spectroscopy that is similar in cadence to the *HST* COS observations, but covers a somewhat longer temporal baseline. Other additional papers will present results on the variable absorption features and on our efforts to decipher the broad emission-line variations and determine the structure and geometry of the BLR.

In Section 2, we describe the observations and data processing, including a discussion of the program design and a complete description of how the standard data reduction pipeline was modified to meet our stringent calibration requirements. We describe our initial data analysis and results in Section 3, and in Section 4, we briefly discuss the first results from our program and place these results in the context of previous monitoring campaigns on NGC 5548. When necessary, we assume a ΛCDM cosmology with $H_0 = 70$ km^{-1}s^{-1} Mpc^{-1}, $\Omega_M = 0.28$, and $\Omega_\Lambda = 0.72$ (Komatsu et al. 2011).

2. OBSERVATIONS AND DATA REDUCTION

2.1. Program Design

RM is a resource-intensive activity that requires obtaining high signal-to-noise ratio (S/N) homogeneous spectra at sufficiently high spectral resolution to resolve the gross kinematics of the BLR. Spectra must be obtained at a high cadence over a temporal baseline that is longer than the typical variability timescale of the AGN. Given the inherent risks of RM programs due to the unpredictability of AGN variability, it is essential that our experimental design assures a successful outcome, yet is as economical with observing time as possible. The first consideration is that each epoch of observation should require no more than one *HST* orbit per "visit" which restricts the integration time per visit to ~45–50 minutes. This consideration limits us to relatively bright nearby Seyfert 1 galaxies. COS is clearly the instrument of choice for such a project, as it is a very sensitive, high spectral resolution spectrometer. Its native resolution ($R > 20{,}000$) is high enough to allow us to trade off resolution and S/N in the data processing phase. In order to schedule the observatory efficiently, a cadence of one visit per day or longer is required.

We therefore want to target an AGN that has a C IV-emitting region several light days in extent, and this requires a source with $\log L_\lambda(1350\,\text{Å})/(\text{ergs s}^{-1}) \gtrsim 43.5$ (e.g., Kaspi et al. 2007). This led us immediately to select as a target the well-studied Seyfert 1 galaxy NGC 5548 ($z = 0.017175$). NGC 5548 is probably the best-studied AGN by RM, with historical optical spectroscopy extending as far back as the early 1970 s (Sergeev et al. 2007). Importantly, it has never been known to go into a "dormant state," as observed recently in the case of Mrk 590 (Denney et al. 2014), that would preclude a successful reverberation campaign and, historically, self-absorption in the UV resonance lines has been minimal (Crenshaw & Kraemer 1999), although strong absorption appeared in 2013 (Kaastra et al. 2014).

The remaining adjustable parameter is the duration of the campaign. We investigated this using Monte Carlo simulations similar to those described by Horne et al. (2004). Using recent developments in statistically modeling AGN light curves (Kelly et al. 2009; Kozłowski et al. 2010; MacLeod et al. 2010, 2012), we can make very robust models of the expected continuum behavior of NGC 5548. Quasar light curves are well-described by a stochastic process, the damped random walk. The process is described by an amplitude σ and a damping timescale τ_d, which for NGC 5548 in the optical are measured to be $\sigma = 0.89^{+0.30}_{-0.20} \times 10^{-15}$ ergs s^{-1} cm^{-2} Å^{-1} and $\tau_d = 77^{+59}_{-34}$ days, respectively (Zu et al. 2011). We used these measured properties of NGC 5548 to simulate the continuum variations; this is a conservative choice as the UV continuum can be expected to show both higher amplitude and shorter time-scale variations, both of which are an advantage. We then convolved the artificial light curves with model velocity–delay maps for several lines to provide an artificial spectrum. As described by Horne et al. (2004), we adopted a BLR model with an extremely challenging velocity–delay map for these simulations, a Keplerian disk with a single two-armed spiral density wave. While this is unlikely to be the actual AGN BLR geometry, it provides a challenging test: if we can recover such a complex velocity–delay map correctly, then we can certainly hope to recover others of comparable complexity and would have no difficulties with geometries like those that have been recovered for optical lines (e.g., Bentz et al. 2010b; Pancoast et al. 2012; Grier et al. 2013; Pancoast et al. 2014).

We modeled the emissivity and response of each line realistically using a grid of photoionization equilibrium models (Horne et al. 2004). We sampled the artificial spectra to match our proposed observations, including noise. We then modeled the artificial spectra to recover the velocity–delay maps using `MEMECHO` (Horne et al. 1994, 2004). Simulations based on characteristics of previous RM experiments yield velocity–delay maps with noise levels similar to those obtained from the actual data, demonstrating the verisimilitude of our simulations (see Horne et al. 2004, for examples).

The goal of our simulations was to determine the minimum duration program that would allow us to recover a velocity–delay map with a high probability of success. For COS-like observations (in terms of S/N per visit and spectral resolution),

our initial simulations indicated that reliable velocity–delay map recovery for a strong line (e.g., C IV) required between 130 and 200 days. A finer grid of models showed that in 10 of 10 simulations, a high-fidelity velocity–delay map was recovered after 180 days, which was thus adopted as the program goal. A much longer program at this sampling rate would in any case be precluded by the accessibility of the target to *HST*.

Because of the long duration of the proposed program, we also considered the possible impact of losses of data due to instrument or spacecraft safing events. Short safing events occur frequently enough that we needed to assess their impact. Based on the record for *HST* and COS in Cycles 17–20, there might be two spacecraft events that lose 2–3 days each and one COS event that loses 2 days over a stretch of 180 consecutive days. By repeating a subset of our simulations, we found that losses of such small numbers of observations would have no impact on our ability to recover the velocity–delay maps. The simulations also allowed us to assess the impact of early termination of our experiment due to a major failure. If a program was terminated at ∼100 days, the probability that the data would yield a useful (but not a detailed) velocity–delay map would be ∼50%. However, a program as short as 75 days would have a very low probability (∼10%) of success.

The key to a successful RM campaign is that it must be long enough that favorable continuum variability characteristics become highly probable. That this is essentially guaranteed to happen during a 180 days experiment played a major role in selecting NGC 5548 as our target.

2.2. COS Observations

Observations were made in single-orbit *HST* COS visits approximately daily from 2014 February 1 through July 27. Of the 179 scheduled visits, 171 observations were executed successfully and 8 were lost to safing events or target acquisition failures (very close to the expected number of losses).

In each visit, we used the G130M and G160M gratings to observe the UV spectrum over the range 1153–1796 Å in four separate exposures. Exposure times were selected to provide S/N $\gtrsim$100 when measured over velocity bins of ∼500 km s^{-1}. During each visit, we obtained two 200 s exposures with G130M centered at 1291 and 1327 Å and two 590 s exposures with G160M centered at 1600 and 1623 Å.

The COS far-ultraviolet detector is a windowless, crossed delay-line microchannel plate stack that is subject to long-term charge depletion. To extend the useful lifetime of the detector, we positioned the spectrum so that bright geocoronal airglow lines (e.g., Ly$\alpha\lambda$1215) and AGN emission lines (e.g., redshifted Lyα) would not always fall on the same area of the detector. First, we alternated the target acquisition between the G130M/1291 and the G130M/1327 configurations. The G130M/1327 configuration is then followed by a G130M/1327/FP-POS = 3 exposure,[43] and by a G130M/1291 exposure alternating among FP-POS = 1, 2, and 4. The G130M/1291 configuration is instead followed by a G130M/1291/FP-POS = 3 exposure, and by a G130M/1327 exposure alternating among FP-POS = 1, 2, and 4. Second, we alternated the FP-POS for the G160M/1623 exposure between FP-POS = 1 and FP-POS = 2. We could not vary the settings for the G160M/1600 and G160M/1623 further because we needed to ensure the coverage of the entire wavelength range while keeping the detector gap from falling on the redshifted C IV λ1549 emission line.

Finally, we used four additional orbits to improve our understanding of the COS flux calibrations (see Section 2.3). During these additional visits, we observed two of the standard stars (WD 0308–565 and WD 1057+719) employed to obtain sensitivity functions (Massa et al. 2014) at the same detector locations we used for the reverberation program. The observations were taken using all the instrument configurations employed in our primary observing program.

2.3. Data Reduction

We used the `CalCOS` pipeline v2.21 for the bulk of our data processing. The absolute flux calibration of the COS reduction pipeline is reported to be accurate to ∼5% and the relative flux calibration is good to better than ∼2% (Holland et al. 2014). We are primarily interested in the quality of the relative flux calibration as we are looking for very small-scale variations on short timescales; we need the fluxes to be stable and repeatable across the spectrum. We found, however, that there were local variations in the precision of the fluxes that necessitated improvements.

To produce a final dataset with a flux calibration that is everywhere precise at the 2% level, we refined the existing calibration reference files and applied a post-`CalCOS` pipeline to further process the data. The main areas of improvement include refinements to the dispersion solution, fixed-pattern noise mitigation, the sensitivity function, and the time dependent sensitivity (TDS) functions, as outlined below. The final data product consists of one combined spectrum per grating per day. Airglow emission lines (O I $\lambda\lambda$1302.2, 1306 and N I $\lambda\lambda$1199.5, 1200.7) were filtered from the data by removing events detected when *HST* was in daylight. The spectra were further binned by 4 pixels in order to increase the S/N per spectral element of the AGN continuum. This binning still results in two binned pixels per COS resolution element.

2.3.1. Dispersion Solution

The COS wavelength solution has a quoted uncertainty of ∼15 km s^{-1} (Holland et al. 2014). As the STIS uncertainty is <5 km s^{-1} (Hernandez et al. 2014), we refined the dispersion solutions for our COS dataset using previous observations of NGC 5548 taken with the STIS E140M/1425 mode in 1998 (PID 7572, PI: Kraemer). To accomplish this, we cross-correlated the line profiles of strong interstellar medium absorption features between each COS observation and the STIS reference spectrum. We used 19 interstellar absorption features, ranging from Si II λ1190 at the short-wavelength end to Al II λ1670 at the long-wavelength end. A linear correction to the initial wavelength solution was then computed across each detector segment and applied directly to the extracted spectra. With this correction, measurements of the rms of the residual offsets decreased from ∼15 to <6 km s^{-1}.

2.3.2. Fixed-pattern Noise

The standard reference files used in the `CalCOS` pipeline correct for only the most prominent fixed-pattern noise features such as the quantum-efficiency gridwires, low-order response

[43] FP-POS values refer to small displacements of the spectrum on the detector in the dispersion direction in order to minimize the effects of fixed-pattern noise.

variations, and large geometric distortion artifacts (Ely et al. 2011). Usually, users combine multiple FP-POS positions to smooth over the remaining features. However, this was not possible for our dataset, since only a single FP-POS setting was used for each central wavelength setting in each orbit (see Section 2.2).

To correct these features to a higher degree we derived one-dimensional pixel-to-pixel flats ("p-flats"). These flats were produced by combining normalized, high S/N white dwarf spectra in detector space, following the method described by Ely et al. (2011). The white dwarf spectra used were taken as part of the *HST*/CAL program 12806 (PI: Maasa) and used the same detector locations as used for the NGC 5548 datasets.

To test the effects of our p-flat correction, we combined the 171 spectra reduced both with and without the application of the p-flats. The S/N per pixel in 5 Å continuum regions increased from ~75 to ~80 for the G130M grating, and from ~60 to ~100 for the G160M grating through the removal of small localized flux calibration errors by the p-flat correction. The improvement for the G130M combined spectrum is less dramatic because (a) we rotated among the four FP-POS settings, and (b) the G130M grating disperses more widely in the cross-dispersion direction, and thus intrinsically averages the fixed-pattern noise over a larger area of the detector.

2.3.3. Sensitivity Functions and TDS

The COS flux calibration is done in two steps: (a) derivation of static sensitivity functions and (b) characterization of the time evolution of the sensitivity through the TDS correction (Holland et al. 2014). Thanks to the existing calibration program that monitors the TDS variations (PID 13520), we had bi-monthly observations of the standard star WD 0308–565 for 3 out of the 4 central wavelength settings we are using in our program (G130M/1291, G130M/1327 and G160M/1623). Standard star data were obtained in 2014 February, April, June, and August. By analyzing these calibration data, together with the data collected during our additional calibration orbits (Section 2.2), we verified that both the static and time-dependent response functions vary more with instrument configuration than currently modeled by the `CalCOS` pipeline. While `CalCOS` assumes that both the sensitivity function and the TDS correction vary only as a function of wavelength, we were able to improve the relative flux calibrations and reach our required level of precision by (a) obtaining sensitivity functions individually for each configuration (one function per wavelength setting per FP-POS per detector segment), and (b) computing the TDS correction individually for each wavelength setting observed as part of the routine calibration program.

We estimate the quality of the flux calibration by inspection of the fractional residuals $f_{\rm res}$ of the calibrated standard star spectra and their respective `CalSPEC` stellar model (the same models employed by the standard pipeline reference file),

$$f_{\rm res} = \frac{f_{\rm WD,obs} - f_{\rm Model}}{f_{\rm Model}}, \quad (2)$$

where both $f_{\rm WD,obs}$ and $f_{\rm Model}$ are binned over 1 Å using a boxcar filter in order to increase the S/N per spectral element. While the visual inspection of the residuals as a function of wavelength allows us to identify and correct for local biases, we use the mean value of the distribution of the residuals as an indicator of a global bias in the calibration. The flux calibration uncertainty is an estimate of the limit of the stability of the flux calibration at a given time. However, since the overall instrument sensitivity evolves with time, and our final spectra are obtained from the combination of multiple settings for each grating, we conservatively define the fractional precision error δ_P for each grating as the maximum fractional uncertainty computed for any of the wavelength settings.

The new sensitivity functions were derived from spectra of the standard star WD 0308–565 for the G130M settings, and of WD 1057+719 for the G160M settings (PID 12806). While one individual sensitivity function per detector segment characterizes the full grating (data from different settings are averaged together) in `CalCOS`, we built one independent sensitivity function for each wavelength setting and FP-POS used in our program.

By comparing the bi-monthly WD 0308–565 data, we found that residuals with respect to the stellar models were greatly reduced if the TDS corrections were computed individually for each of the wavelength settings (G130M/1291, G130M/1327, and G160M/1623), instead of averaging the data over multiple modes. Additional improvements were obtained by increasing the number of time intervals over which the TDS trends are computed and by redefining the wavelength ranges used in the analysis. Unfortunately, there are insufficient calibration data for the longest wavelengths in the G160M spectra, so we were forced to truncate these spectra at 1750 Å.

In spite of these improvements, the available data did not allow us to conduct any tests on the remaining setting (G160M/1600). This setting is particularly important for our scientific goals since it includes most of the broad C IV emission line (Section 1.3). Moreover, since all the calibration data for TDS monitoring purposes are obtained only using FP-POS = 3, they did not allow us to test for any residual dependence of the TDS correction on FP-POS configuration. These are the two reasons that motivated us to request further calibration data (see Section 2.2). These data for WD 0308–565 and WD 1057+719 collected in 2014 September allowed us to derive an independent set of sensitivity functions. By comparing the new sensitivity functions with the originals, appropriately corrected for time evolution of the TDS, we were able:

1. To identify the best possible TDS correction attainable for the G160M/1600 setting with the current TDS calibration data. The current `CalCOS` TDS correction for this configuration was obtained from combining both G160M/1577 and G160M/1623 data. Although this correction is not ideal, it minimizes both the global bias and the flux calibration uncertainty when compared to the TDS corrections obtained individually from either the G160M/1577 or the G160M/1623 settings.
2. To verify that the TDS correction does not vary strongly with FP-POS settings. While comparing the residuals with respect to the stellar models shows structure unique to each FP-POS setting, the level of the local biases is such that both the global bias and the flux calibration uncertainty can be considered stable for each wavelength setting (the maximum deviation in the width of the residual distribution is ~0.2%).

With the new flux calibration and TDS characterization, our global biases are consistent with zero and the overall fractional precision is $\delta_P \sim 1.1\%$ and ~1.4%, respectively, for the

G130M and G160M settings, compared to $\delta_P \sim 1.4\%$ and ~3.5% for the standard pipeline. We intend to make these improvements available to other COS users.

2.3.4. Sensitivity Offsets For the Final Week of Data

During the final week of the observing campaign, the operating high voltage (HV) for one of the COS detector segments was increased to combat the negative effects of "gain-sag" (Sahnow et al. 2011). While necessary to provide well-calibrated data, this HV change also has the effect of introducing small changes in the detector response. Using WD 0308–565 observations from our calibration orbits taken at the same HV as the rest of the campaign and contemporaneous TDS monitoring observations of the same calibration target (taken at the increased HV), we were able to estimate a HV bias correction for the G130M grating from a direct comparison of the spectra. This bias was measured to be 1% without any detectable dependence on wavelength or cenwave setting. Unfortunately, the same procedure could not be done for the G160M grating as our additional orbits and the TDS observations used different standard stars (WD 0308–565 instead of WD 1057+719). Instead, the bias estimate for this grating was obtained by analyzing the time evolution of the mean flux in overlapping regions of G130M/1327 at the lower HV setting and G160M/1600 at the higher HV setting. This analysis gave a plausible estimate of a 1% bias. However, with such a limited amount of data at the lower HV and a narrow overlapping wavelength range, the estimate lacks the accuracy of the G130M bias estimate.

3. DATA ANALYSIS

3.1. Mean and rms Spectra

For an initial look at the spectral variations, we define G130M and G160M mean spectra as

$$\overline{F}(\lambda) = \frac{1}{N}\sum_{i=1}^{N} F_i(\lambda), \quad (3)$$

where F_i is the ith spectrum of the series of $N = 171$ spectra. Similarly, the rms residual spectrum (hereafter referred to simply as the rms spectrum) is defined as

$$S(\lambda) = \left\{\frac{1}{N-1}\sum_{i=1}^{N}\left[F_i(\lambda) - \overline{F}(\lambda)\right]^2\right\}^{1/2}. \quad (4)$$

The rms spectrum is especially useful as it isolates the variable part of the spectrum; constant components disappear, though sometimes small residuals are visible in the case of strong features. The statistical uncertainty in the mean spectra is

$$\sigma_{\overline{F}}(\lambda) = \frac{1}{N}\left\{\sum_{i=1}^{N}\sigma_{F_i}^2(\lambda)\right\}^{1/2}, \quad (5)$$

where σ_{F_i} is the error spectrum of the ith spectrum in the series.

The total uncertainty in the mean spectra consists of this statistical uncertainty and our estimate of the fractional uncertainty in precision as described above, which amounts to $\delta_P(\mathrm{G130M}) \approx 1.1\%$ and $\delta_P(\mathrm{G160M}) \approx 1.4\%$. To determine the total uncertainty, the statistical uncertainty (Equation (5)) and the uncertainty in precision ($\delta_P \overline{F}(\lambda)$) are added in quadrature. The mean and rms spectra for the G130M and G160M settings are shown in Figures 1 and 2, respectively. The rms spectrum resulting from Equation (4) combines both the intrinsic variability and the variance due to noise, as discussed by Park et al. (2012) and Barth et al. (2015). In order to isolate the rms spectrum of the intrinsic variations σ_0, we model the distribution of the residuals of each pixel about the mean. The combined statistical and systematic noise in each pixel of spectrum i is thus $(\sigma_i^2 + (\delta_P F_i)^2)^{1/2}$. Assuming that the flux measurement errors and the intrinsic variations arise from independent Gaussian random processes, we find maximum likelihood estimates for the optimal average,[44] $\overline{F_\mu}$, and σ_0 by minimizing

$$-2\ \ln L\left(\overline{F_\mu}, \sigma_0\right) = \chi^2 + \sum_{i=1}^{N}\ln\left[\sigma_0^2 + \sigma_i^2 + \left(\delta_P F_i\right)^2\right], \quad (6)$$

where

$$\chi^2 = \sum_{i=1}^{N}\frac{\left(F_i - \overline{F_\mu}\right)^2}{\sigma_0^2 + \sigma_i^2 + \left(\delta_P F_i\right)^2}, \quad (7)$$

and $\delta_P F_i$ is the precision of the ith spectrum. This estimate of the intrinsic rms spectrum (σ_0) is also shown in Figures 1 and 2.

3.2. Integrated Light Curves

The next step in our initial analysis is to produce light curves for the continuum and emission lines. At this stage, our goal is to make simple measurements from the reduced spectra, introducing as few assumptions as possible. All flux measurements are performed on spectra in the observed frame. We have not corrected the spectra for Galactic extinction in order to facilitate the cleanest comparison with other measurements to be reported elsewhere in this series of papers (e.g., broadband photometry).

There are bad pixels throughout the spectrum, and their location and severity change with time, instrument settings, and airglow subtraction (e.g., if a spectrum is taken entirely in orbital bright time, the flux in the airglow windows is set to zero and the pixels are flagged as bad pixels). To prevent the introduction of artificial variations in the relative flux estimates, bad pixels are masked throughout the dataset. This means that if a pixel is bad in any of the visits, the pixel is masked out in each of the 171 spectra. We further mask Galactic Lyα absorption and airglow region. Integration ranges (listed in Table 1) were chosen using the mean spectra in Figures 1 and 2 as a guide. Continuum ranges are chosen to be as uncontaminated as possible by absorption lines and broad emission-line wings. In the case of overlapping emission lines (e.g., C IV and He II), the boundary wavelength corresponds to the wavelength at which the fluxes of the two lines are comparable. We do not mask absorption lines at this stage in our analysis. We are unable to cleanly separate N V and Lyα using this simple procedure.

Continuum fluxes are measured as the weighted mean of the flux density in the integration region, with weights equal to the

[44] The unweighted average $\overline{F}$ in Equation (3) is formally distinct from the optimal average $\overline{F_\mu}$, though practically they are indistinguishable for these data.

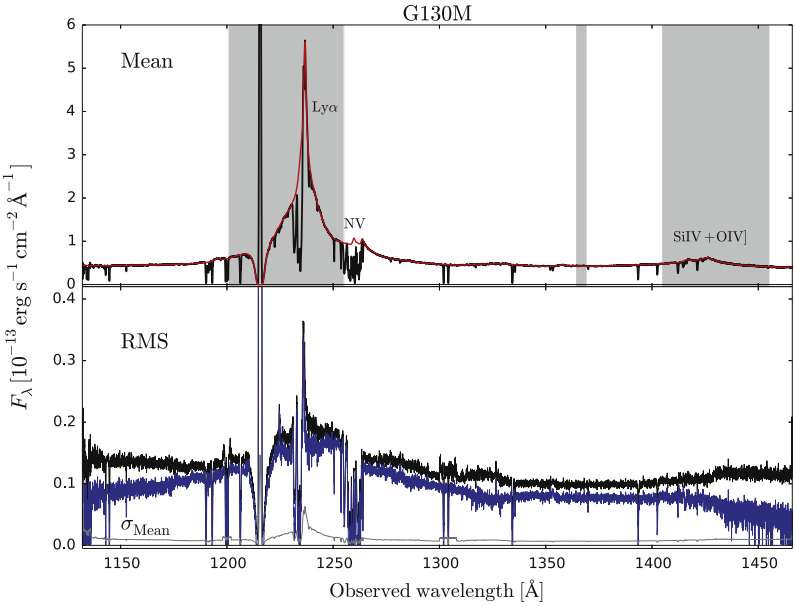

Figure 1. Spectra obtained with the G130M grating. The shaded areas show the integration regions defined in Table 1. Top panel: the mean spectrum, as defined in Equation (3), is shown as a black solid line. The spectral model described in Section 3.5 is shown in red. The deep trough centered at 1215 Å is Galactic Lyα absorption and the strong narrow emission line at the center of this trough is geocoronal Lyα emission. The narrow Galactic absorption lines, although generally saturated, are never black at line center because the thermal broadening of this cold gas is still far below the resolution of COS. Bottom panel: the rms spectrum, as defined in Equation (4), is shown as a black solid line, while the intrinsic rms spectrum σ_0 (see Section 3.1) is shown in blue. In gray we show the total error on the mean, which is the statistical error (Equation (5)) combined in quadrature with the fractional error in precision, $\delta_P = 1.1\%$ for the G130M spectra. Note the difference in the flux scale between the two panels.

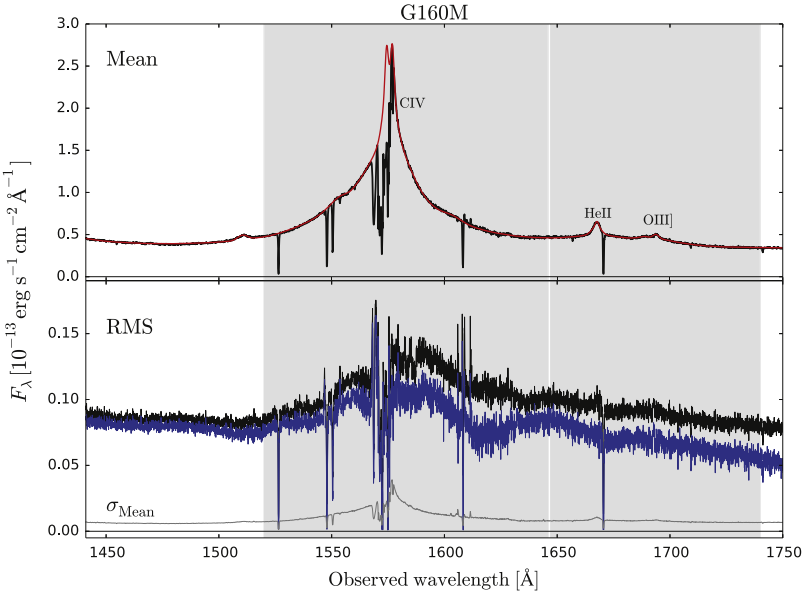

Figure 2. Spectra obtained with the G160M grating. The shaded areas show the integration regions defined in Table 1. Top panel: the mean spectrum, as defined in Equation (3), is shown as a black solid line. The spectral model described in Section 3.5 is shown in red. The narrow Galactic absorption lines, although generally saturated, are never black at line center because the thermal broadening of this cold gas is still far below the resolution of COS. Bottom panel: the rms spectrum, as defined in Equation (4), is shown as a black solid line, while the intrinsic rms spectrum σ_0 (see Section 3.1) is shown in blue. In gray we show the total error on the mean, which is the statistical error (Equation (5)) combined in quadrature with the fractional error in precision, $\delta_P = 1.4\%$ for the G160M spectra. Note the difference in the flux scale between the two panels.

Table 1
Integration Limits for Light Curves

Emission Component	Integration Limits	Shortward Continuum Region	Longward Continuum Region
F_λ(1367 Å)	1364.5–1369.5	...	...
Lyα λ1215	1201.0–1255.0	1155.0–1160.0	1364.5–1369.5
Si IV λ1400[a]	1405.0–1455.0	1364.5–1369.5	1460.0–1463.5
C IV λ1549	1520.0–1646.0	1475.0–1482.0	1743.0–1749.0
He II λ1640[b]	1647.0–1740.0	1475.0–1482.0	1743.0–1749.0

Note. All regions are in the observed frame (Å).
[a] Integration range also includes O IV] λ1402.
[b] Integration range also includes O III] λ1663.

inverse of the variance,

$$F_\lambda = \left(\sum_{i=1}^{N} w_i\ F_i\right)\left(\sum_{i=1}^{N} w_i\right)^{-1}, \quad (8)$$

where $w_i = \sigma_{F_i}^{-2}$ as in Equation (5). Statistical uncertainties computed by `CalCOS` are corrected for low counts following Gehrels (1986). Statistical uncertainties on the mean fluxes are obtained through standard error propagation,

$$\sigma_{F_\lambda} = \left(\sum_{i=1}^{N} w_i\right)^{-1/2}. \quad (9)$$

In all cases, bad pixels are excluded from the computation.

Emission-line fluxes are measured as the numerical integral of the emission flux above a locally defined continuum defined by the relatively featureless windows given in Table 1. To estimate the local continuum underneath the line we performed a χ^2 linear fit of the continuum flux in the selected regions. The linear local continuum is then subtracted from the emission component, again masking bad pixels. The line flux is numerically integrated over the integration limits given in Table 1 using Simpson's method. We do not interpolate over bad pixels. We note, however, that the difference between integrating over the bad pixels and computing the integral excluding them is <0.1%. Statistical errors are computed numerically by creating $N_{\rm sample} = 5000$ realizations of the line flux and the underlying linear continuum. The flux F_λ is randomly generated from a Gaussian distribution having mean equal to the flux of the spectral element and width σ equal to the statistical error on the flux. For the linear continuum, we generate $N_{\rm sample}$ fits having a mean equal to the best fit values and covariance equal to their covariance matrix. For each realization, a line-flux estimate is then obtained by subtracting the linear continuum and by performing the numerical integration of the residuals. Confidence levels (1σ) are finally obtained from the distribution of the $N_{\rm sample}$ line fluxes. When the error bars are asymmetric, we adopt the larger error as the statistical error associated with the integrated flux.

As noted above, we adopt as the fractional error in precision $\delta_P = 1.1\%$ and $\delta_P = 1.4\%$ for the G130M and G160M settings, respectively. This is added in quadrature to statistical error of the integrated fluxes. The error in the precision dominates throughout the G160M spectra and in the G130M spectra as well, except at wavelengths shortward of ~1180 Å longward of ~1425 Å, and in the core of the Lyα complex.

The final continuum and emission-line light curves are listed in Table 2 and shown in Figure 3. The light curve statistics are given in Table 3. The average interval between two consecutive observations is $\langle \Delta t \rangle = 1.0$ days with an rms $\sigma(\Delta t) = 0.3$ days. The median interval between observations is $\Delta t_{\rm med} = 1.0$ days. The largest gaps between consecutive observations are three days (on two occasions) and two days (on six occasions).

3.3. Time-series Measurements

Certain simplifying assumptions underlie the RM technique. Most time-series analyses start with the assumption that the emission-line light curves are simply scaled, time-delayed, and possibly smoothed versions of the continuum light curve. Inspection of the light curves in Figure 3 suggests that this is an entirely reasonable assumption for the first half of the campaign. However, approximately halfway through the campaign, the emission-line response becomes more complicated. Between approximately HJD 2456780 and 2456815, the emission-line light curves are either flat (Lyα, He II) or decreasing (C IV) while the continuum is slowly rising. Moreover, the intensity ratio between the last two strong peaks in the continuum light curve at around HJD 2456820 and 2456840 seems to be almost inverted in the lines, with the second peak being stronger than the first one (especially in C IV). There is also a small event in the continuum light curve around HJD 2456785 that does not appear to have counterparts in the emission-line light curves. The line light curve that seems to best trace the continuum is the He II light curve, which is sensitive to the continuum at energies above 4 Ryd. It is also the only strong line in the COS spectra that is neither a resonance line nor self-absorbed. Moreover, it is the line that arises closest to the continuum source, as we will show below.

Because of the changing character of the emission-line response, for our initial analysis we measure emission-line lags (a) for the entire data set and (b) for subsets that divide the data into two separate halves of 85 and 86 observations, respectively. The first subset, which we will refer to as "T1," runs from HJD 2456690 to 2456780 and the second subset, "T2," runs from HJD 2456781 to 2456865.

We first measured the emission-line lags relative to the continuum variations by cross-correlation of the light curves. We used the interpolation cross-correlation (ICCF) method as implemented by Peterson et al. (2004). In this method, uncertainties are estimated using a model-independent Monte Carlo method referred to as "flux randomization and random subset selection." For each realization, N data points are selected from a light curve with N independent values, without regard to whether or not any particular point has been previously selected. For data points selected n times in a given realization, the flux error associated with that data point is reduced by a factor of $n^{1/2}$. The flux measured at each data point is then altered by adding or subtracting a random Gaussian deviate scaled by the flux uncertainty ascribed to that point. Each realization yields a cross-correlation function that has a maximum linear correlation coefficient $r_{\rm max}$ that occurs at a lag $\tau_{\rm peak}$. We also compute the centroid $\tau_{\rm cent}$ of the cross-correlation function using all the points near $\tau_{\rm peak}$ with $r(\tau) \geq 0.8\ r_{\rm max}$. Typically a few thousand realizations are used to construct distribution functions for the ICCF centroid and peak. We adopt the median values of the cross-correlation centroid distribution and the cross-correlation peak distribution as our lag measurements. The uncertainties, which are not

Table 2
Continuum and Emission-line Light Curves

G130M				G160M		
HJD[a]	F_λ (1367 Å)[b]	F(Lyα)[c]	F(Si IV)[c]	HJD[a]	F(C IV)[c]	F(He II)[c]
6690.6120	34.27 ± 0.64	39.66 ± 0.47	4.04 ± 0.26	6690.6479	53.24 ± 0.79	6.92 ± 0.31
6691.5416	35.45 ± 0.65	39.88 ± 0.48	4.47 ± 0.30	6691.5760	53.06 ± 0.79	6.99 ± 0.34
6692.3940	37.71 ± 0.67	39.88 ± 0.48	4.83 ± 0.27	6692.4084	53.30 ± 0.80	6.51 ± 0.35
6693.3237	38.14 ± 0.68	39.22 ± 0.47	4.19 ± 0.28	6693.3380	53.08 ± 0.80	6.64 ± 0.36
6695.2701	40.94 ± 0.71	39.52 ± 0.47	3.92 ± 0.29	6695.3145	53.09 ± 0.81	7.36 ± 0.35
6696.2459	44.25 ± 0.75	39.49 ± 0.48	3.72 ± 0.29	6696.2602	52.76 ± 0.80	7.25 ± 0.36
6697.3080	45.30 ± 0.75	40.16 ± 0.49	4.38 ± 0.30	6697.3223	53.77 ± 0.82	8.00 ± 0.36
6698.3041	48.27 ± 0.79	40.04 ± 0.48	4.14 ± 0.30	6698.3184	55.40 ± 0.83	8.75 ± 0.36
6699.2338	45.80 ± 0.76	41.43 ± 0.51	4.80 ± 0.35	6699.2481	55.65 ± 0.84	8.77 ± 0.37
6700.2299	46.00 ± 0.76	41.13 ± 0.50	4.37 ± 0.30	6700.2442	55.13 ± 0.83	7.73 ± 0.38
6701.3588	47.46 ± 0.78	41.75 ± 0.50	4.52 ± 0.33	6701.3731	54.82 ± 0.83	8.41 ± 0.38
6702.1557	47.74 ± 0.78	41.98 ± 0.51	4.41 ± 0.34	6702.1700	55.64 ± 0.84	8.72 ± 0.39
6703.1518	47.56 ± 0.78	42.33 ± 0.51	4.70 ± 0.32	6703.1661	55.63 ± 0.84	9.27 ± 0.37
6705.3432	45.77 ± 0.76	43.80 ± 0.53	5.57 ± 0.33	6705.3575	57.85 ± 0.86	9.31 ± 0.34

Note. Full table is given in the published version. Integrated light curves in the observed frame. Flux uncertainties include both statistical and systematic errors.
[a] Midpoint of the observation (HJD—2450000).
[b] Units of 10^{-15} erg s^{-1} cm^{-2} Å^{-1}.
[c] Units of 10^{-13} erg s^{-1} cm^{-2}.

(This table is available in its entirety in machine-readable form.)

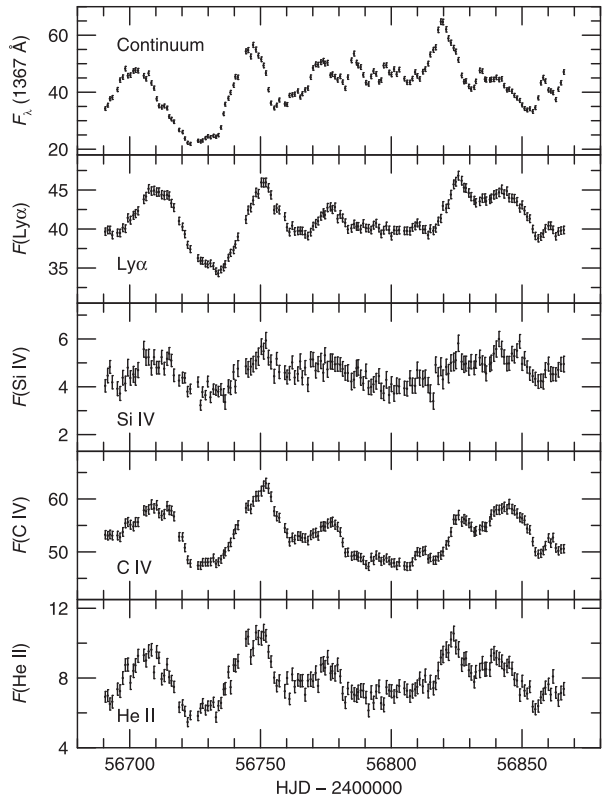

Figure 3. Integrated light curves. The continuum flux at 1367 Å is in units of 10^{-15} erg s^{-1} cm^{-2} Å^{-1} and the line fluxes are in units of 10^{-13} erg s^{-1} cm^{-2} and are in the observed frame. Flux uncertainties include both statistical and systematic errors.

necessarily symmetric, correspond to a 68% confidence level. In general, $\tau_{\rm cent}$ is found to be a more reliable indicator of the BLR size than $\tau_{\rm peak}$, though we record both. The ICCF measurements of $\tau_{\rm peak}$ and $\tau_{\rm cent}$ for the four strongest UV emission lines are given in the second and third columns, respectively, in Table 4.

We have also estimated emission-line lags using JAVELIN, which is an improved version of SPEAR (Zu et al. 2011). JAVELIN assumes that the emission-line light curves are shifted and smoothed versions of the continuum light curve (as with the ICCF analysis), where the continuum is modeled as a damped random walk (Kelly et al. 2009; Kozłowski et al. 2010; MacLeod et al. 2010) with uncertainties determined using the Markov Chain Monte Carlo method. We model the full dataset, and each line light curve was run independently with the continuum. The results, given in column (4) of Table 4, are in good agreement with the ICCF analysis, as expected.

In columns (5) and (6) of Table 4, we also give the ICCF centroid values for the T1 and T2 subsets. We also show the ICCFs for the entire sample and the T1 and T2 subsamples in Figure 4. In general, the lags for the T1 subsample have the smallest uncertainties and the ICCFs have the largest peak correlation coefficients $r_{\rm max}$, as expected. The T2 subset, on the other hand, yields lags with larger uncertainties and ICCFs with lower values of $r_{\rm max}$ (indeed, *much* lower in the case of Si IV and C IV), again as expected from visual inspection of the light curves. The T2 lags are also larger than those from T1, probably only in small part because the continuum is on average brighter (by ∼15% on average) during the second half of the campaign so the BLR gas that is most responsive to continuum changes is farther away from the central source.

3.4. Velocity-binned Results

As noted earlier (Section 2.1), this program was designed to recover kinematic information about the BLR by resolving the emission-line response as a function of radial velocity. This will be explored in detail in subsequent papers in this series. Here we carry out a simple preliminary analysis intended to show only whether velocity-dependent information is present in the data. We isolate the Lyα and C IV profiles as described

Table 3
Light Curve Statistics

Emission Component (1)	Mean and rms Flux (2)	Mean Fractional Error (3)	F_{var} [a] (4)	Maximum Flux (5)	Minimum Flux (6)	R_{max} [b] (7)
F_λ(1367 Å)[c]	42.64 ± 8.60	0.017	0.201	64.74	21.87	2.96 ± 0.08
F(Lyα)[d]	41.22 ± 2.71	0.012	0.065	46.84	34.31	1.37 ± 0.02
F(Si IV)[d]	4.62 ± 0.55	0.065	0.099	6.00	3.23	1.86 ± 0.15
F(C IV)[d]	53.28 ± 3.91	0.015	0.072	62.97	47.23	1.33 ± 0.03
F(He II)[d]	7.93 ± 1.13	0.046	0.135	10.62	5.47	1.94 ± 0.12

Note. Light curves statistics are in the observed frame.
[a] Excess variance, defined as

$$F_{\rm var} = \frac{\sqrt{\sigma^2 - \delta^2}}{\langle F \rangle} \quad (10)$$

where σ is the rms of the observed fluxes (column 2), δ is the mean statistical uncertainty (column 3 times $\langle F \rangle$), and $\langle F \rangle$ is the mean flux in column (2) (Rodríguez-Pascual et al. 1997).
[b] Ratio between maximum and minimum flux.
[c] Units of 10^{-15} erg s^{-1} cm^{-2} Å^{-1}.
[d] Units of 10^{-13} erg s^{-1} cm^{-2}.

Table 4
Emission-line Lags

Emission Line	τ_{peak} [a]	τ_{cent} [a]	$\tau_{JAVELIN}$ [a]	$\tau_{cent,\ T1}$ [b]	$\tau_{cent,\ T2}$ [c]
Lyα	$6.1^{+0.4}_{-0.5}$	$6.19^{+0.29}_{-0.25}$	$5.80^{+0.36}_{-0.39}$	$5.90^{+0.30}_{-0.29}$	$7.73^{+0.76}_{-0.57}$
Si IV	$5.5^{+1.1}_{-1.1}$	$5.44^{+0.70}_{-0.71}$	$5.94^{+0.53}_{-0.55}$	$4.99^{+0.75}_{-0.68}$	$7.22^{+1.33}_{-1.06}$
C IV	$5.2^{+0.7}_{-0.6}$	$5.33^{+0.44}_{-0.48}$	$4.59^{+0.68}_{-0.42}$	$4.61^{+0.36}_{-0.35}$	$9.24^{+1.04}_{-1.04}$
He II	$2.4^{+0.3}_{-0.8}$	$2.50^{+0.34}_{-0.31}$	$2.42^{+0.67}_{-0.06}$	$2.11^{+0.43}_{-0.38}$	$3.87^{+0.71}_{-0.58}$

Note. Delays measured in light days in the rest frame of NGC 5548.
[a] Complete dataset: 171 visits.
[b] T1 dataset: visits 1–85.
[c] T2 dataset: visits 86–171.

earlier (Section 3.2) but then integrate the fluxes in bins of width 500 km s^{-1}, except in the shortward wing of Lyα ($-10{,}000$ km s^{-1} $\leqslant \Delta V \leqslant -7000$ km s^{-1}) where we use 1000 km s^{-1} bins on account of the low flux in the blue wing of this line.

We show the ICCF centroids for each velocity bin in the C IV emission-line profile in the bottom panel of Figure 5. For the two subsets as well as the entire dataset, we see that there is a clear ordered structure in the kinematics. We cannot infer much from such a simple analysis, of course, because we cannot accurately characterize a complex velocity field with a single number. It is reassuring, however, that the general pattern is similar to what has been seen in other objects and is qualitatively consistent with a virialized region (i.e., the high velocity wings respond first). The middle panel of Figure 5 shows the rms spectra for the entire dataset and the two subsets.

In the bottom panel of Figure 6, we show the velocity-binned ICCF centroids for the Lyα emission line. Again, a clear pattern emerges, as the lags in each velocity bin are highly correlated with those of adjacent bins. However, the pattern that emerges is unlike what is seen in C IV; the largest lags are at intermediate velocities and the lags decrease toward line center. However, given the severe blending and strong absorption, detailed modeling will be required before any meaningful conclusions can be drawn.

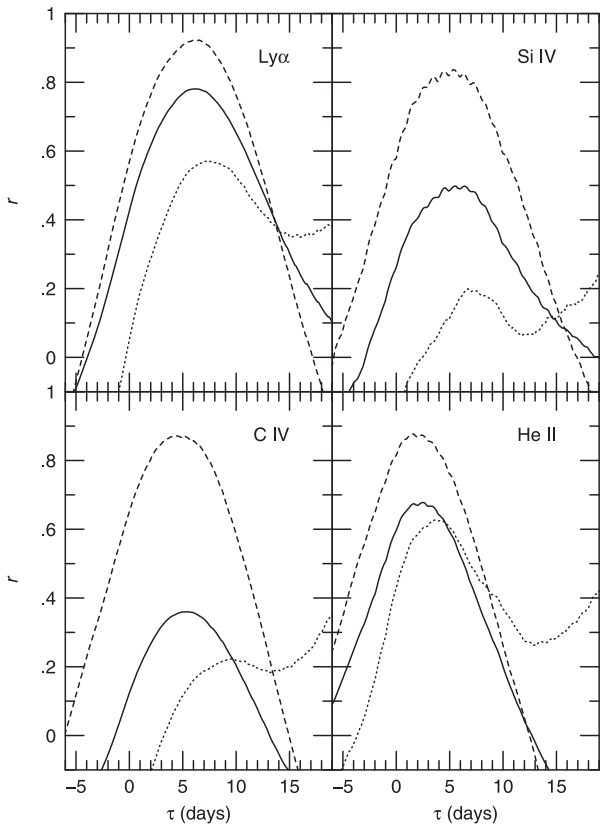

Figure 4. Interpolated cross-correlation functions (ICCFs) computed by cross-correlating each emission-line light curve with the 1367 Å continuum light curve. The solid line is the ICCF for the entire data set. The dashed line is for the T1 subsample (the first 85 visits) and the dotted line is for the T2 subsample (the last 86 visits).

104

3.5. Modeling the Mean Spectrum

The mean spectra shown in Figures 1 and 2 can be compared with earlier UV spectra of NGC 5548 obtained with *HST* (e.g.,

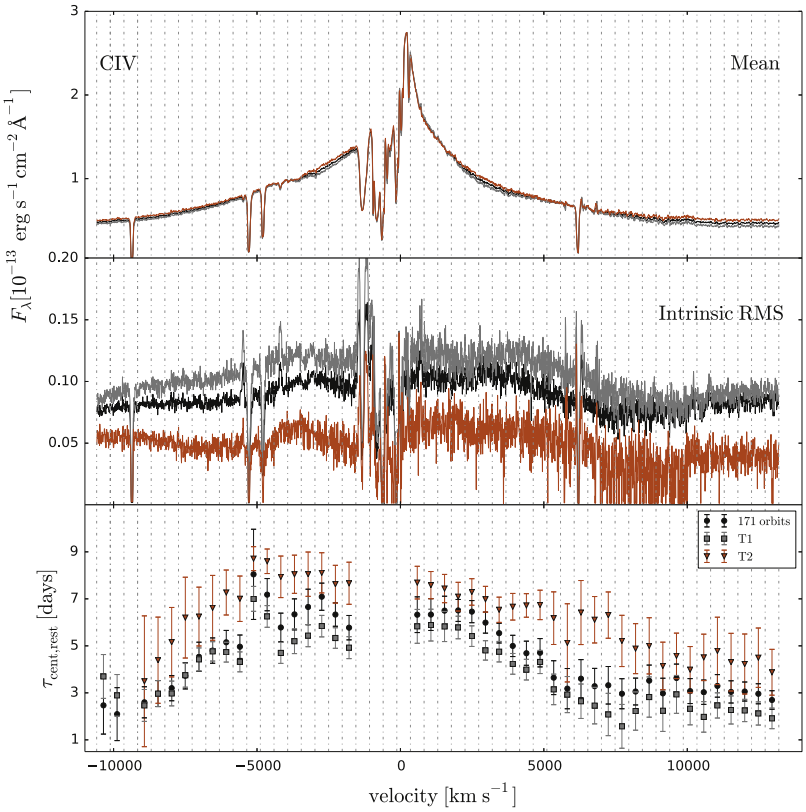

Figure 5. Velocity-binned results for the C IV λ1549 emission line. The top and middle panels show the mean and intrinsic rms (σ_0) spectra, respectively. The bottom panel shows the centroid of the cross-correlation function for each individual velocity bin, corrected to the rest frame of NGC 5548. Velocity bins with no lag measurement contain too little total flux to reliably characterize the variations. In each case, the black line represents the entire dataset, and the T1 (first 85 visits) and T2 (last 86 visits) subsets are shown in gray and orange, respectively. Note that the shortest lags are found for the highest-velocity gas.

Korista et al. 1995; Kaastra et al. 2014). The earliest high-quality UV spectra of NGC 5548 showed only weak absorption in the resonance lines (Lyα, N V, Si IV, and C IV), a factor that contributed to our selection of NGC 5548 as a target for this investigation. The 2013 spectra (Kaastra et al. 2014), however, revealed not only several strong narrow absorption features in the resonance lines, but also evidence for a relatively large "obscurer" that strongly absorbs the emission in the blue wings of the resonance lines. This feature is still present in our spectra obtained a year later, but is weaker than it was in 2013. The presence of this absorption, combined with the blending of various emission features (Lyα and N V, Si IV and O IV], C IV and He II), complicates analysis of these spectra. To characterize the emission-line structure of NGC 5548 and guide our selection of continuum windows for our emission-line flux measurements, we fit a heuristic model to the lines and continuum in the mean spectra. Our model for NGC 5548 is similar to that adopted by Kaastra et al. (2014), and it includes the broad absorption features associated with all permitted transitions in the spectrum. Our adopted continuum is a reddened power law of the form $F_\lambda(\lambda) = F_\lambda(1000\ \text{Å})(\lambda/1000\ \text{Å})^{-\alpha}$. We correct for $E(B-V) = 0.017$ mag of Galactic extinction (Schlegel et al. 1998; Schlafly & Finkbeiner 2011) using the prescription of Cardelli et al. (1989) and $R_V = 3.1$. We do not apply any correction for possible internal extinction in NGC 5548. Longward of 1550 Å, we also include blended Fe II emission as modeled by Wills et al. (1985), broadened with a Gaussian with FWHM = 4000 km s^{-1}. We model the emission lines with multiple Gaussian components. These are not an orthogonal set, and the decomposition is not rigorously unique, but they characterize each line profile well.

For the brightest lines, we start with a narrow component, typically with FWHM $\approx$ 300 km s^{-1}. This component is essentially identical to the narrow component used by Crenshaw et al. (2009) for fitting the 2004 STIS spectrum of NGC 5548. Since this narrow component is difficult to deblend from the broader components of each line, and since Crenshaw et al. (2009) saw little variation in narrow-line intensity over time, we fix the flux and widths of the narrow components of Lyα, N V, C IV, and He II to the values we used to fit the 2004 STIS spectrum. The Si IV lines do not have a detectable narrow-line component. We note that while Peterson et al. (2013) detected changes in the strength of the narrow [O III] $\lambda\lambda$4959, 5007 lines over timescales of years, the variations over the last decade have been only at the few percent level. Similar variations in the narrow components of the UV lines would not be easily detected here because the narrow components are all so weak.

Next we add an intermediate-width component with FWHM $\approx$ 800 km s^{-1} without ascribing physical meaning to it, using the STIS 2004 spectrum as a model. An intermediate-width component is included in Lyα, N V, Si IV, C IV, and He II, as well as in the fainter lines C III* λ1176, Si II λ1260, Si II

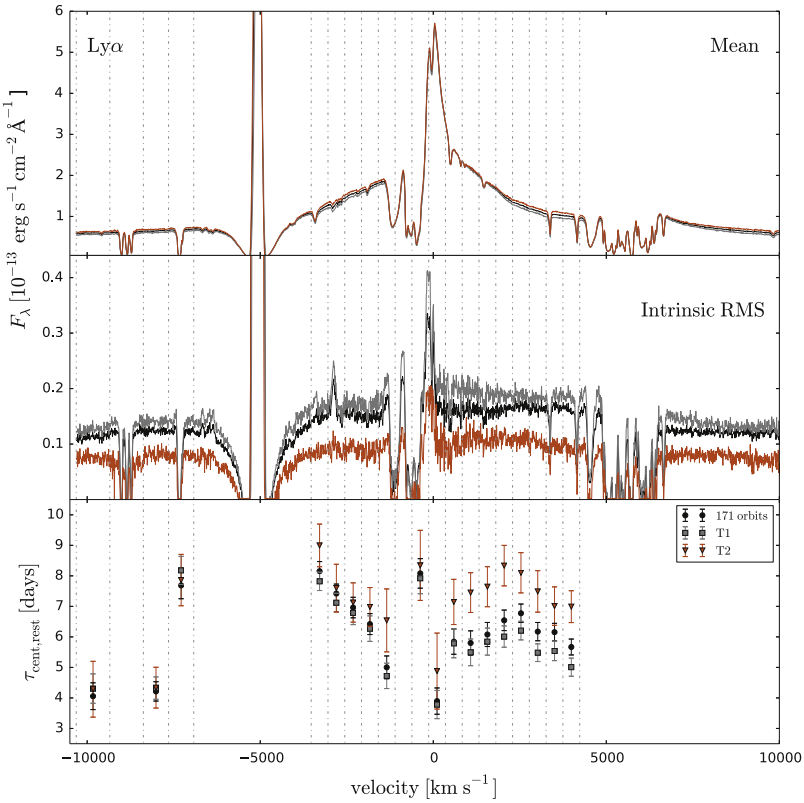

Figure 6. Velocity-binned results for the Lyα λ1215 emission line. The top and middle panels show the mean and intrinsic rms (σ_0) spectra, respectively. The bottom panel shows the centroid of the cross-correlation function for each individual velocity bin, corrected to the rest frame of NGC 5548. Velocity bins with no lag measurement contain too little total flux to reliably characterize the variations. In each case, the black line represents the entire dataset, and the T1 (first 85 visits) and T2 (last 86 visits) subsets are shown in gray and orange, respectively. The large gap at around −5000 km s^{-1} avoids the region of the spectrum affected by geocoronal emission and Galactic absorption.

+O I λ1304, C II λ1335, N IV] λ1486, O III] λ1663, and N III] λ1750. For the weaker lines, this is often the only component detected, so its flux, width, and position are all allowed to vary. For the stronger lines, as for the NLR components, we again keep the fluxes and widths of the intermediate-width components fixed at the values found for the STIS 2004 spectrum since Crenshaw et al. (2009) found that these components vary only slightly in flux over several years. For the stronger lines, we next include broader components with FWHM ≈ 3000, 8000, and 15,000 km s^{-1}, respectively. For the doublets of N V, Si IV, and C IV, we assume the line-emitting gas is optically thick and fix the flux ratio of each pair to 1:1, although for the 15,000 km s^{-1} component, only a single Gaussian is used. Finally, as can be seen in the rms spectrum in Figure 2, there are two weak bumps that appear on the red and blue wings of the C IV emission-line profile at ∼1554 and ∼1604 Å in the observed frame. These bumps are also present in the mean spectrum; we include a single Gaussian component to account for each of these bumps.

As described by Kaastra et al. (2014), we use an asymmetric Gaussian with negative flux to model the broad absorption troughs. The asymmetry in these Gaussian profiles is introduced by specifying a larger dispersion on the blue side of line center than on the red side. The asymmetry is fitted as a free parameter, and the resultant absorption line has a roughly rounded triangular shape with a blue wing extending from the deepest point in the absorption profile (for an illustration, see Kaastra et al. 2014). During the first part of our reverberation campaign, when these absorption features were strongest, an additional depression appeared on the high-velocity blue tail of the main absorption trough. We use a single, symmetric Gaussian to model the shape of this additional shallow depression. For absorption by N V, Si IV, and C IV, since the individual doublet profiles are unresolved, we assume the lines are optically thick, so each line in the doublet has the same strength and profile.

As a final component, we include absorption by damped Galactic Lyα with a column density of N(H I) = 1.45 × 10^{20} cm^{-2} (Wakker et al. 2011). The full spectral model for NGC 5548, excluding the narrow absorption, is shown in the upper panels of Figures 1 and 2, superposed on the observed mean spectra.[45] In future papers, we will apply this model to individual spectra to isolate the individual emission-line fluxes and to study absorption-line variability.

4. DISCUSSION

To put the results reported here in context, we note that NGC 5548 has been monitored in the UV for RM purposes on two previous occasions, as noted in Section 1.2. In 1989, NGC 5548 was observed once every four days for eight months with *IUE* (Clavel et al. 1991). In early 1993, it was observed

[45] The complete model of C IV showing each of the individual components appears in the Supplementary Materials that accompany Kaastra et al. (2014) at http://www.sciencemag.org/cgi/content/full/science.1253787/DC1.

every other day with *IUE* for a period of two months, and during the latter part of that campaign, it was also observed daily for 39 days with the *HST* Faint Object Spectrograph (Korista et al. 1995). The primary goals of these two experiments were quite different: the 1989 campaign was the first massive coordinated RM experiment and it was designed to measure the mean lags for the strong UV lines. The 1993 campaign was a higher time-resolution experiment that was designed to eliminate ambiguities from the 1989 campaign. Specifically, its goals were:

1. To measure the lag of the most rapidly responding line, He II λ1640.
2. To determine whether or not there is a lag between the UV and optical continuum variations.
3. To determine whether the wings and core of the C IV emission line have different lags.

The first of these goals was met, but in the case of the other two, the data only hinted at results that are being confirmed by this project (Paper II and Figure 5).

In addition to these RM programs, several *HST* COS spectra of NGC 5548 were obtained in 2013 with the primary goal of studying absorption features in the UV as support for an intensive X-ray monitoring program undertaken with *XMM-Newton* (Kaastra et al. 2014). Our own results on variable absorption features constitute an extension of that effort and will be the subject of a future paper.

Again, for broader context, during the AGN STORM campaign NGC 5548 was at about the same mean continuum luminosity as it was during the 1989 campaign (but with a somewhat lower amplitude of variability), somewhat brighter than in the 1993 campaign, and decidedly brighter than it was in 2013, which was near the end of a lower-than-normal state that lasted several years (Peterson et al. 2013). The resonance lines showed much more self-absorption in this campaign than in either the 1989 or 1993 observations, but less than seen in 2013. The emission-line lags were somewhat larger during the 1989 campaign and the emission-line fluxes were higher, at least in part on account of much lower absorption in 1989. The 1993 emission-line lags were similar to those obtained in this experiment, but again the line fluxes were larger, but less self-absorbed.

As already noted, the response of the emission lines becomes complicated during the second half of the present campaign. The He II λ1640 light curve seems to match the 1367 Å continuum most closely; this line responds primarily to continuum emission at $\lambda < 228$ Å, implying that the variations in the 1367 Å continuum provide a reasonable proxy for the behavior of the hydrogen-ionizing continuum ($\lambda < 912$ Å). He II arises closer to the central source than the other emission lines, and it is also the only non-resonance line. More detailed analysis will be undertaken once the He II λ4686 and Balmer-line results become available from our contemporaneous ground-based monitoring program (L. Pei et al. 2015, in preparation).

In addition to determining the geometry and kinematics of the BLR, we also wish to use these data to improve on previous estimates of the mass of the central black hole. However, the strong absorption in the blue wings of the resonance lines, which was very weak if even present in the 1989 and 1993 campaigns, precludes using simple measurements of the rms spectra (e.g., Peterson et al. 2004) to make a mass estimate. More detailed modeling that we hope will lead to a more accurate black hole mass will be undertaken in future papers.

To summarize briefly, we have presented the first results from a UV spectroscopic RM study of NGC 5548 undertaken with *HST* COS in 2014. We detect strong variations in the continuum and find clear delayed response of the strong emission lines, Lyα, N V, Si IV, C IV, and He II. A preliminary investigation shows that there is indeed a strong velocity-dependence of the emission-line lags, at least in the case of Lyα and C IV, although blending and strong resonance absorption will make interpretation challenging. However, we have also shown that a heuristic multicomponent model can account for virtually all the spectral features. In future contributions, we will use this model as a starting point to explore the UV spectral variations in detail. We will also undertake a similar analysis of contemporaneous optical spectra in an effort to more completely understand the BLR geometry and kinematics. In the accompanying Paper II, we combine the continuum light curve presented here with high-cadence observations with *Swift* for a similar reverberation study of the accretion disk structure in NGC 5548.

Support for *HST* program number GO-13330 was provided by NASA through a grant from the Space Telescope Science Institute, which is operated by the Association of Universities for Research in Astronomy, Inc., under NASA contract NAS5-26555. We are grateful for the dedication and hard work by the Institute staff to make this program a success. G.D.R., B.M.P., C. J.G., M.M.F., and R.W.P. are grateful for the support of the National Science Foundation through grant AST-1008882 to The Ohio State University. A.J.B. and L.P. have been supported by NSF grant AST-1412693. M.C.B. gratefully acknowledges support through NSF CAREER grant AST-1253702 to Georgia State University. K.D.D. is supported by an NSF Fellowship awarded under grant AST-1302093. R.E. gratefully acknowledges support from NASA under awards NNX13AC26G, NNX13AC63G, and NNX13AE99G. J.M.G. gratefully acknowledges support from NASA under award NNH13CH61C. P.B.H. is supported by NSERC. SRON is financially supported by NWO, the Netherlands Organization for Scientific Research. B.C. K. is partially supported by the UC Center for Galaxy Evolution. C.S.K. acknowledges the support of NSF grant AST-1009756. P. L. acknowledges support from Fondecyt grant #1120328. A.P. acknowledges support from a NSF graduate fellowship and a UCSB Dean's Fellowship. J.S.S. acknowledges CNPq, National Council for Scientific and Technological Development (Brazil) for partial support and The Ohio State University for warm hospitality. T.T. has been supported by NSF grant AST-1412315. T.T. and B.C.K. acknowledge support from the Packard Foundation in the form of a Packard Research Fellowship to T.T. T.T. thanks the American Academy in Rome and thee Observatory of Monteporzio Catone for kind hospitality. The Dark Cosmology Centre is funded by the Danish National Research Foundation. MV gratefully acknowledges support from the Danish Council for Independent Research via grant No. DFF 4002-00275. This research has made use of the NASA/IPAC Extragalactic Database (NED), which is operated by the Jet Propulsion Laboratory, California Institute of Technology, under contract with the National Aeronautics and Space Administration. The authors acknowledge with great sadness the loss of our long-time collaborator in the planning phases of this project, Professor David J. Axon, who passed away on 2012 April 5.

REFERENCES

Baldwin, J. A., Ferland, G. J., Korista, K. T., & Verner, D. 1995, ApJ, 455, L119
Barth, A. J., Bennert, V. N., Canalizo, G., et al. 2015, ApJS, 217, 26
Bentz, M. C., & Katz, S. 2015, PASP, 127, 67
Bentz, M. C., Peterson, B. M., Netzer, H., Pogge, R. W., & Vestergaard, M. 2009, ApJ, 697, 160
Bentz, M. C., Peterson, B. M., Pogge, R. W., Vestergaard, M., & Onken, C. A. 2006, ApJ, 644, 133
Bentz, M. C., Denney, K. D., Cackett, E. M., et al. 2007, ApJ, 662, 205
Bentz, M. C., Denney, K. D., Grier, C. J., et al. 2013, ApJ, 767, 149
Bentz, M. C., Horne, K., Barth, A. J., et al. 2010b, ApJ, 720, 46
Bentz, M. C., Walse, J. L., Barth, A. J., et al. 2010a, ApJ, 716, 993
Blandford, R. D., & McKee, C. F. 1982, ApJ, 255, 419
Bottorff, M., Korista, K. T., Shlosman, I., & Blandford, R. D. 1997, ApJ, 479, 200
Brewer, B. J., Treu, T., Pancoast, A., et al. 2011, ApJL, 733, L33
Cackett, E. M., & Horne, K. 2006, MNRAS, 365, 1180
Cackett, E. M., Horne, K., & Winkler, H. 2007, MNRAS, 380, 669
Capriotti, E. R., Foltz, C. B., & Byard, P. L. 1980, ApJ, 241, 903
Cardelli, J. A., Clayton, G. C., & Mathis, J. S. 1989, ApJ, 345, 245
Clavel, J., Wamsteker, W., & Glass, I. S. 1989, ApJ, 337, 236
Clavel, J., Boksenberg, A., Bromage, G. E., et al. 1990, MNRAS, 246, 668
Clavel, J., Reichert, G. A., Alloin, D., et al. 1991, ApJ, 366, 64
Collier, S. J., Crenshaw, D. M., Peterson, B. M., et al. 2001, ApJ, 561, 146
Collier, S. J., Horne, K., Kaspi, S., et al. 1998, ApJ, 500, 162
Crenshaw, D. M., & Kraemer, S. B. 1999, ApJ, 521, 572
Crenshaw, D. M., Kraemer, S. B., Schmitt, H. R., et al. 2009, ApJ, 698, 281
Crenshaw, D. M., Rodríguez-Pascual, P. M., Penton, S. V., et al. 1996, ApJ, 470, 322
De Rosa, G., Venemans, B. P., Decarli, R., et al. 2014, ApJ, 790, 145
Denney, K. D., Peterson, B. M., Pogge, R. W., et al. 2009, ApJL, 704, L80
Denney, K. D., Peterson, B. M., Pogge, R. W., et al. 2010, ApJ, 721, 715
Denney, K. D., De Rosa, K., Croxall, K., et al. 2014, ApJ, 796, 134
Done, C., & Krolik, J. H. 1996, ApJ, 463, 144
Edelson, R., Gelbord, J. M., Horne, K., et al. 2015, ApJ, 806, 129
Elvis, M. 2004, in ASP Conf. Ser. 311, AGN Physics with the Sloan Digital Sky Survey, ed. G. T. Richards & P. B. Hall (San Francisco, CA: ASP), 109
Ely, J., Massa, D., Ake, T., et al. 2011, COS FUV Gridwire Flat Field Template, Instrument Science Report COS 2011–03 (Baltimore: STScI)
Eracleous, M., & Halpern, J. P. 1994, ApJS, 90, 1
Eracleous, M., & Halpern, J. P. 2003, ApJ, 599, 886
Everett, J. E. 2003, in ASP Conf. Ser. 290, Active Galactic Nuclei: From Central Engine to Host Galaxy, ed. S. Collin, F. Combes, & I. Shlosman (San Francisco, CA: ASP), 199
Gehrels, N. 1986, ApJ, 303, 336
Gehrels, N., Chincarini, G., Giommi, P., et al. 2004, ApJ, 611, 1005
Gezari, S., Halpern, J. P., & Eracleous, M. 2007, ApJS, 169, 167
Green, J. C., Froning, C. S., Osterman, S., et al. 2012, ApJ, 744, 60
Greene, J. E., & Ho, L. C. 2005, ApJ, 630, 122
Grier, C. J., Peterson, B. M., Horne, K., et al. 2013, ApJ, 764, 47
Grupe, D., & Mathur, S. 2004, ApJL, 606, L41
Guerras, E., Mediavilla, E., Jimenez-Vicente, J., et al. 2013, ApJ, 764, 160
Hamann, F., & Sabra, B. 2004, in ASP Conf. Ser. 311, AGN Physics with the Sloan Digital Sky Survey, ed. G. T. Richards & P. B. Hall (San Francisco, CA: ASP), 203
Hernandez, S., et al. 2014, in STIS Instrument Handbook, Version 13.0 (Baltimore, MD: STScI)
Holland, S. T., et al. 2014, in Cosmic Origins Instrument Handbook, Version 6.0 (Baltimore, MD: STScI)
Horne, K. 1994, in ASP Conf. Ser. 69, Reverberation Mapping of the Broad-Line Region in Active Galactic Nuclei, ed. P. M. Gondhalekar, K. Horne, & B. M. Peterson (San Francisco, CA: ASP), 23
Horne, K., Peterson, B. M., Collier, S. J., & Netzer, H. 2004, PASP, 116, 465
Horne, K., Welsh, W. F., & Peterson, B. M. 1991, ApJL, 367, L5
Jarvis, M. J., & McLure, R. J. 2006, MNRAS, 369, 182
Kaastra, J., Kriss, G. A., Coppi, M., et al. 2014, Sci, 345, 64
Kaspi, S., Brandt, W. N., Maoz, D., et al. 2007, ApJ, 659, 997
Kaspi, S., Maoz, D., Netzer, H., et al. 2005, ApJ, 629, 61
Kaspi, S., & Netzer, H. 1999, ApJ, 524, 71
Kaspi, S., Smith., P. S., Netzer, H., et al. 2000, ApJ, 533, 631
Kelly, B. C., Bechtold, J., & Siemiginowska, A. 2009, ApJ, 698, 895
Kollatschny, W. 2003, A&A, 407, 461
Kollmeier, J., Onken, C. A., Kochanek, C. S., et al. 2006, ApJ, 648, 128
Komatsu, E., Smith, K. M., Dunkley, J., et al. 2011, ApJS, 192, 18
Korista, K. T., & Goad, M. R. 2000, ApJ, 586, 234
Korista, K. T., Alloin, D., Barr, P., et al. 1995, ApJS, 97, 285
Kozłowski, S., Kochanek, C. S., Udalski, A., et al. 2010, ApJ, 708, 927
Kriss, G. A., Arav, N., & Kaastra, J. 2011, A&A, 534, 41
Krolik, J. H., Horne, K., Kallman, T. R., et al. 1991, ApJ, 371, 541
Krongold, Y., Nicastro, F., Brickhouse, N. S., Elvis, M., & Mathur, S. 2005, ApJ, 622, 842
Krongold, Y., Nicastro, F., Elvis, M., et al. 2007, ApJ, 659, 1022
Lewis, K. T., Eracleous, M., & Storchi-Bergmann, T. 2010, ApJS, 187, 416
Massa, D., Ely, J., Osten, R., et al. 2014, Updated Absolute Flux Calibration of the COS FUV Modes, Instrument Science Report COS 2013–09 (Baltimore: STScI)
MacLeod, C. L., Ivezić, Z., Kochanek, C. S., et al. 2010, ApJ, 721, 1014
MacLeod, C. L., Ivezić, Z., Sesar, B., et al. 2012, ApJ, 753, 106
Marconi, A., Axon, D. J., Maiolino, R., et al. 2008, ApJ, 678, 693
Mathur, S., & Grupe, D. 2005, A&A, 432, 463
McLure, R. J., & Jarvis, M. J. 2002, MNRAS, 337, 109
McGill, K. L., Woo, J.-H, Treu, T., & Malkan, M. A. 2008, ApJ, 673, 703
McHardy, I. M., Cameron, D. T., Dwelly, T., et al. 2014, MNRAS, 444, 1469
Murray, N., & Chiang, J. 1997, ApJ, 474, 91
Netzer, H., & Marziani, P. 2010, ApJ, 724, 318
Netzer, H., & Trakhtenbrot, B. 2014, MNRAS, 438, 672
O'Brien, P. T., Dietrich, M., Leighly, K., et al. 1998, ApJ, 509, 163
Pancoast, A., Brewer, B. J., Treu, T., et al. 2014, MNRAS, 445, 3073
Pancoast, A., Brewer, B. J., Treu, T., et al. 2012, ApJ, 754, 49
Park, D., Woo, J.-H., Bennert, V. N., et al. 2015, ApJ, 799, 164
Park, D., Woo, J.-H., Denney, K. D., & Shin, J. 2013, ApJ, 770, 87
Park, D., Woo, J.-H., Treu, T., et al. 2012, ApJ, 747, 30
Peterson, B. M. 1993, PASP, 105, 247
Peterson, B. M. 2014, SSRv, 183, 253
Peterson, B. M., & Wandel, A. 1999, ApJL, 521, L95
Peterson, B. M., & Wandel, A. 2000, ApJL, 540, L13
Peterson, B. M., Wanders, I., Horne, K., et al. 1998, PASP, 110, 660
Peterson, B. M., Berlind, P., Bertram, R., et al. 2002, ApJ, 581, 197
Peterson, B. M., Bentz, M. C., Desroches, L.-B., et al. 2005, ApJ, 641, 638
Peterson, B. M., Denney, K. D., De Rosa, G., et al. 2013, ApJ, 779, 109
Peterson, B. M., Ferrarese, L., Gilbert, K. M., et al. 2004, ApJ, 613, 682
Peterson, B. M., Grier, C. J., Horne, K., et al. 2014, ApJ, 795, 149
Proga, D., Stone, J. M., & Kallman, T. R. 2000, ApJ, 543, 686
Reichert, G. A., Rodríguez-Pascual, P. M., Alloin, D., et al. 1994, ApJ, 425, 582
Rodríguez-Pascual, P. M., Alloin, D., Clavel, J., et al. 1997, ApJS, 110, 9
Salviander, S., Shields, G. A., Gebhardt, K., & Bonning, E. W. 2007, ApJ, 662, 128
Sahnow, D., Oliveira, C., Aloisi, A., et al. 2011, SPIE, 8145, 0
Schlafly, E. F., & Finkbeiner, D. 2011, ApJ, 737, 103
Schlegel, D. J., Finkbeiner, D. P., & Davis, M. 1998, ApJ, 500, 525
Scott, A. E., Brandt, W. N., Behar, E., et al. 2014, ApJ, 797, 105
Sergeev, S. G., Doroshenko, V. T., Dzyuba, S. A., et al. 2007, ApJ, 668, 708
Sergeev, S. G., Doroshenko, V. T., Golubinskiy, Yu. V., Merkulova, N. I., & Sergeeva, E. A. 2005, ApJ, 622, 129
Shappee, B. J., Prieto, J. L., Grupe, D., et al. 2014, ApJ, 788, 48
Shen, Y., Richards, G. T., Strauss, M. A., et al. 2011, ApJS, 194, 45
Shields, G. A., Gebhardt, K., Salviander, S., et al. 2003, ApJ, 583, 124
Smith, J. E., Robinson, A., Alexander, D. M., et al. 2004, MNRAS, 350, 140
Strateva, I. V., Strauss, M. A., Hao, L., et al. 2003, AJ, 126, 1720
Treu, T., Woo, J.-H., Malkan, M. A., & Blandford, R. D. 2007, ApJ, 667, 117
Ulrich, M.-H., & Horne, K. 1996, MNRAS, 283, 748
Vestergaard, M. 2002, ApJ, 571, 733
Vestergaard, M. 2004, ApJ, 601, 676
Vestergaard, M., Fan, X., Tremonti, C. A., Osmer, P. S., & Richards, G. T. 2008, ApJL, 674, L1
Vestergaard, M., & Osmer, P. S. 2009, ApJ, 699, 800
Vestergaard, M., & Peterson, B. M. 2006, ApJ, 641, 689
Vestergaard, M., Wilkes, B. J., & Barthel, P. D. 2000, ApJ, 302, 56
Wakker, B. P., Lockman, F. J., & Brown, J. M. 2011, ApJ, 728, 159
Wanders, I., Goad, M. R., Korista, K. T., et al. 1995, ApJ, 453, 74
Wanders, I., Peterson, B. M., Alloin, D., et al. 1997, ApJS, 113, 69
Wills, B. J., Netzer, H., & Wills, D. 1985, ApJ, 288, 94
Wills, B. J., & Browne, I. W. A. 1986, ApJ, 302, 56
Young, S., Axon, D. J., Robinson, A., Hough, J. H., & Smith, J. E. 2007, Natur, 450, 74
Zu, Y., Kochanek, C. S., & Peterson, B. M. 2011, ApJ, 735, 80

SPACE TELESCOPE AND OPTICAL REVERBERATION MAPPING PROJECT. II. SWIFT AND HST REVERBERATION MAPPING OF THE ACCRETION DISK OF NGC 5548

The Astrophysical Journal, 806:129 (14pp), 2015 June 10 doi:10.1088/0004-637X/806/1/129

SPACE TELESCOPE AND OPTICAL REVERBERATION MAPPING PROJECT. II. *SWIFT* AND *HST* REVERBERATION MAPPING OF THE ACCRETION DISK OF NGC 5548

R. Edelson[1], J. M. Gelbord[2,3], K. Horne[4], I. M. McHardy[5], B. M. Peterson[6,7], P. Arévalo[8], A. A. Breeveld[9], G. De Rosa[6,7,10], P. A. Evans[11], M. R. Goad[11], G. A. Kriss[10,12], W. N. Brandt[13], N. Gehrels[14], D. Grupe[15], J. A. Kennea[13], C. S. Kochanek[6,7], J. A. Nousek[13], I. Papadakis[16,17], M. Siegel[13], D. Starkey[4], P. Uttley[18], S. Vaughan[11], S. Young[1], A. J. Barth[19], M. C. Bentz[20], B. J. Brewer[21], D. M. Crenshaw[20], E. Dalla Bontà[22,23], A. De Lorenzo- Cáceres[4], K. D. Denney[6,7,40], M. Dietrich[24,25], J. Ely[10], M. M. Fausnaugh[6], C. J. Grier[6,13], P. B. Hall[26], J. Kaastra[27,28,29], B. C. Kelly[30], K. T. Korista[31], P. Lira[32], S. Mathur[6,7], H. Netzer[33], A. Pancoast[30], L. Pei[20], R. W. Pogge[6,7], J. S. Schimoia[6,34], T. Treu[30,35,41], M. Vestergaard[36,37], C. Villforth[4], H. Yan[38], and Y. Zu[6,39]

[1] Department of Astronomy, University of Maryland, College Park, MD 20742-2421, USA
[2] Spectral Sciences Inc., 4 Fourth Avenue, Burlington, MA 01803, USA
[3] Eureka Scientific Inc., 2452 Delmer St. Suite 100, Oakland, CA 94602, USA
[4] SUPA Physics and Astronomy, University of St. Andrews, Fife, KY16 9SS Scotland, UK
[5] University of Southampton, Highfield, Southampton, SO17 1BJ, UK
[6] Department of Astronomy, The Ohio State University, 140 W 18th Ave, Columbus, OH 43210, USA
[7] Center for Cosmology and AstroParticle Physics, The Ohio State University, 191 West Woodruff Ave, Columbus, OH 43210, USA
[8] Instituto de Física y Astronomía, Facultad de Ciencias, Universidad de Valparaíso, Gran Bretana N 1111, Playa Ancha, Valparaíso, Chile
[9] Mullard Space Science Laboratory, University College London, Holmbury St. Mary, Dorking, Surrey RH5 6NT, UK
[10] Space Telescope Science Institute, 3700 San Martin Drive, Baltimore, MD 21218, USA
[11] University of Leicester, Department of Physics and Astronomy, Leicester, LE1 7RH, UK
[12] Department of Physics and Astronomy, The Johns Hopkins University, Baltimore, MD 21218, USA
[13] Department of Astronomy and Astrophysics, Eberly College of Science, Penn State University, 525 Davey Laboratory, University Park, PA 16802, USA
[14] Astrophysics Science Division, NASA Goddard Space Flight Center, Greenbelt, MD 20771, USA
[15] Space Science Center, Morehead State University, 235 Martindale Drive, Morehead, KY 40351, USA
[16] Department of Physics and Institute of Theoretical and Computational Physics, University of Crete, GR-71003 Heraklion, Greece
[17] IESL, Foundation for Research and Technology, GR-71110 Heraklion, Greece
[18] Astronomical Institute "Anton Pannekoek," University of Amsterdam, Postbus 94249, NL-1090 GE Amsterdam, The Netherlands
[19] Department of Physics and Astronomy, 4129 Frederick Reines Hall, University of California, Irvine, CA 92697
[20] Department of Physics and Astronomy, Georgia State University, 25 Park Place, Suite 605, Atlanta, GA 30303, USA
[21] Department of Statistics, The University of Auckland, Private Bag 92019, Auckland 1142, New Zealand
[22] Dipartimento di Fisica e Astronomia "G. Galilei," Università di Padova, Vicolo dell'Osservatorio 3, I-35122 Padova, Italy
[23] INAF-Osservatorio Astronomico di Padova, Vicolo dell'Osservatorio 5 I-35122, Padova, Italy
[24] Department of Physics and Astronomy, Ohio University, Athens, OH 45701, USA
[25] Department of Physical and Earth Sciences, Worcester State University, 486 Chandler Street, Worcester, MA 01602, USA
[26] Department of Physics and Astronomy, York University, Toronto, ON M3J 1P3, Canada
[27] SRON Netherlands Institute for Space Research, Sorbonnelaan 2, 3584 CA Utrecht, The Netherlands
[28] Department of Physics and Astronomy, Univeristeit Utrecht, P.O. Box 80000, 3508 Utrecht, The Netherlands
[29] Leiden Observatory, Leiden University, P.O. Box 9513, 2300 RA Leiden, The Netherlands
[30] Department of Physics, University of California, Santa Barbara, CA 93106, USA
[31] Department of Physics, Western Michigan University, 1120 Everett Tower, Kalamazoo, MI 49008-5252, USA
[32] Departamento de Astronomia, Universidad de Chile, Camino del Observatorio 1515, Santiago, Chile
[33] School of Physics and Astronomy, Raymond and Beverly Sackler Faculty of Exact Sciences, Tel Aviv University, Tel Aviv 69978, Israel
[34] Instituto de Física, Universidade Federal do Rio do Sul, Campus do Vale, Porto Alegre, Brazil
[35] Department of Physics and Astronomy, University of California, Los Angeles, CA 90095-1547, USA
[36] Dark Cosmology Centre, Niels Bohr Institute, University of Copenhagen, Juliane Maries Vej 30, DK-2100 Copenhagen, Denmark
[37] Steward Observatory, University of Arizona, 933 North Cherry Avenue, Tucson, AZ 85721, USA
[38] Department of Physics and Astronomy, University of Missouri, Columbia, MO 65211, USA
[39] Department of Physics, Carnegie Mellon University, 5000 Forbes Avenue, Pittsburgh, PA 15213, USA
Received 2015 January 23; accepted 2015 April 3; published 2015 June 12

ABSTRACT

Recent intensive *Swift* monitoring of the Seyfert 1 galaxy NGC 5548 yielded 282 usable epochs over 125 days across six UV/optical bands and the X-rays. This is the densest extended active galactic nucleus (AGN) UV/optical continuum sampling ever obtained, with a mean sampling rate <0.5 day. Approximately daily *Hubble Space Telescope* UV sampling was also obtained. The UV/optical light curves show strong correlations ($r_{\max} = 0.57 - 0.90$) and the clearest measurement to date of interband lags. These lags are well-fit by a $\tau \propto \lambda^{4/3}$ wavelength dependence, with a normalization that indicates an unexpectedly large disk radius of $\sim 0.35 \pm 0.05$ lt-day at 1367 Å, assuming a simple face-on model. The *U* band shows a marginally larger lag than expected from the fit and surrounding bands, which could be due to Balmer continuum emission from the broad-line region as suggested by Korista and Goad. The UV/X-ray correlation is weaker ($r_{\max} < 0.45$) and less consistent over time. This indicates that while *Swift* is beginning to measure UV/optical lags in general agreement with accretion disk theory (although the derived size is larger than predicted), the relationship with X-ray variability is less well understood. Combining this accretion disk size estimate with those from quasar microlensing studies suggests that AGN disk sizes scale approximately linearly with central black hole mass over a wide range of masses.

[40] NSF Postdoctoral Research Fellow.
[41] Packard Fellow.

Key words: galaxies: active – galaxies: individual (NGC 5548) – galaxies: nuclei – galaxies: Seyfert

Supporting material: machine-readable tables

1. INTRODUCTION

Because of their great distances and small sizes, the central regions of active galactic nuclei (AGNs) cannot be resolved directly with current technology. Thus it is necessary to use indirect methods to gain information about AGN structure and physical conditions. Variability studies, along with gravitational microlensing (e.g., Morgan et al. 2010; Mosquera et al. 2013; Blackburne et al. 2014; Jiminez-Vicente et al. 2014), have emerged as powerful techniques for probing the central regions of AGNs.

In particular, the "reverberation mapping" (RM) technique (Blandford & McKee 1982) has proven quite effective at taking advantage of strong AGN line and continuum variability to probe the structure of the broad emission line region (BLR). The fundamental idea of RM is that if the variability in band B is powered by variability in band A, with only light travel times affecting the light curves, then variations in band A will be seen in band B, but delayed and smoothed by the size and geometry of the latter emitting region. The first unambiguous application of RM came in an *IUE* campaign on the Seyfert 1 galaxy NGC 5548, which found that variations in the driving UV continuum (band A in this picture) were highly correlated with those in emission lines such as C IV line (band B). The line variations lagged the continuum by ∼10 days, indicating that the C IV-emitting region was of order 10 lt-days in size (Clavel et al. 1991). Optical emission lines showed similarly strong correlation but with larger lags. For example, Hβ showed a lag of ∼20 days (Peterson et al. 1991), indicating a stratified BLR in which higher-ionization lines are formed closer to the central engine. The distance estimate, when combined with the line width, allows estimation of the mass of the central black hole. For NGC 5548 the current best mass estimate is $M_{\rm BH} \sim 3.2{\times}10^7\,M_\odot$ (Denney et al. 2010; Pancoast et al. 2014). This technique is now a standard tool for AGN astronomy, yielding BLR size, stratification information and black hole mass estimates and physical conditions for ∼50 AGNs (see, e.g., Bentz & Katz 2015 for a recent compilation). For a more extensive general discussion of BLR RM, please see the first paper in this series (de Rosa 2015; Paper I hereafter).

The structure and physics of the central engine that produces the continuum emission is currently less well understood than the reverberation-mapped BLR. Observations and accretion disk theory both suggest that the inner accretion disk/corona region emits short wavelength continuum, i.e., X-ray, ultraviolet (UV hereafter), and much of the optical, which then illuminates and ionizes the gas in the more distant BLR and beyond. The prevailing picture is that the black hole is surrounded by a small, hot ($T \sim 10^9$ K), and relatively spherical corona and a larger, cooler ($T_{\rm max} \sim 5 \times 10^5$ K), and relatively flat accretion disk (e.g., Haardt & Maraschi 1991). Gravitational lensing studies also indicate that this putative corona is small enough to be considered point-like relative to the disk (∼5$R_{\rm Sch}$; Dai et al. 2010; Morgan et al. 2012; Mosquera et al. 2013; Blackburne et al. 2014, 2015). The energy released by the accretion process heats both the optically thick disk—producing the thermal UV/optical emission—and the corona, which in turn can illuminate the disk as an external heating source. The fraction of the energy that goes into heating the corona has not been established and therefore it is not clear whether the disk is mainly heated internally or externally. In either case, however, the disk is expected to have a stratified temperature structure with the hotter, UV-emitting regions closer in and the cooler, optically-emitting regions farther out. Quasar microlensing studies find that accretion disk sizes increase with wavelength (e.g., Poindexter et al. 2008), supporting this picture. We note, however, that this picture contains important unreconciled discrepancies. For instance gravitational lensing disk sizes are typically reported to be a factor of ∼4 larger than predicted (e.g., Morgan et al. 2010), and the observed UV spectrum is too steep with a Lyman discontinuity that is typically smaller than predicted or not seen (e.g., Koratkar & Blaes 1999; Collin 2001). Recent improvements in AGN accretion disk models (e.g., Dexter & Agol 2011) may overcome these difficulties, but see also Antonucci (2013).

Just as RM of the BLR allows us to estimate the distances at which each line is formed, RM of the accretion disk could allow us to constrain the temperature structure of the disk and test the standard α-disk model (Shakura & Sunyaev 1973 or any other predictive model). Repeated efforts have been made to implement RM of the accretion disk by correlating X-ray light curves gathered with space-based observatories with optical light curves typically from ground-based observatories (e.g., Edelson et al. 1996; Nandra et al. 1998; Suganuma et al. 2006; Arévalo et al. 2008, 2009; Breedt et al. 2009, 2010; Cameron et al. 2012; Gliozzi et al. 2013). However the optical time resolution of these early experiments was typically limited by the diurnal cycle to $\Delta T > 1$ day, resulting in lag measurements that were suggestive but not statistically significant ($1 - 2\sigma$), although often in the expected sense, with X-rays leading the optical. Other experiments from this period used *Hubble Space Telescope* (*HST*; Edelson et al. 2000) or *XMM-Newton* (Mason et al. 2002) to attain finer optical time resolution at the cost of shorter monitoring periods (∼1–2 days). Again the results were suggestive but inadequate to make a definitive lag measurement. Further, these experiments typically only sampled a single optical or UV band, and thus were unable to explore temperature stratification in the disk. Ground-based multicolor optical/IR studies also yielded tentative evidence of shorter wavelength variations leading longer wavelength variations in some AGNs (Sergeev et al. 2005; Cackett et al. 2007; Lira et al. 2011).

The unique capabilities of the *Swift* observatory (Gehrels et al. 2004), originally optimized to detect γ-ray burst counterparts, are also ideally suited for AGN monitoring. Its rapid slew/acquisition times and large sky coverage make it feasible to sample AGN light curves (which show variability over a broad range of temporal frequencies) with high cadence over a long duration. Further, the coaligned UltraViolet-Optical Telescope (UVOT; Roming et al. 2005) and X-Ray Telescope (XRT; Burrows et al. 2005) cover the entire energy range of interest (the X-ray/UV/optical) with a single space-based telescope, so data quality is no longer limited by the diurnal cycle or weather.

This is leading to important advances in accretion disk RM, as highlighted by the success of two recent *Swift* AGN

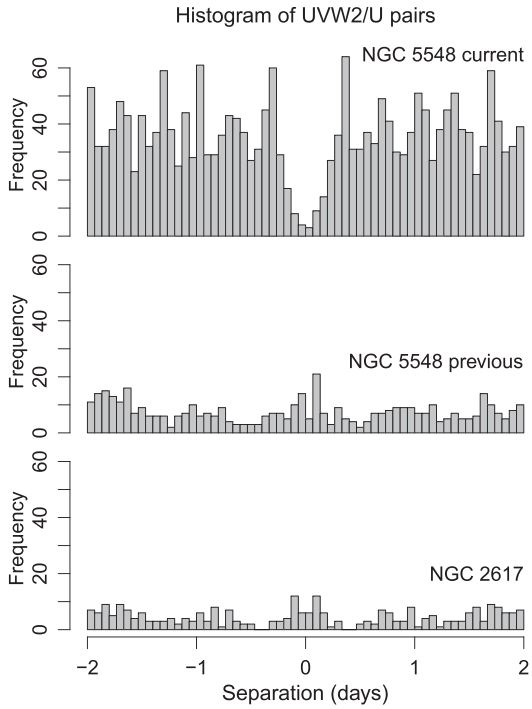

Figure 1. Histograms showing the number of *UVW2/U* pairs for the current intensive NGC 5548 monitoring campaign (top), the earlier NGC 5548 campaign (middle, McHardy et al. 2014), and the NGC 2617 campaign (bottom, Shappee et al. 2014). Data are binned by orbit, and all pairs with separations of less than half an orbit are excluded. *UVW2* was used because it was the most frequently observed UVOT band, while *U*, a typically less-well sampled band, was used because that band is particularly interesting (see Section 4.2). The range ± 2 days is shown because this is the key cadence range that has not previously been well sampled. Note that the current campaign samples these short cadences ∼5–8 times more frequently than the previous NGC 5548 and NGC 2617 campaigns.

monitoring campaigns. After detecting from the ground that the relatively normal galaxy NGC 2617 had transitioned into a Seyfert 1, Shappee et al. (2014) used *Swift* to cover a ∼50 day period with approximately daily cadence, generally in all six UVOT filters. Ground-based optical/infrared coverage of the first part of this period was obtained at a lower cadence. McHardy et al. (2014) analyzed 359 "visits" (separated by 1 orbit or longer; see Section 2.1) to the archetypical Seyfert 1 galaxy NGC 5548, over ∼2 years (2012 February–2014 February). Approximately 20% of the visits utilized all six filters. In both cases, the data show significant ($>3\sigma$) interband lags throughout the UV/optical, with increasing lags to longer wavelengths, consistent with a $\lambda^{4/3}$ dependence as predicted by the standard α-disk model under the assumption that time lags are dominated by light travel times.

The experiment detailed herein combines *Swift*'s powerful capabilities with simultaneous, intensive UV spectroscopic monitoring by *HST* to yield the densest X-ray/UV/optical coverage—in both time and wavelength—ever obtained. NGC 5548 is the target of this campaign. Figure 1 shows that this campaign yields a factor of ∼2.5–4 improvement in the number of UVOT filter data pairs available for correlation compared to the two best previous campaigns. This provides superior power to measure small (<2 day) interband lags with high precision.

The result, presented in this paper, is a clear measurement of lags across the entire UV/optical range, with shorter wavelength bands leading the longer wavelength bands. The timescales generally increase to longer wavelengths as expected for a standard α-disk, but direct fitting indicates a larger than expected disk (∼0.35 ± 0.05 lt-day at 1367 Å). The *U*-band lag is slightly longer than expected from the fits, apparently consistent with contamination from BLR continuum emission as predicted by Korista & Goad (2001). The X-rays show a relatively weak and less coherent relation to the UV/optical. Finally combining RM and microlensing disk size estimates suggest that disk size scales roughly linearly with black hole mass over a wide range of masses.

This paper is organized as follows. Section 2 describes the observations and data reduction, Section 3 presents cross-correlation analyses applied to these data, Section 4 discusses the theoretical implications of these results, and Section 5 concludes with a brief summary of this work and implications for the future.

2. OBSERVATIONS AND DATA REDUCTION

2.1. Observations

The target of this experiment, NGC 5548 ($z = 0.01717$; de Vaucouleurs et al. 1991), shows strong, reliable variability across the entire X-ray/UV/optical wavelength range accessible to *Swift*. It is also among the brightest AGN in the sky at these wavelengths. In 2014 February–June, *Swift* executed a monitoring campaign on NGC 5548 that was ground-breaking in two respects: 1) it was comprised of 360 separate visits over a ∼4 month period, of which 282 successful visits were obtained, for a sampling rate (after removing bad data) better than one visit every ∼0.5 day, and 2) it utilized all six UVOT filters (Poole et al. 2008) in each visit, with 239 (84%) providing usable measurements in all six filters. (For the purposes of this paper, a visit is defined as an observation in which at least one UVOT filter measurement is obtained. Multiple observations within a single ∼96 minute orbit are combined to form a single visit.) This entailed a significant commitment of spacecraft resources given the limit of 500 time-critical non-GRB guest investigator visits per year and the desire to minimize wear on the filter wheel.[42]

In addition, a parallel *HST* emission-line RM campaign yielded daily UV spectroscopic monitoring of NGC 5548 over a slightly longer period (see Paper I). This provided mutual synergies: the *HST* 1367 Å continuum light curve was used in the cross-correlation functions (CCFs) reported herein, while the *Swift* optical, ultraviolet, and X-ray light curves can be used to better define the continuum variability characteristics needed to understand the emission-line RM results.

These observations are summarized in Table 1. Start and stop times for *Swift* observations are originally recorded in MET (Mission Elapsed Time; seconds since the start of 2001) and corrected for the drift of the onboard *Swift* clock and leap-seconds. These times were averaged and converted to Heliocentric Julian Date (HJD), the standard for this observing campaign. Throughout this paper we utilize the truncated HJD, defined as THJD = HJD − 2,456,000. We reduced all *Swift* data on NGC 5548 for both the UVOT and XRT, but restricted scientific analysis to observations taken during the intensive

[42] http://swift.gsfc.nasa.gov/proposals/tech_appd/swiftta_v11/node42.html

Table 1
Monitoring Information

(1) Band	(2) Central λ (Å)	(3) Wavelength Range (Å)	(4) Number of Points	(5) Sampling Rate (days)
HX	4.4	1.2–15.5	272	0.46
SX	25.3	15.5–41.3	272	0.46
HST	1367	1364.5–1369.5	121	1.03
UVW2	1928	1650–2250	262	0.47
UVM2	2246	2000–2500	254	0.49
UVW1	2600	2250–2950	266	0.47
U	3465	3050–3900	266	0.47
B	4392	3900–4900	265	0.47
V	5468	5050–5800	258	0.48

Note. Column 1: Observing band name. Column 2: Central wavelength of that band. Column 3: FWHM wavelength range of that band, estimated from Poole et al. (2008). Column 4: Total number of good data points in that band. Column 5: Mean sampling rate in that band.

monitoring period, from THJD 706 to THJD 831 (approximately 2014 February 17.5–June 22.5 UTC).

The *HST* 1367 Å data reduction is detailed in Paper I. The following two subsections will describe the reduction of the *Swift* UVOT and XRT data.

2.2. UVOT Data Reduction

Swift observed NGC 5548 for a total of 2935 exposures in six UVOT filters from the beginning of the mission through THJD 876. All UVOT data were reprocessed for uniformity, applying standard FTOOLS utilities (Blackburn 1995; from version 6.15.1 of HEASOFT[43]). The astrometry of each field was refined using up to 35 isolated field stars drawn from the *HST* GSC 2.3.2 (Lasker et al. 2008) and Tycho-2 (Høg et al. 2000) catalogs, yielding residual offsets that were typically ∼0.3 arcsec. Fluxes were measured using a 5 arcsec circular aperture and concentric 40–90 arcsec regions were used to measure the sky background level. The final values include corrections for aperture losses, coincidence losses, and variation in the detector sensitivity across the image plane. The galaxy contributes a fraction of the observed flux within the UVOT apertures (see Section 4.4) but no attempt was made to remove the contribution of host galaxy flux, as this contamination is constant and will not affect measurement of interband temporal correlations or absolute variability amplitudes.

We screened the data to eliminate exposures affected by significant tracking errors. To identify observations with distortions in the wings of their point-spread function (PSF), we measured the ratio of counts in annuli from 5 to 7 and 7 to 10 arcsec, determined the distribution of these ratios for each filter, and discarded any observations that were found to be outliers by at least 3.5σ (defined iteratively). In addition, we measured the PSFs of the isolated field stars used for astrometric refinement, flagging any observations for which either the average PSF FWHM differed by more than 1.0 arcsec from the nominal UVOT FWHM (2.2–2.9 arcsec depending upon the filter; Breeveld et al. 2010) or the average FWHM of the stellar PSF projections along the *X* and *Y* axes differed by more than 0.75 arcsec. All flagged observations were manually inspected, leading to the rejection of one additional exposure in which the stars were streaks 15 arcsec long. In total, 30 exposures are rejected.

The resulting light curves exhibited occasional, anomalously low points, especially in the UV. Subsequent investigation found that these "dropouts" occur when the source falls within specific regions of the detector. Data potentially affected by these suspect detector regions are identified and removed using a new methodology discussed in the Appendix, eliminating 7.4% of the exposures. Finally we combined fluxes and errors in quadrature so there is no more than one data point per filter per orbit for any orbit in which multiple measurements were made in the same filter. The final light curves are presented in Figure 2 and data from the full mission are given in Table 2.

2.3. XRT Data Reduction

The *Swift* XRT data were gathered in photon counting mode and analyzed using the tools described by Evans et al. (2009)[44] to produce light curves which are fully corrected for instrumental effects such as pile up, dead regions on the CCD and vignetting. We generated soft X-ray (SX; 0.3–0.8 keV) and hard X-ray (HX; 0.8–10 keV) light curves. We utilized "snapshot" binning, which produces one bin for each spacecraft orbit. As with the UVOT data, we averaged multiple ObsIDs within a single orbit in quadrature. We investigated the use of other bands by subdividing HX into 0.8–2.8 keV and 2.8–10 keV but made no change after finding the correlation properties of the sub-bands to be very similar to the original choice.

The gap in the X-ray light curves during THJD 812–819 (2014 June 4–10; Figure 2) corresponds to the time that the *Swift* XRT was in an anomaly state (Burrows et al. 2014a, 2014b; Kennea & Burrows 2014b), during which time XRT was either disabled or collected data in a non-standard, not-fully calibrated mode. We excluded the data taken during this time interval from our analysis. We additionally excluded all visits where the total good integration time was less than 120 sec. This resulted in a final light curve having 272 X-ray points over the 125 day intensive monitoring period (see Table 1). The complete NGC 5548 XRT data are presented in Table 3.

2.4. Light Curves

Although the *Swift* data for NGC 5548 span many years, Figure 2 and Table 1 cover only the ∼125 day intensive monitoring period THJD 706–831. The light curves are presented in order of descending frequency with the highest frequency band at the top and the lowest at the bottom. The *HST* light curve plays a critical role as the only data set not gathered by *Swift*. This means that CCFs relative to this band will not suffer from "correlated errors" (see Edelson & Krolik 1988). The *HST* light curve also has much higher signal-to-noise ratios and better exclusion of BLR emission than the *Swift* data, but with less than half the sampling cadence.

3. INTERBAND CORRELATION AND VARIABILITY ANALYSES

In this section we estimate the interband correlation and lag between continuum bands. Before performing these correlation

[43] http://heasarc.gsfc.nasa.gov/ftools/

[44] http://www.swift.ac.uk/user_objects.

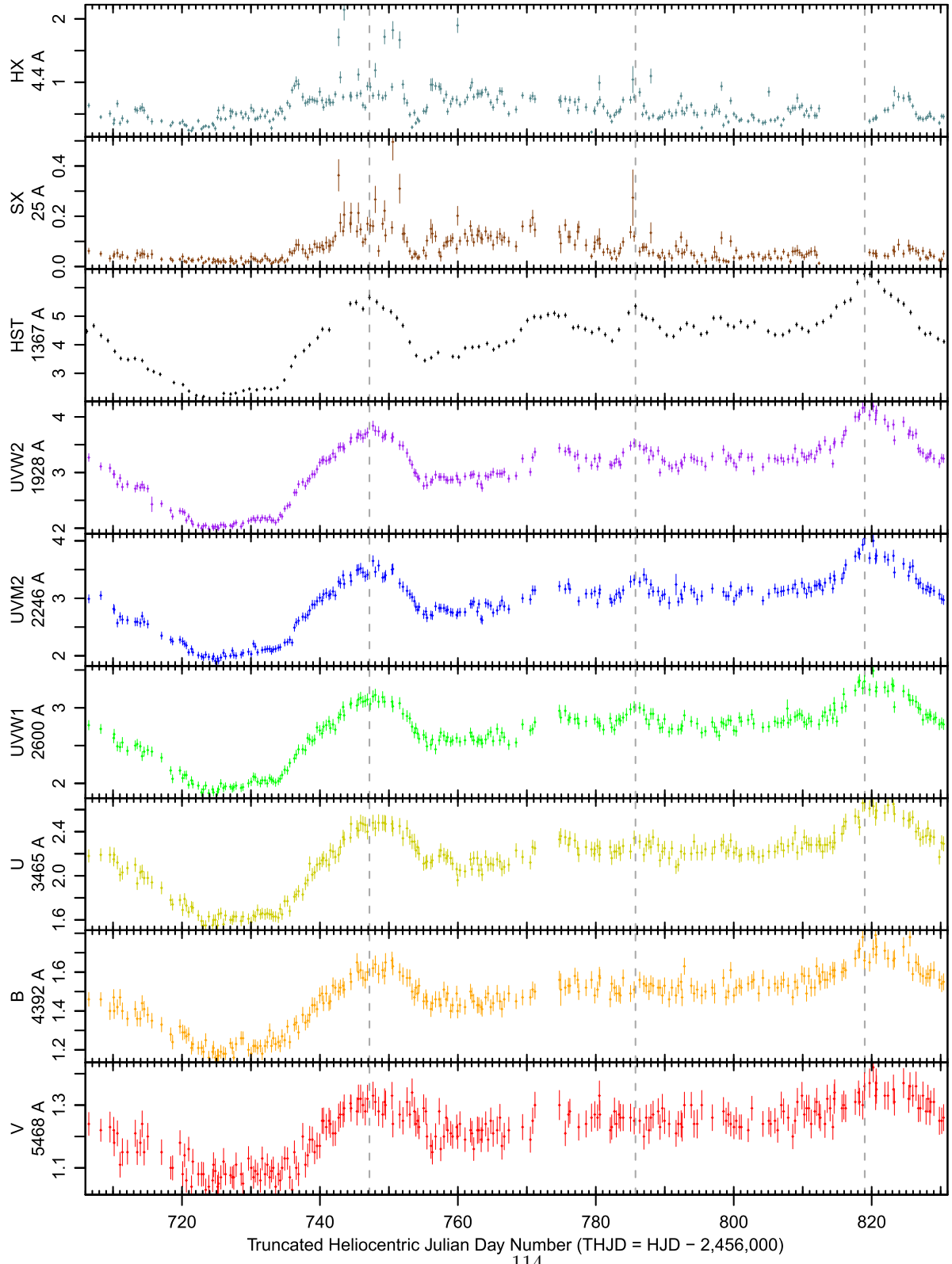

Figure 2. Light curves for the intensive monitoring period (HJD 2,456,706–2,456,831), going from shortest wavelength (top) to longest (bottom). The band name and central wavelength are given on the left of each panel. Top two panels show the *Swift* hard and soft X-ray (HX and SX, respectively) light curves, in units of c/s. Third panel shows the *HST* light curve, in units of 10^{-14} erg cm^{-2} s^{-1} Å^{-1}. Error bars for this light curve are typically ∼1.5%, just barely visible in the plot. The bottom six panels show the *Swift* light curves, again in units of 10^{-14} erg cm^{-2} s^{-1}Å^{-1} . Dashed gray lines show times THJD 747.179, 785.752 and 818.993, three local maxima of the *HST* light curve.

Table 2
UVOT Data

(1) HJD	(2) Filter	(3) Flux	(4) Error
2454270.833	*UVW2*	0.625	0.018
2454270.905	*UVW2*	0.632	0.015
2454276.539	*UVW2*	0.671	0.017
2454276.606	*UVW2*	0.663	0.017
2454283.359	*UVW2*	0.701	0.019
2454283.427	*UVW2*	0.701	0.019
2454283.492	*UVW2*	0.707	0.020
2454290.329	*UVW2*	0.802	0.023
2454290.378	*UVW2*	0.796	0.020
2454290.445	*UVW2*	0.796	0.020

Note. Column 1: Heliocentric Julian Date. Column 2: Observing Filter. Column 3: Measured flux in units of 10^{-14} erg cm^{-2} s^{-1} Å^{-1}. Column 4: Measured 1σ error in the same units. Note that this table includes all usable *Swift* observations of NGC 5548, not just those from the intensive monitoring period. The data are sorted first by filter, then by HJD. Only a portion of this table is shown here to demonstrate its form and content.

(This table is available in its entirety in machine-readable form.)

Table 3
XRT Data

(1) HJD	(2) HX Flux	(3) HX Error	(4) SX Flux	(5) SX Error
2453468.872	0.324	0.039	0.093	0.023
2453469.005	0.361	0.051	0.061	0.021
2453469.139	0.282	0.049	0.156	0.042
2453470.283	0.425	0.057	0.114	0.030
2453470.349	0.343	0.037	0.075	0.019
2453470.418	0.360	0.028	0.076	0.013
2453470.814	0.353	0.024	0.088	0.012
2453470.882	0.469	0.043	0.088	0.019
2453473.227	0.496	0.055	0.175	0.033
2453475.169	0.384	0.049	0.073	0.021

Note. Column 1: Heliocentric Julian Date. Columns 2 and 3: Measured HX flux and 1σ error, in ct sec^{-1}. Columns 4 and 5: Measured SX flux and 1σ error, in ct sec^{-1}. Note that this table includes all usable *Swift* observations of NGC 5548, not just those from the intensive monitoring period, sorted by HJD. Only a portion of this table is shown here to demonstrate its form and content.

(This table is available in its entirety in machine-readable form.)

analyses we detrended the data by subtracting a 30 day boxcar running mean. This was done to remove long-term trends that could potentially degrade our ability to measure the expected small lags.

In all correlation analyses we reference the correlation of one band (the *HST* band) relative to all other bands (the eight *Swift* UVOT and XRT bands), restricting our analysis to just the data shown in Figure 2. We used the interpolated CCF (ICCF) as implemented by Peterson et al. (2004), to measure and characterize temporal correlations within these data. These results are shown in Table 4 and discussed in the following subsection. The second subsection reports the result of fits to these data, and the third describes our characterization of the variable UVOT spectral energy distribution (SED).

Table 4
Interband Correlation Coefficients and Lags

(1) Band	(2) $r_{\max}$	(3) Lag (days)
HX	0.35	-0.66 ± 0.46
SX	0.44	$+0.08 \pm 0.52$
HST	1.00	$+0.00 \pm 0.25$
UVW2	0.90	$+0.40 \pm 0.17$
UVM2	0.87	$+0.35 \pm 0.16$
UVW1	0.85	$+0.61 \pm 0.20$
U	0.81	$+1.35 \pm 0.24$
B	0.74	$+1.23 \pm 0.29$
V	0.57	$+1.56 \pm 0.50$

Note. Column 1: Band for which correlation was measured relative to *HST* 1367 Å. Column 2: Maximum correlation coefficient. Column 3: Measured centroid lag and associated 1σ error in days.

3.1. Correlation Analysis

The traditional CCF (e.g., Jenkins & Watts 1968) requires evenly sampled data, but most astronomical data are not evenly sampled. The ICCF performs a piecewise linear interpolation in the reference (*HST*) band with a user-defined interpolation step of 0.1 day, and then measures the correlation relative to the non-interpolated data in the other band. These data are then shifted and correlated to build up the correlation function. In this case, the *HST* data, with an initial cadence of ∼1.1 day, are resampled to a grid with 0.1 day spacing, and then the CCF of each *Swift* light curve is measured relative to the *HST* light curve.

The results are shown in Figure 3(a). The third panel shows the auto-correlation function (ACF) of the *HST* data; all others are CCFs measured relative to the *HST* light curve, so a positive lag indicates that variations in that band lag behind the *HST* light curve. Two points are clear. First, there is a tendency for peak lags to increase with wavelength: the HX band shows a negative lag relative to *HST*, the SX band shows approximately zero lag, the lags are positive and small within the *Swift* UV (longer wavelengths lag *HST*), and the lags are positive and larger between *HST* and the *Swift* optical. Second, the strength of the correlation is larger between the *HST* and UVOT data (peak correlation coefficients $r_{\max} = 0.57 - 0.90$) than between the *HST* and XRT data ($r_{\max} < 0.45$).

In order to quantify the uncertainties on the interband lag estimates, we utilized the flux randomization/random subset selection (FR/RSS) technique of Peterson et al. (1998) as modified by Peterson et al. (2004) to produce the cross-correlation centroid distribution (CCCD), as shown in Figure 3(b). FR/RSS is a model-independent Monte Carlo technique that attempts to deal with both flux uncertainties in individual measurements and uncertainties due to sampling of the time series. In "RSS," for a light curve of N data points, one randomly selects N data points without regard to whether a data point has been previously selected or not. Thus, approximately $1/e$ of the original points in the light curve are not selected in a given realization, and the remaining points are selected one or more times. For data points selected n times in a given realization, the uncertainty associated with the data point is reduced by $n^{-1/2}$. "FR" consists of altering the observed flux by random Gaussian deviates whose standard deviation is equal to the flux uncertainty on the data point. The CCCD is built by

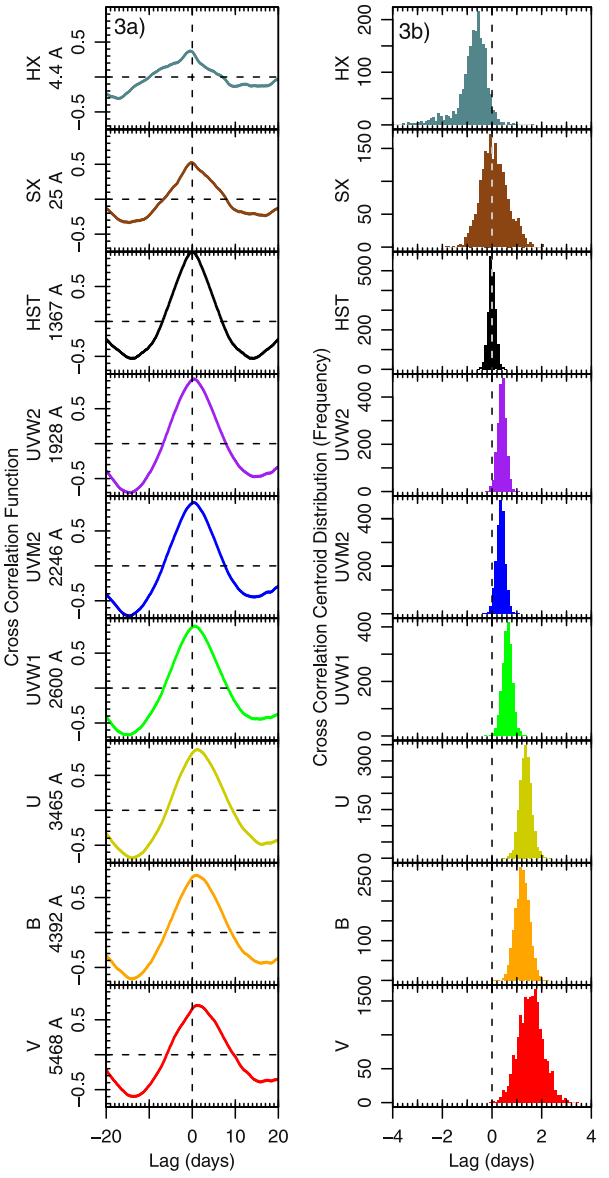

Figure 3. (3a) ICCFs for the intensive monitoring period light curves (Figure 2), with all correlations measured relative to the *HST* light curve, after removing long term trends (see Section 3). The band name and central wavelength are given on the left of panel 3a and the band name on the left of panel 3b. Note that the interband lag goes from negative to increasingly positive as the band's wavelength increases. Note also that the UV/optical correlations are all strong ($r_{\max} = 0.57$–0.90) but the X-ray/UV correlations are much weaker, ($r_{\max} < 0.45$). (3b) Cross-correlation centroid histograms derived from the CCFs as discussed in the text. The band name and central wavelength are given on the left of each panel. All distributions except HX appear consistent with a Gaussian.

combining the results from 2000 realizations, with results that are summarized in Table 4.

A number of factors can contribute to the widths of the histograms and thus the error estimates on the interband lags. These include the sampling cadence and finite duration of the campaign, measurement errors, and deviations from the stationarity assumption implicit in the FR/RSS method. An example of the second contribution could be the appearance of somewhat different lags at different epochs, as may be occurring with the BLR (see Paper I). At present it is not possible to determine the relative contribution of each effect.

3.2. Lag-wavelength Fits

As discussed in the introduction, the standard model predicts a relationship between lag and wavelength because the disk is expected to be hotter at smaller, inner radii and cooler at larger, outer radii. Following the analysis of McHardy et al. (2014) and Shappee et al. (2014), Figure 4 presents the CCF lag (τ) results as a function of wavelength (λ). We fit the wavelength dependence of the lags with the function $\tau = A + B((\lambda/\lambda_0)^C - 1)$. The top three sets of panels show the effect of restricting the fitting function by first setting $C = 4/3$ and then setting $A = 0$. This yields only a slight increase in χ^2_ν, which is acceptable in all cases. For instance the third panel has reduced χ^2 of $\chi^2_\nu = 0.98$, corresponding to a probability value $p = 0.45$. Thus we conclude these data are fully consistent with a single-parameter fit, $\tau = B((\lambda/\lambda_0)^{4/3} - 1)$. The fit parameter B gives an estimate of the size of the disk at $\lambda_0 = 1367$ Å, the *HST* reference wavelength, assuming a face-on geometry. This is the most important result of this paper, discussed in detail in Section 4.1.

The bottom three sets of panels explore the effect of excluding particular bands from the fit. The third panel shows the effect of excluding the *HST* ACF lag, which of course should be identically zero. This has no effect on the number of degrees of freedom (dof) as the fit parameter A is dropped as well (as discussed above).

The fourth panel shows the additional effect of dropping the two X-ray lags, HX and SX. This has essentially no effect on fit quality, which is not surprising because the correlation coefficients are low and the lags have by far the largest errors of any waveband. That is, the X-ray variations do not show a clear, consistent relation to the UV/optical variations. The implications of this divergence is explored in detail in Section 4.4.

Another new result of this experiment is that the *U*-band lag is consistently larger than predicted by the fits. The fifth set of panels show that additionally excluding the *U*-band lag from the fit shown in the fourth panel greatly reduces the χ^2_ν although, as mentioned earlier, the fits are acceptable in all cases. This is discussed in Section 4.2.

3.3. Spectral Variability

In this section we utilize the fact that emission from the AGN (central engine and surrounding regions) is variable while starlight from the underlying galaxy is not to separate these components and characterize the spectral shape of the AGN component. For most analyses, emission from the underlying galaxy is a complication to be removed from the UV/optical SED before proceeding. One way to do this is image decomposition, as has been performed for NGC 5548 by Bentz et al. (2009, 2013) and Mehdipour (2015). Here we use an alternate approach to estimate the shape of the variable SED (although not its normalization) directly from *Swift* data alone.

We first filter the intensive monitoring data to include only orbits with observations in all six UVOT filters in order to obtain a uniform data set. For each band, we next measure the standard deviation of the flux (σ) and the mean error ($\bar{\epsilon}$) and

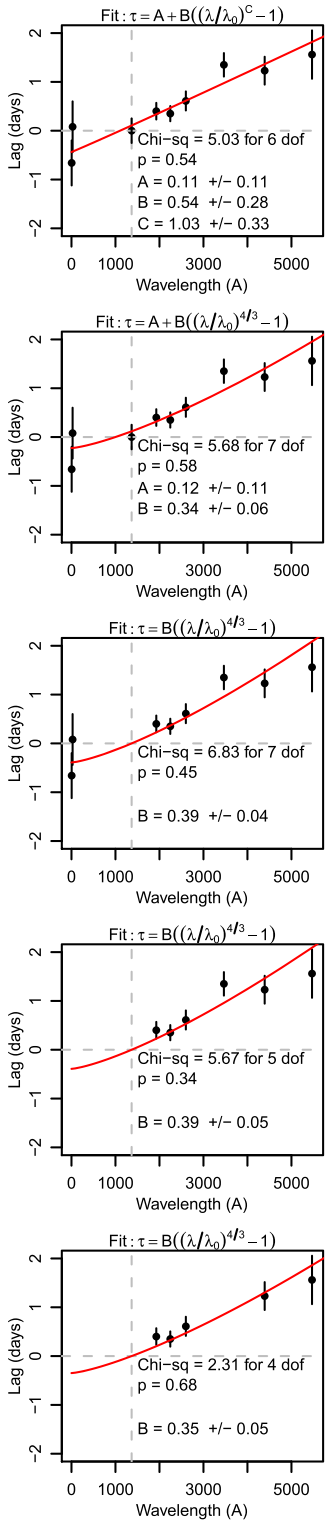

Figure 4. Lag-wavelength fits based on the data in Tables 1 and 4. The top row shows the most general fit, $\tau = A + B((\lambda/\lambda_0)^C - 1)$, with the power-law index C allowed to float. The next row fixes the index at the theoretically expected value $C = 4/3$. All data are included in the first two sets of fits. In the third row the intercept is fixed at $A = 0$ and the *HST* ACF data are excluded. The fourth row shows these fits with the X-ray data HX and SX also excluded, while the fifth row additionally excludes the *U*-band data. See the text for further details.

then calculate the error-corrected standard deviation, $\sigma_C = \sqrt{\sigma^2 - \bar{\epsilon}^2}$, although the error correction was always small, typically ~1%. This provides a direct estimate of the intrinsic variability in each band but does not include the mean flux of the AGN. We then take the logarithm of both quantities and fit a function of the form $\log_{10}(\sigma_C(\lambda)) = \alpha \log_{10}(\lambda) + \beta$, which is equivalent to $\sigma_C(\lambda) \propto \lambda^\alpha$, in order to measure the power-law slope α of the variable component. As shown in Figure 5, this fit yields $\alpha = -1.88 \pm 0.20$. In order to estimate the intrinsic shape of the variable AGN SED, we perform the same exercise after first dereddening the data (assuming $E(B-V) = 0.017$; see Paper I). This yields a slope of $\alpha = -1.98 \pm 0.20$. We note that this is consistent with predicted thin accretion disk slopes of $\alpha = -2$ to -2.33 (Davis et al. 2007).

4. DISCUSSION

4.1. Reverberation Mapping of the Accretion Disk

The standard model of a geometrically thin, optically thick AGN accretion disk predicts that the disk will be hotter in the inner radii and cooler in the outer radii, with dependencies on the black hole mass (and thus the Schwarzschild radius) and Eddington ratio. This is for instance quantified in Equation (3.20) of Peterson 1997,

$$T(r) \approx 6.3 \times 10^5 \left(\frac{\dot{M}}{\dot{M}_{\rm Edd}}\right)^{1/4} M_8^{-1/4} \left(\frac{r}{R_{\rm S}}\right)^{-3/4} {\rm K} \qquad (1)$$

where $T(r)$ is the temperature at radius r, $\dot{M}/\dot{M}_{\rm Edd}$ is the mass accretion rate divided by the Eddington rate, assuming a radiative efficiency of $\eta = 0.1$, M_8 is the black hole mass in units of $10^8\,M_\odot$, and $R_{\rm Sch}$ is the Schwarzschild radius.

Combining Equation (1) with Wien's law ($\lambda_{\rm max} = 2.9\times10^7/T$, where λ is measured in Ångstroms and T in Kelvin) and the idea that the lags are dominated by light travel times from the center (so $\tau = r/c$) yields the relation $\tau \propto \lambda^{4/3}$. Note that while this derivation was for a disk heated "internally" by viscous processes, the same $\lambda^{4/3}$ dependence will arise in a disk heated "externally" by the putative central corona. This is shown in Equations (1) and (2) of Cackett et al. (2007) and Equation (4.56) of Netzer (2013). However, these derivations all assume a relatively flat disk. If the disk is strongly warped or if the corona is distributed across the disk (Dexter & Agol 2011), then an externally-heated disk will be hotter at large radii, leading to a flatter lag-wavelength relation. The consistency of the observed $\tau - \lambda$ relation with the predicted relation broadly supports the standard accretion disk temperature profile.

Equation (1) can also be used to estimate source parameters under the simple assumption of a face-on disk in which each annulus at temperature $T(r)$ radiates all its luminosity at $\lambda_{\rm max}$ as given above. The observed relation $\tau = B((\lambda/\lambda_0)^{4/3} - 1)$ has a single free parameter $B \approx 0.35$ day, which indicates, for a face-on disk, that an annulus of radius ~0.35 lt-day radiates at $T = 2.9 \times 10^7/\lambda_0 = 2.2 \times 10^4$ K for $\lambda_0 = 1367$ Å. This distance of 0.35 lt-day corresponds to $r/R_{\rm Sch} = 90$ for a $3.2 \times 10^7\,M_\odot$ black hole.

A more realistic picture would account for the fact that each annulus radiates as a blackbody of temperature $T(r)$ instead of radiating at a single wavelength $\lambda_{\rm max}$. Accounting for that will

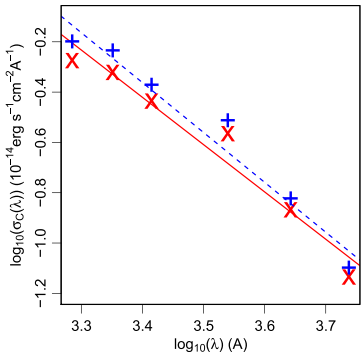

Figure 5. The error-subtracted variable flux ($\sigma_C(\lambda)$) as a function of wavelength (λ). The original data are shown as red Xs and the dereddened data as blue crosses. A fit to the function $\log_{10}(\sigma_C(\lambda)) = \alpha \log_{10}(\lambda) + \beta$ yielded $\alpha = -1.88 \pm 0.20$ for the original data (solid red line) and $\alpha = -1.98 \pm 0.20$ for the dereddened data (dashed blue line).

yield a larger value for the radius at which the disk emission peaks at λ_{max} because more flux at a given wavelength is produced by hotter blackbody emission interior to radius R than by cooler blackbody radiation exterior to R. A future paper in this series (D. Starkey et al. 2015, in preparation) utilizes direct modeling of each UV/optical light curve to produce a more rigorous analysis.

Nonetheless these large sizes may cause problems for the standard Shakura & Sunyaev (1973) α-disk model. Assuming a value for $\dot{M}/\dot{M}_{\rm Edd} = L/L_{\rm Edd} = 0.03$, derived using a disk luminosity L that is ~37% of the total luminosity, yields an accretion disk radius of only $r/R_{\rm Sch} = 40$ using the same formula and assumptions as above. We note that there are models that produce effectively larger disks which can potentially better explain the UV/optical variability properties of AGNs, such as the inhomogeneous disk model of Dexter & Agol (2011).

4.2. Contribution of BLR Emission

Another interesting result shown in Figure 4 is the longer U-band lag, relative to the fit and to the lags of nearby bands. Excluding the U-band data from the fit yielded a significant improvement in χ^2_ν, although the overall fit is acceptable in either case. The final fit on the bottom of Figure 4, which excludes U band, predicts a U-band lag of $\tau = 0.85$ while the observed value is $\tau = 1.35 \pm 0.24$, a difference of 2σ. In retrospect, one can see in both the previous NGC 5548 campaign (McHardy et al. 2014) and the NGC 2617 campaign (Shappee et al. 2014) that the U-band lags were larger than the B-band lags, although those campaigns measured lags with much larger errors, so the deviation was not significant. The vastly superior short timescale sampling provided by the current campaign (see Figure 1) allows for the measurement of this apparent effect with higher significance.

There is a simple explanation for this excess lag, discussed by Korista & Goad (2001): Balmer continuum emission (both thermal diffuse and reflected incident continuum) and other pseudo-continuum emission from BLR clouds (e.g., UV Fe II) contribute significantly to the observed U-band flux, and since the BLR is much larger than the optically-bright accretion disk, it will increase the observed lag. This effect was seen by Maoz et al. (1993) in NGC 5548 RM data from the 1989 campaign. The sensitivity of the strength of the diffuse continuum component to the presence of high gas densities and high ionizing photon fluxes make it an important diagnostic of the physical conditions within the BLR. A possible alternative is that the Balmer continuum (and other pseudo-continua) is produced in an "intermediate" region smaller in size than the classical BLR but larger than the accretion disk. This could more naturally explain the relatively small increment in the U-band lag, although it would also mean adding a previously-unknown emission component to the many already required to explain AGN SEDs.

We note that continuum light curves measured at longer wavelengths and/or with narrower bands will be much less sensitive to this effect. This cannot be done with *Swift*, but future papers in this series will analyze an expanded set of *HST* and optical photometric bands (M. Fausnaugh et al. 2015, in preparation) and ground-based spectroscopy of NGC 5548 (L. Pei et al. 2015, in preparation), providing a more sensitive test of the degree to which these CCFs are contaminated by emission from hot gas surrounding the central engine.

4.3. The Accretion Disk Size–Black Hole Mass Relation

As discussed in Section 1, quasar gravitational microlensing studies have been used to estimate accretion disk sizes, finding a tendency for disk sizes to increase with black hole mass (Morgan et al. 2010; Mosquera et al. 2013). Disk RM measurements of Seyfert galaxies can be used to extend such relations to lower masses, luminosities, and (probably) Eddington ratios, generally with smaller uncertainties because of the greatly reduced physical complexity of the measurement. Figure 6 shows a summary of microlensing sizes estimates (the half-light–radius $R_{1/2}$ at rest frame 2500 Å) from Mosquera et al. (2013) as open triangles. Microlensing studies frequently focus on $R_{1/2}$ because estimates of its value are relatively insensitive to changes in the underlying (disk) emission profile (Mortonson et al. 2005). A fit to these data as a power-law, $\log_{10}(R_{1/2}) = A + B \log_{10}(M/M_0)$, with $M_0 \equiv 3 \times 10^8\, M_\odot$ to minimize covariances between the parameter estimates and assuming 0.3 dex uncertainties in the black hole mass estimates, yields $A = \log(R_0/{\rm cm}) = 15.81 \pm 0.16$ and $B = 1.29 \pm 0.33$ with $\chi^2 = 8.73$ for 9 dof, a statistically acceptable fit. The slope of the fit is driven by the higher mass systems, leading it to lie below the measurements in the mass range of NGC 5548.

The comparable disk RM size from the present study is the distance corresponding to the lag for the *UVW1* filter centered at 2600 Å, which we show as the filled square labeled "N5548." This combines the parameter B (= 0.35 ± 0.04 day for the simple face-on model in Figure 4) with the *HST* UV to *UVW1* lag (0.61 ± 0.20 days), to give an estimate that $R_{1/2} = 0.96 \pm 0.21$ light-days. This assumes that the size corresponding to the observed lag corresponds to $R_{1/2}$, which may not be correct, but is a reasonable assumption pending a theoretical model for how the disk RM lag should be interpreted in detail. For example, $R_{1/2}$ is 2.44 times larger than the radius at which the photon wavelength matches the disk temperature discussed in Section 4.1. A similar procedure was used to add the *UVW1* size estimate for NGC 2617 from Shappee et al. (2014), where the error bar is designed to span their systematic uncertainties.

While there are residual systematic uncertainties in this comparison, such as the meaning of the disk RM lag as a physical size and potential differences in the Eddington ratios of

the nearby lower luminosity Seyfert 1 s and the distant high luminosity quasars, the results from the two very different methods are broadly consistent. If we simply fit the combined data, we find $A = 15.96 \pm 0.12$ and $B = 0.98 \pm 0.23$ with $\chi^2 = 13.51$ for 11 dof, which is shown by the dashed line in Figure 6. The slope is flatter and better defined, the fit is consistent with the combined data, and the parameters are consistent with the results using only the microlensing results. Interestingly, the slope B is almost exactly unity (and thus the fit line is nearly parallel with the last stable orbit, shown as a solid line in Figure 6), indicating that the disk size in units of Schwarzschild radii is nearly constant, $R_{1/2}(2500\ \text{Å}) \sim 100R_{\rm Sch}$, over a very wide range of AGN masses. That these two radically different methods agree this well seems remarkable given the different underlying physics and the possible range of systematic effects.

4.4. Relation of X-Ray to UV/Optical Continua

Figure 3 shows that compared to the strong ($r_{\rm max} = 0.57 - 0.9$) correlations within the UV/optical, the correlation between the *HST* 1367 Å and the X-ray bands is much weaker ($r_{\rm max} = 0.35-0.44$). This is surprising because it is well established that the optical and X-ray light curves of NGC 5548 are very well correlated ($r_{\rm max} = 0.95$) on longer timescales of years (Uttley et al. 2003). That is, the strong long timescale optical/X-ray correlation does not translate to strong short timescale UV/X-ray correlations in NGC 5548. Visual examination of the NGC 5548 UV and X-ray light curves both in this paper and McHardy et al. (2014) shows that there are some periods in which the UV appears to lead the X-rays, some in which the UV appears to lag the X-rays, and some in which there is no simple discernible relationship.

Periods of uncorrelated X-ray/optical variations are also seen in other Seyferts (e.g., NGC 3516; Maoz et al. 2002 and Mkn 79; Breedt et al. 2009). The phenomenon may be linked to internal heating fluctuations in the disk which are not "seen" by the X-ray emitting region, perhaps linked to mass accretion fluctuations which do not propagate to the central X-ray emiting region due to viscous damping (e.g., the explanation of a similar phenomenon seen on equivalent, mass-scaled timescales in a stellar mass black hole X-ray binary Cassatella et al. 2012). This may indicate that a significant fraction of the UV/optical emission is not due to reprocessing of X-ray photons, but rather is generated internally. In this case, the observed time lags would not be dominated by light travel effects, but instead would depend on the physics of the internal disk variations.

Alternatively, the lack of correlation between the UV/optical and X-ray could be a signature of absorption due to intervening material, but then one would expect the UV to be better correlated with the HX than the SX, because the latter would be much more strongly affected (and the light curves more decorrelated) by "warm" absorption. We do know that NGC 5548 shows strong variable absorption in the X-rays (Mehdipour 2015), and there are indications that the absorption was changing (decreasing) during the *Swift* campaign. Nonetheless the fact that the HX show a smaller correlation coefficient than the SX suggests that this may not be a complete explanation. A somewhat different scenario, based on a correlation between SX excess and far-UV also observed by (Mehdipour 2015), is that both are associated with

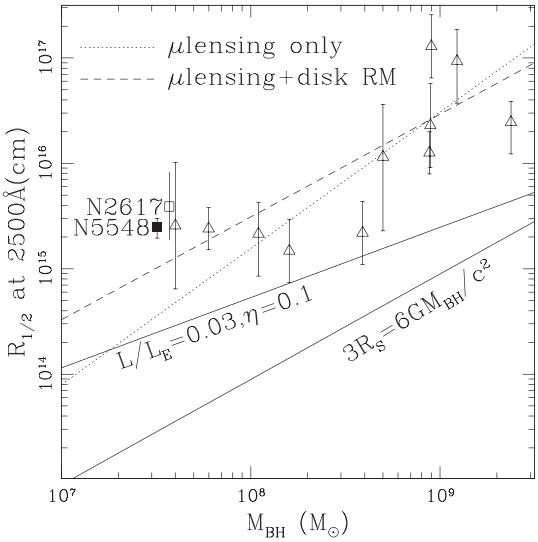

Figure 6. Accretion disk size estimates from quasar microlensing studies (open triangles; Mosquera et al. 2013), the current study of NGC 5548 (black filled square) and NGC 2617 (open square, Shappee et al. 2014) as a function of black hole mass. The dotted line shows the fit to just the microlensing data and the dashed line the fit to all data points including the Seyfert 1 RM measurements. To give a sense of other scales associated with accretion disks, the lower solid line shows the last stable orbit of a non-rotating black hole at $R = 3R_{\rm Sch} = 6GM/c^2$ and the upper solid lines shows $R_{1/2}$ at 2500 Å for a simple thin disk with Eddington ratio $L/L_{\rm Edd} = 0.03$ and efficiency $\eta = 0.1$ to provide a sense of scale. The latter curve can be shifted as $(L/L_{\rm Edd})^{1/3}$ for different choices of these factors.

Comptonization. Finally, it could simply mean that the observed 0.3–10 keV X-ray band is a poor proxy for emission from the putative hot corona, which should emit the bulk of its luminosity at harder energies. At this point it is not possible to say with certainty which, if any, of these explanations is correct.

5. CONCLUSIONS

This paper presents the results of the most intensive X-ray/UV/optical AGN monitoring ever, spanning a duration of months. We find that the UV/optical light curves are all well correlated with lags of ~1–2 days increasing to longer wavelengths. These lags are well-fitted by the relation $\tau \propto \lambda^{4/3}$, in agreement with standard steady-state accretion disk predictions under the assumption that time lags are dominated by light travel times. The fits yield a disk size of $\sim 0.35 \pm 0.05$ lt-day at 1367 Å, larger than expected from standard α-disk models or extrapolation from higher-mass microlensing studies. Interestingly the U-band lag is anomalously large, suggesting that the U band is affected by Balmer continuum emission from the BLR. The X-ray/UV correlations are weaker and less consistent, however, so these data do not confirm all predictions of the reprocessing picture.

We are planning a series of future papers to explore these results in greater detail. M. Fausnaugh et al. (2015, in preparation) will present ground-based optical and further *HST* continuum data, allowing a check on the wavelength dependence of the observed interband lags. L. Pei et al. (2015,

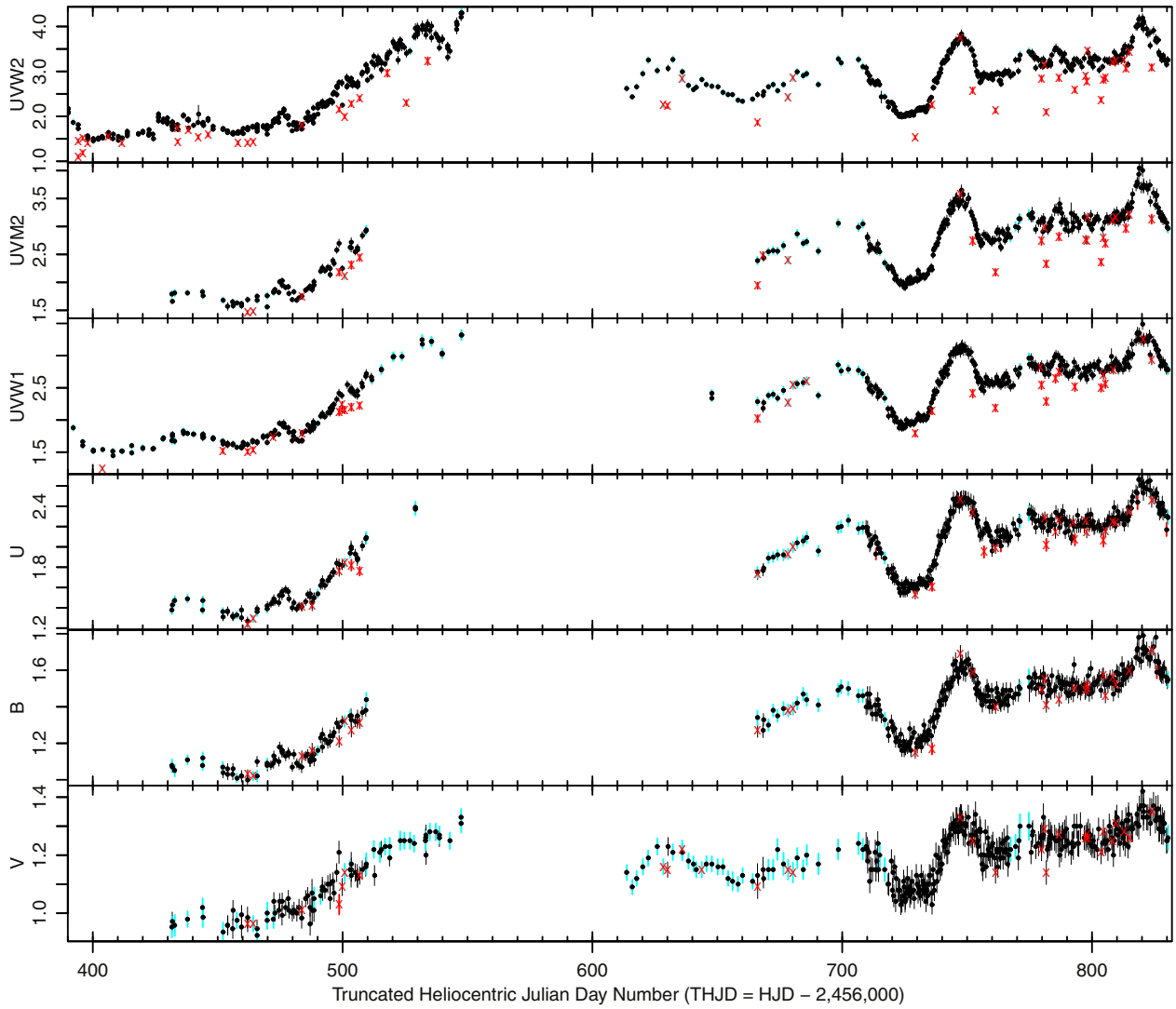

Figure 7. Initial UVOT light curves of NGC 5548 for the period THJD 390–832. The error bar colors indicate the results of the dropout test: black errors indicated that the point passed the dropout test (small deviation), red error bars indicated that it failed the test (large deviation) and cyan error bars indicate that it was not tested (as it lacked sufficient nearby neighbors). The symbols show if the point fell inside/outside the UVOT boxes (shown in Figure 9): black dots fell outside the boxes and thus were used in the final light curve (shown in Figure 1) and red Xs fell inside the boxes and were excluded from the final light curves.

in preparation) will use ground-based spectroscopy to measure the continuum in narrow spectral windows much less affected by BLR emission, further refining this analysis. D. Starkey et al. (2015, in preparation) will apply Markov Chain Monte Carlo methods to directly model disk emission from these continuum data, allowing a much more direct probe of the physical conditions.

This RM disk size estimate of a relatively low-mass Seyfert 1 galaxy forms a nice complement to more numerous but more uncertain accretion disk size estimates derived from generally higher-mass quasar microlensing studies. The combination of the two datasets allows improved determination of the accretion disk size–black hole mass relation, which interestingly suggests 2500 Å accretion disk sizes of $R_{1/2} \approx 100 R_{\rm Sch}$. Further Seyfert 1 accretion disk RM experiments will allow this relation to be tested and refined.

Most important for the long term is that this experiment demonstrates how dense and broad coverage in both wavelength and time can be used to probe a nearby AGN accretion disk with unprecedented detail. *Swift* was named "the premier facility for multi-wavelength time domain astronomy" by the latest NASA Senior Review Panel.[45] There is certainly no other observatory that can single-handedly monitor AGNs with such dense and broad temporal and frequency coverage in the UV/optical and X-rays. We expect that this experiment will become a template for future *Swift* campaigns that characterize the accretion disks of a sample of AGNs covering a range of black hole masses, Eddington ratios, and other source parameters.

[45] http://science.nasa.gov/media/medialibrary/2014/05/15/Final_Report_Astro2014_SeniorReview_Panel.pdf

Support for *HST* program number GO-13330 was provided by NASA through a grant from the Space Telescope Science Institute, which is operated by the Association of Universities for Research in Astronomy, Inc., under NASA contract NAS5-26555. R.E. gratefully acknowledges support from NASA under awards NNX13AC26G, NNX13AC63G, and NNX13AE99G. J.M.G. gratefully acknowledges support from NASA under award NNH13CH61C. B.M.P., G.D.R., C.J.G., M.M.F., and R.W.P. are grateful for the support of the National Science Foundation through grant AST-1008882 to The Ohio State University. A.J.B. and L.P. have been supported by NSF grant AST-1412693. M.C.B. gratefully acknowledges support through NSF CAREER grant AST-1253702 to Georgia State University. K.D.D. is supported by an NSF Fellowship awarded under grant AST-1302093. P.B. H. is supported by NSERC. SRON is financially supported by NWO, the Netherlands Organization for Scientific Research. B.C.K. is partially supported by the UC Center for Galaxy Evolution. C.S.K. acknowledges the support of NSF grant AST-1009756. P.L. acknowledges support from Fondecyt grant #1120328. A.P. acknowledges support from a NSF graduate fellowship and a UCSB Dean's Fellowship. J. S.S. acknowledges CNPq, National Council for Scientific and Technological Development (Brazil) for the partial support and The Ohio State University for warm hospitality. T.T. has been supported by NSF grant AST-1412315. T.T. and B.C.K. acknowledge support from the Packard Foundation in the form of a Packard Research Fellowship to T.T. T.T. thanks the American Academy in Rome and the Observatory of Monteporzio Catone for kind hospitality. The Dark Cosmology Centre is funded by the Danish National Research Foundation. M.V. gratefully acknowledges support from the Danish Council for Independent Research via grant No. DFF 4002-00275. This research has made use of the NASA/IPAC Extragalactic Database (NED), which is operated by the Jet Propulsion Laboratory, California Institute of Technology, under contract with the National Aeronautics and Space Administration.

APPENDIX

As discussed in Section 2.2 we discovered "dropouts" in the UVOT light curve in the course of the data reduction: isolated points with fluxes many sigma below those of their nearest neighbors. Figure 7 shows the UVOT light curves of NGC 5548 after initial flux measurements and removal of data points affected by tracking problems. The dropouts are the points with red error bars, most frequently seen in the UV bands. In order to quantify this effect, we first parametrized the deviation for every point in the light curve as $df = (F_N - 0.5\times(F_{N-1} + F_{N+1}))/\sigma_N$, where F_N and σ_N are the measured flux and 1σ error bar for visit N. To minimize the effects of intrinsic variability, we only tested data with observing gaps $t_{N+1} - t_{N-1} < 2.5$ days (t_N is the THJD of the Nth visit); all visits with longer gaps between their nearest neighbors were ignored.

We then flagged all points with negative excursions greater than the largest positive excursion seen in that filter as dropouts. The largest positive excursions used to define the threshold of what is a dropout are themselves sensitive to dropout measurements, in that the largest *df* values tend to be found when the $N - 1$ or $N + 1$ flux measurement is a dropout. We therefore redefine these thresholds iteratively, removing the dropout points and then re-evaluating the largest positive excursions. This is repeated until the largest positive excursion remained the same, that is, it was not associated with a dropout. This procedure limits the number of false positives to of order one per light curve. Note the strong dependence on UVOT band, with 33, 13, 21, 11, 2, and 1 dropouts for the *UVW2, UVM2, UVW1, U, B*, and *V* bands, respectively.

We then mapped the source location of every exposure for the three UV filters (*UVW2, UVM2, UVW1*) to the UVOT detector coordinates (Figure 8). Blue dots show the points used in the analysis, red Xs the dropouts as defined above, and open black circles the points ignored because they lacked nearby (in time) neighbors. Figure 9 is a blow-up of the

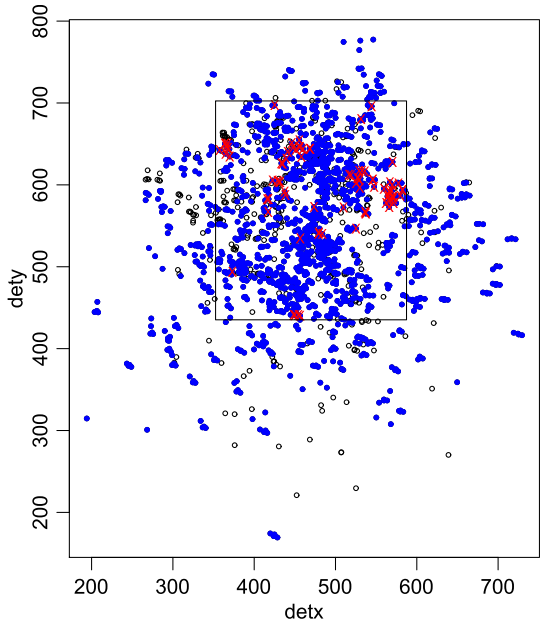

Figure 8. UVOT detector coordinates of the *UVW2, UVM2*, and *UVW1* data in Figure 7. Data that were tested for dropouts are shown as blue dots and those that were not tested (due to their not having sufficiently nearby neighbors) are shown as open black circles. The points that failed the dropout test are marked with red Xs. The black rectangle denotes the region shown in Figure 9.

Table 5
UVOT Detector Bad Boxes

*x*1	*x*2	*y*1	*y*2
357	371	634	651
415	440	582	632
441	469	634	655
448	457	440	442
479	484	539	542
516	537	596	619
536	538	564	568
545	583	573	607

Note. UVOT detector coordinates (x1, x2, y1, y2) for the eight "bad" boxes shown in Figure 9. These are image coordinates for a full-frame raw UVOT image with 2×2 binning (the default UVOT image mode).

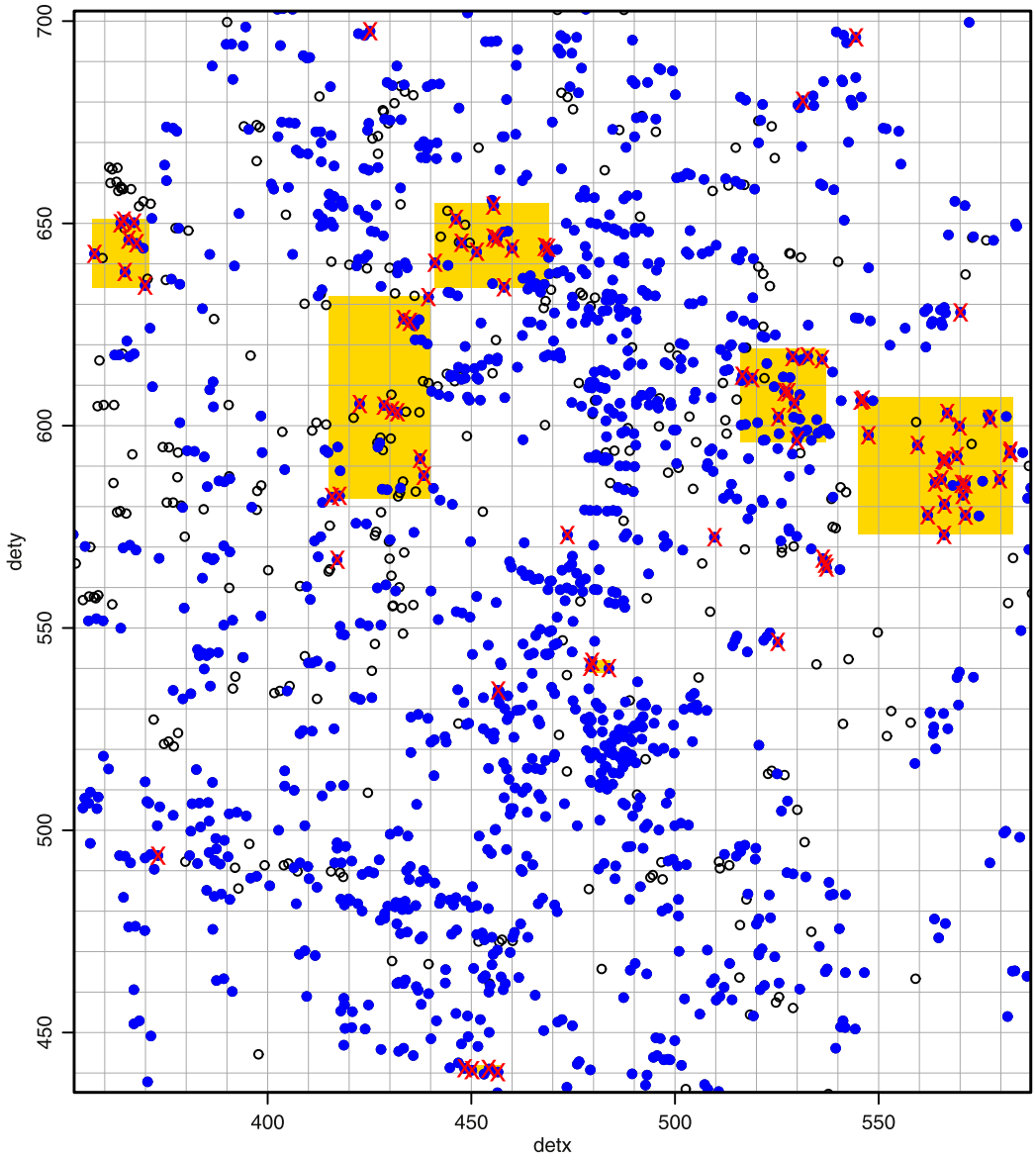

Figure 9. The detector region containing all the observed UVOT dropouts. The black circles, blue dots, and red Xs have the same meaning as in Figure 8. Clusters of three or more dropouts are shown as gold boxes. Eight such boxes enclose most red Xs and are used to define suspect regions on the UVOT detector. All data points within these regions were eliminated to form the final light curve (Figure 2), regardless of whether or not they failed the dropout test. Note that the two boxes in the bottom half of the figure ($y > 550$) are too small to be clearly visible. The box positions are given in Table 5.

region with the dropouts. Note that the dropouts cluster together such that most can be enclosed by a small number of boxes. We define eight rectangles in the detector plane, one for each cluster of at least three dropout points. The coordinates of these boxes are given in Table 5. We then went back to all six filters (including the optical *UBV* bands) and flagged every visit/filter that falls in any of these boxes.

These additional suspect points are shown as red Xs in Figure 7. We ran Kolmogorov-Smirnov tests on each band to test if the deviation for points in the suspect regions (the red Xs in Figure 7) derives from the same population as the unaffected data (black dots in Figure 7). We find that for five of the six UVOT filters (all except *V*) the two samples are not consistent at the 10^{-4}–10^{-16} level, with the strongest differences at the highest frequencies. We then eliminated all data points in any filter that fell in these eight boxes. These points are shown as red Xs in Figure 7. The remaining points (the black dots in Figure 7) then formed the final light curve shown in Figure 2 of the main section of this paper.

REFERENCES

122
Antonucci, R. 2013, Natur, 495, 165
Arévalo, P., Uttley, P., Kaspi, S., et al. 2008, MNRAS, 389, 1479
Arévalo, P., Uttley, P., Lira, P., et al. 2009, MNRAS, 397, 2004
Bentz, M. C., Denney, K. D., Grier, C. J., et al. 2013, ApJ, 767, 149

Bentz, M. C., & Katz, S. 2015, PASP, 127, 67
Bentz, M. C., Peterson, B. M., Netzer, H., Pogge, R. W., & Vestergaard, M. 2009, ApJ, 697, 160
Blackburn, J. K. 1995, adass IV, 77, 367
Blackburne, J. A., Kochanek, C. S., Chen, B., Dai, X., & Chartas, G. 2014, ApJ, 789, 125
Blackburne, J. A., Kochanek, C. S., Chen, B., Dai, X., & Chartas, G. 2015, ApJ, 798, 95
Blandford, R., & McKee, C. 1982, ApJ, 255, 419
Breedt, E., Arévalo, P., McHardy, I. M., et al. 2009, MNRAS, 394, 427
Breedt, E., McHardy, I. M., Arévalo, P., et al. 2010, MNRAS, 403, 605
Breeveld, A. A., Curran, P. A., Hoversten, E. A., et al. 2010, MNRAS, 406, 1687
Burrows, D. N., Hill, J. E., Nousek, J. A., et al. 2005, SSRv, 120, 165
Burrows, D. N., Kennea, J. A., Nousek, J. A., & Gehrels, N. 2014a, GCN Circular, 16349
Burrows, D. N., & Kennea, J. A. 2014b, GCN Circular, 16356
Cackett, E. M., Horne, K., & Winkler, H. 2007, MNRAS, 380, 669
Cameron, D. T., McHardy, I., Dwelly, T., et al. 2012, MNRAS, 422, 902
Cassatella, P., Uttley, P., & Maccarone, T. J. 2012, MNRAS, 427, 2985
Clavel, J., Reichert, G. A., Alloin, D., et al. 1991, ApJ, 366, 64
Collin, S. 2001, in Proc. SAC Conf., Advanced Lectures on the Starburst–AGN Connection, ed. I. Aretxaga, D. Kunth, & R. Mújica (Singapore: World Scientific), 167
Dai, X., Kochanek, C. S., Chartas, G., et al. 2010, ApJ, 709, 278
Davis, S. W., Woo, J.-H., & Blaes, O. M. 2007, ApJ, 668, 682
Denney, K. D., Peterson, B. M., Pogge, R. W., et al. 2010, ApJ, 721, 715
De Rosa, G., et al. 2015, ApJ, 806, 128 (Paper I)
de Vaucouleurs, G., de Vaucouleurs, A., Corwin, H. G., Jr., et al. 1991, Third Reference Catalogue of Bright Galaxies (New York: Springer)
Dexter, J., & Agol, E. 2011, ApJL, 727, L24
Edelson, R., Alexander, T., Crenshaw, D. M., et al. 1996, ApJ, 470, 364
Edelson, R., & Krolik, J. H. 1988, ApJ, 333, 646
Edelson, R., Koratkar, A., Nandra, K., et al. 2000, ApJ, 534, 180
Evans, P. A., Beardmore, A. P., Page, K. L., et al. 2009, MNRAS, 397, 1177
Gehrels, N., Chincarini, G., Giommi, P., et al. 2004, ApJ, 611, 1005
Gliozzi, M., Papadakis, I. E., Grupe, D., Brinkmann, W. P., & Rath, C. 2013, MNRAS, 433, 1709
Haardt, F., & Maraschi, L. 1991, ApJL, 380, L51
Høg, E., Fabricius, C., Makarov, V. V., et al. 2000, A&A, 355, L27
Jenkins, G. M., & Watts, D. G. 1968, Spectral Analysis and its Applications (Michigan: Holden-Day)
Jiminez-Vicente, J., Mediavilla, E., Kochanek, C. S., et al. 2014, ApJ, 783, 47
Kennea, J., & Burrows, D. N. 2014b, GCN Circular, 16378
Koratkar, A., & Blaes, O. 1999, PASP, 111, 1
Korista, K. T., & Goad, M. R. 2001, ApJ, 553, 695
Lasker, B. M., Lattanzi, M. G., McLean, B. J., et al. 2008, AJ, 136, 735
Lira, P., Arévalo, P., Uttley, P., McHardy, I., & Breedt, E. 2011, MNRAS, 415, 1290
Maoz, D., Markowitz, A., Edelson, R., & Nandra, K. 2002, AJ, 124, 1988
Maoz, D., Netzer, H., Peterson, B. M., et al. 1993, ApJ, 404, 576
Mason, K. O., McHardy, I. M., Page, M. J., et al. 2002, ApJL, 580, L117
McHardy, I. M., Cameron, D. T., Dwelly, T., et al. 2014, MNRAS, 444, 1469
Mehdipour, M., et al. 2015, A&A, in press (arXiv:1501.01188)
Morgan, C. W., Kochanek, C. S., Morgan, N. D., & Falco, E. E. 2010, ApJ, 712, 1129
Morgan, C. W., Hainline, L. J., Chen, B., et al. 2012, ApJ, 756, 52
Mortonson, M. J., Schechter, P. L., & Wambsganss, J. 2005, ApJ, 628, 594
Mosquera, A. M., Kochanek, C. S., Chen, B., et al. 2013, ApJ, 769, 53
Nandra, K., Clavel, J., Edelson, R., et al. 1998, ApJ, 505, 594
Netzer, H. 2013, The Physics and Evolution of Active Galactic Nuclei (Cambridge: Cambridge Univ. Press)
Pancoast, A., Brewer, B. J., Treu, T., et al. 2014, MNRAS, 445, 3073
Peterson, B. M. 1997, An introduction to active galactic nuclei (Cambridge: Cambridge Univ. Press)
Peterson, B. M., Balonek, T. J., Barker, E. S., et al. 1991, ApJ, 368, 119
Peterson, B. M., Ferrarese, L., Gilbert, K. M., et al. 2004, ApJ, 613, 682
Peterson, B. M., Wanders, I., Horne, K., et al. 1998, PASP, 110, 660
Poindexter, S., Morgan, N., & Kochanek, C. S. 2008, ApJ, 673, 34
Poole, T. S., Breeveld, A. A., Page, M. J., et al. 2008, MNRAS, 383, 627
Roming, P. W. A., Kennedy, T. E., Mason, K. O., et al. 2005, SSRv, 120, 95
Sergeev, S. G., Doroshenko, V. T., Golubinskiy, Y. V., Merkulova, N. I., & Sergeeva, E. A. 2005, ApJ, 622, 129
Shappee, B. J., Prieto, J. L., Grupe, D., et al. 2014, ApJ, 788, 48
Shakura, N. I., & Sunyaev, R. A. 1973, A&A, 24, 337
Suganuma, M., Yoshii, Y., Kobayashi, Y., et al. 2006, ApJ, 639, 46
Uttley, P., Edelson, R., McHardy, I. M., Peterson, B. M., & Markowitz, A. 2003, ApJL, 584, L53

Referências

[1] ANTONUCCI, R. Unified models for active galactic nuclei and quasars. **Annual Review of Astronomy and Astrophysics**, v. 31, p. 473–521, 1993.

[2] BALDRY, I. K.; GLAZEBROOK, K.; BRINKMANN, J.; IVEZIĆ, Ž.; LUPTON, R. H.; NICHOL, R. C.; SZALAY, A. S. Quantifying the Bimodal Color-Magnitude Distribution of Galaxies. **Astrophysical Journal**, v. 600, p. 681–694, Jan. 2004.

[3] BALDWIN, J. A.; STONE, R. P. S. Southern spectrophotometric standards for large telescopes. II. **Monthly Notices of the Royal Astronomical Society**, v. 206, p. 241–245, Jan. 1984.

[4] BENTZ, M. C.; PETERSON, B. M.; NETZER, H.; POGGE, R. W.; VESTERGAARD, M. The Radius-Luminosity Relationship for Active Galactic Nuclei: The Effect of Host-Galaxy Starlight on Luminosity Measurements. II. The Full Sample of Reverberation-Mapped AGNs. **Astrophysical Journal**, v. 697, p. 160–181, May 2009.

[5] BON, E.; POPOVIĆ, L. Č.; GAVRILOVIĆ, N.; MURA, G. L.; MEDIAVILLA, E. Contribution of a disc component to single-peaked broad lines of active galactic nuclei. **Monthly Notices of the Royal Astronomical Society**, v. 400, p. 924–936, Dec. 2009.

[6] BOROSON, T. A.; OKE, J. B. Detection of the underlying galaxy in the QSO 3C48. **Nature**, v. 296, p. 397–399, Apr. 1982.

[7] BOWER, G. A.; WILSON, A. S.; HECKMAN, T. M.; RICHSTONE, D. O. Double-Peaked Broad Emission Lines in the Nucleus of M81. **Astronomical Journal**, v. 111, p. 1901, May 1996.

[8] BURROWS, D. N.; HILL, J. E.; NOUSEK, J. A.; KENNEA, J. A.; WELLS, A.; OSBORNE, J. P.; ABBEY, A. F.; BEARDMORE, A.; MUKERJEE, K.; SHORT, A. D. T.; CHINCARINI, G.; CAMPANA, S.; CITTERIO, O.; MORETTI, A.; PAGANI, C.; TAGLIAFERRI, G.; GIOMMI, P.; CAPALBI, M.; TAMBURELLI, F.; ANGELINI, L.; CUSUMANO, G.; BRÄUNINGER, H. W.; BURKERT, W.; HARTNER, G. D. The Swift X-Ray Telescope. **Space Science Reviews**, v. 120, p. 165–195, Oct. 2005.

[9] CARDELLI, J. A.; CLAYTON, G. C.; MATHIS, J. S. The relationship between infrared, optical, and ultraviolet extinction. **Astrophysical Journal**, v. 345, p. 245–256, Oct. 1989.

[10] CHEN, K.; HALPERN, J. P. Structure of line-emitting accretion disks in active galactic nuclei - ARP 102B. **Astrophysical Journal**, v. 344, p. 115–124, Sep. 1989.

[11] CHEN, K.; HALPERN, J. P.; FILIPPENKO, A. V. Kinematic evidence for a relativistic Keplerian disk - ARP 102B. **Astrophysical Journal**, v. 339, p. 742–751, Apr. 1989.

[12] CID FERNANDES, R.; MATEUS, A.; SODRÉ, L.; STASIŃSKA, G.; GOMES, J. M. Semi-empirical analysis of Sloan Digital Sky Survey galaxies - I. Spectral synthesis method. **Monthly Notices of the Royal Astronomical Society**, v. 358, p. 363–378, Apr. 2005.

[13] DE ROSA, G.; PETERSON, B. M.; ELY, J.; KRISS, G. A.; CRENSHAW, D. M.; HORNE, K.; KORISTA, K. T.; NETZER, H.; POGGE, R. W.; ARÉVALO, P.; BARTH, A. J.; BENTZ, M. C.; BRANDT, W. N.; BREEVELD, A. A.; BREWER, B. J.; DALLA BONTÀ, E.; DE LORENZO-CÁCERES, A.; DENNEY, K. D.; DIETRICH, M.; EDELSON, R.; EVANS, P. A.; FAUSNAUGH, M. M.; GEHRELS, N.; GELBORD, J. M.; GOAD, M. R.; GRIER, C. J.; GRUPE, D.; HALL, P. B.; KAASTRA, J.; KELLY, B. C.; KENNEA, J. A.; KOCHANEK, C. S.; LIRA, P.; MATHUR, S.; MCHARDY, I. M.; NOUSEK, J. A.; PANCOAST, A.; PAPADAKIS, I.; PEI, L.; SCHIMOIA, J. S.; SIEGEL, M.; STARKEY, D.; TREU, T.; UTTLEY, P.; VAUGHAN, S.; VESTERGAARD, M.; VILLFORTH, C.; YAN, H.; YOUNG, S.; ZU, Y. Space Telescope and Optical Reverberation Mapping Project.I. Ultraviolet Observations of the Seyfert 1 Galaxy NGC 5548 with the Cosmic Origins Spectrograph on Hubble Space Telescope. **Astrophysical Journal**, v. 806, p. 128, Jun. 2015.

[14] DENNEY, K. D.; PETERSON, B. M.; POGGE, R. W.; ADAIR, A.; ATLEE, D. W.; AU-YONG, K.; BENTZ, M. C.; BIRD, J. C.; BROKOFSKY, D. J.; CHISHOLM, E.; COMINS, M. L.; DIETRICH, M.; DOROSHENKO, V. T.; EASTMAN, J. D.; EFIMOV, Y. S.; EWALD, S.; FERBEY, S.; GASKELL, C. M.; HEDRICK, C. H.; JACKSON, K.; KLIMANOV, S. A.; KLIMEK, E. S.; KRUSE, A. K.; LADÉROUTE, A.; LAMB, J. B.; LEIGHLY, K.; MINEZAKI, T.; NAZAROV, S. V.; ONKEN, C. A.; PETERSEN, E. A.; PETERSON, P.; POINDEXTER, S.; SAKATA, Y.; SCHLESINGER, K. J.; SERGEEV, S. G.; SKOLSKI, N.; STIEGLITZ, L.; TOBIN, J. J.; UNTERBORN, C.; VESTERGAARD, M.; WATKINS, A. E.; WATSON, L. C.; YOSHII, Y. Reverberation Mapping Measurements of Black Hole Masses in Six Local Seyfert Galaxies. **Astrophysical Journal**, v. 721, p. 715–737, Sep. 2010.

[15] DI MATTEO, T.; COLBERG, J.; SPRINGEL, V.; HERNQUIST, L.; SIJACKI, D. Direct Cosmological Simulations of the Growth of Black Holes and Galaxies. **Astrophysical Journal**, v. 676, p. 33–53, Mar. 2008.

[16] DI MATTEO, T.; SPRINGEL, V.; HERNQUIST, L. Energy input from quasars regulates the growth and activity of black holes and their host galaxies. **Nature**, v. 433, p. 604–607, Feb. 2005.

[17] DIETRICH, M.; PETERSON, B. M.; GRIER, C. J.; BENTZ, M. C.; EASTMAN, J.; FRANK, S.; GONZALEZ, R.; MARSHALL, J. L.; DEPOY, D. L.; PRIETO, J. L. Optical Monitoring of the Broad-line Radio Galaxy 3C 390.3. **Astrophysical Journal**, v. 757, p. 53, Sep. 2012.

[18] ELITZUR, M.; HO, L. C.; TRUMP, J. R. Evolution of broad-line emission from active galactic nuclei. **Monthly Notices of the Royal Astronomical Society**, v. 438, p. 3340–3351, Mar. 2014.

[19] ELVIS, M.; WILKES, B. J.; MCDOWELL, J. C.; GREEN, R. F.; BECHTOLD, J.; WILLNER, S. P.; OEY, M. S.; POLOMSKI, E.; CUTRI, R. Atlas of quasar energy distributions. **Astrophysical Journal Supplement Series**, v. 95, p. 1–68, Nov. 1994.

[20] ERACLEOUS, M.; HALPERN, J. P. Doubled-peaked emission lines in active galactic nuclei. **Astrophysical Journal Supplement Series**, v. 90, p. 1–30, Jan. 1994.

[21] ERACLEOUS, M.; HALPERN, J. P. NGC 3065: A Certified LINER with Broad, Variable Balmer Lines. **Astrophysical Journal**, v. 554, p. 240–244, Jun. 2001.

[22] ERACLEOUS, M.; LIVIO, M.; HALPERN, J. P.; STORCHI-BERGMANN, T. Elliptical accretion disks in active galactic nuclei. **Astrophysical Journal**, v. 438, p. 610–622, Jan. 1995.

[23] FABER, S. M.; WILLMER, C. N. A.; WOLF, C.; KOO, D. C.; WEINER, B. J.; NEWMAN, J. A.; IM, M.; COIL, A. L.; CONROY, C.; COOPER, M. C.; DAVIS, M.; FINKBEINER, D. P.; GERKE, B. F.; GEBHARDT, K.; GROTH, E. J.; GUHATHAKURTA, P.; HARKER, J.; KAISER, N.; KASSIN, S.; KLEINHEINRICH, M.; KONIDARIS, N. P.; KRON, R. G.; LIN, L.; LUPPINO, G.; MADGWICK, D. S.; MEISENHEIMER, K.; NOESKE, K. G.; PHILLIPS, A. C.; SARAJEDINI, V. L.; SCHIAVON, R. P.; SIMARD, L.; SZALAY, A. S.; VOGT, N. P.; YAN, R. Galaxy Luminosity Functions to z˜1 from DEEP2 and COMBO-17: Implications for Red Galaxy Formation. **Astrophysical Journal**, v. 665, p. 265–294, Aug. 2007.

[24] FILIPPENKO, A. V.; SARGENT, W. L. W. A search for 'dwarf' Seyfert 1 nuclei. I - The initial data and results. **Astrophysical Journal Supplement Series**, v. 57, p. 503–522, Mar. 1985.

[25] FLOHIC, H. M. L. G. Variability of Double-Peaked Emission Lines in AGNs as a Probe of the Broad-Line Region Structure. **Baltic Astronomy**, v. 20, p. 386–391, Aug. 2011.

[26] FRANK, J.; KING, A.; RAINE, D. J. **Accretion Power in Astrophysics: Third Edition**: Jan. 2002.

[27] GASKELL, C. M.; PETERSON, B. M. The accuracy of cross-correlation estimates of quasar emission-line region sizes. **Astrophysical Journal Supplement Series**, v. 65, p. 1–11, Sep. 1987.

[28] GEZARI, S.; HALPERN, J. P.; ERACLEOUS, M. Long-Term Profile Variability of Double-peaked Emission Lines in Active Galactic Nuclei. **Astrophysical Journal Supplement Series**, v. 169, p. 167–212, Apr. 2007.

[29] GILBERT, A. M.; ERACLEOUS, M.; FILIPPENKO, A. V.; HALPERN, J. P. Accretion Disk Models and Long-Term Variability of Double-Peaked Balmer Line Profiles in AGNs. In: STRUCTURE AND KINEMATICS OF QUASAR BROAD LINE REGIONS, Gaskell, C. M.; Brandt, W. N.; Dietrich, M.; Dultzin-Hacyan, D.; Eracleous, M., editores, v. 175 of **Astronomical Society of the Pacific Conference Series**, p. 189, 1999.

[30] GRIER, C. J.; PETERSON, B. M.; HORNE, K.; BENTZ, M. C.; POGGE, R. W.; DENNEY, K. D.; DE ROSA, G.; MARTINI, P.; KOCHANEK, C. S.; ZU, Y.; SHAPPEE, B.; SIVERD, R.;

BEATTY, T. G.; SERGEEV, S. G.; KASPI, S.; ARAYA SALVO, C.; BIRD, J. C.; BORD, D. J.; BORMAN, G. A.; CHE, X.; CHEN, C.; COHEN, S. A.; DIETRICH, M.; DOROSHENKO, V. T.; EFIMOV, Y. S.; FREE, N.; GINSBURG, I.; HENDERSON, C. B.; KING, A. L.; MOGREN, K.; MOLINA, M.; MOSQUERA, A. M.; NAZAROV, S. V.; OKHMAT, D. N.; PEJCHA, O.; RAFTER, S.; SHIELDS, J. C.; SKOWRON, J.; SZCZYGIEL, D. M.; VALLURI, M.; VAN SADERS, J. L. The Structure of the Broad-line Region in Active Galactic Nuclei. I. Reconstructed Velocity-delay Maps. **Astrophysical Journal**, v. 764, p. 47, Feb. 2013.

[31] GRIER, C. J.; PETERSON, B. M.; POGGE, R. W.; DENNEY, K. D.; BENTZ, M. C.; MARTINI, P.; SERGEEV, S. G.; KASPI, S.; MINEZAKI, T.; ZU, Y.; KOCHANEK, C. S.; SIVERD, R.; SHAPPEE, B.; STANEK, K. Z.; ARAYA SALVO, C.; BEATTY, T. G.; BIRD, J. C.; BORD, D. J.; BORMAN, G. A.; CHE, X.; CHEN, C.; COHEN, S. A.; DIETRICH, M.; DOROSHENKO, V. T.; DRAKE, T.; EFIMOV, Y. S.; FREE, N.; GINSBURG, I.; HENDERSON, C. B.; KING, A. L.; KOSHIDA, S.; MOGREN, K.; MOLINA, M.; MOSQUERA, A. M.; NAZAROV, S. V.; OKHMAT, D. N.; PEJCHA, O.; RAFTER, S.; SHIELDS, J. C.; SKOWRON, J.; SZCZYGIEL, D. M.; VALLURI, M.; VAN SADERS, J. L. Reverberation Mapping Results for Five Seyfert 1 Galaxies. **Astrophysical Journal**, v. 755, p. 60, Aug. 2012.

[32] HALPERN, J. P. Line emission from another relativistic accretion disk - 3C 332. **Astrophysical Journal Letters**, v. 365, p. L51–L54, Dec. 1990.

[33] HALPERN, J. P.; ERACLEOUS, M. Emergence of double-peaked emission lines in the broad-line radio galaxy Pictor A. **Astrophysical Journal Letters**, v. 433, p. L17–L20, Sep. 1994.

[34] HECKMAN, T. M. Activity in the nuclei of normal galaxies. **Highlights of Astronomy**, v. 5, p. 185–190, 1980.

[35] HO, L. C. The Spectral Energy Distributions of Low-Luminosity Active Galactic Nuclei. **Astrophysical Journal**, v. 516, p. 672–682, May 1999.

[36] HO, L. C. "Low-State" Black Hole Accretion in Nearby Galaxies. **Astrophysics and Space Science**, v. 300, p. 219–225, Nov. 2005.

[37] HO, L. C. Nuclear Activity in Nearby Galaxies. **Annual Review of Astronomy and Astrophysics**, v. 46, p. 475–539, Sep. 2008.

[38] HO, L. C.; FILIPPENKO, A. V.; SARGENT, W. L. A search for 'dwarf' Seyfert nuclei. 2: an optical spectral atlas of the nuclei of nearby galaxies. **Astrophysical Journal Supplement Series**, v. 98, p. 477–593, Jun. 1995.

[39] HO, L. C.; FILIPPENKO, A. V.; SARGENT, W. L. W. A Search for "Dwarf" Seyfert Nuclei. III. Spectroscopic Parameters and Properties of the Host Galaxies. **Astrophysical Journal Supplement Series**, v. 112, p. 315–390, Oct. 1997a.

[40] HO, L. C.; FILIPPENKO, A. V.; SARGENT, W. L. W.; PENG, C. Y. A Search for "Dwarf" Seyfert Nuclei. IV. Nuclei with Broad Hα Emission. **Astrophysical Journal Supplement Series**, v. 112, p. 391–414, Oct. 1997b.

[41] HO, L. C.; RUDNICK, G.; RIX, H.-W.; SHIELDS, J. C.; MCINTOSH, D. H.; FILIPPENKO, A. V.; SARGENT, W. L. W.; ERACLEOUS, M. Double-peaked Broad Emission Lines in NGC 4450 and Other LINERS. **Astrophysical Journal**, v. 541, p. 120–125, Sep. 2000.

[42] KALBERLA, P. M. W.; BURTON, W. B.; HARTMANN, D.; ARNAL, E. M.; BAJAJA, E.; MORRAS, R.; PÖPPEL, W. G. L. The Leiden/Argentine/Bonn (LAB) Survey of Galactic HI. Final data release of the combined LDS and IAR surveys with improved stray-radiation corrections. **Astronomy and Astrophysics**, v. 440, p. 775–782, Sep. 2005.

[43] KAUFFMANN, G.; HECKMAN, T. M.; TREMONTI, C.; BRINCHMANN, J.; CHARLOT, S.; WHITE, S. D. M.; RIDGWAY, S. E.; BRINKMANN, J.; FUKUGITA, M.; HALL, P. B.; IVEZIĆ, Ž.; RICHARDS, G. T.; SCHNEIDER, D. P. The host galaxies of active galactic nuclei. **Monthly Notices of the Royal Astronomical Society**, v. 346, p. 1055–1077, Dec. 2003.

[44] KOSHIDA, S.; YOSHII, Y.; KOBAYASHI, Y.; MINEZAKI, T.; SAKATA, Y.; SUGAWARA, S.; ENYA, K.; SUGANUMA, M.; TOMITA, H.; AOKI, T.; PETERSON, B. A. Variation of Inner Radius of Dust Torus in NGC4151. **Astrophysical Journal Letters**, v. 700, p. L109–L113, Aug. 2009.

[45] LA MURA, G.; DI MILLE, F.; CIROI, S.; POPOVIĆ, L. Č.; RAFANELLI, P. Balmer Emission Line Profiles and Complex Properties of Broad-Line Regions in Active Galactic Nuclei. **Astrophysical Journal**, v. 693, p. 1437–1448, Mar. 2009.

[46] LEWIS, K. T.; ERACLEOUS, M.; STORCHI-BERGMANN, T. Long-term Profile Variability in Active Galactic Nucleus with Double-peaked Balmer Emission Lines. **Astrophysical Journal Supplement Series**, v. 187, p. 416–446, Apr. 2010.

[47] LYNDEN-BELL, D. Galactic Nuclei as Collapsed Old Quasars. **Nature**, v. 223, p. 690–694, Aug. 1969.

[48] MALKAN, M. A. The ultraviolet excess of luminous quasars. II - Evidence for massive accretion disks. **Astrophysical Journal**, v. 268, p. 582–590, May 1983.

[49] MARCONI, A.; AXON, D. J.; MAIOLINO, R.; NAGAO, T.; PASTORINI, G.; PIETRINI, P.; ROBINSON, A.; TORRICELLI, G. The Effect of Radiation Pressure on Virial Black Hole Mass Estimates and the Case of Narrow-Line Seyfert 1 Galaxies. **Astrophysical Journal**, v. 678, p. 693–700, May 2008.

[50] NARAYAN, R.; MCCLINTOCK, J. E. Advection-dominated accretion and the black hole event horizon. **New Astronomy Reviews**, v. 51, p. 733–751, May 2008.

[51] NEMMEN, R. S.; STORCHI-BERGMANN, T.; YUAN, F.; ERACLEOUS, M.; TERASHIMA, Y.; WILSON, A. S. Radiatively Inefficient Accretion Flow in the Nucleus of NGC 1097. In: REVISTA MEXICANA DE ASTRONOMIA Y ASTROFISICA CONFERENCE SERIES, v. 26 of **Revista Mexicana de Astronomia y Astrofisica Conference Series**, p. 204, Jun. 2006.

[52] NENKOVA, M.; IVEZIĆ, Ž.; ELITZUR, M. Dust Emission from Active Galactic Nuclei. **Astrophysical Journal Letters**, v. 570, p. L9–L12, May 2002.

[53] NETZER, H.; MARZIANI, P. The Effect of Radiation Pressure on Emission-line Profiles and Black Hole Mass Determination in Active Galactic Nuclei. **Astrophysical Journal**, v. 724, p. 318–328, Nov. 2010.

[54] O'BRIEN, P. T.; DIETRICH, M.; LEIGHLY, K.; ALLOIN, D.; CLAVEL, J.; CRENSHAW, D. M.; HORNE, K.; KRISS, G. A.; KROLIK, J. H.; MALKAN, M. A.; NETZER, H.; PETERSON, B. M.; REICHERT, G. A.; RODRíGUEZ-PASCUAL, P. M.; WAMSTEKER, W.; ANDERSON, K. S. J.; BOCHKAREV, N. G.; CHENG, F.-Z.; FILIPPENKO, A. V.; GASKELL, C. M.; GEORGE, I. M.; GOAD, M. R.; HO, L. C.; KASPI, S.; KOLLATSCHNY, W.; KORISTA, K. T.; MACALPINE, G.; MARLOW, D.; MARTIN, P. G.; MORRIS, S. L.; POGGE, R. W.; QIAN, B.-C.; RECONDO-GONZALEZ, M. C.; RODRíGUEZ ESPINOSA, J. M.; SANTOS-LLEÓ, M.; SHAPOVALOVA, A. I.; SHULL, J. M.; STIRPE, G. M.; SUN, W.-H.; TURNER, T. J.; VIO, R.; WAGNER, S.; WANDERS, I.; WILLS, K. A.; WU, H.; XUE, S.-J.; ZOU, Z.-L. Steps toward Determination of the Size and Structure of the Broad-Line Region in Active Galactic Nuclei. XIII. Ultraviolet Observations of the Broad-Line Radio Galaxy 3C 390.3. **Astrophysical Journal**, v. 509, p. 163–176, Dec. 1998.

[55] OKE, J. B. Faint spectrophotometric standard stars. **Astronomical Journal**, v. 99, p. 1621–1631, May 1990.

[56] PEREZ, E.; MEDIAVILLA, E.; PENSTON, M. V.; TADHUNTER, C.; MOLES, M. An accretion disc in the broad-line radio galaxy 3C 390.3? **Monthly Notices of the Royal Astronomical Society**, v. 230, p. 353–362, Feb. 1988.

[57] PETERSON, B. M. **An Introduction to Active Galactic Nuclei**: Feb. 1997.

[58] PETERSON, B. M.; BERLIND, P.; BERTRAM, R.; BISCHOFF, K.; BOCHKAREV, N. G.; BORISOV, N.; BURENKOV, A. N.; CALKINS, M.; CARRASCO, L.; CHAVUSHYAN, V. H.; CHORNOCK, R.; DIETRICH, M.; DOROSHENKO, V. T.; EZHKOVA, O. V.; FILIPPENKO, A. V.; GILBERT, A. M.; HUCHRA, J. P.; KOLLATSCHNY, W.; LEONARD, D. C.; LI, W.; LYUTY, V. M.; MALKOV, Y. F.; MATHESON, T.; MERKULOVA, N. I.; MIKHAILOV, V. P.; MODJAZ, M.; ONKEN, C. A.; POGGE, R. W.; PRONIK, V. I.; QIAN, B.; ROMANO, P.; SERGEEV, S. G.; SERGEEVA, E. A.; SHAPOVALOVA, A. I.; SPIRIDONOVA, O. I.; TAO, J.; TOKARZ, S.; VALDES, J. R.; VLASIUK, V. V.; WAGNER, R. M.; WILKES, B. J. Steps toward Determination of the Size and Structure of the Broad-Line Region in Active Galactic Nuclei. XVI. A 13 Year Study of Spectral Variability in NGC 5548. **Astrophysical Journal**, v. 581, p. 197–204, Dec. 2002.

[59] PETERSON, B. M.; FERRARESE, L.; GILBERT, K. M.; KASPI, S.; MALKAN, M. A.; MAOZ, D.; MERRITT, D.; NETZER, H.; ONKEN, C. A.; POGGE, R. W.; VESTERGAARD, M.; WANDEL, A. Central Masses and Broad-Line Region Sizes of Active Galactic Nuclei. II. A Homogeneous Analysis of a Large Reverberation-Mapping Database. **Astrophysical Journal**, v. 613, p. 682–699, Oct. 2004.

[60] PETERSON, B. M.; WANDEL, A. Evidence for Supermassive Black Holes in Active Galactic Nuclei from Emission-Line Reverberation. **Astrophysical Journal Letters**, v. 540, p. L13–L16, Sep. 2000.

[61] PETERSON, B. M.; WANDERS, I.; HORNE, K.; COLLIER, S.; ALEXANDER, T.; KASPI, S.; MAOZ, D. On Uncertainties in Cross-Correlation Lags and the Reality of Wavelength-dependent Continuum Lags in Active Galactic Nuclei. **Publications of the Astronomical Society of the Pacific**, v. 110, p. 660–670, Jun. 1998.

[62] POOLE, T. S.; BREEVELD, A. A.; PAGE, M. J.; LANDSMAN, W.; HOLLAND, S. T.; ROMING, P.; KUIN, N. P. M.; BROWN, P. J.; GRONWALL, C.; HUNSBERGER, S.; KOCH, S.; MASON, K. O.; SCHADY, P.; VANDEN BERK, D.; BLUSTIN, A. J.; BOYD, P.; BROOS, P.; CARTER, M.; CHESTER, M. M.; CUCCHIARA, A.; HANCOCK, B.; HUCKLE, H.; IMMLER, S.; IVANUSHKINA, M.; KENNEDY, T.; MARSHALL, F.; MORGAN, A.; PANDEY, S. B.; DE PASQUALE, M.; SMITH, P. J.; STILL, M. Photometric calibration of the Swift ultraviolet/optical telescope. **Monthly Notices of the Royal Astronomical Society**, v. 383, p. 627–645, Jan. 2008.

[63] POPOVIC, L. C.; MEDIAVILLA, E.; BON, E.; ILIC, D. Emission Line Region in a sample of 12 active galactic nuclei. In: THE INTERPLAY AMONG BLACK HOLES, STARS AND ISM IN GALACTIC NUCLEI, Storchi-Bergmann, T.; Ho, L. C.; Schmitt, H. R., editores, v. 222 of **IAU Symposium**, p. 355–356, Nov. 2004.

[64] PRINGLE, J. E.; REES, M. J. Accretion Disc Models for Compact X-Ray Sources. **Astronomy and Astrophysics**, v. 21, p. 1, Oct. 1972.

[65] RIFFEL, R. A.; STORCHI-BERGMANN, T.; MCGREGOR, P. J. The Dusty Nuclear Torus in NGC 4151: Constraints from Gemini Near-Infrared Integral Field Spectrograph Observations. **Astrophysical Journal**, v. 698, p. 1767–1770, Jun. 2009.

[66] RIFFEL, R. A.; STORCHI-BERGMANN, T.; RIFFEL, R. An Outflow Perpendicular to the Radio Jet in the Seyfert Nucleus of NGC 5929. **Astrophysical Journal Letters**, v. 780, p. L24, Jan. 2014.

[67] ROBINSON, E. L. The structure of cataclysmic variables. **Annual Review of Astronomy and Astrophysics**, v. 14, p. 119–142, 1976.

[68] ROMING, P. W. A.; KENNEDY, T. E.; MASON, K. O.; NOUSEK, J. A.; AHR, L.; BINGHAM, R. E.; BROOS, P. S.; CARTER, M. J.; HANCOCK, B. K.; HUCKLE, H. E.; HUNSBERGER, S. D.; KAWAKAMI, H.; KILLOUGH, R.; KOCH, T. S.; MCLELLAND, M. K.; SMITH, K.; SMITH, P. J.; SOTO, J. C.; BOYD, P. T.; BREEVELD, A. A.; HOLLAND, S. T.; IVANUSHKINA, M.; PRYZBY, M. S.; STILL, M. D.; STOCK, J. The Swift Ultra-Violet/Optical Telescope. **Space Science Reviews**, v. 120, p. 95–142, Oct. 2005.

[69] ROMING, P. W. A.; KOCH, T. S.; OATES, S. R.; PORTERFIELD, B. L.; VANDEN BERK, D. E.; BOYD, P. T.; HOLLAND, S. T.; HOVERSTEN, E. A.; IMMLER, S.; MARSHALL, F. E.; PAGE, M. J.; RACUSIN, J. L.; SCHNEIDER, D. P.; BREEVELD, A. A.; BROWN,

P. J.; CHESTER, M. M.; CUCCHIARA, A.; DEPASQUALE, M.; GRONWALL, C.; HUNSBERGER, S. D.; KUIN, N. P. M.; LANDSMAN, W. B.; SCHADY, P.; STILL, M. The First Swift Ultraviolet/Optical Telescope GRB Afterglow Catalog. **Astrophysical Journal**, v. 690, p. 163–188, Jan. 2009.

[70] SALPETER, E. E. Accretion of Interstellar Matter by Massive Objects. **Astrophysical Journal**, v. 140, p. 796–800, Aug. 1964.

[71] SCHIMOIA, J. S.; STORCHI-BERGMANN, T.; NEMMEN, R. S.; WINGE, C.; ERACLEOUS, M. Short Timescale Variations of the Hα Double-peaked Profile of the Nucleus of NGC 1097. **Astrophysical Journal**, v. 748, p. 145, Apr. 2012.

[72] SCHNORR-MÜLLER, A.; STORCHI-BERGMANN, T.; NAGAR, N. M.; FERRARI, F. Gas inflows towards the nucleus of the active galaxy NGC 7213. **Monthly Notices of the Royal Astronomical Society**, v. 438, p. 3322–3331, Mar. 2014a.

[73] SCHNORR-MÜLLER, A.; STORCHI-BERGMANN, T.; NAGAR, N. M.; ROBINSON, A.; LENA, D.; RIFFEL, R. A.; COUTO, G. S. Feeding and feedback in the inner kiloparsec of the active galaxy NGC 2110. **Monthly Notices of the Royal Astronomical Society**, v. 437, p. 1708–1724, Jan. 2014b.

[74] SERGEEV, S. G.; DOROSHENKO, V. T.; DZYUBA, S. A.; PETERSON, B. M.; POGGE, R. W.; PRONIK, V. I. Thirty Years of Continuum and Emission-Line Variability in NGC 5548. **Astrophysical Journal**, v. 668, p. 708–720, Oct. 2007.

[75] SHAKURA, N. I.; SUNYAEV, R. A. Black holes in binary systems. Observational appearance. **Astronomy and Astrophysics**, v. 24, p. 337–355, 1973.

[76] SHAPOVALOVA, A. I.; POPOVIĆ, L. Č.; BURENKOV, A. N.; CHAVUSHYAN, V. H.; ILIĆ, D.; KOLLATSCHNY, W.; KOVAČEVIĆ, A.; BOCHKAREV, N. G.; VALDÉS, J. R.; TORREALBA, J.; PATIÑO-ÁLVAREZ, V.; LEÓN-TAVARES, J.; BENITEZ, E.; CARRASCO, L.; DULTZIN, D.; MERCADO, A.; ZHDANOVA, V. E. Spectral optical monitoring of a double-peaked emission line AGN Arp 102B. Variability of spectral lines and continuum. **Astronomy and Astrophysics**, v. 559, p. A10, Nov. 2013.

[77] SHIELDS, J. C.; RIX, H.-W.; MCINTOSH, D. H.; HO, L. C.; RUDNICK, G.; FILIPPENKO, A. V.; SARGENT, W. L. W.; SARZI, M. Evidence for a Black Hole and Accretion Disk in the LINER NGC 4203. **Astrophysical Journal Letters**, v. 534, p. L27–L30, May 2000.

[78] SMITH, J. E.; ROBINSON, A.; ALEXANDER, D. M.; YOUNG, S.; AXON, D. J.; CORBETT, E. A. Seyferts on the edge: polar scattering and orientation-dependent polarization in Seyfert 1 nuclei. **Monthly Notices of the Royal Astronomical Society**, v. 350, p. 140–160, May 2004.

[79] STAUFFER, J.; SCHILD, R.; KEEL, W. ARP 102B - A new and unusual broad-line galaxy. **Astrophysical Journal**, v. 270, p. 465–470, Jul. 1983.

[80] STORCHI-BERGMANN, T. Feeding and Feedback in nearby AGN - Comparison with the Milky Way center. **ArXiv e-prints**, Dec. 2014.

[81] STORCHI-BERGMANN, T.; BALDWIN, J. A.; WILSON, A. S. Double-peaked broad line emission from the LINER nucleus of NGC 1097. **Astrophysical Journal Letters**, v. 410, p. L11–L14, Jun. 1993.

[82] STORCHI-BERGMANN, T.; ERACLEOUS, M.; LIVIO, M.; WILSON, A. S.; FILIPPENKO, A. V.; HALPERN, J. P. The variability of the double-peaked Balmer lines in the active nucleus of NGC 1097. **Astrophysical Journal**, v. 443, p. 617–624, Apr. 1995.

[83] STORCHI-BERGMANN, T.; NEMMEN DA SILVA, R.; ERACLEOUS, M.; HALPERN, J. P.; WILSON, A. S.; FILIPPENKO, A. V.; RUIZ, M. T.; SMITH, R. C.; NAGAR, N. M. Evolution of the Nuclear Accretion Disk Emission in NGC 1097: Getting Closer to the Black Hole. **Astrophysical Journal**, v. 598, p. 956–968, Dec. 2003.

[84] STRATEVA, I. V.; BRANDT, W. N.; ERACLEOUS, M.; GARMIRE, G. A Chandra Look at Five of the Broadest Double-Peaked Balmer Line Emitters. **Astrophysical Journal**, v. 687, p. 869–883, Nov. 2008.

[85] STRATEVA, I. V.; BRANDT, W. N.; ERACLEOUS, M.; SCHNEIDER, D. P.; CHARTAS, G. The X-Ray Properties of Active Galactic Nuclei with Double-peaked Balmer Lines. **Astrophysical Journal**, v. 651, p. 749–766, Nov. 2006.

[86] STRATEVA, I. V.; STRAUSS, M. A.; HAO, L.; SCHLEGEL, D. J.; HALL, P. B.; GUNN, J. E.; LI, L.-X.; IVEZIĆ, Ž.; RICHARDS, G. T.; ZAKAMSKA, N. L.; VOGES, W.; ANDERSON, S. F.; LUPTON, R. H.; SCHNEIDER, D. P.; BRINKMANN, J.; NICHOL, R. C. Double-peaked Low-Ionization Emission Lines in Active Galactic Nuclei. **Astronomical Journal**, v. 126, p. 1720–1749, Oct. 2003.

[87] SUGANUMA, M.; YOSHII, Y.; KOBAYASHI, Y.; MINEZAKI, T.; ENYA, K.; TOMITA, H.; AOKI, T.; KOSHIDA, S.; PETERSON, B. A. Reverberation Measurements of the Inner Radius of the Dust Torus in Nearby Seyfert 1 Galaxies. **Astrophysical Journal**, v. 639, p. 46–63, Mar. 2006.

[88] SULENTIC, J. W.; MARZIANI, P.; ZWITTER, T.; CALVANI, M. Pictor A: A new double-peaked emission-line quasar. **Astrophysical Journal Letters**, v. 438, p. L1–L4, Jan. 1995.

[89] SYER, D.; CLARKE, C. J. The viscous evolution of elliptical accretion discs. **Monthly Notices of the Royal Astronomical Society**, v. 255, p. 92–104, Mar. 1992.

[90] VANDEN BERK, D. E.; RICHARDS, G. T.; BAUER, A.; STRAUSS, M. A.; SCHNEIDER, D. P.; HECKMAN, T. M.; YORK, D. G.; HALL, P. B.; FAN, X.; KNAPP, G. R.; ANDERSON, S. F.; ANNIS, J.; BAHCALL, N. A.; BERNARDI, M.; BRIGGS, J. W.; BRINKMANN, J.; BRUNNER, R.; BURLES, S.; CAREY, L.; CASTANDER, F. J.; CONNOLLY, A. J.; CROCKER, J. H.; CSABAI, I.; DOI, M.; FINKBEINER, D.; FRIEDMAN, S.; FRIEMAN, J. A.; FUKUGITA, M.; GUNN, J. E.; HENNESSY, G. S.; IVEZIĆ, Ž.; KENT, S.; KUNSZT, P. Z.;

LAMB, D. Q.; LEGER, R. F.; LONG, D. C.; LOVEDAY, J.; LUPTON, R. H.; MEIKSIN, A.; MERELLI, A.; MUNN, J. A.; NEWBERG, H. J.; NEWCOMB, M.; NICHOL, R. C.; OWEN, R.; PIER, J. R.; POPE, A.; ROCKOSI, C. M.; SCHLEGEL, D. J.; SIEGMUND, W. A.; SMEE, S.; SNIR, Y.; STOUGHTON, C.; STUBBS, C.; SUBBARAO, M.; SZALAY, A. S.; SZOKOLY, G. P.; TREMONTI, C.; UOMOTO, A.; WADDELL, P.; YANNY, B.; ZHENG, W. Composite Quasar Spectra from the Sloan Digital Sky Survey. **Astronomical Journal**, v. 122, p. 549–564, Aug. 2001.

[91] WHITE, R. J.; PETERSON, B. M. Comments on cross-correlation methodology in variability studies of active galactic nuclei. **Publications of the Astronomical Society of the Pacific**, v. 106, p. 879–889, Aug. 1994.

[92] ZEL'DOVICH, Y. B. The Fate of a Star and the Evolution of Gravitational Energy Upon Accretion. **Soviet Physics Doklady**, v. 9, p. 195, Sep. 1964.